JPL Document D-94792

Exoplanet Exploration Coronagraph Technology

Technology Milestone #3A
Final Report

Coronagraph Starlight Suppression Model Validation

Stuart Shaklan, Erkin Sidick, Eric Cady, Brian Kern, Kunjithapatham Balasubramanian, John Krist

June 17, 2015

Approvals

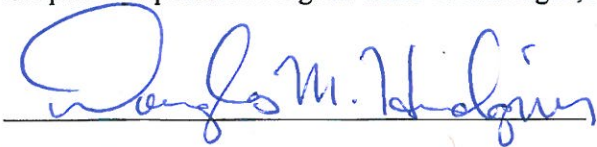Released by:

(signature)   6-29-2015

Stuart Shaklan
Principal Investigator, JPL

Approved by:

(signature)   6/29/15

Nick Siegler
Exoplanet Exploration Program Chief Technologist, JPL

(signature)   7/29/2015

Douglas Hudgins
Exoplanet Exploration Program Scientist, NASA HQ

Acknowledgement

The work reported here was carried out in large part by Erkin Sidick and Eric Cady. Eric ran the testbed for all of the experiments and performed all of the preprocessing of the data to create the dark holes. He ensured that the data was of the highest quality and kept detailed records that have proved invaluable in subsequent analysis. Eric also performed the Coherent and Incoherent Estimation analysis reported in Section V.F, and he wrote the SPIE paper on the subject.

Erkin Sidick tirelessly performed all of the analysis reported in Sections V.A-E. He wrote all of the MATLAB analysis code and tested it along with the MACOS model, comparing results to the PROPER model created by John Krist. He generated every figure and table in these sections, and much of the text. Erkin worked with great transparency and thoroughness, and was always open to peeling back another layer of the HCIT onion when necessary. All who work with him appreciate his positive attitude and work ethic. Erkin wrote the initial Milestone 3A modeling paper for the 2011 SPIE meeting, and several subsequent SPIE papers reporting the results of this TDEM. He will author the final two Milestone 3A papers at the 2015 SPIE meeting.

Other important contributors include Brian Kern, whose knowledge of the HCIT testbed and coronagraph behavior were critical to the success of the tests and analyses; John Krist, who worked closely with us to ensure the accuracy and consistency of our models; and K. "Bala" Balasubramanian, who created and calibrated the coherent spots on the Mask, and meticulously characterized the masks using optical, scanning electron, and atomic force microscopes.

Table of Contents

I.   Introduction

The goal of our work was to address Technology Milestone 3A (MS 3A) by demonstrating the ability of modeling tools to predict the performance sensitivities of a high-contrast imaging system at levels consistent with exoplanet detection requirements. In support of this milestone, we have carried out a battery of tests on the High Contrast Imaging Testbed (HCIT) and used optical models to predict the results. The tests addressed the major items that limit coronagraph performance, including pointing errors, defocus, image plane mask contamination, optical bandwidth, wavefront estimation, and wavefront control. This document is the final report on the results of the testing and model validation.

This report is organized as follows: First we state the milestone and the success criteria from the MS 3A White Paper. In Section II we describe the testbed and testbed models, operating assumptions, and approximations. Section III is an overview of the tests performed, including dates, filenames, and experimental conditions. Then in Section IV we present temperature data for the full run and selected experiments. The key experimental results are detailed in Section V. Many of the results of our MS 3A work have been reported in the literature. These papers are attached as Appendices to this report and are frequently reference throughout.   Additional appendices describe the chromatic and photometric calibrations.   These calibrations are unchanged from our earlier TDEM work on "Advanced Speckle Sensing for Internal Coronagraphs" (ASSIC) and the appendix is copied from the ASSIC final report.

Milestone statement

A set of 3 technology milestones for optical direct imaging was defined in Dooley (2005). Milestone 1 was the demonstration of 10^{-9} contrast imaging in monochromatic light, at a working angle of 4 λ/D (roughly the 4th Airy ring, Trauger, 2006). Milestone 2 required the same contrast and working angle but over a 10% optical band (Kern, 2008). The successful completions of Milestones 1 and 2 were certified by an independent review board in 2006 and 2008, respectively.

These milestones were achieved with the assistance of high-fidelity models that guided the design, implementation, and operation of the testbed. The purpose of Milestone 3 is to show the ability of the models to predict performance. Milestone 3 was originally drafted in two parts, A and B. Part A addresses model fidelity specifically for HCIT, while part B applies the models to the on-orbit prediction of a space mission. The milestone requirements are:

Milestone MS 3A: Demonstrate that starlight suppression performance predictions from high-fidelity optical models of the HCIT, utilizing measured data on specific testbed components, are consistent with actual measured results on the testbed. Correlation of model predictions with experimental testbed results validates models at a baseline contrast ratio of better than 1 $\times 10^{-9}$ (goal 1 $\times 10^{-10}$) over a 60-nm bandwidth.

Milestone MS 3B: Demonstrate, using the modeling approach validated against the HCIT performance combined with appropriate telescope models and the current mission error budget, that TPF-C could achieve a baseline contrast of 1 $\times 10^{-10}$ over the required optical bandwidth

necessary for detecting Earth-like planets, characterizing their properties and assessing habitability.

The focus in our MS 3A experiments was coronagraph model sensitivity validation in the HCIT testbed. Our bandpass was from 760 – 840 nm, a 10% bandpass divided equally into five 2% bands. (While the requirement specifies a bandwidth of 60 nm, we interpreted this to mean a minimum bandwidth.) These are the same filters that were used in the Milestone 2 experiments. The minimum working angle was $4\lambda/D$ at 800 nm. We used both the Milestone 2 nickel-on-glass occulting mask, as well as a second one manufactured to the same specifications. The overall layout of the testbed was similar to the Milestone 2 work with one important difference: we used a 64 x 64 element deformable mirror (DM) stopped down to a 48 x 48 mm clear aperture. This changed the f/# of the system such that the 50% transmission point on the mask was at 3.5 λ/D at 800 nm.

The success criteria for achieving the milestone were defined in the Milestone 3A White Paper. It stated; the measurement to be evaluated is: the comparison between the contrast

SUMMARY TABLE

OPEN-LOOP TEST: PERTURBATION OCCURS AFTER WFCS HAS SET THE DM.

Test	Tolerancing and Sensitiivity	Status	Result	Report Guide	Comment
Source Lateral and Focus Position	How does contrast depend on a change in the source lateral position and mask focus?	Completed. Published in SPIE vol 8864 (2013).	Model prediction errors < 1e-9 for lateral translations +/- 1 um. Most predictions within factor of 2 of observations.	Section V.A, Figures 14 and 15, Table 9.	Significant difference in MACOS and PROPER predictions for lateral motion, even though on-axis cases agree to a few percent.

CLOSED LOOP TESTS: WFCS TURNED ON DURING/AFTER PERTURBATION IS INTRODUCED

Test	Tolerancing and Sensitivity	Status	Result	Report Guide	Comment
Occulter Mask Defect	What is the contrast when the occulter has an obscuring spot?	Completed. Two opaque spots of 8x8 um were written on the mask. Published in SPIE vol 8864. (2013).	1e-6 speckle in image plane. Model predictions over 10% band accurate to 50% for contrast range 1e-8 -1e-6 in composite broadband image. Model - data always > 1e-9.	Section V.B, Figures 17 and 18, Table 10.	Spots were characterized with AFM and SEM. OD was derived from spot height and fed to the model. Model was not iterated.
Dark Hole Size	How does contrast depend on the number of actuators compared to the size of the dark hole?	Completed study of size of dark hole. Published in SPIE vol. 8864 (2014).	Predictions good to < 1e-9 contrast over full dark hole up to 20 λ/D when a model of local mask defects is used.	Section V.C, Figure 24, Table 11	Dark holes up to 24 l/d were formed. Contamination/defect model assumes that optical path picks up pi phase for OD=1.
Bandwidth	What is the best contrast achievable at a given bandwidth?	Completed multiple cases of control in single narrow and multiple narrow bands.	Predictions usually good to < 1e-9 with local mask defect model. But poor agreement when only ends of 10% bandpass are used for control.	Section V.D, Table 12, Figures 26-31	Model predicts best contrast should always be in the measured band. Experimentally this was not always the case.
Pegged Actuators	How severe is degradation due to a dead actuator?	Completed multiple cases with pairs of actuators pegged at +/- 132 nm.	Predictions good to < 1e-9 when a model of local mask defects is used. Pupil map in good agreement around pegged actuators, poor agreement around edge of DM.	Section V.E, Figure 36	Overall dark hole contrast roughly unchanged as dark hole grows to Nyqust limit of DM.
Incoherent Light Estimation Accuracy	How accurate is the coherent light estimator?	Completed, but without planet light. Published in SPIE vol. 9143 (2014).	~25% of coherent signal is incorrectly treated as incoherent in a 10% bandpass. Estimation good to 2e-10 contrast in 2% bandpass.	Section V.F, Figures 38 and 39	Incoherent light shown to be stable for days, but unexplained spatial variation when comparing spectral bands.

2

predicted by the model and the contrast achieved in the experiment. *In each open loop test, the perturbation to be introduced shall change the model contrast from nominal by at least s x 10^-9, where s is the step number (1, 2, 3) and shall be in agreement with the model prediction to 1 x 10^-9. In closed loop tests, the change in model contrast is evaluated after the wavefront control system (WFCS) has operated. Closed loop perturbations shall change the post-WFCS model contrast by at least 2 x 10^-9 from nominal. Multiple step closed loop tests do not necessarily involve progressive delta-contrast steps.* Predicting a contrast of 3 x 10^{-9} to a level of 1 x 10^{-9} represents 33% agreement between the model and the experiment. This puts us within the factor of 2 model reserve factor that has been carried in the TPF-C error budget.

The main results of our work are summarized here and in the Summary Table, above. We performed open loop tests, in which the mask was translated along, and orthogonal to, the optical axis. These tests were performed using a 2% wide optical filter with the wavefront control turned off once the dark hole had been formed. Both MACOS and PROPER models were compared to the experiment. The main results were that the quadratic coefficient of the contrast with lateral translation was predicted to 67%, the predicted lateral location of the minimum flux was off by a factor of up to 5 at different axial offsets, and the minimum contrast achieved was (for the PROPER model) correct to better than $5x10^{-10}$ for contrast ranging up to 10^{-8}. The minimum contrast value prediction includes an offset of ~$4x10^{-10}$ derived from the experiment to account for incoherent light in the system since our models only predict the coherent light level. *The open loop test achieved better than 10^{-9} model vs. experiment agreement averaged over the full dark hole when the contrast changed by < $3x10^{-9}$. Agreement was worse than 1e-9 in the "small box" region 4-5 λ/D.*

In the closed loop experiments we measured absolute contrast achieved after wavefront control. Without invoking a model of localized imperfections, e.g. blemishes and particulates, on the coronagraph mask, the predicted coherent broadband contrast, and the coherent contrast in any 2% band, was typically an order of magnitude better than the achieved experimental contrast. It is only by invoking a model of localized mask imperfections, based on microscope images of the mask, that the observed contrast floor and the dependence of contrast on the varied parameter could be shown to agree with the models. In this model, it is assumed that the light passing through a semi-transparent particle has a phase shift that is proportional to the optical density (OD), defined by $OD = -\log_{10}(T)$, where T is the optical transmission. We found that a phase shift given by $\phi = \pi*OD$ was the best match to the measured dark hole. However, we are not currently able to justify the phase model through physics arguments. Further, we based our model on microscope images limited to ~1 um in spatial resolution. Many of the defects are smaller than this, and thus the model does not capture the actual linear dependence of phase on measured OD.

We added opaque spots to a coronagraph mask and measured the chromaticity of the resulting image plane speckle. The spots were 6 x 6 micron platinum squares. These dimensions were chosen as the near-minimum to reliably create and characterize the spots for input to our models. The spots caused a speckle to form with a contrast of ~10^{-6}. Thus it was well above the $3x10^{-9}$ level called for in the success criteria. The model predicted the measured contrast at all bands with a worst-case error factor of < 3. At these levels of contrast, 100x above the experiment noise floor, the mask imperfection model was of no consequence. *Model vs experiment*

agreement was typically a few x 10^{-9} over the full dark hole, and within a factor of 2 at the 1e-6 contrast scatter peak.

For the pegged actuator and dark hole size tests, we found that the dark hole floor changed by less than $3x10^{-9}$ over the full range of the tests, including dark holes formed at the theoretical outer working angle set by the number of DM actuators, and for up to 4 pairs of "pegged" actuators. Thus we were unable to verify the models in the manor called out in the milestone statement. For these tests the models agreed with the experimental data to within a factor of 2 (again, only after invoking a model of mask imperfections). Qualitatively, the models do a beautiful job of predicting the behavior of the DMs around the pegged actuators, but they do a poor job of predicting the behavior around the edge of the DM. The edge of the DM is, by virtue of the chromatic smearing of the pupil image at the Lyot plane, where much of the broad-band wavefront balancing takes place. *Model vs. experiment agreement was better than 1e-9 for dark holes up to 20 λ/D wide.*

For the bandwidth test, in which wavefront control was accomplished using one or more of the five 2%-wide filters, the contrast was a strong function of the wavelength and this was generally predicted by the models to within a factor of 2 over contrasts ranging from $< 5x10^{-10}$ to $> 2x10^{-8}$. We found, however, that when the two end-bands were controlled, the model failed to qualitatively predict the observed behavior of contrast vs. wavelength. *Model vs. experiment agreement was usually better than 10^{-9}, though this is largely a function of the mask contamination model.*

Finally, due to hardware failures, we were unable to perform the test with an artificial planet adjacent to the artificial star. However, we were still able to determine the accuracy of the estimate of coherent light (and thus the ability to separate planet light from instrument-induced speckles) by tracking the total light level as the testbed converged. This led to an observation of a chromatic dependence of the incoherent light spatial morphology which we have not been able to explain through models.

II.   Experiment Overview

The schematic diagram of the HCIT layout in the *xz*-plane is shown in Figure 1. Artificial starlight is created by a 5μm pinhole illuminated by an optical fiber illuminated in a 2% band through one of the aforementioned filters. An off-axis parabolic mirror (OAP1) collimates the light from the pinhole and directs it to a high-density, 64x64 actuator deformable mirror (DM), which performs wavefront control. A circular aperture mask on the DM defines the system pupil of the HCIT, and can have a diameter of up to *D*=64mm. However, the current HCIT was implemented with *D*=48mm inscribed in an area covered by 48x48 actuators, so we will use this *D* value in the simulations of this paper. After the DM, the collimated light is imaged onto the focal plane of the occulting mask by OAP2 and a flat-mirror (FM). The occulting mask attenuates the starlight, and almost has no effect on the light of a planet if present. The "back-end" of the system, from the occulting mask to the back focal plane, supports experimentation with diverse coronagraph configurations and apodizations. OAP3 re-collimates the light passing through the occulter mask and forms a same-size sharp image of the DM pupil at the Lyot plane. A Lyot stop blocks the ring-like residual light diffracted off the occulting mask while letting most of the planet light through. After OAP4 forms an image from the remaining stellar and

planet lights, it is then magnified (M ≈3) by the OAP5-OAP6 pair for proper sampling on the CCD science camera located at the back focal plane. More information on the HCIT and the DM can be found in Trauger (2006) and Kern (2008).
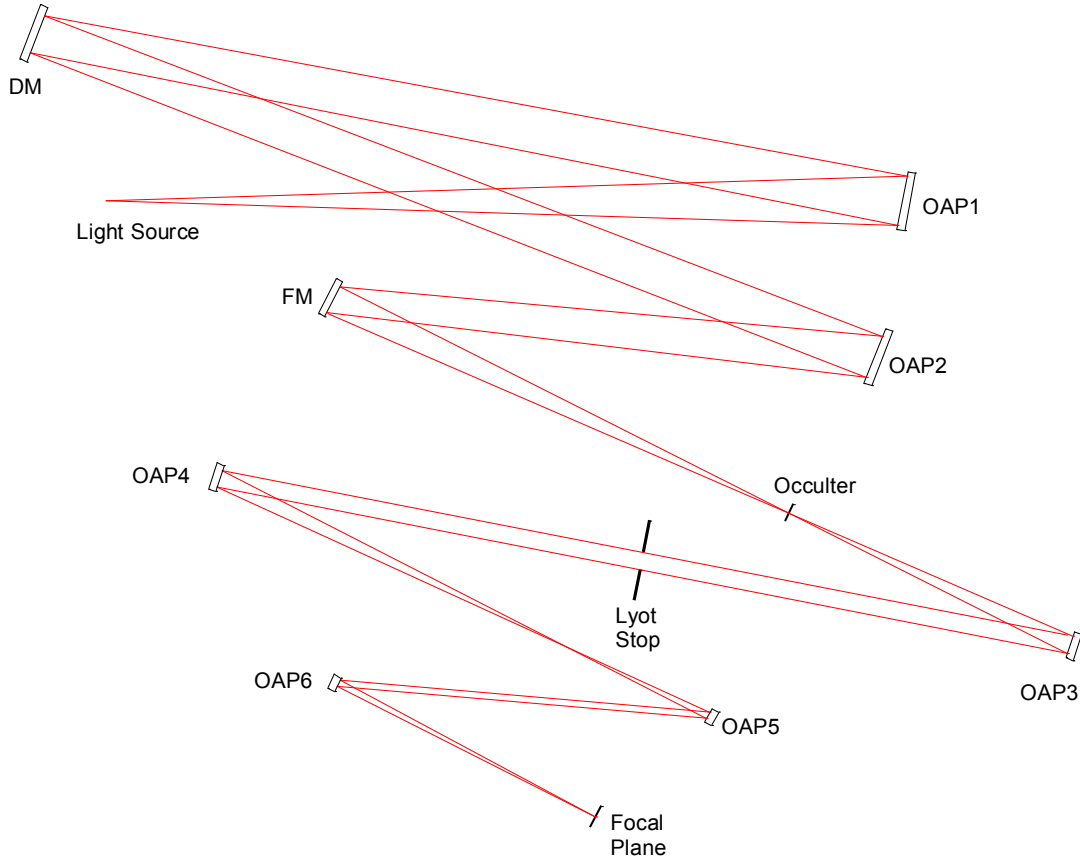

Figure 1 Schematic diagram of the High Contrast Imaging Testbed (HCIT) layout. The light source ("starlight") is a 50m pinhole illuminated by an optical fiber, and a CCD science camera is located at the back focal plane for detecting the image of the "starlight."

A.   Occulting Mask

The HCIT uses a modified one-dimensional band-limited occulter whose OD profile at wavelength $\lambda = 800$nm is truncated and smoothed by convolution with a Gaussian function. Specifically, the sinc^2 intensity transmission profile is $T_{\mathrm{sinc}}(x) = \{1-[\sin(\pi x/w)/(\pi x/w)]^2\}^2$, $\mathrm{OD}_{\mathrm{sinc}}(x) = -\log_{10} T_{\mathrm{sinc}}(x)$, with $w = 142$μm. The truncation and smoothing gives $\mathrm{OD}_{\mathrm{rel}}(x) = \min[\mathrm{OD}_{\mathrm{sinc}}(x), 8] \otimes G(x)$ with $G(x) = (2\pi\sigma^2)^{-1/2} \exp[-x^2/(2\sigma^2)]$, $\sigma = 9$μm. For practical reasons, the maximum transmission is often less than unity, so the final transmission is $T(x) = T_0 10^{-\mathrm{ODrel}(x)}$, for some maximum transmission T_0. The above two OD profiles are shown graphically in Fig. 2(a). The spatially-varying transmission profile is optically realized by spatially varying the thicknesses of Ni layers, deposited on a fused quartz substrate. Because Ni
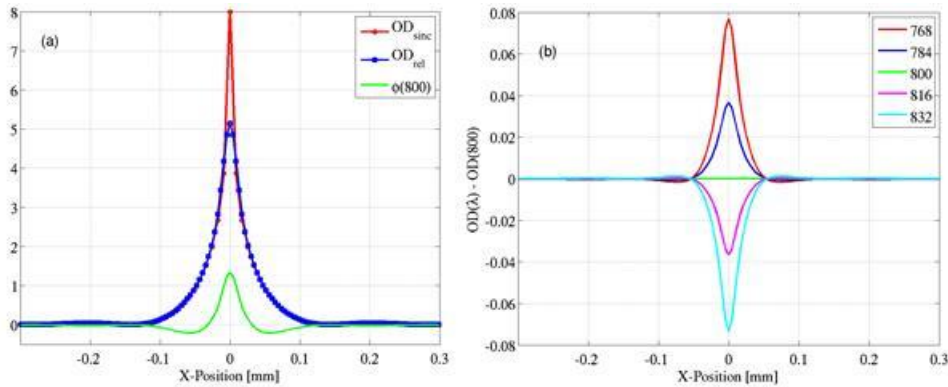
Figure 2 (a) The x-profiles of occulter Optical Densities, ODsinc and ODrel, as well as transmitted occulter phase at λ = 800nm, φ(800), where the latter is given in radians. (b) Occulter OD dispersion, where the figure legend shows five wavelength values in nm. These parameters correspond to a linear sinc^2 occulting mask consisting of Ni deposited on a fused quartz substrate.

has a large index of refraction ($n \sim 2.5$ at 800nm), regions of the occulter with higher OD (lower transmission, thicker Ni) also have a greater optical path length in transmission than low OD regions. The spatially-varying transmitted e-field is therefore complex-valued. In addition to the spatial variations in OD and phase, the OD and phase also vary with wavelength. Ni was chosen for this application because its OD and phase vary less with wavelength than other practical materials (Balasubramanian, 2008). We will include the dispersion of both occulter OD and phase in our simulations. The profile of the occulter phase at λ=800nm, φ(800) is also shown in Fig. 2(a) in radians. Figure 2(b) shows the variation of the occulter OD at five wavelength values relative to that at λ=800nm, or the OD dispersion. The occulter phase dispersion is weaker than the OD dispersion, and the φ(λ) - φ(800) has the largest value of -0.012 radians at the center of occulter and at λ = 768nm. For this occulter, $T(x) = 0.5$ at $x/f = 3.3\lambda/D$, where $D = 48\text{mm}$ is the diameter of the system clear aperture and f is the focal length. The front end F-number (F/#) of this optical system is 31.25.

B.   Other Optical Components

The DM used on the HCIT has 64x64 actuators arrayed on a 1mm pitch and ~350 nm of stroke (700 nm of wavefront). Its description is similar to the 32x32 actuator DM described in detail in Dooley (2005), and will not be repeated here.

Our Lyot stop is made from a simple blackened piece of sheet metal with a sharp edge. Its opening (Lyot stop aperture) has an eye-shape defined by two circles that are shifted with respect to each other in the horizontal direction by a distance of ε in units of D. The value of ε needs to be chosen based on the value of the occulting mask width parameter w, and ε=0.36 in this paper.

In our simulations, we include representative surface errors of six OAP's and a FM which combined form an exit pupil shown in Figure 3. We do not have surface maps for all of the optics in the testbed at the time of the M3A experiments and instead use representative maps from the previous HCIT setup.

C.   Definitions of Half Dark-Hole Area and Contrast

For the current optical system with only one DM, we carry out wavefront control (WFC) over a region Ω_b, where Ω_b is a D-shaped dark-hole region bound by $X \geq X_{\min}$ and $R \leq R_{\max}$, with $X = x/f$, $Y = y/f$, $R = \sqrt{X^2 + Y^2}$, x and y are the horizontal and the vertical position variables on the corresponding image-plane, and f is the focal length.   In this paper we used $[X_{\min}, R_{\max}] = [3.5 \ 11] \lambda/D$ for Ω_b. We evaluate the performance of the HCIT using the normalized intensity,

$$I_n(x,y) = I(x,y)/I_0,\tag{1}$$

or the contrast,

$$C(x,y) = I_n(x,y)[T_0/T(x,y)] = [I(x,y)/I_0][T_0/T(x,y)],\tag{2}$$

where $I(x,y)$ is the image intensity of the occulted star, and I_0 is the maximum value of the un-occulted star intensity, $T(x,y)$ is the occulter transmittance, and T_0 is the maximum value of the $T(x,y)$.   We will keep track of the following two contrast quantities in this report: (i) C_b, the mean contrast inside a "Big" rectangular region Ω_b; and (ii) C_s, the mean contrast inside a "Small" square region Ω_s defined by $[X_1 \ X_2 \ Y_1 \ Y_2] = [4 \ 5 \ -0.5 \ 0.5]\lambda/D$.   Similarly, we also use I_b and I_s to denote the big-region mean and the small-region mean of the normalized intensity $I_n(x,y)$. The intensities modeled under idealized assumptions obtained for a narrowband light with $\lambda_0 = 800$nm and the error-free optical system (even the occulter phase is set to zero) without conducting any wavefront control are $[I_b \ I_s] = [0.37 \ 2.8] \times 1E-8$, respectively.   If we use the
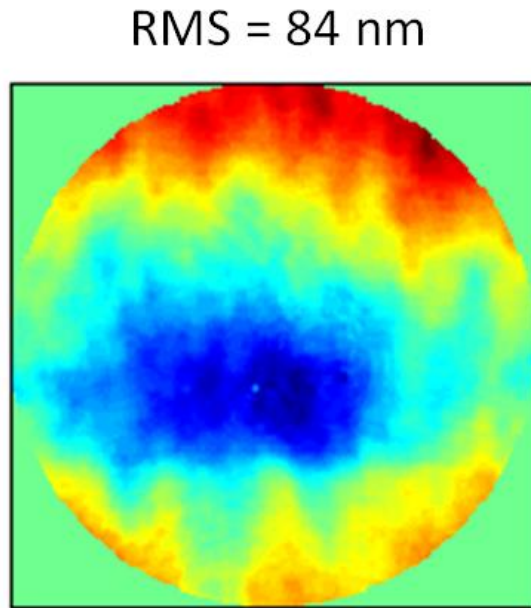
RMS = 84 nm

Figure 3 Measured wavefront errors of representative HCIT optics are summed to form the system exit-pupil wavefront map.

designed transmission profile $T_{sinc}(x)$ of the occulter, we obtain much better contrast values: $[0.77\ 8.7] \times 1E-12$. This is because $OD_{max} = 8$ for $T_{sinc}(x)$ at the center of the occulter, while $T(x)$ has only $OD_{max} = 5.14$. When the phase errors of the seven optics as well as the occulter phase are included in simulation, the above intensity values change to $[0.39\ 4.7] \times 1E-5$, respectively.

D. The Wavefront Control (WFC) Algorithm

In this work, we use a control algorithm similar to the "minimum-wavefront and optimal control compensator" described in detail in Give'on (2009). This approach is also called "Actuator regularization" [4]. The WFC algorithm described in Ref. [10] uses the wavefront at the system exit pupil as its input, and calculates the actuator commands as its output. In the present case we set the DM actuators to superpose the negative of the e-field onto the image plane, with a goal to make the image intensity zero on the region Ω_c. Therefore, the WFC algorithm uses an e-field column-vector $\vec{\mathbf{e}}$ as its input, where

$$\vec{\mathbf{e}} = \begin{bmatrix} \Re(\vec{\mathbf{E}}) \\ \Im(\vec{\mathbf{E}}) \end{bmatrix}.$$

(3)

The joint cost function now becomes as

$$J = \frac{1}{2}\left(\vec{\mathbf{e}}^T \vec{\mathbf{e}} + \gamma_{wu} \vec{\mathbf{u}}^T \vec{\mathbf{u}}\right),$$

(4)

and the gain matrix $\tilde{\mathbf{G}}$ is obtained from

$$\tilde{\mathbf{G}} = \left[\tilde{\mathbf{S}}^T \tilde{\mathbf{S}} + \gamma_{wu} \tilde{\mathbf{I}}\right]^{-1} \tilde{\mathbf{S}}^T.$$

(5)

In Eq. (3), $\vec{\mathbf{E}}$ is the column-vector of the complex e-field on region Ω_c. It is formed by stacking the elements of the complex e-field on region Ω_c in a certain order, as was explained in Eq. (1) of Ref. [10]. The $\Re(\vec{\mathbf{E}})$ and the $\Im(\vec{\mathbf{E}})$ are the real and the imaginary parts of $\vec{\mathbf{E}}$, respectively. In Eq. (5), the $\tilde{\mathbf{S}}$ is the sensitivity matrix consisting of the influence functions of all actuators, created by propagating the wavefront from each actuator through the system. In this model the influence functions are all treated identically. The MACOS and PROPER simulation tools calculate the complex e-field at the final focal plane directly. Therefore, the e-field estimation step is actually not needed in our simulation and we will do not use it in this work. The simulation creates a 512x512-pixel image map, with ~4 pixels per $f\lambda/D$. Considering only the pixels in the dark hole gives an e-field vector, $\vec{\mathbf{e}}$, having a size of 3521x1 pixels per wavelength on the average. There are a total of 2304 DM actuators in the current 1-DM system, but we use only 1907 (~83%) actuators excluding those with zero or very weak influences.

III. Overview of Tests

The Milestone 3 test sequence began on January 7, 2013 with the tank closed and pumped, and completed running March 10, 2013. In between, the tank was opened on February 21st for a few hours, to replace a failed source-stage picomotor and to introduce an additional coronagraphic mask to the occulter stage. During this time, six tests were run:

1. Defocus and lateral translation
2. Correction bandpass
3. Pegged actuators
4. Dark hole size
5. Star-planet photometry
6. Mask spots

A seventh, the effect of a slow sinusoidal source-position drift during correction, was not able to be completed due to time constraints and the repeated failure of the picomotor driving the source stage.

All tests were run on nickel-coated band-limited Lyot masks, using one of two masks. The mask with the internal designation of Ni080521 (hereafter the ``clean mask'') was used to perform the first five tests. The second mask, with the designation of Ni080401 (hereafter the ``Milestone 2 mask''), was taken to the Kavli Nanoscience Institute at Caltech, where a number of precisely located platinum spots were applied; this mask was then inserted on February 21st.

Except as noted below, all tests were run in closed loop, correcting with an implementation of the electric field conjugation (EFC) algorithm over a specified dark hole and using *a stopping condition* to determine when to terminate the iterations. The stopping condition used: if the absolute value of the slope of the mean dark-hole contrast (versus iteration number) over the previous 9 iterations was less than 2×10^{-12}, then the correction sequence would terminate. Electric field estimation was done by taking 5 images at a time: one modified image, and four ``probe'' images which add a combination of sincs and sines to the DM to piston the phase in $\pi/2$ steps across the dark hole in the image plane. From these, the real and imaginary parts of the coherent field can be estimated, as well as the incoherent background.

All images were taken through one of the five 2% narrowband filters mounted in a pair of filter wheels prior to coupling the supercontinuum light into the fiber going to the tank, centered at 768 nm, 784 nm, 800 nm, 816 nm, and 832 nm. In many cases, multiple filters were used in a single correction; in these cases, a set of probe images sn taken for each filter.

After each closing and pumpdown of the chamber, a standard set of start-up procedures was performed to return the system to a ready state. In particular, this included a set of iterations of modified Gerchberg-Saxton (MGS) phase retrieval and deformable mirror (DM) correction to create a flat wavefront in the pupil; the two flat DM settings for the two pumpdowns were used at times as initial conditions for EFC. (For reference, they are stored in dm202.fits and dm228.fits.) In other cases, DM settings corresponding to previous dark holes were used, with the intention that starting from a case which was known to be good at a previous time would cause EFC to converge and stop more efficiently. (This was found to be the case in practice.) The EFC iteration algorithm used picks a regularization---a factor which compensates for mismatch between the propagation in the model and in the real system---by alternating correction steps with images taken only with regularization varied. Often once the system reaches high contrast, the best regularization does not change from iteration to iteration, and this step may be disabled for speed.

Except as noted below, all tests were run with corrections being applied to a D-shaped dark hole, with an inner working angle (along the lateral x-direction) of 3.5 λ/D and an outer radius of 11 λ/D. The mask-spot test was run on the left side of the Milestone 2 mask, as this is where the platinum spots were applied; on the clean mask, a section of the right side was used, as images taken of the mask with a diffuser suggested this region was the most free of small contaminating particles. Contrast numbers are taken as the mean value over this dark hole. The Milestone 3 whitepaper specified that three tests would be run for each experiment to verify repeatability. In some cases, this was done by running the same experiment on three different days; in others, this was done by running three related tests. (In the case of the bandpass tests, both were done.)

All closed-loop output data is stored in FITS files with a naming convention of runXXXitYYYYY.fits. For all data resulting from these experiments, the run number XXX is "428", and the iteration number YYYYY is a five-digit integer, left zero-padded, which is incremented with every cycle of measurement and correction. Tables below will identify these FITS files by their iteration numbers.

A.   Defocus and lateral translation

Uniquely of all the tests, the defocus and lateral tests were run open-loop, without a stopping condition. Rather, they began from a dark hole with high contrast and shifted the occulting mask along the optical axis (z-motion) and along the direction of the sinc^2 pattern of the mask (x-motion) without engaging any control.

Table 1: Defocus and lateral translation

Date	$\Delta z = -0.2$mm	$\Delta z = -0.1$mm	$\Delta z = 0$mm	$\Delta z = 0.1$mm	$\Delta z = 0.2$mm	Contrast
1/16	z32.40mm.fits	z32.50mm.fits	z32.60mm.fits	z32.70mm.fits	z32.80mm.fits	1.820×10^{-10}
1/17	z32.40mm2.fits	z32.50mm2.fits	z32.60mm2.fits	z32.70mm2.fits	z32.80mm2.fits	1.629×10^{-10}
1/18	z32.40mm3.fits	z32.50mm3.fits	z32.60mm3.fits	z32.70mm3.fits	z32.80mm3.fits	1.488×10^{-10}
1/27	z32.40mm4.fits	z32.50mm4.fits	z32.60mm4.fits	z32.70mm4.fits	z32.80mm4.fits	1.539×10^{-10}

The dark hole was created at a z axis value of 32.6mm, 0.8mm from the best focal position, using a single 2% filter centered at 800nm. This choice was based on previous experience and modeling which suggested the deepest dark holes following wavefront control were not achieved with the band-limited mask at the exact focal position. Offsets of 0.1 and 0.2 mm were made in either direction from this z-location, and at each of these positions 17 images were taken with lateral shifts from -4.0 μm to 4.0 μm in steps of 0.5 μm.

Table 2: Correction bandpass

Test #	Date	768 nm	784 nm	800 nm	816 nm	832 nm	Correction bands only	All five bands	Contrast
1	1/22			x			it01220	it01221	1.420×10^{-10}
2	1/22	x				x	it01253	it01254	2.191×10^{-9}
3	1/22	x					it01281	it01282	1.775×10^{-10}
4	1/23					x	it01330	it01331	2.650×10^{-10}
5	1/23	x				x	it01431	it01432	2.776×10^{-9}
6	1/25	x	x	x	x	x	it01569	it01570	1.285×10^{-9}
7	1/27			x			it01656	it01657	1.329×10^{-10}
8	1/28			x			it01815	it01817	1.990×10^{-10}
9	1/28	x					it01832	it01833	1.855×10^{-10}
10	1/28	x				x	it01874	it01875	1.997×10^{-9}
11	1/28		x	x	x		it01898	it01899	5.922×10^{-10}
12	1/29	x					it01924	it01925	2.147×10^{-10}
13	1/29					x	it01941	it01942	3.299×10^{-10}
14	2/1		x	x	x		it02445	it02446	5.276×10^{-10}

This set of tests was run first, and the dark hole in the first data set was not terminated with a stopping condition, as this condition had not been implemented yet. Instead, the contrast was terminated manually; this resulted in a contrast floor in the absence of defocus and lateral shift higher than that seen in the next two sets. Correspondingly, a fourth set was taken with the stopping condition used to create the initial hole, which resulted in a floor consistent with other sets (and subsequent results).

The list of data sets, along with the dates taken and the measured monochromatic contrast at the start of each test, are given in Table 1.

B.   Correction Bandpass

In this test, a dark hole was created with some subset of the five 2% filters. Once the stopping condition was reached, a final image was taken in all five bands with probes. To meet the milestone requirement, three of the tests (800nm only; 768nm and 832nm; 768nm only) were were run three times, the 768-800-816 nm test was run twice, and the full five-band correction was run once.

Table 3: Pegged actuators

Date	# pokes	Starting DM	Ending DM	Starting phase	Ending phase	Correction bands only	All five bands	Contrast
1/29	0	dm202.fits		gsly_206ph.fits				
1/29	1	pegtest1.fits	pegtestpost1.fits	gsly_210ph.fits	gsly_215ph.fits	it02096	it02097	1.402×10^{-9}
1/30	2	pegtest2.fits	pegtestpost2.fits	gsly_214ph.fits	gsly_216ph.fits	it02320	it02321	4.117×10^{-9}
2/1	3	pegtest3.fits	pegtestpost3.fits	gsly_218ph.fits	gsly_219ph.fits	it02767	it02768	1.660×10^{-9}
2/4	4	pegtest4.fits	pegtestpost4.fits	gsly_221ph.fits	gsly_222ph.fits	it02994	it02995	2.480×10^{-9}
2/7	3	pegtest3.fits	pegtestpost5.fits	gsly_218ph.fits	gsly_223ph.fits	it03222	it03223	1.716×10^{-9}
2/8	2	pegtest2.fits	pegtestpost6.fits	gsly_214ph.fits	gsly_224ph.fits	it03438	it03439	2.054×10^{-9}
2/10	1	pegtest1.fits	pegtestpost7.fits	gsly_210ph.fits	gsly_225ph.fits	it03588	it03589	1.723×10^{-9}

The list of images, along with their control bands and contrast, are given in Table 2. Note that the contrast number is given only within the correction bands, not evaluated over all five.

C.   Pegged actuators

In this test, actuators were pegged, that is, offset significantly higher or lower from a flat DM setting and disconnected from control. (The flat setting used was the DM in dm202.fits.) The pokes were done with pairs of adjacent actuators, whose DM setting was chosen such that the pair gave a 125nm-peak offset in a localized region in the pupil. The phase difference introduced was determined---and initially set---using MGS phase retrieval. 125nm was chosen as a compromise between the need to introduce a large phase offset (to provide a strong signal to compare the models to) and the need to limit the step between adjacent actuators on the DM (to protect the DM from damage). We ran with 1, 2, 3, and 4 pairs poked, with the pokes alternating between introducing positive and negative OPD; phase retrieval maps are given in Figure 4.

EFC was run using three-band control with the 2% filters centered at 768nm, 800nm, and 832nm. After the stopping condition was met, a final image was taken with all 5 2% filters. A phase retrieval was also taken for the DM setting before and after each run. (While there were seven runs, there were only four unique initial DM settings used, and so ``before'' phase images were only taken for those four cases.)

Despite being disconnected from control, the requested DM voltage for the pegged actuators is altered by a second automated routine that prevents the step between adjacent actuators from being too large. In practice we find that this does happen, particularly as actuators in the vicinity
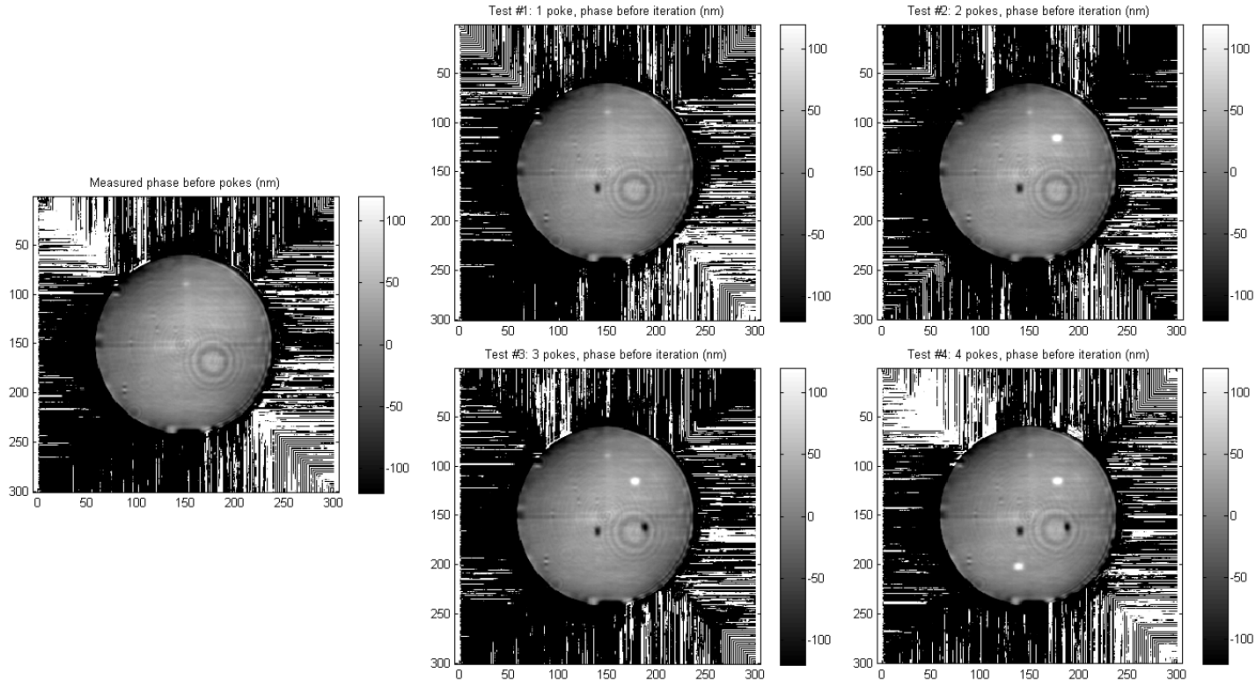
Figure 4 Phase retrieval maps for the 4 poke sequences used for these tests.

of the pegged actuators tend to be pulled in the opposite direction, and thus the actual phase step introduced at the pegged actuator tends to be worn down over many iterations.

Output data is given in Table 3, and includes DM settings, phase retrievals, and both 3- and 5-band images. The contrast value given is evaluated over the three control bands, not all five.

D.   Dark Hole Size

In this test, the outer extent of the dark hole was increased to near to, and beyond, 24 λ/D, to assess the effect of dark hole extent on the ability of wavefront control to create and maintain a dark hole. (Although the DM has 64 x 64 actuators, a stop was placed in front of the DM with a 48-actuator diameter, which limits the frequencies controllable by the DM to 24 λ/D.) Originally, the test had been to examine the effect of binning actuators, effectively decreasing the extent of the dark hole by limiting the controllable spatial frequencies. However, it proved difficult to get the deformable mirror to bin down correctly, and so we instead switched to this test with the intention of investigating the same effect.

Five tests were run, two with D-shaped dark holes and three with rectangular dark holes. In each

Table 4: Dark hole size (D-shape)

Run (D-shape)	Date	Probe x	Probe y	Score x_{min}	Score r_{max}	Contrast	Correction bands only	All five bands	Contrast list
Baseline	-	3-13	±13	3.5	11	-	-	-	-
#1	2/14	3-17	±17	3.5	15	1.259×10^{-9}	it04032	it04033	-
#2	2/15	3-22	±22	3.5	20	1.034×10^{-9}	it04092	it04093	-

Table 5: Dark hole size (rectangle)

Run (Rectangle)	Date	Probe x	Probe y	Score x	Score y	Contrast	Correction bands only	All five bands	Contrast list
#3	2/18	3-24	±11	3.5-24	±10	1.811×10^{-9}	it04204	it04205	-
#4	2/19	3-28	±11	3.5-28	±10	DNC	-	-	test4contrasts.txt
#5	2/20	3-25	±11	3.5-25	±10	DNC	-	-	test5contrasts.txt

case, as before, the center and two end wavelengths were used as a proxy for all five bands, and a five-band image was actually taken after convergence. All began with 0.3s exposures, and transitioned to 8s exposures once the contrast was in the vicinity of a few x 10^{-8}. If the regularizations seemed to be consistently selecting a value, they were turned off as well, for speed. Otherwise, no changes were made to the default EFC configuration.

Three runs converged. We attempted to control beyond the DM limit of 24 l/D in the 4th and 5th runs and these did not converge. Tables 4 and 5 give the pertinent numbers for all five tests, and file names associated with images (for the runs that converged) or lists of contrasts (for the ones that did not). The contrast sequences for the ones that did not are also plotted in Figure 5.

E.   Star-planet photometry

In this test, a planet was simulated by physically moving and stopping down the source. To position the planet accurately and repeatedly, a closed-loop picomotor, mounted on a stage beneath the assembly holding the entrance fiber was moved laterally by 3000 1/16 μm steps (0.1875mm total). (The original plan had called for using 3 different offsets, but was not done for reasons explained below.) During this time, the camera was set to expose continuously. As the vacuum tank is shuttered externally, we opened the shutter to simulate the star, moved the source and adjusted the light level, then opened and closed again to simulate the planet.

To reach a 10^{-9} contrast between the star and planet in all 5 narrowband filters, we 1) partially blocked the supercontinuum with an actuated edge blocker in the light path external to the tank, and 2) used a different exposure time (40-80 times longer for the star than the planet). The blocker is an edge moved into the beam to reduce the amount of light that enters the starlight fiber. The position of the blocker for a given attenuation changes with wavelength. We calibrated the blocker setting as a function of wavelength by moving the source to the planet location and exposing over a grid of block positions and filters. The peak values for the planet were then normalized using previously-obtained photometry, and appropriate block settings and exposure times were chosen for each 2% band. The calibration data is shown in Figure 6.
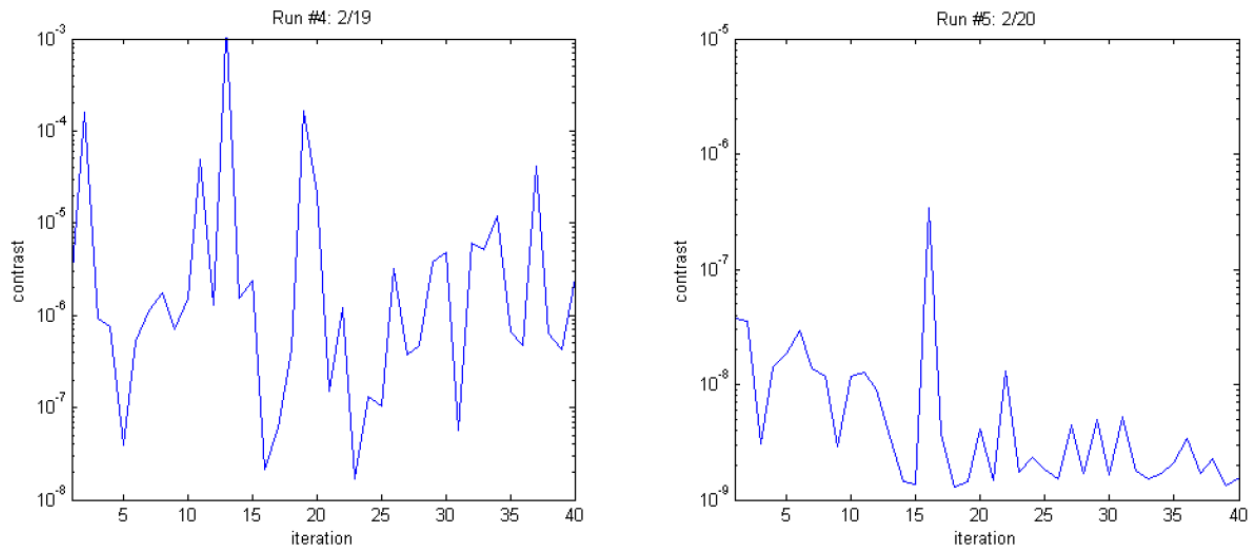

Figure 5 Dark-hole iterations sequences for test #4 (did not converge) and test #5 (stopped early for hardware fixes).

Prior to the planet simulation, a three-band correction was run until the standard stopping condition was met, using the source in an on-axis configuration. A routine was written to do the full estimation and correction based on probe images with planet and star at each iteration, but given the issues detailed below, this was not implemented. Rather, a single set of probe images with star and planet were taken after the system had converged, in all five bands; this was then processed into coherent and incoherent parts.

While attempting to implement this plan, it was discovered (the hard way) that the source picomotor was not capable of making these moves for any length of time; two picomotors were burned out in an attempt to get this to work, one of which was fresh out of the package before being inserted into the tank. The cause is unclear, though overloading (from the mass of the source assembly or the force of the spring in the assembly x-stage) or overheating are possible explanations. As a result, only three usable data sets total were taken over the course of the run in the HCIT, all at the 3000-step offset, and one of the three was a test set taken prior to the contrast

Figure 6 Planet contrast calibration data for the star-planet tests. Supercontinuum block values were chosen at the intersection of the gold line with the curve for each narrowband filter.

calibration, with the field stop out. Further, the failure of the second picomotor occurred at the tail end of the third data set, and required some post-processing to recover. Nonetheless, these

Table 6: Star-planet photometry

Date	5-band image	Calibration file
1/10	it00880	–
1/15	it01030	p80635.mat
2/27	it04747	111500.mat

Table 7: Mask spots

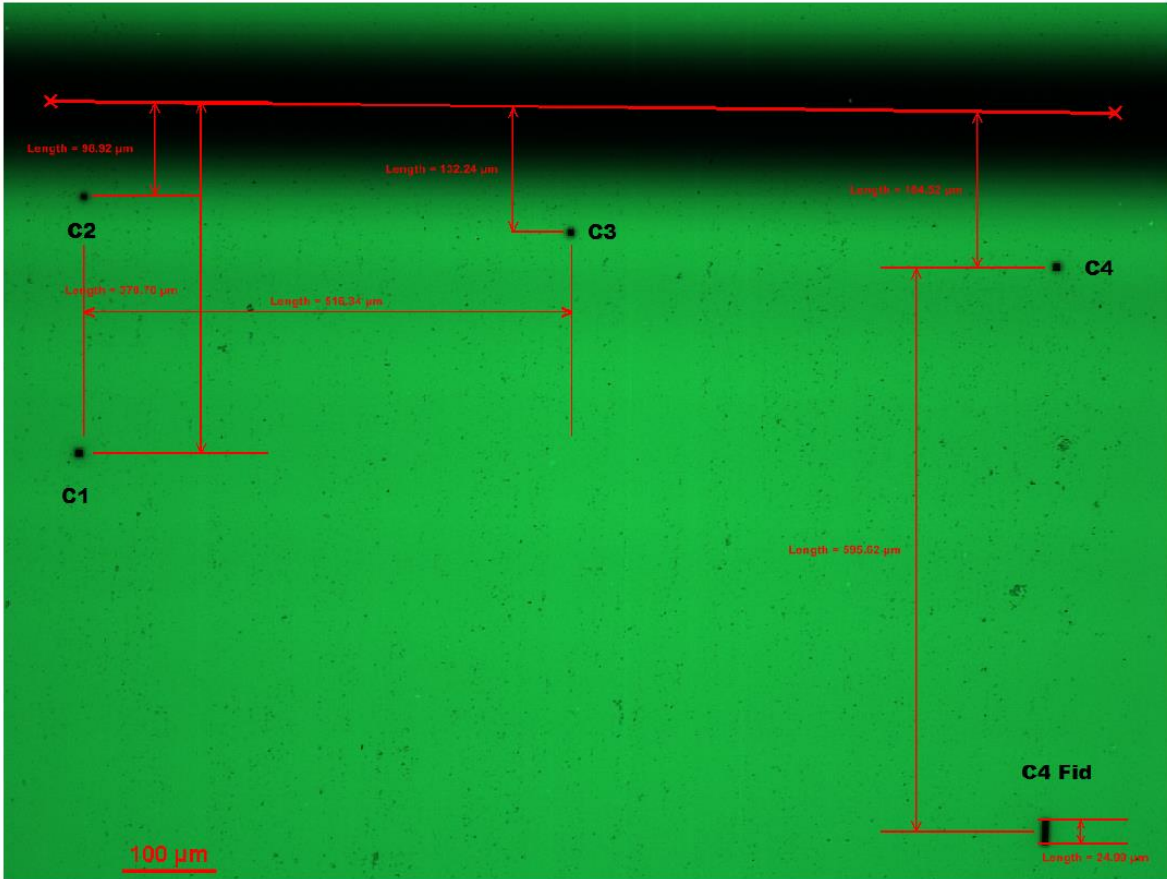| Date	Iteration number at termination	Contrast sequence
3/4	it05051	c4n1.mat
3/5	it05152	c4n2.mat
3/6	it05178	c4n3.mat
3/7	it05255	c4n4.mat
3/10	it05441	c3n1.mat

Figure 7 Optical microscope image of spots placed on the Milestone 2 mask, taken shortly before insertion into the vacuum chamber by K. Balasubramanian. Other spots were present previously.

runs are given in Table 6 below, along with the name of calibration file used to set the supercontinuum block positions.

F.   Mask spots

To test the sensitivity to local mask defects, a series of 6 x 6 μm platinum spots were placed on the Milestone 2 mask by K. Balasubramanian, using a focused ion beam (FIB) machine located at Caltech's Kavli Nanoscience Institute, along with regular fiducial marks 25 μm in length. We chose 6 x 6 μm because that is the smallest dimension we felt we could reliably characterize. Figure 7 shows a microscope image of some of the spots made prior to insertion in the tank, denoted C1 through C4, and an accompanying fiducial mark. The mask was inserted in the vacuum chamber on 2/21/13, when it was opened for four hours; the picomotor replacement was also done at this time.
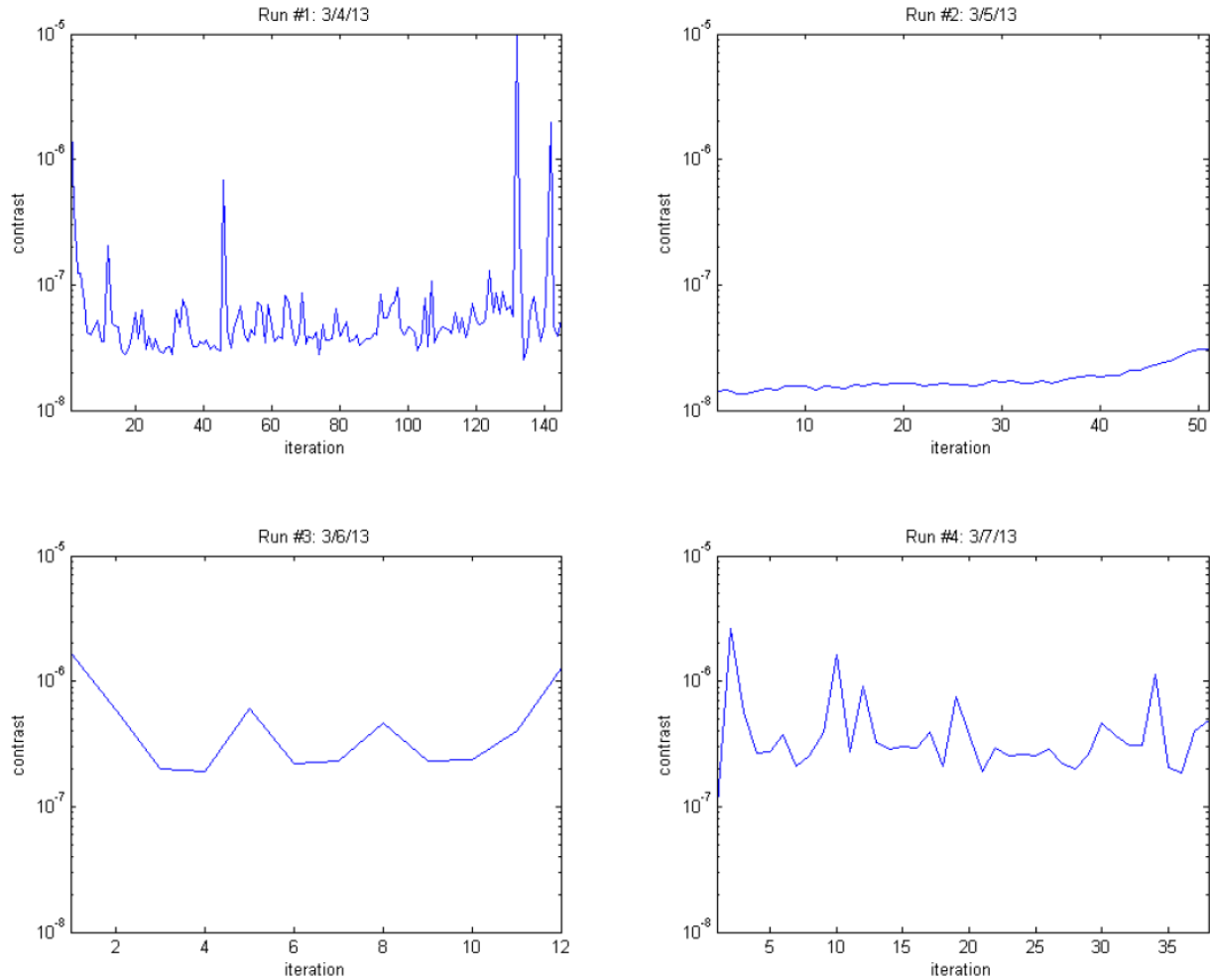
Figure 8 Contrast sequences for the four tests done with the dark hole centered on the C4 mark. None met the convergence criterion

Initially, these spots were located by scanning along the mask y-axis with the diffuser in place; once they were found, their spacing was verified against prior microscopy using the known pixel scale. As the mask mount is on a 5° angle to mitigate reflections, motion in y also requires motion in z to maintain the same location relative to focus, and so appropriate z-positions were also determined at this time.

For each test, the occulting mask was oriented to place a spot at the y-axis center of the standard D-shaped dark hole. No other changes were made to the standard iteration procedure. Initial runs were done on the C4 spot, with a final test being done on the C3 spot; associated data files are given in Table 7.

Four tests were conducted on the C4 spot, and in no case did the contrast converge; rather, it oscillated about a baseline level with occasional single-iteration spikes to an atypically large contrast value. These sequences are given in Figure 8. In each case, the run was terminated manually after inspection of the contrast sequence showed no downward trend or a contrast floor sufficiently high that the 2×10^{-12} stopping condition did not appear feasible.

At this point, a region on the mask was identified as being clear of both pre-existing debris and new platinum marks, and located on the same side of the linear mask as the new marks. EFC was run with the 3-band configuration and a standard D-shaped dark hole; the contrast successfully reached a stopping condition with a contrast of 2.8×10^{-9}. A final run with the dark hole centered vertically at the location of the C3 spot was run, but a software failure meant that only a portion of the contrasts were recorded before the HCIT run ended, whose convergence properties are unclear. These are given in Figure 9.

A seventh test was planned if time permitted, to move the source during an estimation sequence; however, the repeated failure of the picomotor, which was required for this test (and the schedule crunch resulting from this and the problems implementing actuator binning) precluded this.

IV.   Temperature Data

We report on temperature data for the full period of the experiments, and specifically for the lateral and axial sensitivity tests, as well as the bandpass tests. There are ~30 temperature sensors in, on, and around the chamber. We have selected 6 representative sensors to keep the plots from getting too crowded. Figure 10 shows the temperatures for the full duration of the experiments, from Jan 7 to March 9, 2013. The selected sensors locations are described in Table 8. Unfortunately, at the time of the experiments, there were no sensors located on the optical

Figure 9 Contrast sequences for the tests done with the dark hole centered on the C3 mark.

bench. The main source of heat is the camera, and it is cooled by the chiller. Recently, sensors have been added to the bench and they show that motorized mounts and power cycling the camera affect the bench temperature at a level of 0.1K. The motors could have had some impact during the axial/lateral sensitivity tests. But they were not used during the other tests except for alignment initialization. Power cycling of the camera was rare as well.

Temperature data for the axial/lateral sensitivity tests is shown in Figure 11. The tests were carried out on 4 days (Table 1) and these dates are highlighted in the bottom of Figure 11. Each run lasted ~2 hours, during which the room temperature variations were
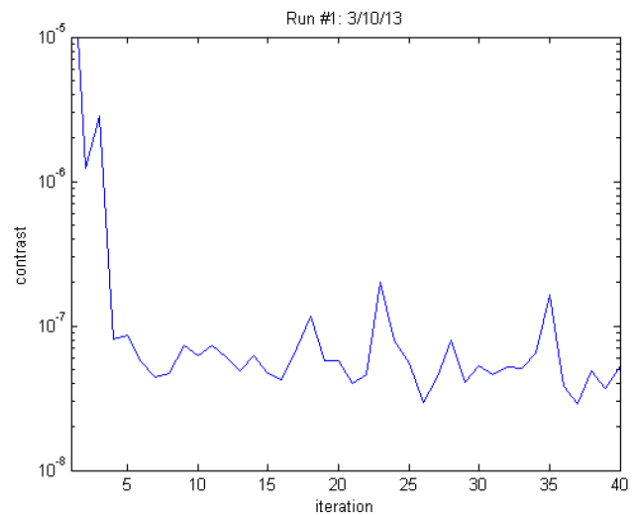
Table 8 Temperature Sensor Locations

Sensor Label	Location
E BH	On outside tank skin, East side, between heaters.
Chill Out	At return of camera chiller line
Room E	In air, east side of Hi Bay
Room S	In air, south side of Hi Bay
W Center	Inside tank skin, west side

17

40-140 mK (1 sigma), and the inside skin of the tank was stable to 1-2 mK (1 sigma).

Temperature data for the bandwidth tests are shown in Figure 12. These data correspond to tests #5 and #12 from Table 2. Later in the report, and for completeness, these data will be shown aligned with the contrast convergence curves for the corresponding tests. However, there is no apparent correlation between contrast stability and these temperature data.
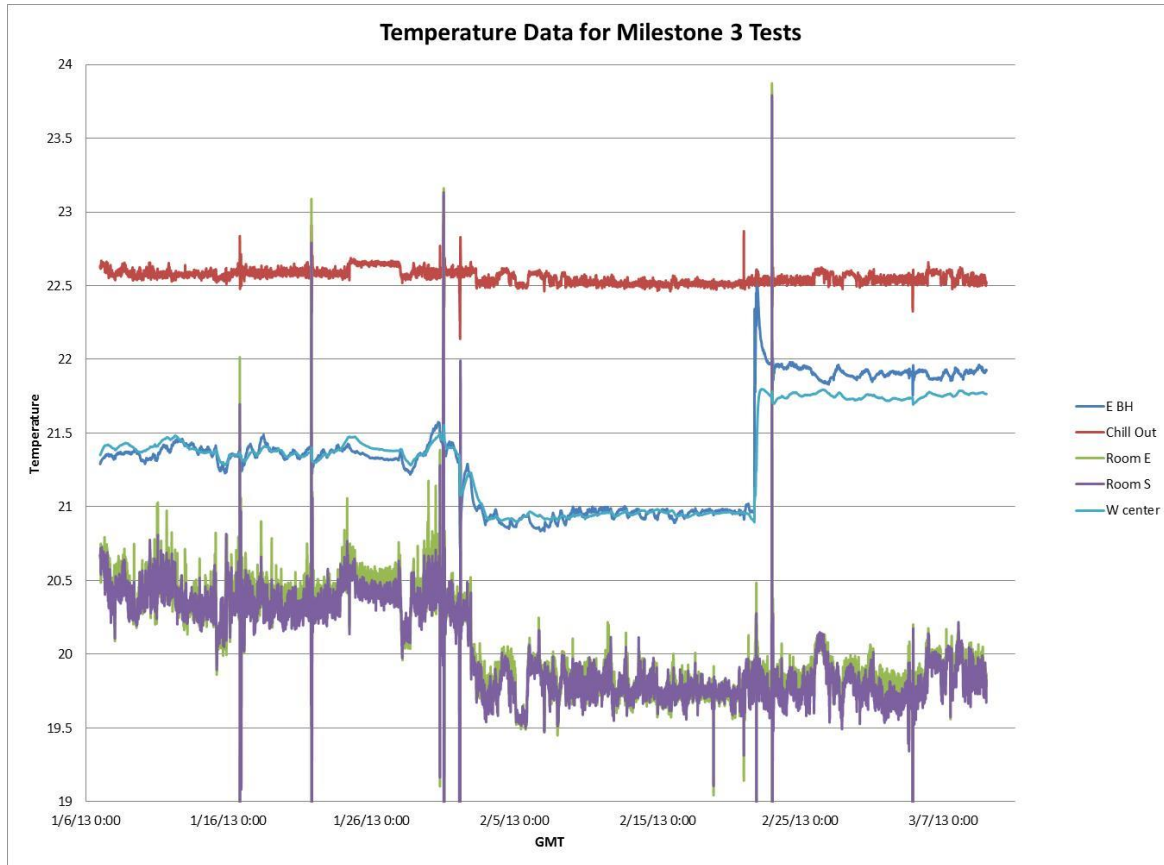

Figure 10 HCIT temperature data (Celsius) for selected sensors, January - March, 2013.
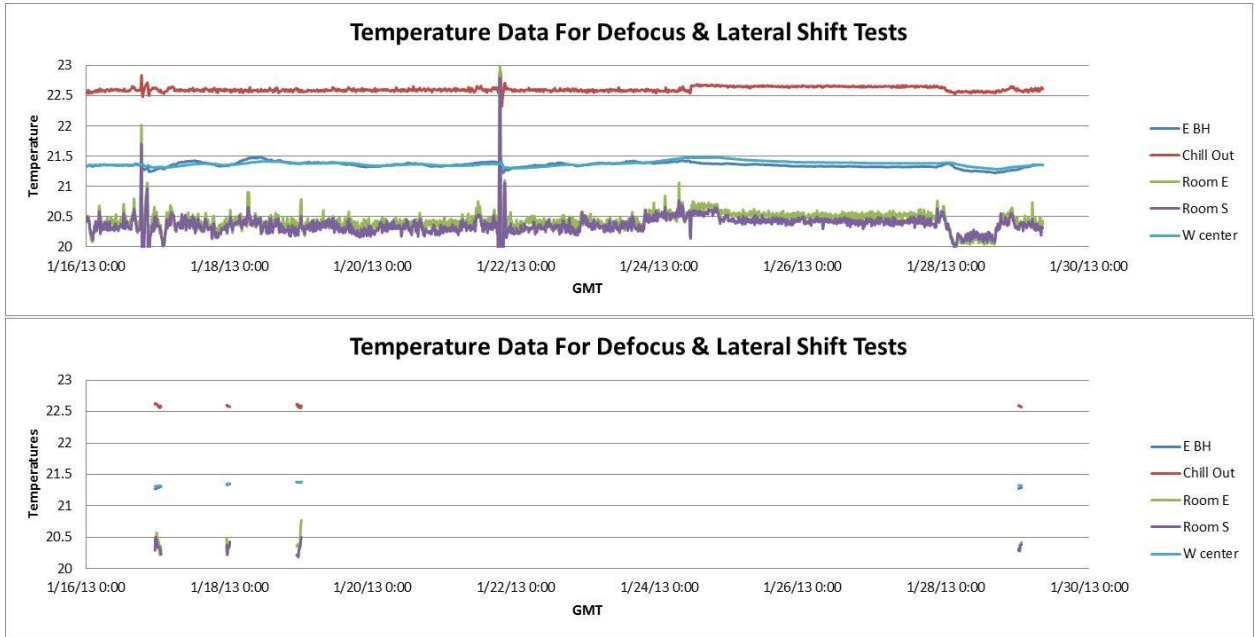
Figure 11 HCIT temperature data covering the dates of the axial/lateral sensitivity tests. Top: all data for the duration of the experiment. Bottom: data for the specific times that data were collected. The four groups of data correspond to the runs listed in Table 1.
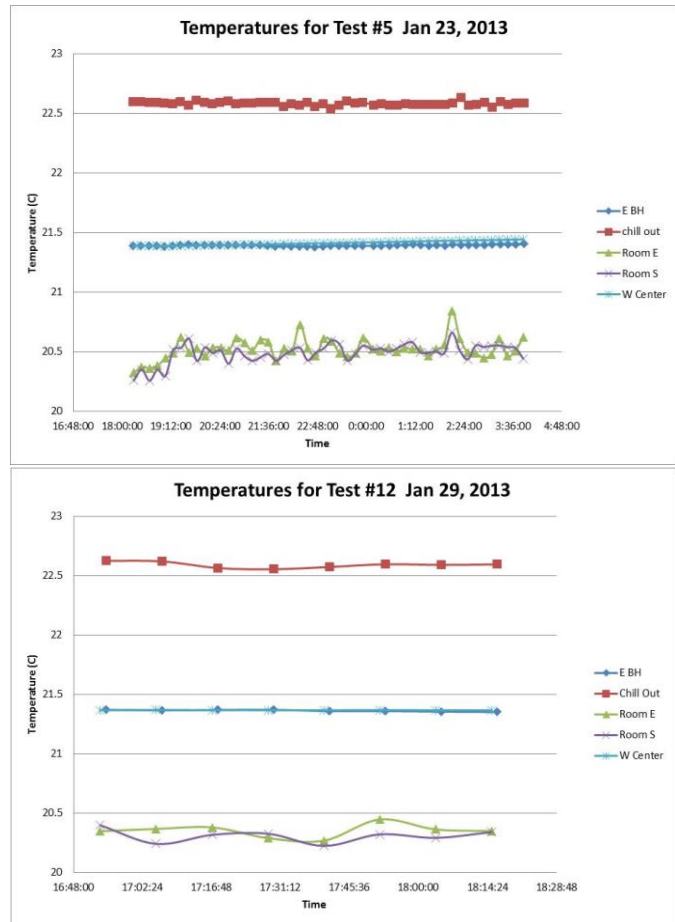
Figure 12 Temperature data for bandwidth tests numbers 5 and 12 (see Table 2).

V.   Key Experimental Results

Most of the results documented here have been reported in the literature and are attached as appendices to this report. Results are summarized in the Summary Table (Section I, and repeated here for convenience). Detailed descriptions of each test follow in sections A-F.

A.   Lateral and Axial Translation

Except where otherwise noted, this section is extracted from "HCIT Contrast Performance Sensitivity Studies: Simulation Versus Experiment," by E. Sidick et al, SPIE Vol 8864, paper 86640Q (2013).

We used a 2% wide filter centered at 800 nm to study the sensitivity of the contrast to defocus and lateral translation.

In Figs. 13(a-f), we plot C_b and C_s (contrast over the full-size dark hole and in a 1 λ/D wide

SUMMARY TABLE

OPEN-LOOP TEST: PERTURBATION OCCURS AFTER WFCS HAS SET THE DM.

Test	Tolerancing and Sensitiivity	Status	Result	Report Guide	Comment
Source Lateral and Focus Position	How does contrast depend on a change in the source lateral position and mask focus?	Completed. Published in SPIE vol 8864 (2013).	Model prediction errors < 1e-9 for lateral translations +/- 1 um. Most predictions within factor of 2 of observations.	Section V.A, Figures 14 and 15, Table 9.	Significant difference in MACOS and PROPER predictions for lateral motion, even though on-axis cases agree to a few percent.

CLOSED LOOP TESTS: WFCS TURNED ON DURING/AFTER PERTURBATION IS INTRODUCED

Test	Tolerancing and Sensitivity	Status	Result	Report Guide	Comment
Occulter Mask Defect	What is the contrast when the occulter has an obscuring spot?	Completed. Two opaque spots of 8x8 um were written on the mask. Published in SPIE vol 8864. (2013).	1e-6 speckle in image plane. Model predictions over 10% band accurate to 50% for contrast range 1e-8 -1e-6 in composite broadband image. Model - data always > 1e-9.	Section V.B, Figures 17 and 18, Table 10.	Spots were characterized with AFM and SEM. OD was derived from spot height and fed to the model. Model was not iterated.
Dark Hole Size	How does contrast depend on the number of actuators compared to the size of the dark hole?	Completed study of size of dark hole. Published in SPIE vol. 8864 (2014).	Predictions good to < 1e-9 contrast over full dark hole up to 20 λ/D when a model of local mask defects is used.	Section V.C, Figure 24, Table 11	Dark holes up to 24 l/d were formed. Contamination/defect model assumes that optical path picks up pi phase for OD=1.
Bandwidth	What is the best contrast achievable at a given bandwidth?	Completed multiple cases of control in single narrow and multiple narrow bands.	Predictions usually good to < 1e-9 with local mask defect model. But poor agreement when only ends of 10% bandpass are used for control.	Section V.D, Table 12, Figures 26-31	Model predicts best contrast should always be in the measured band. Experimentally this was not always the case.
Pegged Actuators	How severe is degradation due to a dead actuator?	Completed multiple cases with pairs of actuators pegged at +/- 132 nm.	Predictions good to < 1e-9 when a model of local mask defects is used. Pupil map in good agreement around pegged actuators, poor agreement around edge of DM.	Section V.E, Figure 36	Overall dark hole contrast roughly unchanged as dark hole grows to Nyqust limit of DM.
Incoherent Light Estimation Accuracy	How accurate is the coherent light estimator?	Completed, but without planet light. Published in SPIE vol. 9143 (2014).	~25% of coherent signal is incorrectly treated as incoherent in a 10% bandpass. Estimation good to 2e-10 contrast in 2% bandpass.	Section V.F, Figures 38 and 39	Incoherent light shown to be stable for days, but unexplained spatial variation when comparing spectral bands.

region from 4-5 λ/D, defined in Section 2C above) as a function of lateral translation T_x and defocus value T_z. As expected, the simulation using both analysis tools MACOS and PROPER yield contrast values better than the measured ones because the simulations do not account for any experimental floor (e.g. incoherent scattered light). Therefore, for the purpose of comparison, we set as the minimum for all model curves the contrast at $T_x = T_z = 0$ and added this value to all the simulated data.
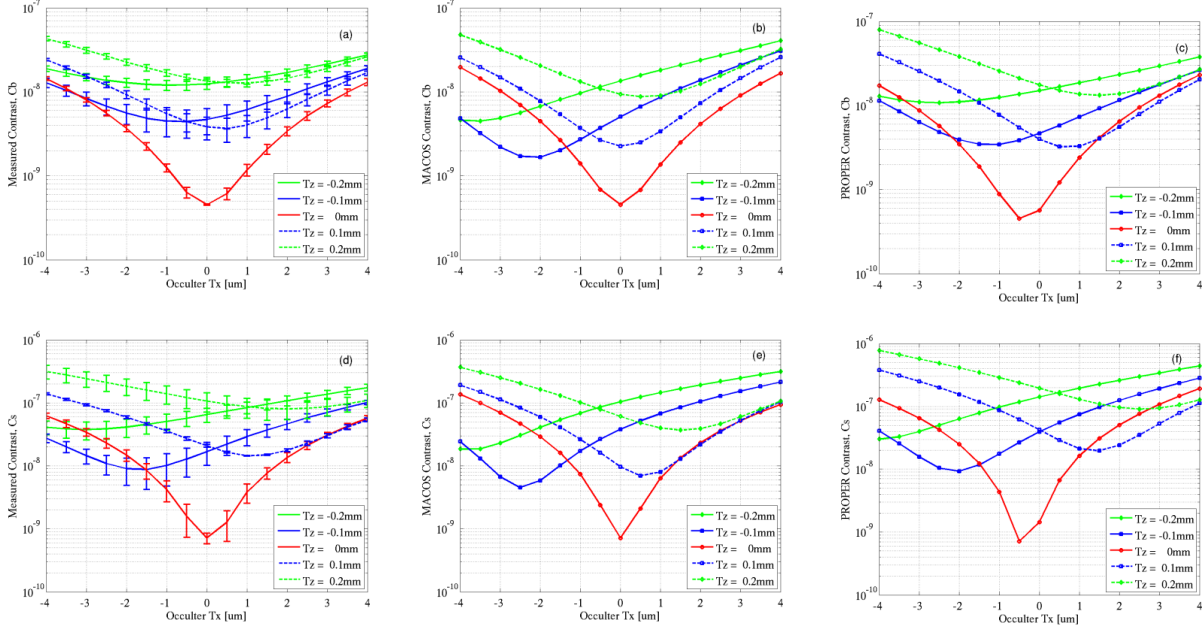
Figure 13 Contrast as a function of occulter lateral translation, T_x, and with longitudinal translation, T_z, as a parameter. The T_x and T_z are defined in the local coordinates of the occulter with T_z parallel to the direction of the chief-ray. (a) Three-day average of the measured C_b. The error bars correspond to the standard deviation (STD) of the three sets data. (b-c) C_b calculated using MACOS and PROPER, respectively. Parts (d-f) are the same as parts (a-c) and show the values of C_s (small box) in place of C_b.

Figures 14(a-d) show the contrast errors between the measured and the modeled C_b and C_s values. The predicted C_b and C_s curves exhibit similar behaviors as those of the measured ones, but the valleys of the $T_z \neq 0$ curves take place at T_x-values slightly different than those of the measured ones. Most predicted data points differ from the measurements with a factor of 2. The exact reasons that cause the difference observed between the prediction and the measurement for these tests is still under investigation. We also need to understand why MACOS and PROPER don't give exactly the same results.

The dependence of contrast leakage in the dark hole is approximately quadratic in the lateral translation parameter. If we fit a second-order polynomial to the curves in Figs. 4(a-c) in the form of
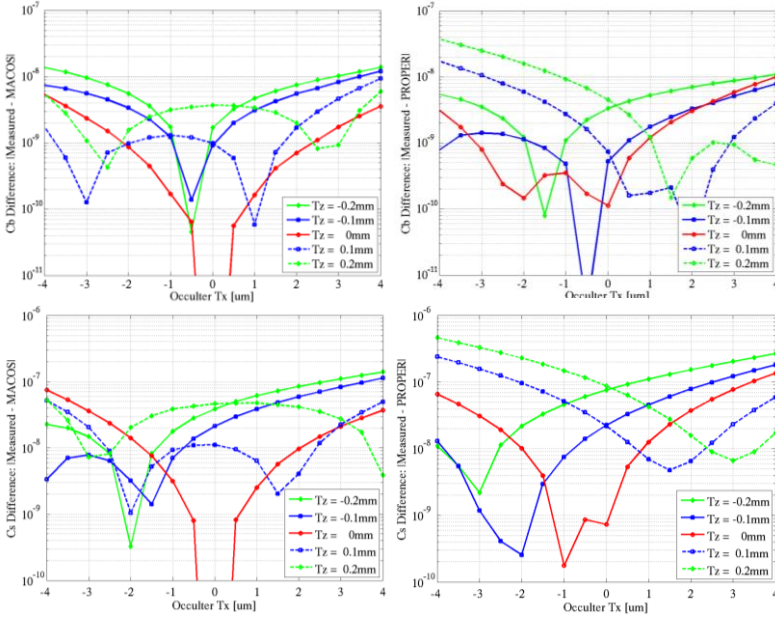
$$C_b = a(T_z)[T_x - x_0(T_z)]^2 + b(T_z),\qquad(6)$$

Figure 14 Contrast error |Calculated – Measured|, as a function of occulter lateral translation, T_x, with longitudinal translation, T_z, as a parameter. (a) C_b error: MACOS versus measured. (b) C_b error: PROPER versus measured. (c) C_s error: MACOS versus measured. (d) C_s error: PROPER versus measured. Shown on the figure legends are T_z-values in mm.

we obtain the fitting parameter values listed in Table 9. The values of $a(T_z)$, $x_0(T_z)$ and $b(T_z)$ are plotted as a function of T_z in Figs. 15(a-c) respectively. These data are useful in predicting the sensitivity of a Lyot coronagraph's narrow-band contrast to the occulter position.

We note that Figure 15 and Table 6 are corrected versions of Figure 6 and Table 1 in the SPIE paper. After publication we found a mistake in the sign of the translation that resulted in the model curves being flipped left-right relative to the data.

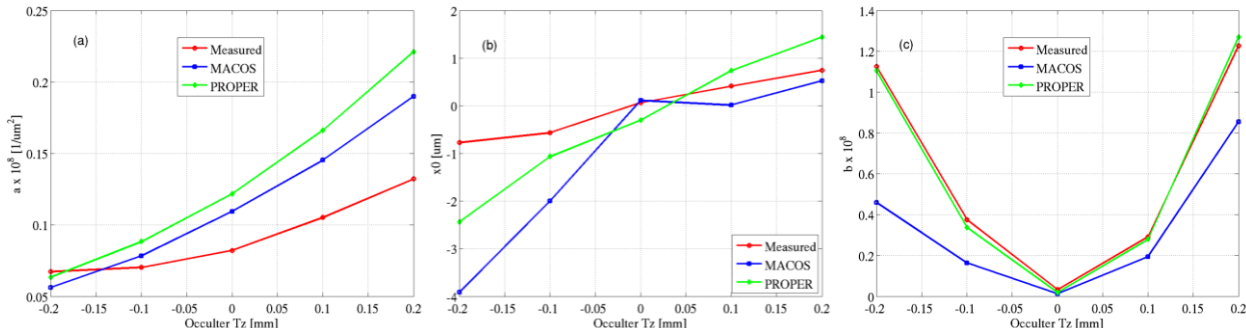A comparison of the measured predicted quadratic behavior coefficients (columns 2, 5, and 8 in Table 9) shows that the worst-case model dependence is the PROPER model at Tz = 0.2, where the coefficient is 0.22 compared to the measured dependence of 0.13, a relative error of 70%. At the nominal focus, the worst error is 0.12 / 0.08, a 50% overestimation by the model. The predicted minimum contrast value for different axial offsets (Figure 15, MACOS curve, right panel) differs by as much as 1.13×10^{-8} / 0.46×10^{-8}, a 145% error, at Tz = -0.2 mm. Notably the PROPER model accurately predicts the minimum contrast at all axial offsets. PROPER was used only for these tests. In the closed loop tests, only MACOS was used.

Figure 15 Fitting parameters defined in Eqn. (1) and listed in Table 1. Left: quadratic coefficient of contrast. Middle: Tx offset position. Right: contrast offset.

22

Table 9 Values of the fitting parameters defined in Eqn. (1).

	Measured			MACOS			PROPER		
Tz [mm]	ax10^8 [1/um^2]	x$_0$ [um]	bx10^8	ax10^8 [1/um^2]	x$_0$ [um]	bx10^8	ax10^8 [1/um^2]	x$_0$ [um]	bx10^8
-0.2	0.0672	-0.7733	1.1261	0.0561	-3.9111	0.4600	0.0634	-2.4388	1.1043
-0.1	0.0702	-0.5677	0.3757	0.0784	-1.9982	0.1638	0.0882	-1.0678	0.3374
0	0.0821	0.0641	0.0328	0.1094	0.1123	0.0133	0.1217	-0.3032	0.0187
0.1	0.1052	0.4132	0.2915	0.1453	0.0119	0.1939	0.1661	0.7386	0.2789
0.2	0.1322	0.7453	1.2267	0.1900	0.5199	0.8539	0.2210	1.4394	1.2688

B. Opaque Spot on Occulter Surface

The next topic of our report is the effect of an opaque spot on 10% broadband contrast. The mask was described above in Section III.F. The results reported here were previously reported in SPIE Vol 8864, paper 86640Q (2013). We added square shaped marks of platinum on this mask at chosen locations as shown in Fig. 7. Figure 16(a) shows one of the marks under a scanning electron microscope (SEM). The projected rectangular shape is due to the 52° tilted observation of square mark. The debris field seen was present on the mask before the marks were written. Mark C3 shown in Fig. 16(b) is about 170 nm tall with optical density ~8. Similarly, the mark C4 in Fig. 16(c) is about 150 nm tall with optical density ~6. These marks are about 6μm squares as measured by an atomic force microscope (AFM) and SEM. Two dimensional optical transmission profiles of these marks were calculated based on 2-D maps of the marks from AFM and using known optical constants of Pt. Figure 16(b) shows the part of the occulter transmission coefficient (amplitude) map on which the fine-sampled C3-spot is superimposed, and Fig. 16(c) shows the same for the C4-spot. This spot shows nearby defects that we also included in the model (and assumed were Pt for lack of other data). Using the AFM and Pt data, the opaque spot was added to the occulter transmission amplitude model. The occulter map was then down-sampled to its normal MACOS pixel-size of 8.492 μm, and wavefront control simulation were carried out with this modified occulting mask.

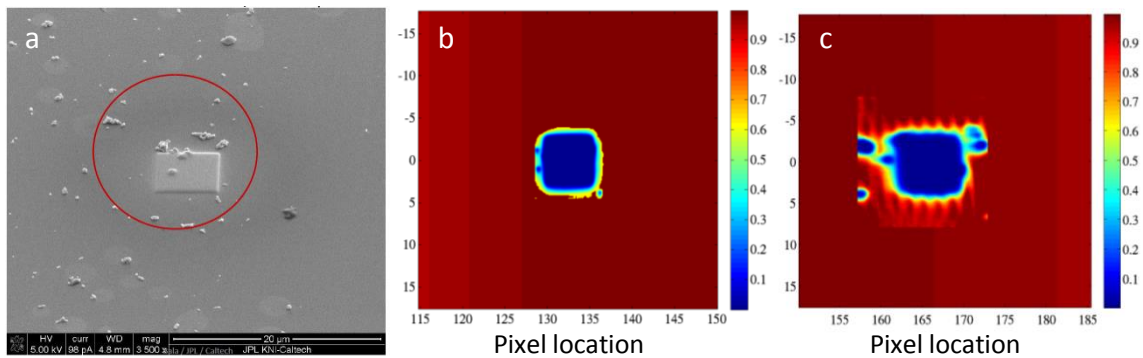Pixel location   Pixel location

Figure 16 (a) SEM image of the C3-spot area on the occulting mask. (b) Measured C3-spot transmission map superimposed into the occulter transmission model.   The pixel size is 0.0984μm.   (c) Measured C4-spot transmission map superimposed into the occulter transmission model. The pixel size is 0.1228μm. These two occulter transmission maps are re-sampled to a pixel size of 8.492μm in MACOS model. In parts (b) and (c), the horizontal and the vertical axis labels are positions in μm.
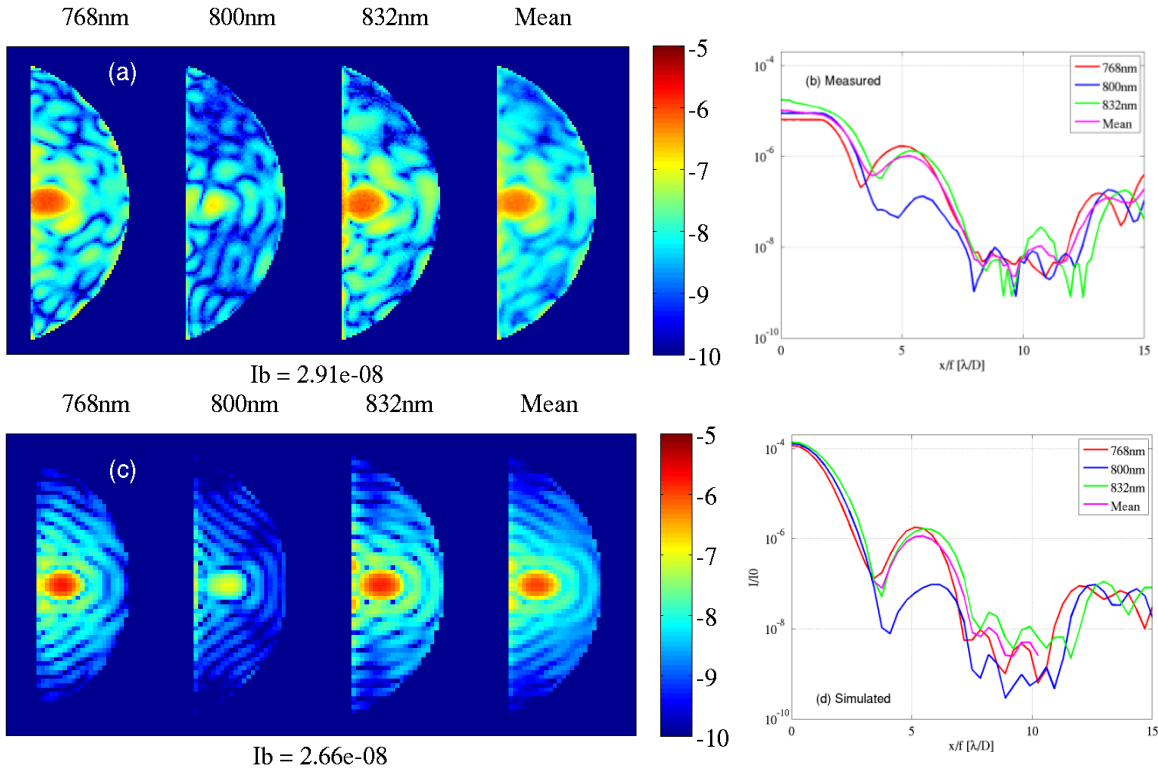
Figure 17 Log-scale normalized intensity, $I_n(x,y)$, maps obtained with the C3-spot occulter area. The top row shows the measured data, and the bottom row shows the corresponding simulated results. The first three maps in parts (a) and (c) correspond to three different 2%-filters, and the fourth parts are their mean values or 8%-broadband $I_n(x,y)$ maps. Parts (b) and (d) show the x-cross sections of the four corresponding $I_n(x,y)$ maps. The I_b –values listed in the bottoms of parts (a) and (c) are the broadband normalized intensities.
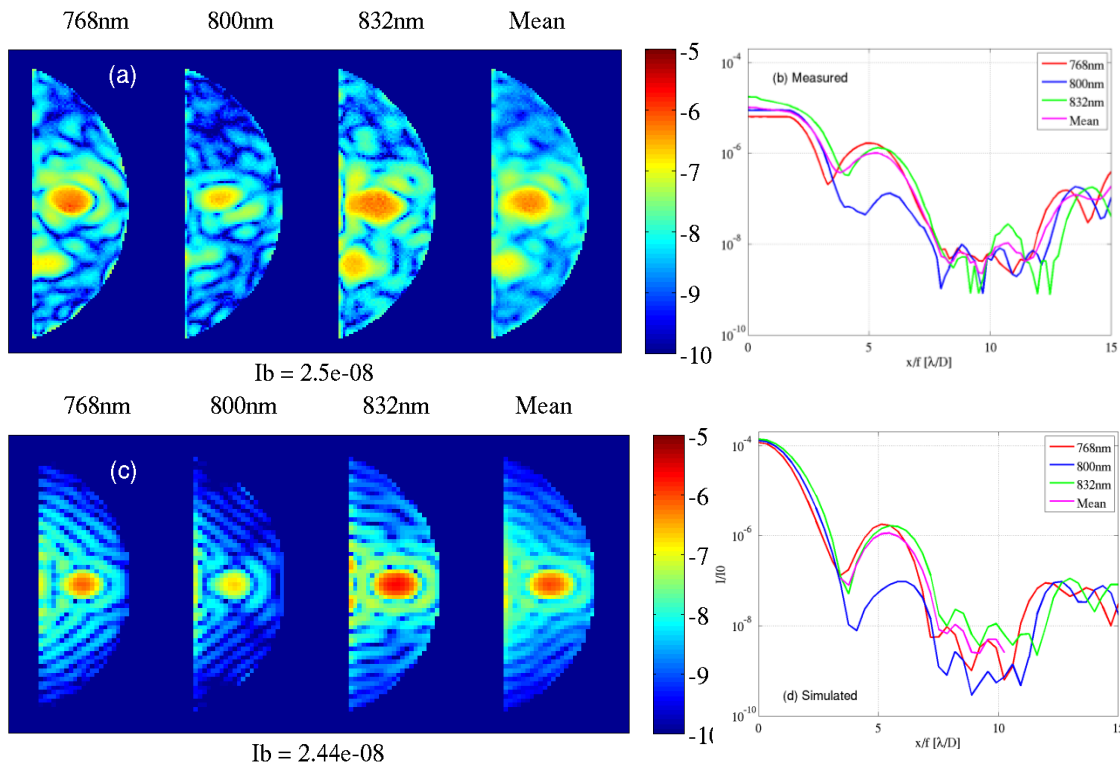
Figure 18 Same as Fig. (9) for the C4-spot area of the occulter.

Figures 17(a-d) compare the predicted maps of the normalized intensity with the measured ones for the C3 occulter spot, and Figs. 18(a-d) show the same results for C4 occulter spot. Among them, part (a) shows the measured individual and the averaged intensity maps, and part (b) shows their x-profiles at $Y = 0$. Parts (c-d) show the corresponding simulated results. The measurements and the predictions come close in this case, especially the broadband I_b–values listed in the bottom of each intensity map plot. The residual Airy-rings are visible in the predicted maps, but they were washed out in the measured ones. One reason for this difference may be that some residual exit-pupil phase error still exists in the experiment, but it was not included in the simulation. The measured normalized intensities in Fig. 18(a) display an evidence of a second occulting defect near C4-spot (but outside the area of the measured spot in Figure 16(c)). That spot was not intentional and was not included in our simulations. In Table 10, we list the I_b–values of the measured and the simulated normalized intensities at three individual wavelengths as well as their average values. As we can see from this table, the agreement between the measurement and the prediction is typically between a factor of 0.7 and 2.

C. Dark Hole Size

This section supersedes the Section 3.4 in SPIE 88640Q. In that paper, the coherent model was compared to the combined incoherent and coherent estimates of the dark hole. Also, we did not have a model of dust particles in that work. That model is included here.

In these tests, we varied the size of the dark hole up to 24 λ/D, the theoretical limit of the 48 x 48 exposed segments. The speckly nature of the observed coherent dark hole floor, and the simple particle distribution model that produces a similar result, indicate that localized mask errors are the likely cause of the contrast floor. We have measured the transmission (amplitude only, not phase) of the occulter using high resolution microscope images to inform a model and see if a mask characterization measurement can be used to predict dark hole contrast. Figure 19 is the transmission image of the front side of the occulter, formed by placing a diffuser between

Table 10 Measured and predicted 2% and 8% (Mean) normalized intensities, or I_b-values, and the measured - model values obtained from the C3- and C4-post areas of the occulter. The simulated results were obtained assuming monochromatic beams.

Box Size	Spot Name	Contrast Type	768 nm	800 nm	832 nm	Mean
Dark-Hole Area	C3-Spot	Measured x 10^{-9}	41.7	6.1	39.6	29.1
		Simulated 10^{-9}	35.5	2.7	41.7	26.6
		|Meas-Sim| x 10^{-9}	6.2	3.4	2.1	2.5
	C4-Spot	Measured x 10^{-9}	28.1	9.2	37.8	25
		Simulated 10^{-9}	15.7	4.8	52.8	24.4
		|Meas-Sim| x 10^{-9}	12.4	4.4	15	0.6
2 λ/D-Wide Spot Area	C3-Spot	Measured x 10^{-9}	1490	80	1060	880
		Simulated 10^{-9}	860	50	890	600
		|Meas-Sim| x 10^{-9}	630	30	170	280
	C4-Spot	Measured x 10^{-9}	910	160	930	670
		Simulated 10^{-9}	340	90	1100	510
		|Meas-Sim| x 10^{-9}	570	70	170	160

the point source and the mask in the HCIT testbed. The vertical blue line is at x = 3.5fλ/D, the red-circle has a radius of r = 20fλ/D; this image roughly corresponds to the area of the occulter
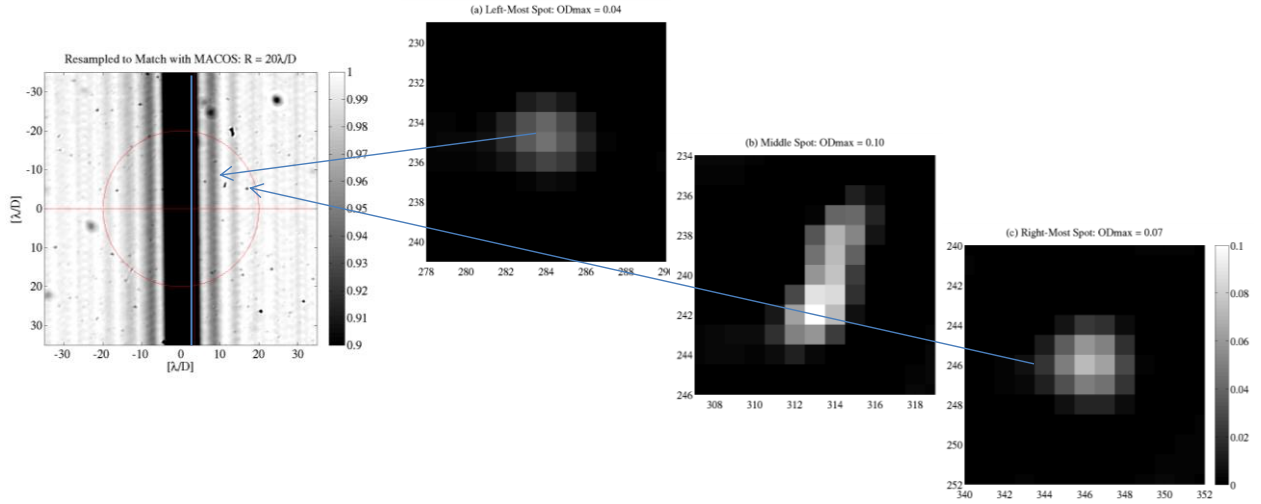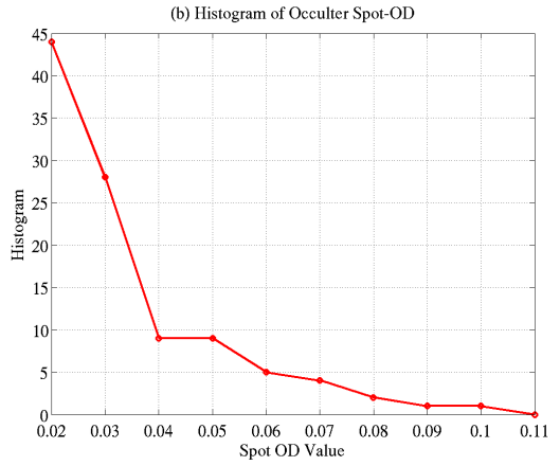

Figure 19 Left: Transmitted amplitude images of occulter's front side. The circle extends to 20 λ/D and is positioned where the beam is centered in the experiment. The three spots on the right side of the box are magnified in the images on the right. Pixel pitch in these images is 4.3 μm.

used in our experiments.

We carried out experiments and simulations for three dark-hole sizes, Ω_b, with [X_{min}, R_{max}] = [3.5 15] and [3.5 20]λ/D in the first two cases and with [X_{min}, X_{max}, Y_{min}, Y_{max}] = [3.5, 24, -10, 10]λ/D in the last one. The experiments were carried out in the 768, 800, and 832 nm filters, with the resulting images combined to form a composite broad-band image.

Contrast predictions for the ideal occulter are well below the measured contrast. When the measured spots are included in the model and treated as simple attenuators (no phase), the contrast is still well below the measurements, as documented in Sidick et al, SPIE 9143, 914336 (2014). We have found that adding a phase term to the spots that varies in proportion to the optical density creates a contrast floor that closely resembles the measured data. However, we presently have no explanation for why the phase term exists, and why a particular value of phase vs. OD works best. The phase term has the form $\varphi_{spot} \approx \pi \times F_{spot}OD_{spot}$, where F_{spot} is a multiplier; we tested at values F_{spot} =0, 0.5, 1, and 1.5.

Figure 20 Histogram of spot OD values that are greater than 0.02 and located with a box extending from [x=+/- 24 λ/D, y=+/- 14 λ/D] after dividing the measured average mask transmission at each x position.

To quantitatively understand the distribution of occulter spots on the occulter surface area of interest, we chose an area extending from [x=+/-24 λ/D, y=+/- 14 λ/D} with the right side of the box nominally registered with the experimental dark hole location. Figure 20 shows the
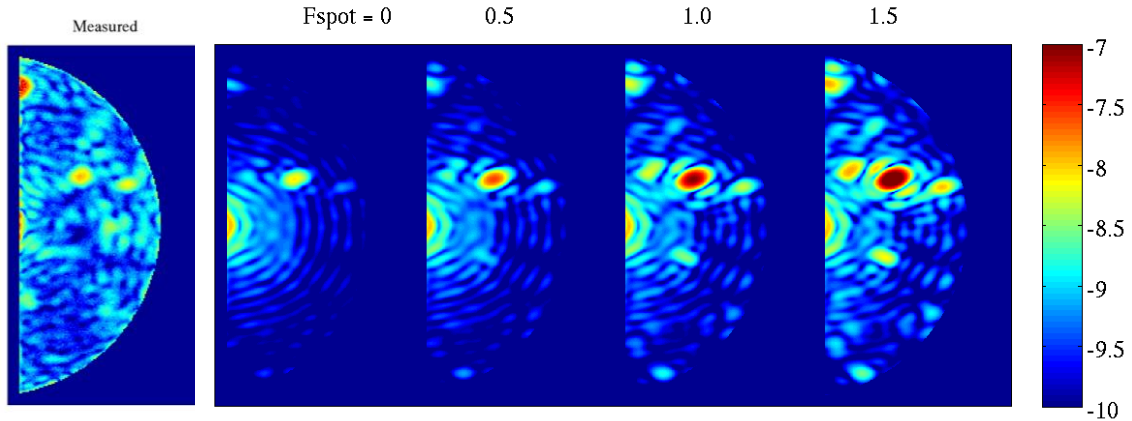
Figure 21 For the case of [X_{min}, R_{max}] = [3.5 20]λ/D, these figure show how the simulated contrast map changes with the value of the Occulter spot-phase factor, F_{spot}. The left-most part of these plots is the measured contrast map.

histogram of OD values for OD>0.02. The deepest spot OD has a value of ~0.1 and occupies only one pixel.

Registration of the dark hole with the mask was confirmed by the presence of 3 spots roughly horizontally aligned within the upper half of the red circle of Figure 19. These spots lead to the largest residuals in our models and are well aligned with dark hole residuals.

In Fig. 21, we obtained four 10%-broadband contrast maps corresponding to different values of F_{spot} (indicated in figure title). We also included the measured composite contrast map on the left for the purpose of comparison. The composite image was formed from three 2% bandpass filters, centered at 768, 800 and 832nm spanning a 10% bandpass. (We chose three instead of all 5 bands to decrease the time to perform the experiment.) In simulations, we used 3 monochromatic beams also centered at 768, 800 and 832nm.

The contrast values corresponding to the occulter spots depend strongly on the spot OD phase. This phenomenon is quantified in Fig. 22, where the 10% broadband I_b values are plotted as a function of F_{spot}, and the measured I_b value is also included for the purpose of comparison. Although there are some differences in the features between the measured and the simulated contrast maps, the simulated contrast map obtained with F_{spot} = 1 has a I_b value closest to the measured one. This is consistent with the similar situation reported in Sidick et al SPIE 9143 (2014).

After determining that F_{spot} = 1 yields the best match in terms of broadband I_b, we carried out simulations using F_{spot} = 1 in two other cases as well. The contrast maps at 3 wavelengths and their average values over the dark holes are shown in Fig. 23, and the corresponding I_b and I_s values are plotted in Fig. 24.

Figure 22 Simulated I_b versus F_{spot} for the case of [X_{min}, R_{max}] = [3.5 20]λ/D.

The I_b and I_s results for all four cases are summarized

in Table 11. The simulated results were obtained with an Occulter spot-phase factor value of $F_{spot} = 1$. Figure 24 and Table 11 show that average dark hole contrast is essentially independent of size up to the Nyquist limit of the DM used (24 λ/D). For the full dark hole (I_b), worst case model agreement assuming a π phase factor at OD=1 is 32% (1.27 x10^{-9} vs 1.88 x 10^{-9}). The prediction for the small dark hole (I_s, 4-5 λ/D) is off by up to a factor of two (7.23 x 10^{-9} vs. 3.7x10^{-9}).
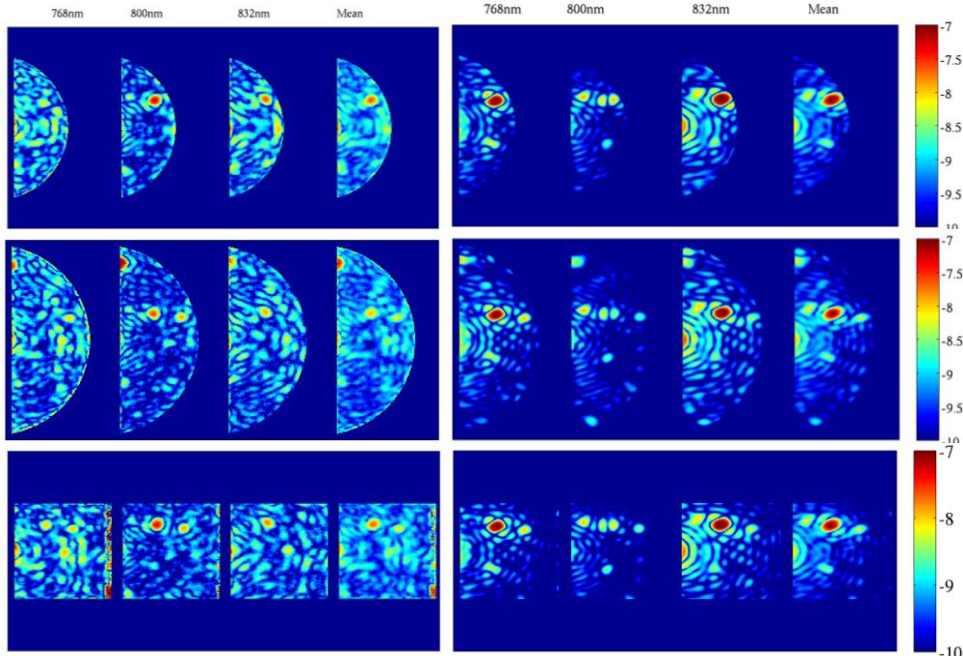
Figure 23 Left-column: Measured $I_n(x,y)$ maps at three 2%-bands and their mean corresponding to two D-shaped dark-hole areas with [X_{min}, R_{max}] = [3.5 15] (top row), and [3.5 20]λ/D middle row), and one rectangular area with [X_{min}, X_{max}, Y_{min}, Y_{max}] = [3.5, 24, -10, 10]λ/D (bottom row). Right-column: The corresponding simulated $I_n(x,y)$ maps obtained with monochromatic beams. The corresponding I_b and I_s values are listed in Table 11. The simulated results were obtained with an Occulter spot-phase factor value of F_{spot} = 1.

While the contrast results and model predictions are in good agreement, we point out that the detailed prediction of speckle positions and amplitudes is not well predicted by the models. In Sidick et al, SPIE 9143, 914336 (2014), we showed how the image plane pattern evolves when a set of particles is placed at different points in the dark hole area, as illustrated in Figure 25. To generate this figure, measured particles were modeled as described above. The EFC algorithm was brought to convergence using a composite 10% spectrum. Then, the particle map was moved down by 21 um (about 1 λ/D) and the process was repeated. Note the dramatic change in the model prediction. Rather than seeing a fixed pattern moving through the images, the pattern evolves in an

Table 11 Broadband contrast values corresponding to three different dark-hole sizes.

Dark-Hole Size		3.5 - 15 λ/D	3.5 - 20 λ/D	3.5 - 24 λ/D, -10 - 10 λ/D
I_b	Measured x 10^{-9}	1.27	9.61	9.42
	Simulated x 10^{-9}	1.88	9.73	1.14
	|Meas - Sim| x 10^{-9}	**0.61**	**0.12**	**8.28**
I_s	Measured x 10^{-9}	3.44	3.48	7.23
	Simulated x 10^{-9}	3.12	4.09	3.7
	|Meas - Sim| x 10^{-9}	**0.32**	**0.61**	**3.53**

unpredictable way. We had hypothesized that the particles would 'light up' when passing over Airy rings, but this is not necessarily the case as the EFC algorithm balances the wavefront to minimize the overall contrast. This example illustrates that we cannot expect the model to be able to predict the exact amplitude and position of the speckles without a very precise knowledge of the particle distribution on the mask.
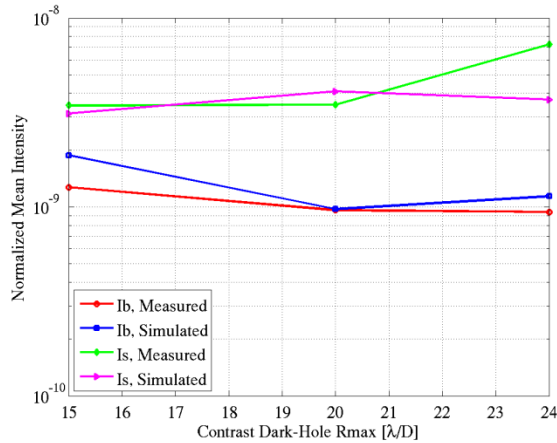

Figure 24 Measured and calculated I_b and I_s values as a function of contrast dark-hole size parameter R_{max}. In the third case, $X_{max} = R_{max}$. $F_{spot} = 1$ is used in the simulations.

D.   Bandwidth Dependence

The wavelength dependence of the wavefront correction is a key factor that affects the operational bandwidth as well as the time required to measure and set the wavefront. We have performed a series of tests to validate the predicted wavelength dependence of the wavefront when it is controlled in a single 2% band, or in multiple bands centered at 768, 784, 800, 816, and 832 nm. In all cases, we evaluated the contrast in all five bands and in the composite band formed by averaging the five bands with equal weighting. The tests were carried out between Jan 22 and Feb 1, 2013 (see Table 2). Most tests were carried out on 3 different days and no test was run more than one time per day. All tests were carried out in a D-shaped dark hole extending from x=3.5 to r=11 λ/D,

Our model uses the measured optical density and $F_{spot}=1$ as described above.

The following figures show the model and measured data and are arranged as follows. For each
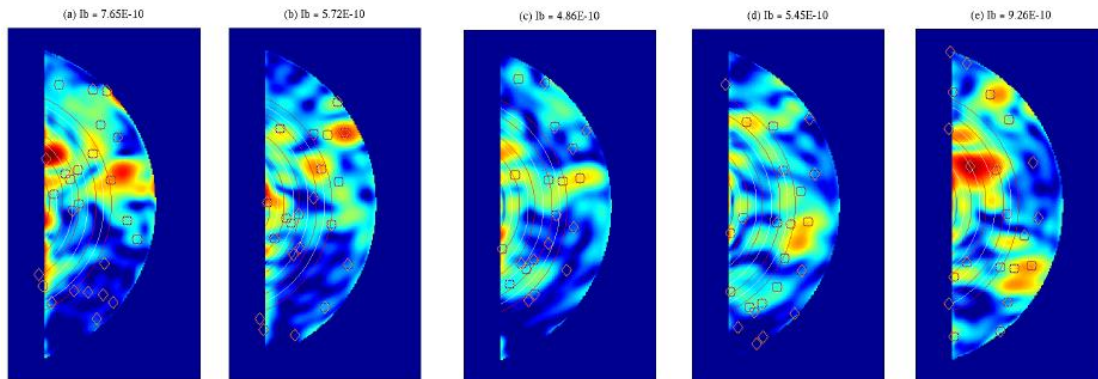

Figure 25 Change in dark hole when occulter particles are moved downward in 21 μm steps. The red and white arc lines indicate the positions of the Airy-ring peaks and valleys at the occulter plane. The markers indicate the locations of the major occulter spots.

29

test (e.g. control at 768 nm, or control at 768 and 832 nm):

- The upper left panel (when looking at the page in "landscape" mode") shows the measured contrast in each band for each run, and the model predictions.
- The lower left panel shows the average contrast of the 2 or three runs, and the model prediction (same as in upper left panel)
- The upper right panel shows the model prediction.
- The other right side panels show the measured data.

We performed the following tests:

- Control at 768 nm.
- Control at 800 nm.
- Control at 832 nm.
- Control at 768 and 832 nm.
- Control at 768, 800, and 832 nm.
- Control at 768, 784, 800, 816, and 832 nm. (This test was run just once.)

Results are summarized in Table 12. Values in the table match the lower left plots in the accompanying figures. It is interesting to compare the two cases where the upper and lower wavelengths are controlled. When the 832 nm wavelength is controlled, the model accurately predicts the contrast in the 768 nm band. But when controlling in the 768 band, the model overestimates the 832 nm band. Further, when controlling in the middle of the band, the model overestimates the 768 band but accurately predicts the 832 band. Values highlighted in bold can be compared to the 10^{-9} contrast prediction criterion.

The model predictions for simultaneous control at the 768 and 832 bands are intuitive; the contrast is best at those extreme bands, and worse in the middle. Yet the testbed did not behave

Table 12 Summary of Bandwidth Control Results

Control Band		768	784	800	816	832	Mean
				Contrast x 1e-9			
768	Measured Data	0.18	0.72	2.51	5.82	11.29	4.05
	Simulated Data	0.285	1.01	4.98	13.8	26	9.21
	|Meas - Sim|	**0.11**	**0.29**	**2.47**	**7.98**	**14.71**	**5.16**
800	Measured Data	2.91	0.82	0.009	0.81	4.33	1.79
	Simulated Data	8.22	1.11	0.0914	0.584	6.36	3.27
	|Meas - Sim|	**5.31**	**0.29**	**0.08**	**0.23**	**2.03**	**1.48**
832	Measured Data	12.07	7.15	3.26	0.91	0.13	4.67
	Simulated Data	11.2	5.29	1.89	0.501	0.125	3.81
	|Meas - Sim|	**0.87**	**1.86**	**1.37**	**0.41**	**0.01**	**0.86**
768 and 832	Measured Data	1.65	1.22	0.96	0.8	1.17	1.16
	Simulated Data	0.268	1.29	2.18	1.5	0.426	1.13
	|Meas - Sim|	**1.38**	**0.07**	**1.22**	**0.70**	**0.74**	**0.03**
784, 800, and 816	Measured Data	2.23	0.74	0.24	0.73	2.98	1.38
	Simulated Data	2.33	0.227	0.148	0.207	2.33	1.05
	|Meas - Sim|	**0.10**	**0.51**	**0.09**	**0.52**	**0.65**	**0.33**
768, 784, 800, 816, and 832	Measured Data	1.58	0.76	0.65	0.78	2.85	1.324
	Simulated Data	0.64	0.37	0.48	0.32	1	0.562
	|Meas - Sim|	**0.94**	**0.39**	**0.17**	**0.46**	**1.85**	**0.76**

this way at all. The middle bands had slightly better contrast than the ends. We do not understand why this happened.

Another significant difference between the model and the experiment is seen in the control at 3 bands, 768, 800, and 832. Here, the model predicts what looks like a quadratic increase in contrast (in the log plots) from the central band outward. But the experiment shows that the contrast increases linearly (again, in log space).

When controlling in all 5 bands, the general behavior is correct, but the model predicts that the 784 nm and 816 nm bands will have the best contrast, while the experiment showed that 800 nm was best. This, at least, is consistent with the 3 band test where the model predicted better behavior for 816 and 784 than was seen in the experiment.
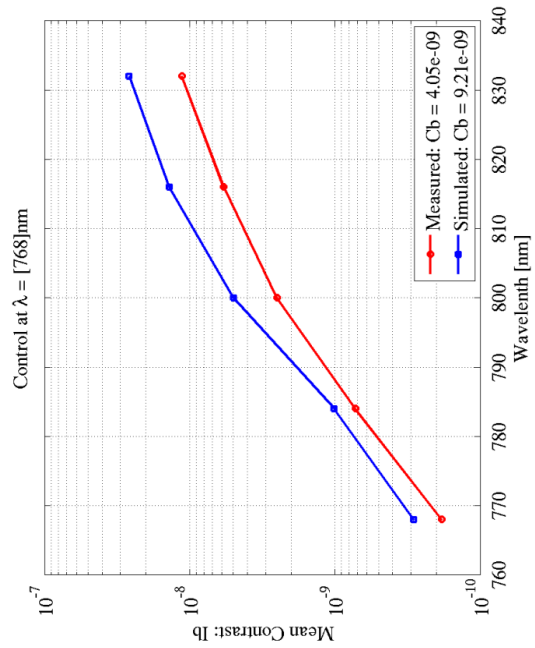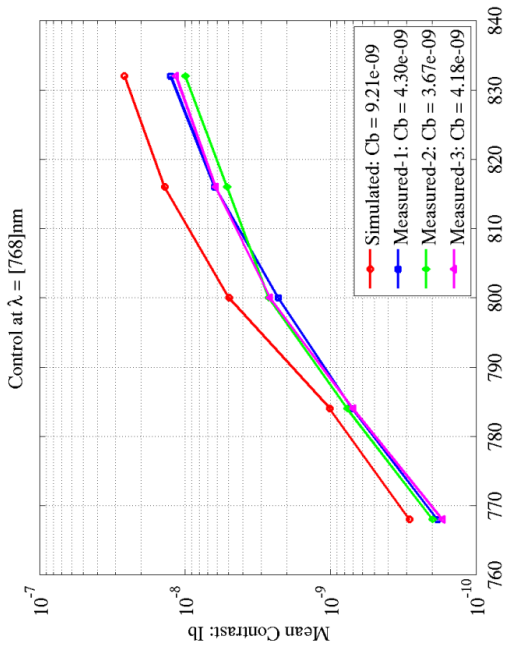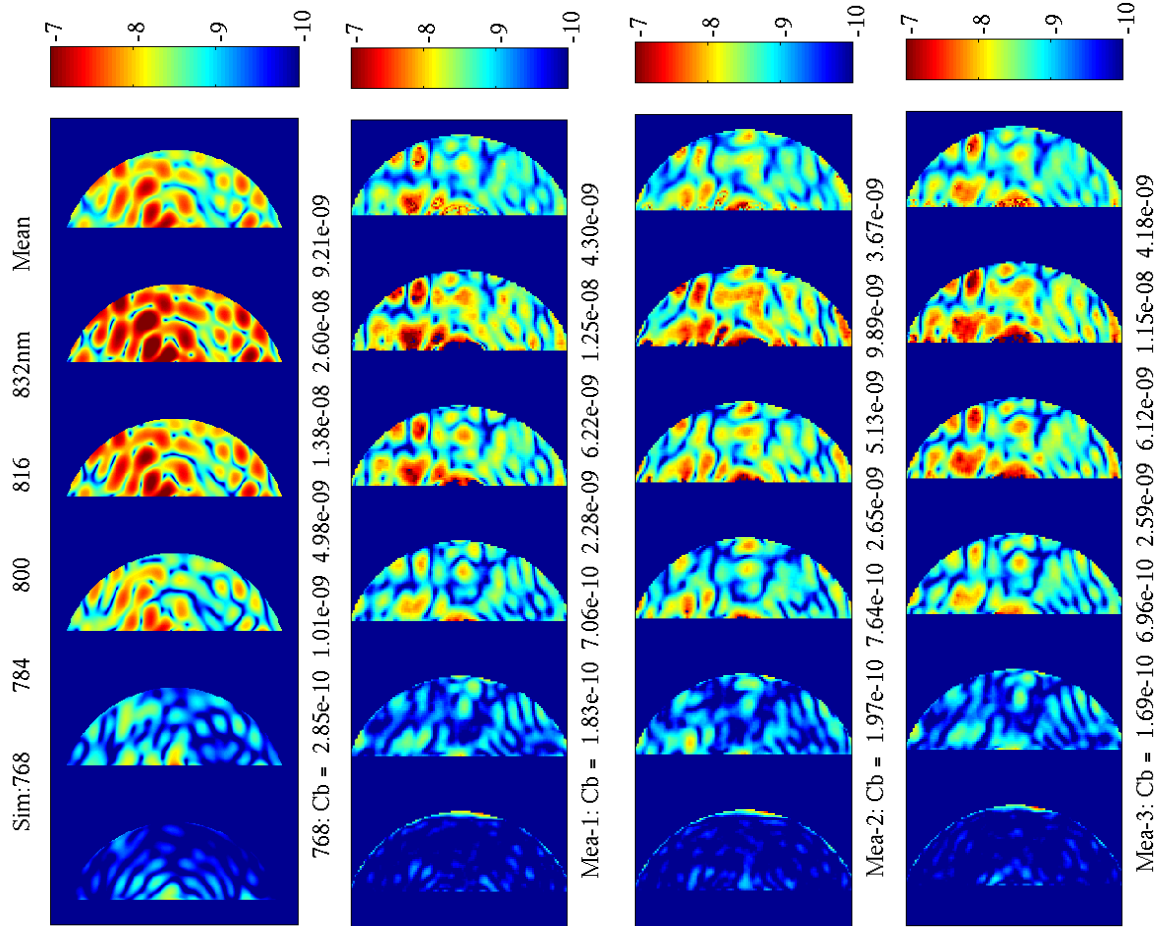
Figure 26 Control at 768 nm
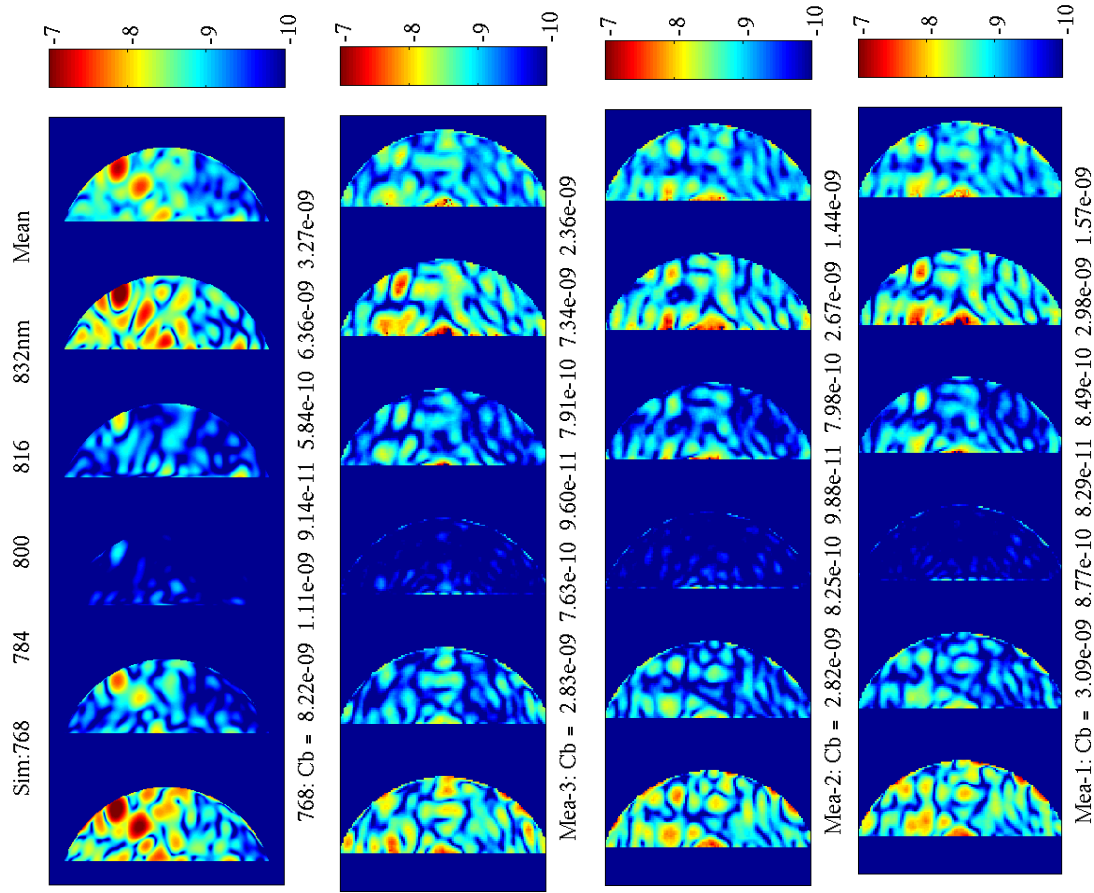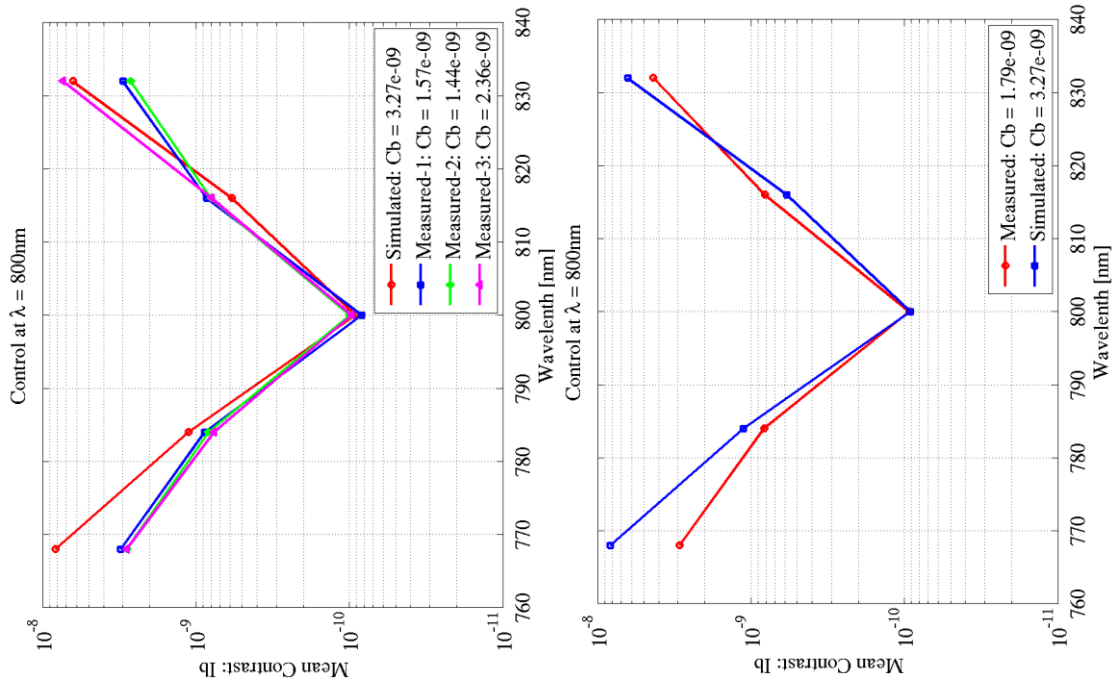
Figure 27 Control at 800 nm
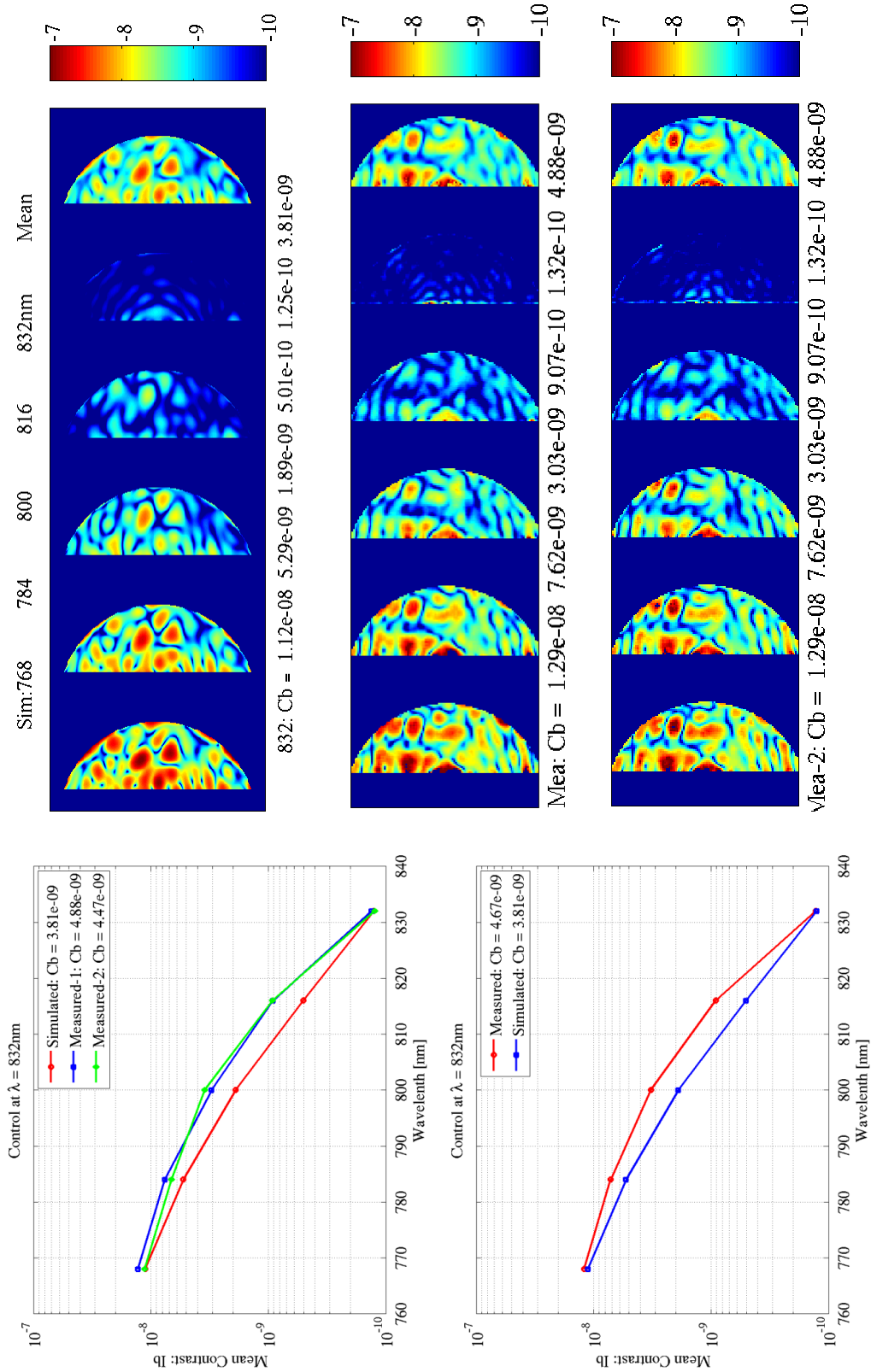
Figure 28 Control at 832 nm
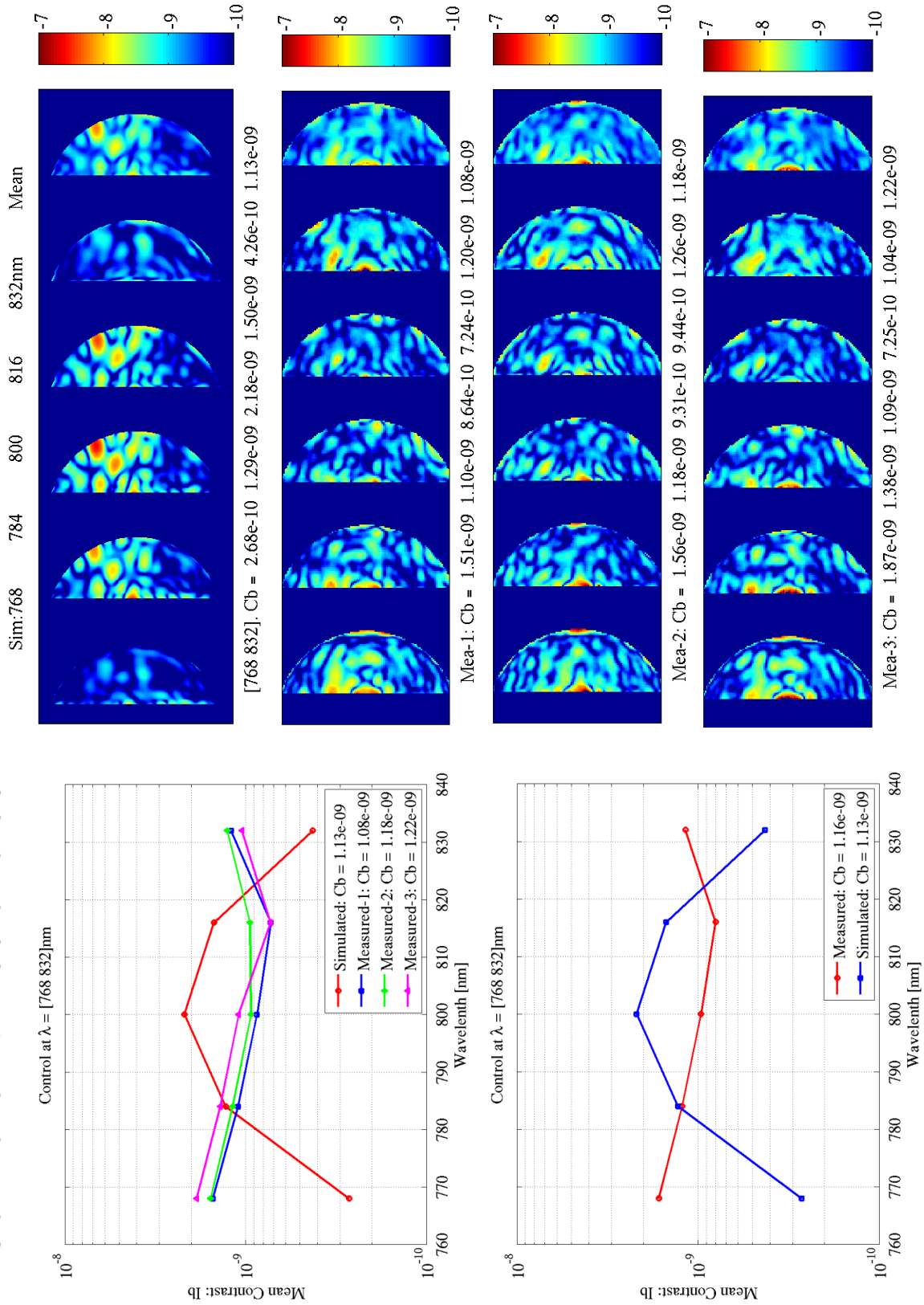
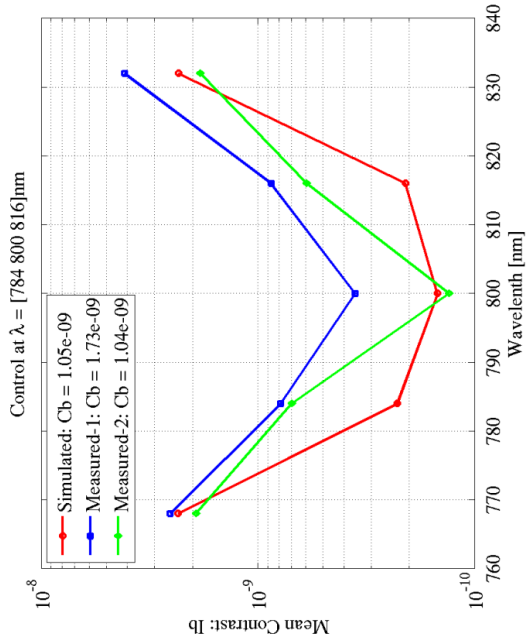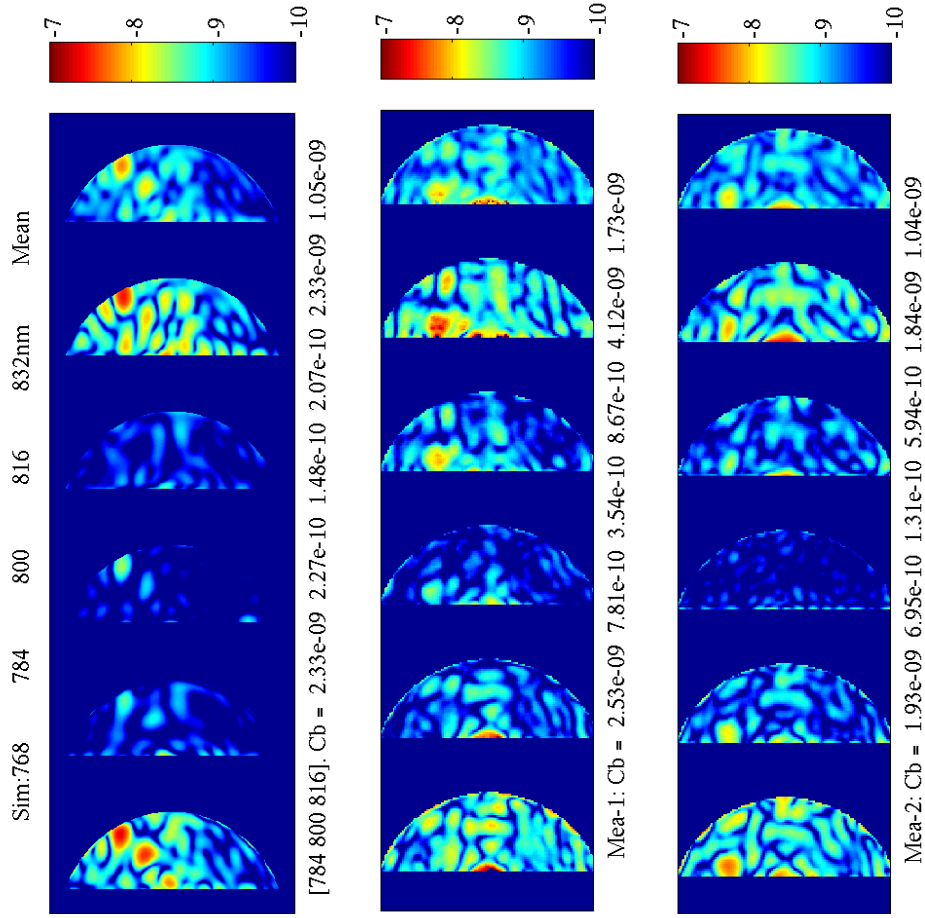**Figure 29 Control at 768 and 832 nm**
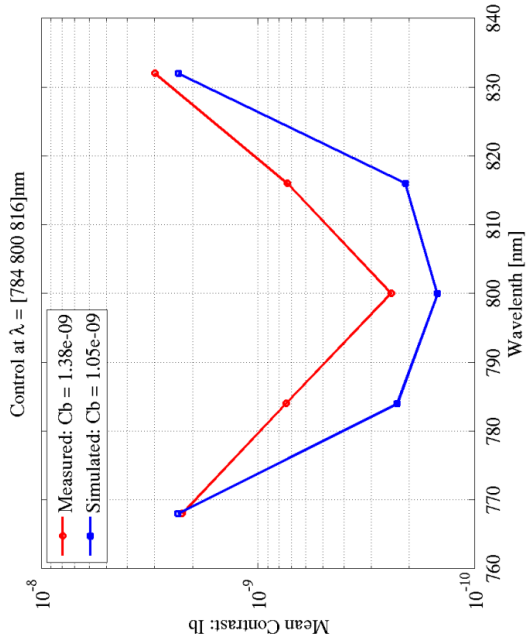
Figure 30 Control at 768, 800, and 832 nm
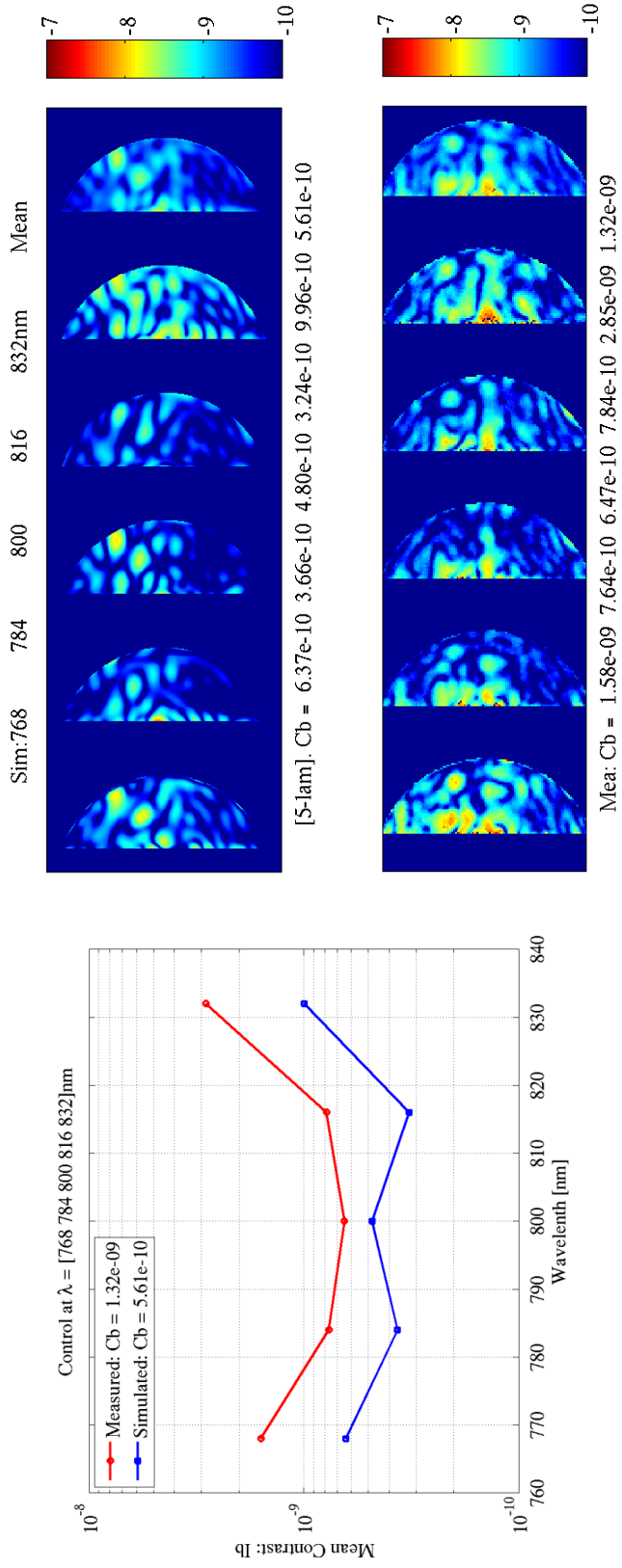
Figure 31 Control in all five bands

E. Frozen Actuators

In this test, actuators were offset significantly higher or lower than the nominal state used to minimize the optical system's total wavefront error. This tests the ability of the wavefront control algorithm to recover from actuators that are 'pegged' near the end of their range of motion. Figure 32 shows the DM's nominal state actuator commands in nm.

Nominal DM Actuator Setting [nm]
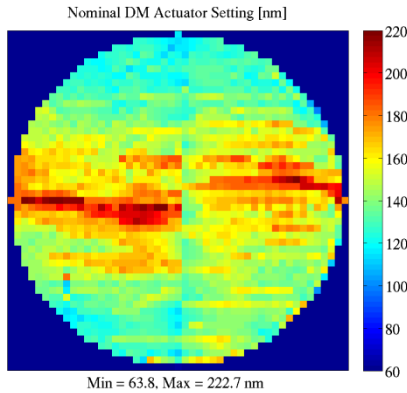
Min = 63.8, Max = 222.7 nm

Figure 32 DM phase when WFE is minimized through the system.

The pokes were done with pairs of adjacent actuators, whose DM settings were chosen such that the pair gave a 125 nm peak-offset in the wavefront in a localized region in the pupil. (See section III.C)

The experiment was run with 1, 2, 3 and 4-pairs of actuators poked, with the pokes alternating between introducing positive and negative OPD. After poking a pre-determined pair of actuators, EFC was run using 3-band control with the 2%-filters centered at 768, 800 and 832nm. Phase retrieval images were also taken for the DM setting before and after

Figure 33 Top: Measured heights of the actuators estimated from phase retrieval data after EFC had converged. Values correspond to Table 13. Second row: Measured heights of all actuators after EFC converged (relative to nominal condition of Figure 32). Third row: Actuator heights from the model (pegged actuators are fixed at the Table 13 values). We call this Sim1. Bottom: Actuator heights from the model when the starting condition is the measured data of the second row, Sim2.
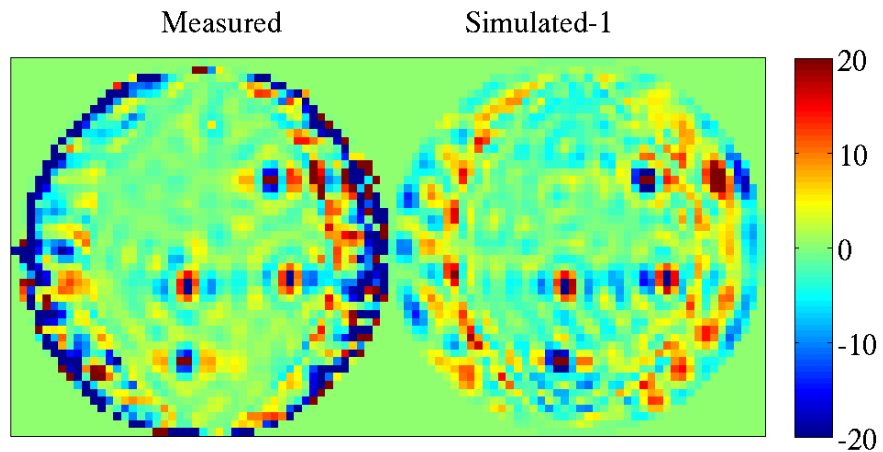
Figure 34 Measured and simulated (Sim1) actuator heights corresponding to 4-pairs of pegged actuators.

each run. Before carrying out broadband EFC simulations, we first determined the actual, post-EFC (experimental) heights of the pegged actuators from the phase-retrieval data. Table 13 lists
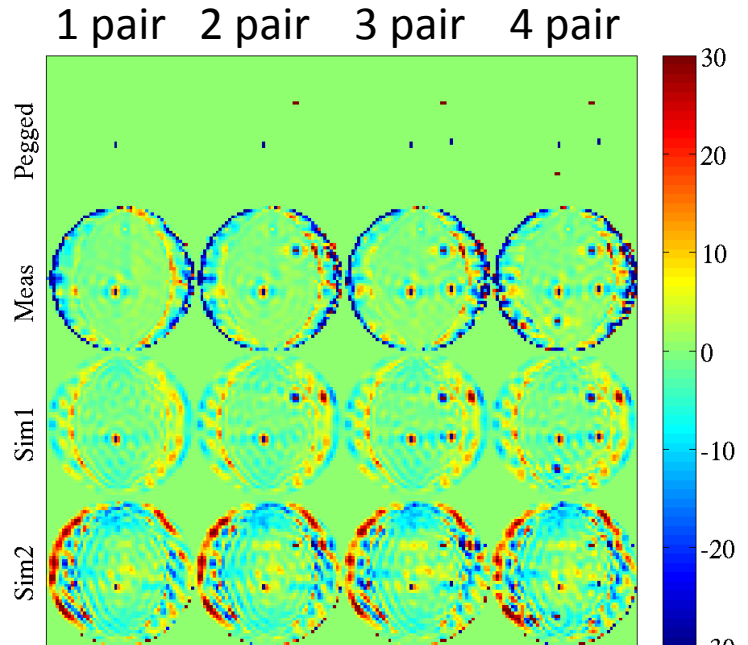
Table 13 Intended and actual heights of the pegged actuators.

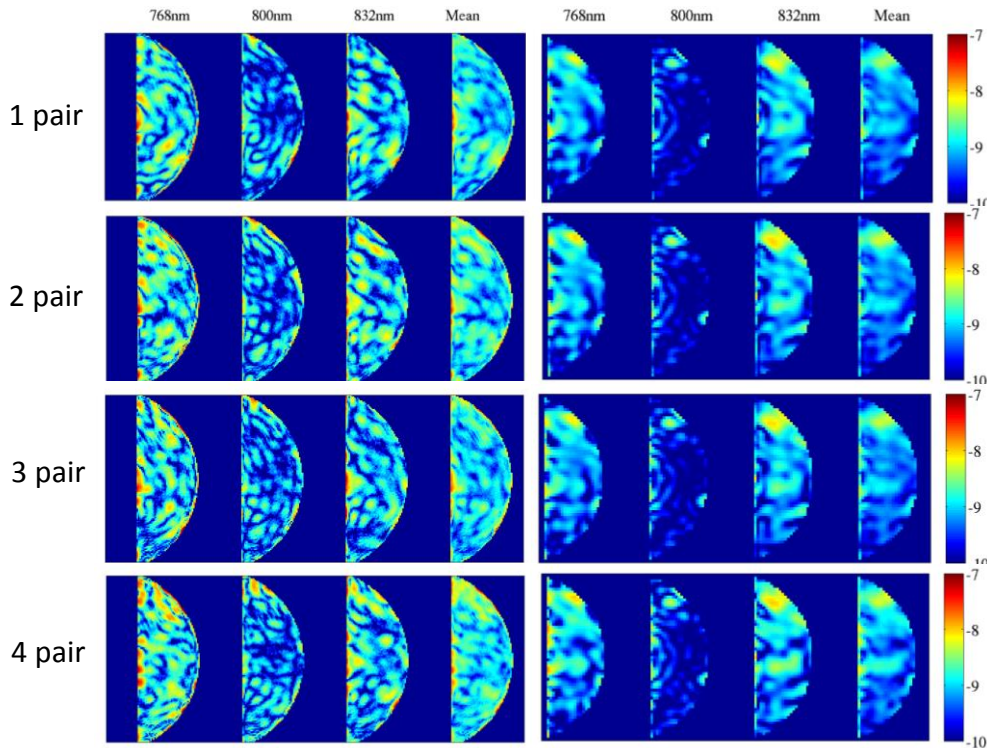|		1st Pair		2nd Pair		3rd Pair		4th Pair		Unit
Intended	All	-62.5	-62.5	62.5	62.5	-62.5	-62.5	62.5	62.5	nm
Actual	1-Pair	-66.5	-50.4							nm
	2-Pairs	-66.6	-50	65.8	55.9					nm
	3-Pairs	-65.8	-49.9	65.8	55.5	-49.4	-53.1			nm
	4-Pairs	-66.4	-49.9	65.8	55.6	-48.4	-52.5	55.1	57.5	nm

Figure 35 Left-column: Measured In(x,y) maps at three 2%-bands and their mean corresponding to two D-shaped dark-hole areas with [Xmin, Rmax] = [3.5 11]λ/D. From top to bottom they correspond to 1-, 2- 3- and 4-pairs of pegged actuators. Right-column: The corresponding simulated In(x,y) maps obtained with monochromatic beams. The corresponding Ib values are plotted in Fig. 4. The simulated results were obtained starting EFC from a flat DM actuator state (Sim1).

the intended and the actual heights of the pegged actuators and Figure 33 (top row) shows their locations. The stroke amplitudes in the figure are ½ the wavefront value in Table 13. The second row of Figure 33 shows the post-EFC wavefront (minus the nominal of Figure 32). This is the change in wavefront that created the dark hole. The pegged actuators are shown at their measured positions. Our model results are in the 3rd and 4th rows of Figure 33. Starting from a flat pupil (the condition that the nominal wavefront of Figure 32 creates), a simulation that we refer to as Sim1, the edge actuators around the Lyot stop move much less in the model than in the experiment. Curious to see if the model could find a good solution close to the experimental

result, we also started with the experimental wavefront (row 2) and let EFC converge, leading to Sim2 shown in row 4. Here there are significantly larger deviations from nominal than in the experiment. Thus the model does not accurately predict the DM settings around the pupil edge. However, it does accurately predict the behavior in the vicinity of the actuators. Figure 34 shows the "zoomed-in" version of the measured and the simulated (Sim1) actuator heights corresponding to 4-pairs of pegged actuators. Note the compensatory negative and positive lobes around the pegged actuators.

The measured and modeled dark hole images are shown in Figure 35. We have used the mask OD map described in section V.C in our model (phase multiplier $F_{spot} = 1$). The corresponding I_b values and their measured-to-simulated ratios are plotted in Figure. 36. It is noted that the dependency of broadband contrast on the number of pegged actuator pairs is fairly weak.
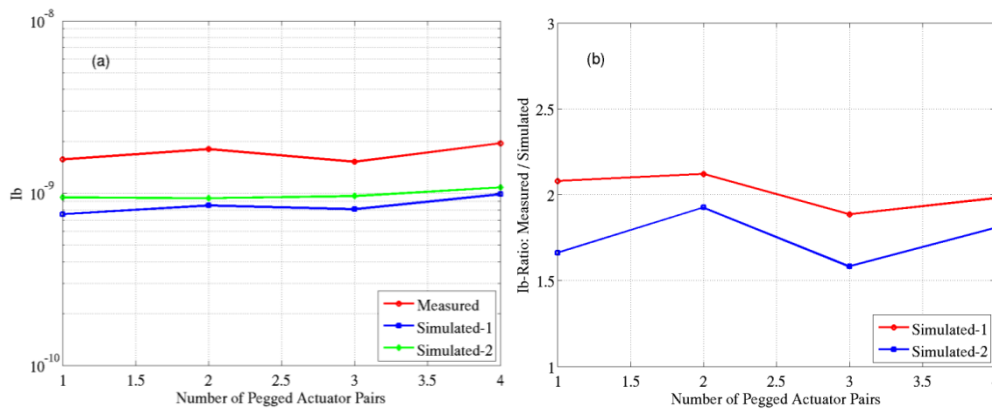

Figure 36 a) Measured and calculated I_b values as a function of the pegged actuator. (b) The ratio of the measured and the simulated I_b values. The measured I_b values were calculated inside [X_{min}, R_{max}] = [3.5 10.6]λ/D because the EFC was carried out up to $R_{max} = 11\lambda/D$ when using the 2%-filter centered at 768nm, and $R_{max} = 11\lambda/D$ at 768nm becomes $R_{max} = 10.6\lambda/D$ at the center wavelength of 800nm.

F.   Coherent and Incoherent Estimation

This section is extracted from E. Cady & S. Shaklan, Proc. SPIE 9143, 914338 (2014), attached in the Appendix to this report.

A major component of the estimation and correction of starlight at very high contrasts is the creation of a dark hole: a region in the vicinity of the core of the stellar point spread function (PSF) where speckles in the PSF wings have been greatly attenuated, up to a factor of 10^{10} for the imaging of terrestrial exoplanets. At these very high contrasts, removing these speckles requires distinguishing between light from the stellar PSF scattered by instrument imperfections, which may be partially corrected across a broad band using deformable mirrors in the system, from light from other sources which generally may not. These other sources may be external or internal to the instrument (e.g. planets, exozodiacal light), but in either case, their distinguishing characteristic is their inability to interfere coherently with the PSF. In the following we discuss the estimation, structure, and expected origin of this "incoherent" signal in the context HCIT experiments. We find that the "incoherent" signal at moderate contrasts is largely estimation error of the coherent signal, while at very high contrasts it represents a true floor which is stable over week-timescales.

The regions of high image-plane contrast ("dark holes") require iterative correction from a wavefront control system to compensate for imperfections in the optical system down to sub-nm scales.To effect this correction, we must first estimate the amplitude and phase of the starlight across the dark hole. Here we use primarily a pairwise-estimation scheme which modulates the electric field by applying known offsets to the DM settings.

In addition to determining the complex electric field associated with the starlight, the pairwise method also makes an estimate of the components of the signal which do not modulate with the DM and thus are not coherent with the star. This signal has been termed the "incoherent" part of the wavefront. This is a something of a misnomer; as will be shown later, some parts are errors in estimating the field which interferes with the DM probes, and some components do genuinely not interfere with the probes. Nonetheless, it has stuck. In a science image this would include the signals from any planets or disks in orbit about the star.

The incoherent signal was initially viewed as a nuisance, as it represented background that could not be used in the correction and had to be subtracted off prior to control. However, it also represents an opportunity, as treating the starlight as the nuisance and subtracting the coherent signal off can serve as a post-processing technique that does not rely on angular or spectral diversity. To show this can work, though, we need to show that 1) an incoherent signal can be shown to exist, *i.e.* the measurement is not an artifact, |and 2) that it can be reliably separated from the starlight.

For details of the analysis, including a description of how we employed the median and the Median Absolute Deviation Normalized (MADN) in place of the mean and standard deviation statistics, we refer the reader to Cady & Shaklan (2014) Briefly, once a deep contrast was attained, the images suffered from significant read noise and shot noise, and the statistics were not Normal, with significant outliers. The median and MADN are robust estimators that suppressed the spurious noise spikes in the processed data. Figure 37 compares the convergence curves for the measured dark hole median contrast and estimated spread with the MADN, to the mean and standard deviation. The median and MADN effectively filter out most of the spurious noise.

In curves such as the ones in Figure 37, we see two distinct regimes of behavior, which depend on the coherent contrast level. In the first, which we can see in Figure 38, the incoherent signal tracks the coherent signal at a nearly-constant level, with the incoherent down by a factor of 2-3, depending on wavelength. In the second, shown in Figure 39, the coherent signal crosses below the incoherent signal, and the incoherent signal reaches a floor in the vicinity of 2×10^{-10}. The exact number has some chromatic dependence, and decorrelates from the coherent signal entirely. (This behavior was also noted in Give'on *et al*, 2011.)
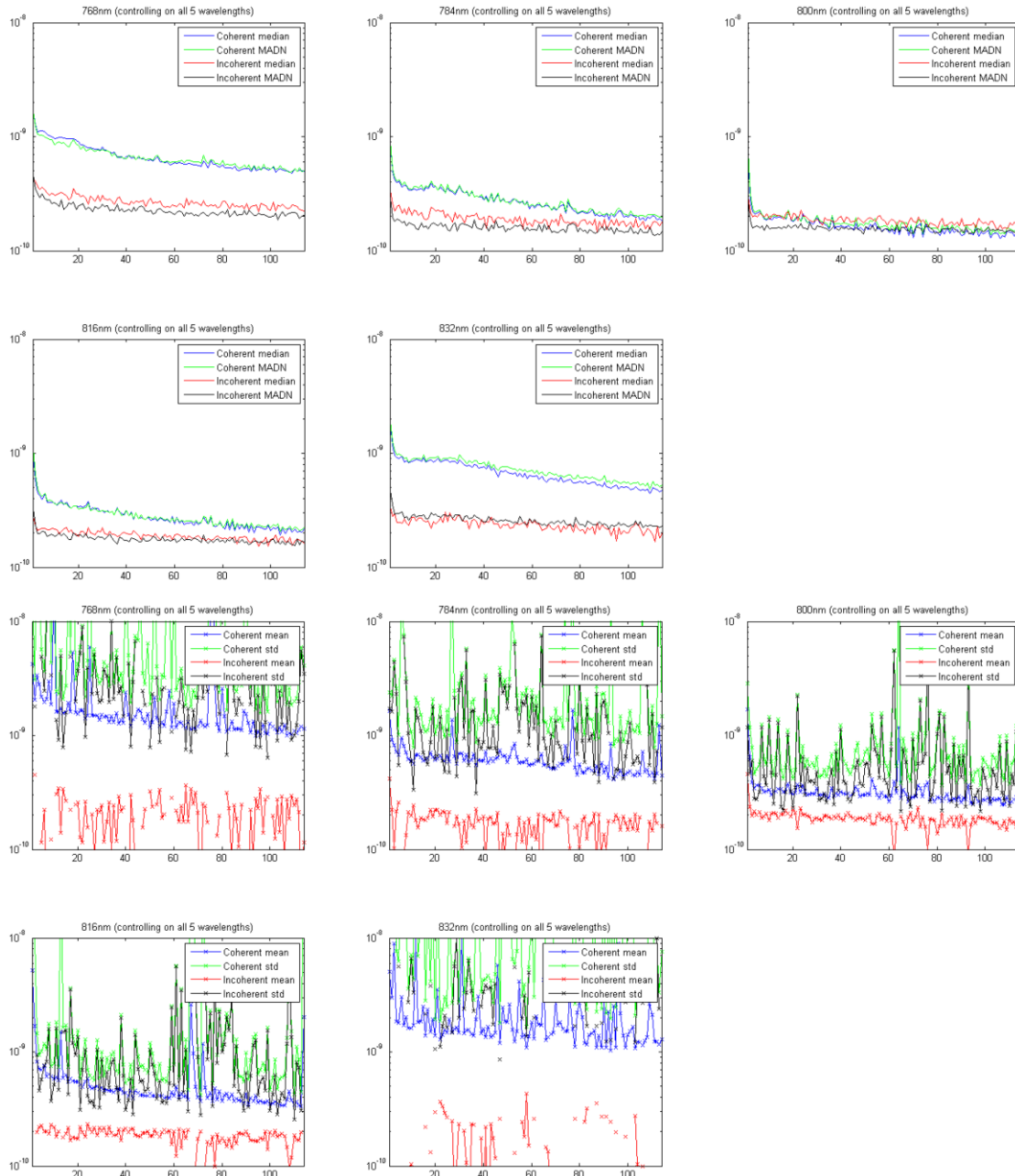
Figure 37 Central location and spread of distribution of coherent and incoherent light across 5 wavelengths, using data taken from test #6. *Top:* **Location estimated with median, spread estimated with MADN.** *Bottom:* **Location estimated with mean, spread estimated with standard deviation. Missing points indicate estimates for the mean intensity in the dark hole less than zero.**

This behavior strongly suggests that above a median coherent intensity of 6x10⁻¹¹ the primary component of the incoherent signal is coherent light that has been incorrectly categorized as not interacting with the starlight.

The cases of the corrections in test #5 and test #12 (see Table 2) are instructive in informing this conclusion. Test #5 was performed on two filters at opposite ends of a 10% bandpass (768nm

and 832nm). As an initial condition, it used a DM flattened by phase retrieval, with no prior attempt at a dark hole. After ~12 iterations, the coherent signal had dropped below 10^{-8}, and continued to decrease until the end of the run. Figure 38 shows the performance across 77 iterations (top). The bottom shows the ratio between the medians of the coherent and incoherent signal, which track at a nearly constant level after the initial corrections. Conversely, test#12 was performed over a single 2% bandpass (centered at 768 nm), and started from a DM setting that created a dark hole over the central three 2% filters (784, 800, and 816 nm). Thus, correction began from a position that already had good suppression, and rapidly pushed the coherent signal to approximately 6×10^{-11}. The incoherent signal maintained its customary floor in the vicinity of 2×10^{-10}; Figure 39 shows the overall performance across the 25 iterations of the test.

The reader is referred to Appendix 9 for the complete results including plots of the coherent and incoherent estimates of the dark hole evolving over time and in different wavelengths. The conclusion of this study is that our ability to extract the estimate of the incoherent noise floor is limited by the magnitude of the coherent field; roughly 25% of the coherent signal is incorrectly treated as incoherent, and this term dominates that signal until the contrast floor is neared. Nonetheless, this represents a factor of 4 suppression in post-processing without invoking any spectral diversity.
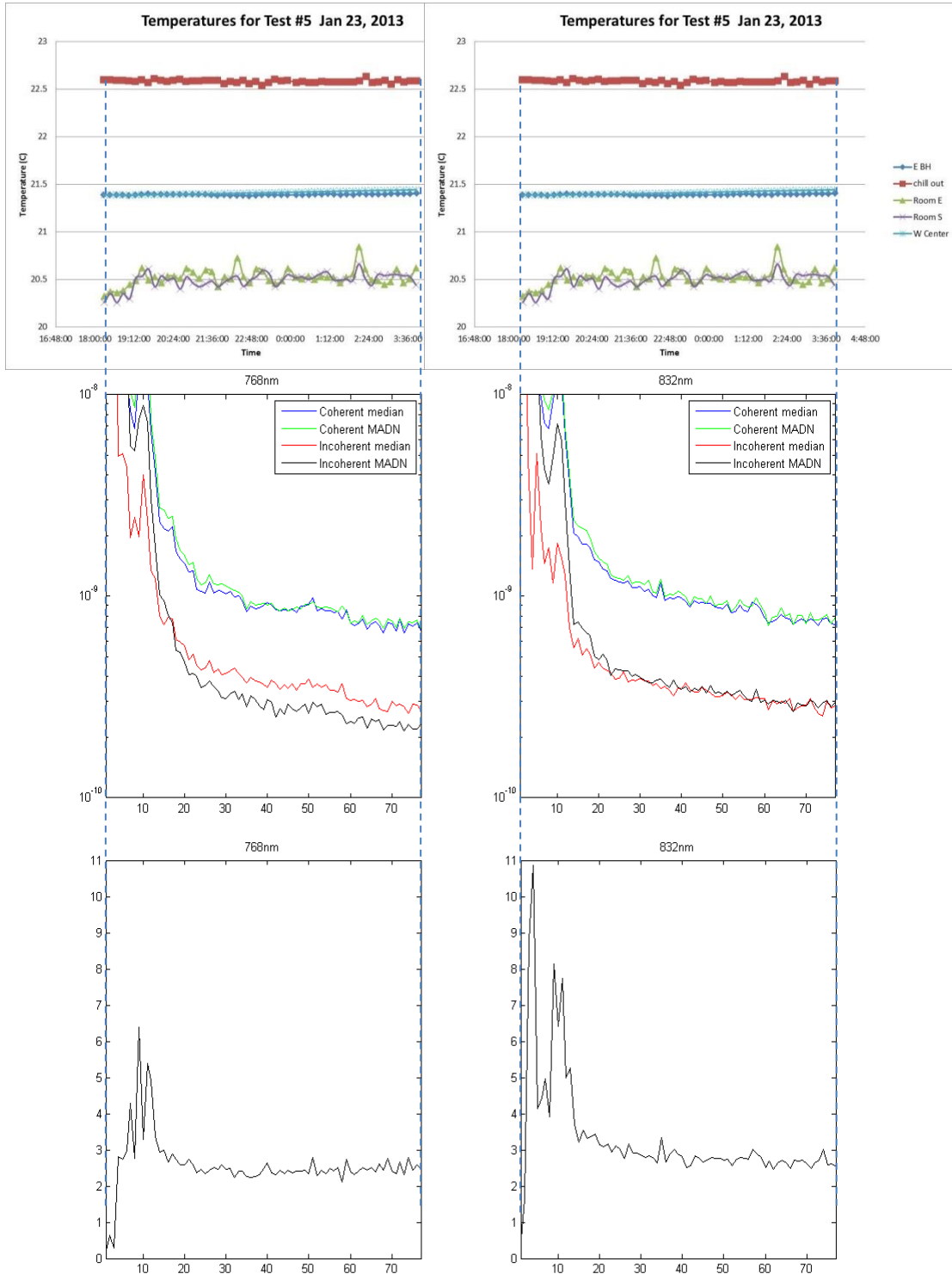
Figure 38 *Top:* **Temperature data for test #5 aligned. The time line is stretched to match the convergence curves below.** *Middle:* **Location and spread of coherent and incoherent light across 2 wavelengths, using data from test #5.   Unlike most of the runs in this data set, this was initializes with a DM corresponding to a mediocre wavefront, rather than one that provides high contrast for a different bandpass,** *Bottom:* **Ratio of coherent and incoherent median.**
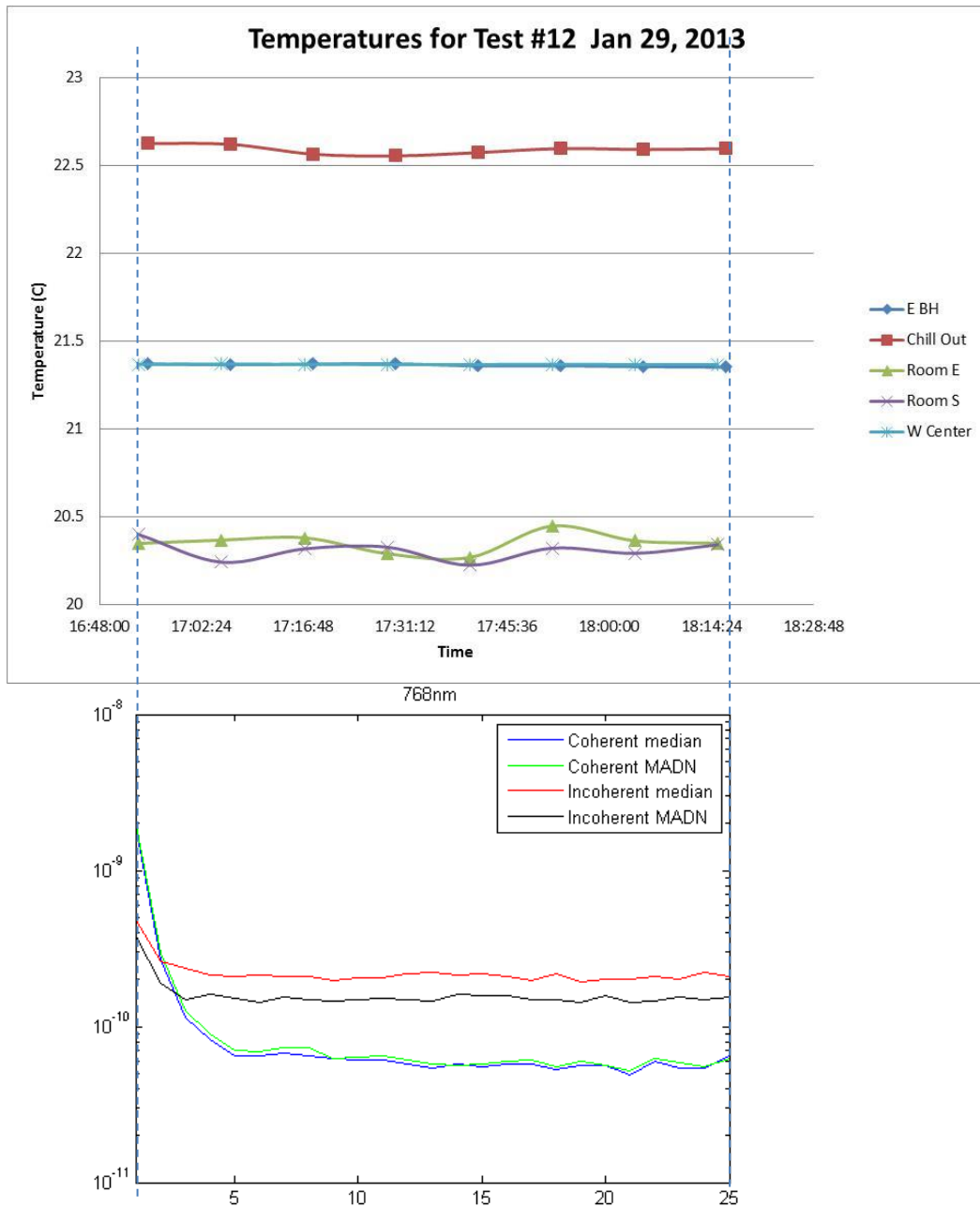
Figure 39 *Top:* **Temperature data for Run #12, aligned with the convergence curves below.** *Bottom:* **Location and spread of coherent and incoherent light in the 2% filter centered at 768nm, using data taken from test #12.**

VI.   Error Budget Terms

The data certification package described in the Milestone White Paper call for an updated HCIT error budget based on measured M3A sensitivities, with appropriate documentation for each error box. The error budget has two distinct parts; the *static* and *dynamic* branches (Figure 40).

The static branch refers to the performance related to the construction and initiation of the testbed including the effectiveness of the wavefront estimation and control algorithm. The dynamic branch refers to the sensitivity to motions and bending of the optics due to thermal drifts and vibrations.

A. Open-Loop Performance

We have generated a detailed dynamics error budget for an upcoming WFIRST/AFTA coronagraph testbed referred to as the Modelable Coronagraph Bench (MCB). The error budget follows directly from published coronagraph error budgets (Shaklan et al, 2005; Marchen & Shaklan, 2009; Shaklan et al, Shaklan et al, 2011) It allocates tolerances to the motions (thermal and jitter) of the optics, and bending of the optics. The error budget assumes open-loop operation; that is, it assumes that the wavefront control system does not correct for the thermal drifts and vibrations that occur once the dark hole has been created with the wavefront control algorithm. It addresses only the right side of the error budget shown in Figure 40.

We performed one open-loop experiment, the lateral and axial mask translation experiment (Table 14, blue box). Here we found that the PROPER diffraction model generally predicted the change in contrast to within 50% of the measured value over a wide range of defocus (+/- 200 um) and lateral motion (+/- 4 um) as seen in Figure 14. The predictions addressed both the "small box" from 4-5 λ/D, and the "big box" covering the D-shape from 4-5 λ/D. The error budget includes a 50% model uncertainty factor (MUF) to account for the difference in observed and predicted sensitivity to motion.

The dynamics budget includes many terms that we were unable to address at high-contrast levels because the specific effects could not be isolated from one another. For example, the error budget computes the effect of beam walk or motion of the beam across imperfect optics. To isolate a change in contrast due to beam walk at contrast levels of interest (e.g. 10^{-7} or 10^{-8}) would have required fabrication of an extremely high precision optic that was beyond the scope of the TDEM. In Sidick et al (2011) we showed that beam walk across an optic with an intentional 2.5 nm amplitude, 4 cycle-aperture sine wave on the surface caused a 2×10^{-5} change in contrast with a small translation. The same paper showed that accurately predicting the contrast change given a measured wavefront of an optic was problematic.

Other important terms in the error budget are aberrations due to motions and bending of the optics. Our M3A tests addressed the three largest terms, focus and tip/tilt. To isolate the effects of other aberrations such as coma and astigmatism would have required either actuation of a DM (this could have been done) or construction of a calibrated low-order deformable mirror (this is being done for the MCB). Implementing a coma term on the DM would have required timely, accurate calibration of the DM beyond the levels so far achieved. There was not time available in the testbed to perform this calibration during the M3A experiments.
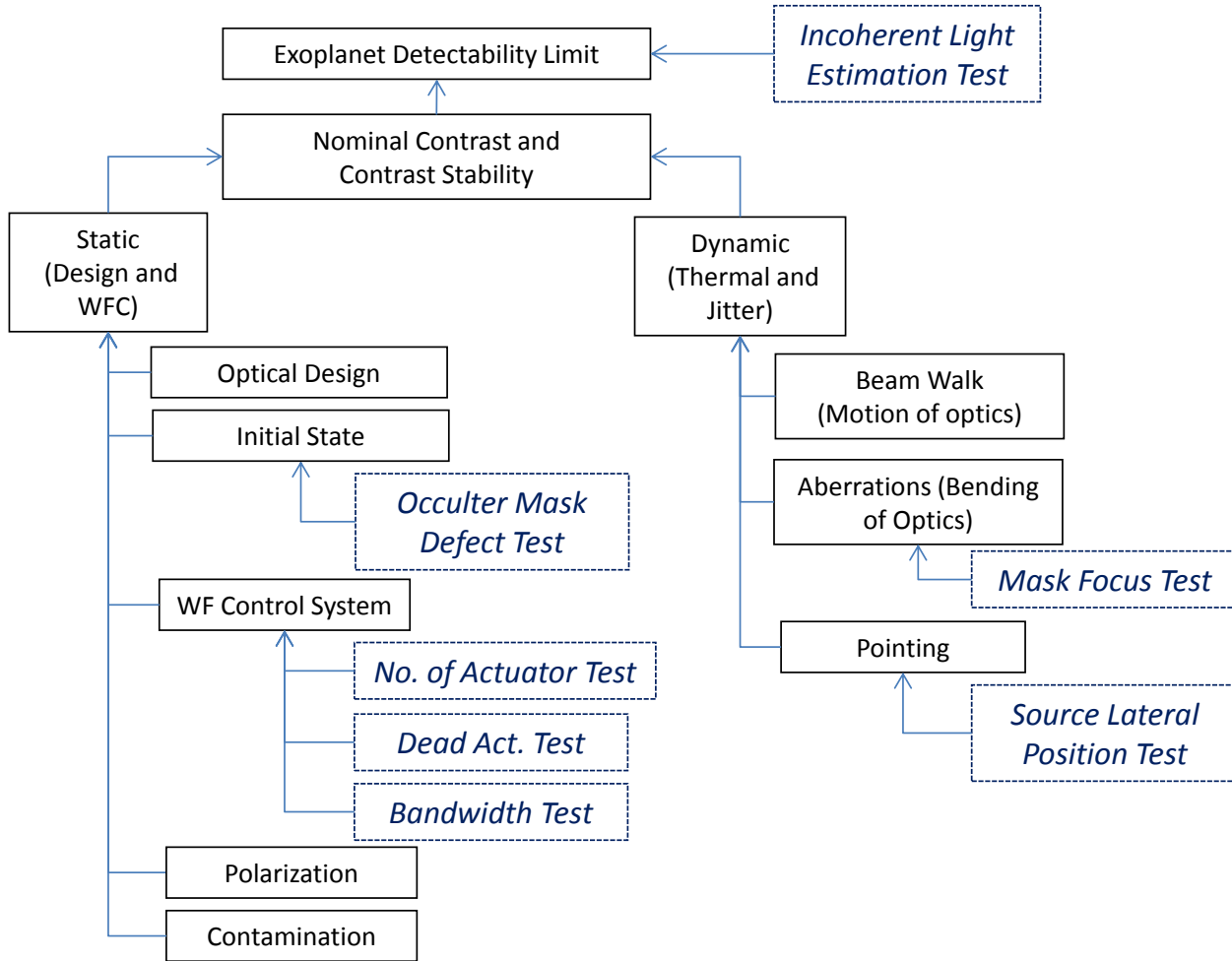
Figure 40 Coronagraph Error Budget Structure. Black: Error budget terms. Blue: Milestone 3A tests

B.   Closed-Loop Performance

Most of the tests and simulations performed were closed-loop (Table 14, green box); a perturbation was introduced, and the wavefront control system was then used to reduce the scatter in the dark hole. Here we found that the dark hole contrast was quite insensitive to asymmetry of the mask, the phase of the Nickel mask transmission coating, and to clipping of the optical density at the center of the mask. At levels expected in the testbed, none of these effects would cause the contrast floor to rise by more than a few x 10^{-10}. Similarly, the models show that the testbed is insensitive to both floating and 'pegged' actuators. Floating actuators, in particular can be tolerated in large numbers.

Table 14 Error Budget Terms explored by M3A Simulations and Experiments

Test	Box	Contrast	Numerical value and reference
Nominal Case	I_b	5.60E-11	10% bandpass.
	I_s	3.98E-10	SPIE 9143, Fig 4
Mask Defects			
Clip OD	I_b	2.60E-10	Clip at OD = 3.5.
	I_s	1.00E-09	Sidick, SPIE 9143, Figs 8, 9
OD Asymmetry	I_b	1.30E-10	OD reduced by 40% one side, OD>1
	I_s	8.45E-10	Sidick SPIE 9143, Figs 8, 9
Phase	I_b	1.30E-09	2x catalog bulk property
	I_s	1.10E-08	Sidick, SPIE 9143, Fig 10
Particles/local defects	I_b	5.60E-10	At levels of M2 mask
	I_s	3.16E-09	Sidick, SPIE 9143, Fig. 16. This report Fig 31
Dark Hole Size	I_b	5.60E-11	3.5 - 20 l/D for a 48x48 DM
	I_s	1.70E-09	Sidick, SPIE 8864, Table 3
Dead Actuators			
Floating	I_b	1.00E-10	200 random unpowered actuators
	I_s	3.16E-10	Sidick, SPIE 8520, Figure 11.
Pegged	I_b	<1e-9	Pairwise at 65 nm, up to 4 pairs
	I_s	<1e-9	This report, Figs 35, 36. Assumes particles present
Mask Focus	I_b	1.00E-09	100 um defocus, effect is quadratic with motion
	I_s	3.50E-09	Sidick, SPIE 8864, Fig 6, Table 1
Mask Lateral Trans.	I_b	3.50E-09	2 um lateral motion, effect is quadratic with motion
	I_s	1.50E-08	Sidick, SPIE 8864, Fig 4
Coherent Estimation Error	I_b, I_s	25%	Cady, SPIE 9143 Fig 4.

However, we found that the testbed static contrast floor behaves as if it is limited by local mask contaminants and non-uniformity. A model of the contaminants that uses the measured optical density and a phase term proportional to the density mimics both the spatial and spectral behavior of the noise floor. Some specific features observed in the dark hole are clearly related to local contaminants. Others, however, have no obvious source. This may be due to the appearance and disappearance of particles between the time of the observations and the time that the mask was removed and measured under a microscope.

With a sufficiently ideal mask, our models show that the testbed should be able to achieve close to 10^{-9} contrast from 4-5 λ/D and better than 10^{-10} average contrast over the full dark hole (to 15

λ/D). Future tests with clean masks are required to determine the validity of the models at 10^{-10} contrast levels.

Finally, we have found that estimation of the incoherent light level (i.e. the planet, zodiacal, and other sources not related to the target starlight) is limited by estimation errors of the coherent light level. Roughly 25% of the coherent light in the system is attributed to incoherent light over a wide range of contrast values down to at least 5×10^{-10}. This sets the planet detectability limit at about the level of the coherent light, since a signal-to-noise ratio of at least 4 is required to claim detection of a planet in the presence of background speckles. Better estimation is required to 'dig' planets out from below the speckle noise floor.

VII. Suggested Follow-On Work

There are several important issues identified in these tests that require follow on work. The following list identifies the most critical items:

1) Fully characterize the coronagraph image plane mask to the extent possible and validate the contamination model. This will require: high resolution microscope images, ideally at the same wavelengths used by the coronagraph; SEM images and spectral characterization of the surface; and AFM images to accurately measure heights. Then we need to develop a physics model of transmission through the mask and use this model to describe the observed background including the observed chromaticity. One can expect some agreement with the Milestone 3A test data, but must keep in mind that the mask may have picked up or lost contaminants and could possibly have changed (e.g. a thin film layer or oxidation) in the intervening years between the experiments and follow-on characterization. Ideally, new experiments with a mask characterized both before and after the experiments would inform the models.

2) Resolve the three open chromatic issues: the broad-band behavior when the two end wavelengths are used together for wavefront estimation, the behavior of the edge of the DM (this largely provides the chromatic leverage in the Lyot coronagraph); and understand the origin of the incoherent light in the Lyot tests. This light has unexplained chromaticity (see Figure 11 of Cady and Shaklan 2014). B. Kern suggests that the way to begin studying the chromaticity is to form a modal decomposition of observable chromatic effects, e.g. form a blue speckle at a particular location in the image plane, and compare to the experiment. It may be best to base this on empirical measurements of the effects of single pokes in the image plane to generate the wavefront estimation Jacobian. For our tests we used only a model-based Jacobian.

3) Test ability to observe out a planet using artificial planet light, completing the experiment that was stopped due to hardware failures. Data sets should be provided to a post-processing team for blind studies. AFTA is assuming a factor of 30 calibration of speckles, about 10x better than we achieved in the Milestone 3A work.

4) Determine the root cause of the differences between MACOS and PROPER results. In our SPIE paper (Sidick et al, 2013) we showed that MACOS and PROPER had excellent agreement in two cases: first, with the Lyot stop removed, the occulter mask was placed at three different axial locations. This showed the evolution of the diffraction rings in the image plane. Second, with the occulter replaced again at three different axial locations, the end-to-end differences were no more than a few percent, even with different sampling (0.15 λ/D vs 0.34 λ/D) in the two codes. Yet when the mask was translated horizontally and the axial runout was determined using an algorithm based on the asymmetry of diffraction lobes with the Lyot stop removed, MACOS and PROPER yielded different results, typically by a factor of 2 at contrast levels of $10^{-8} - 10^{-7}$.

It is important to understand the differences between MACOS and PROPER because both codes are important for high contrast coronagraphy. MACOS performs full ray tracing and diffraction of the optical system based on its actual prescription (e.g. all off-axis terms are used). It is readily interfaced to mechanical codes and was designed to be part of an integrated structural/thermal/optical (STOP) modeling code run from a Matlab environment. Ideally, it is a "one stop shop" for all optical modeling in the system. Unfortunately, it is poorly documented and is only supported on an as-needed basis. PROPER is a fully supported, well-documented, IDL-based code that has a TDEM-validation pedigree and is the 'gold standard' code for coronagraph modeling. It idealizes the optical system into an on-axis representation and does not perform ray-tracing. It can be used in STOP modeling environments (but requires an IDL-to-Matlab or a Python or other interface to the other tools) when coupled to a separate ray-trace program, but off-axis terms in the perturbed system will only be captured in the exit-pupil of the ray-trace, rather than interacting with diffraction and other perturbations throughout the system. This is not expected to be a major limitation since the coronagraphs are only moderately off-axis (a necessity for polarization control).

VIII. References

Balasubramanian, K., "Band-limited image plane masks for the Terrestrial Planet Finder Coronagraph: materials and designs for broadband performance," Appl. Opt., 47, 116-125 (2008).

Cady, E., and Shaklan, S., "Measurements of incoherent light and background structure at exo_Earth detection levels in the High Contrast Imaging Testbed," Proc. SPIE 9143, 914338 (ed. J. Oschmann, M. Clampin, G. Fazio, H. MacEwen) 2014.

Dooley, J., and Lawson, P., "Terrestrial Planet Finder Coronagraph (TPF-C) Technology Plan", JPL Publication 05-8, Jet Propulsion Laboratory, March 2005 http://planetquest.jpl.nasa.gov/TPF/TPF-CTechPlan.pdf

Kern, B, Kuhnert, A. and Trauger, J., "Exoplanet Exploration Coronagraph Technology Milestone 2 Report - Broadband Contrast", JPL D-35484, Jet Propulsion Laboratory, August 2008, http://planetquest.jpl.nasa.gov/TPF-C/HCIT-Milestone2Signed-2008-08-08.pdf

Give'on, A., "A unified formalism for high contrast imaging correction algorithms," Proc. SPIE 7440 (ed. S. Shaklan) 2009.

Marchen, L, and Shaklan, S., "A general tool for evaluating high-contrast coronagraphic telescope performance error budgets," Proc. SPIE 7440, 74400V (ed. S. Shaklan) 2009.

Shaklan, S., et al, "The Terrestrial Planet Finder Coronagraph Dynamics Error Budget," Proc. SPIE 5905, 59050D (ed. D. Coulter) 2005.

Shaklan, S., et al, "Stability error budget for an aggressive coronagraph on a 3.8 m telescope," Proc. SPIE 8151, 815109 (ed. S. Shaklan) 2011.

Sidick, E., Fang Shi, Scott Basinger, Dwight Moody, Andrew E. Lowman, Andreas C. Kuhnert, and John T. Trauger, "Performance of TPF's High-Contrast Imaging Testbed: Modeling and simulations, " *Proc. SPIE*, **6265**, 62653L (2006).

Sidick, E., et al, "Studies of the effects of optical system errors on the HCIT contrast performance," Proc. SPIE 8151, 815106 (ed. S. Shaklan) 2011.

Sidick, E., Shaklan., S., and Balasubramanian, K., "HCIT broadband contrast performance sensitivity studies," Proc. SPIE 8520, 85200M (Ed. J. Dolne, T. Karr, V. Gamiz) 2012.

Sidick, E., et al, "HCIT contrast performance sensitivity studies: simulation vs. experiment," Proc. SPIE 8864, 88640Q (ed. S. Shaklan) 2013.

Sidick, E., et al, "High contrast coronagraph performance in the presence of focal plane mask defects," Proc. SPIE 9143, 914336 (ed. J. Oschmann, M. Clampin, G. Fazio, H. MacEwen) 2014.

Trauger, J., Kern, B. and Kuhnert, A., "Terrestrial Planet Finder Coronagraph (TPF-C) Milestone 1 Report - Monochromatic Contrast", JPL D-35484, Jet Propulsion Laboratory, July 2006. http://planetquest.jpl.nasa.gov/TPF-C/TPFC_M1_Report_060710_final.pdf

IX.   Appendix: Spectrum and Spectral Calibration

This section is extracted from the TDEM Final report "Advanced Speckle Sensing for Internal Coronagraphs" (ASSIC, JPL Document D-73509, 2012). The source and filters used for the MS 3A experiments are the same as in the ASSIC experiments.

The light source and filters used in our experiments were the same ones used to satisfy TPF-C Milestone #2. The light source was a single-mode supercontinuum photonic crystal fiber propagating high-power laser pulses. Non-linear interactions of the pulses and guiding structure lead to a broad spectrum that is shown in fig. 5. This spectrum was measured with an Ocean Optics spectrometer at the output of a single-mode (SM) fiber before it is connected to the SM fiber that runs into the vacuum chamber. Light is passed through each of the five bandpass filters, centered at roughly 768, 784, 800, 816, and 832 nm before entering the spectrometer. We have normalized the total measured power in all bands to be equal to one another as shown in the upper plot of fig. 5. We created an effective bandpass by summing
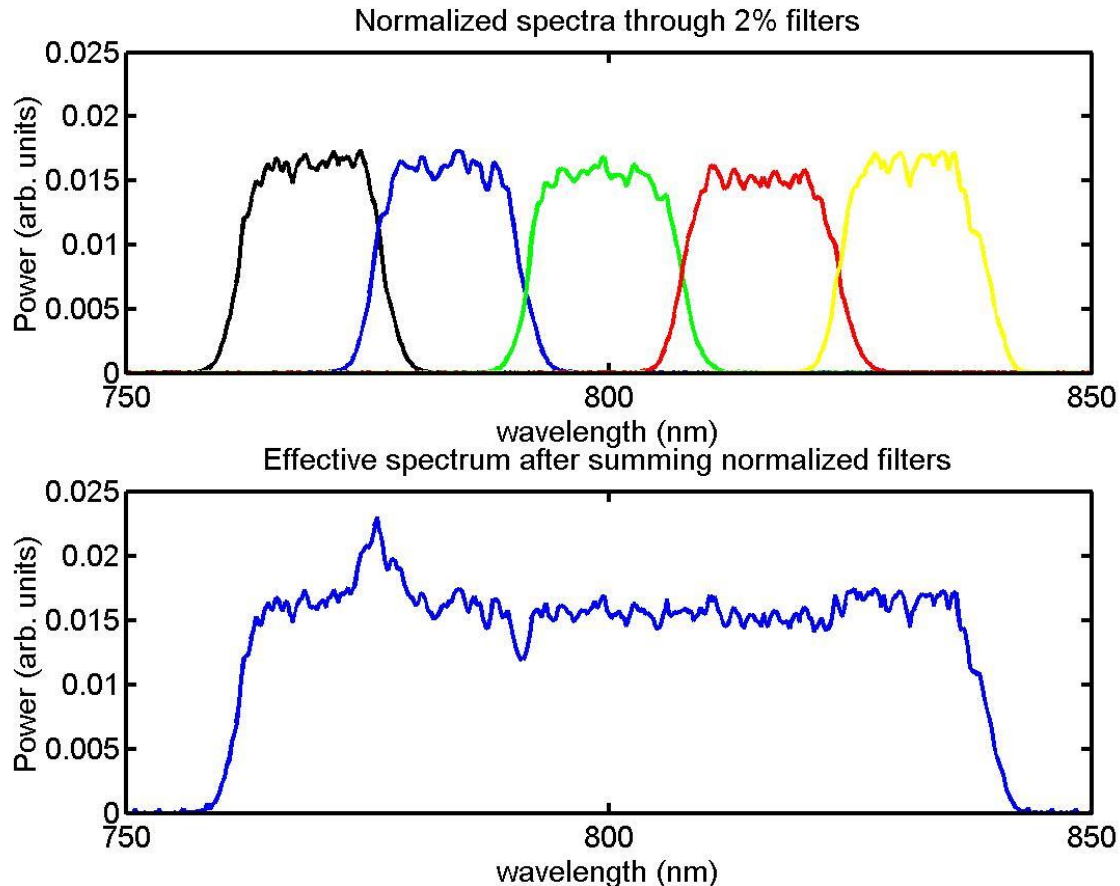

Figure 5. Top: we separately recorded the light through each of five 2% bandpass filters and have normalized all five to have the same total light. Bottom: we sum the recorded signals with equal weight to form an effective spectrum. The spectrum full-width half maximum spans 761.5 – 839.5 nm, leading to a spectrum centered at 800.5 nm with a bandwidth of 9.74%.

together the 5 normalized bandpasses, as shown in the bottom plot. The spectrum is flat except where it appears that the 784 nm filter is shifted slightly toward the blue creating a peak at 776 nm and a valley at 791 nm. The full width at half-maximum (FWHM) of the synthetic spectrum spans 761.5 – 839.5 nm, leading to a FWHM bandwidth of 9.74% centered at 800.5 nm.

We give each filter equal weight in all of our broad-band analyses, so the bottom plot of fig. 5 is the effective spectrum of our experiment, modulo chromatic differences in quantum efficiency and throughput of the HCIT relative to the Ocean Optics spectrometer. These differences will be small over the individual 2% bandpass filters and will not significantly change the effective bandpass. Our results are nearly identical to those shown in figure 14 of the TPF-C Milestone #2 report.

We acknowledge that the 9.74% bandpass is just shy of the required 10% bandpass. This is the same spectrum that was used to satisfy TPF-C Milestone #2. Contrast loss generally scales as the square of the bandpass, so one would expect our results to be worse by about $(10/9.74)^2 = 1.054$ had we used a full 10% bandpass. As will be shown below, our results had substantially more than 5% margin against the Milestone, so that the spectral underrun should not be an issue. Furthermore, in the TPF-C Milestone #2 report, Table 3 showed that a reweighting of the measured spectrum to an effective 10% bandpass yielded contrast results that differed by no more than 10^{-11} of the equal-weighted results. The same difference is expected in our experiments.

X.   Appendix: Photometric Calibration

This section is extracted from the TDEM Final report "Advanced Speckle Sensing for Internal Coronagraphs" (ASSIC, JPL Document D-73509, 2012). The photometric calibration used in the MS 3A experiments are the same as in the ASSIC experiments

All images with the coronagraph fully assembled are normalized to the unocculted star peak brightness, i.e., an unocculted image would reach a normalized intensity of 1.0 at the peak. With the coronagraph fully assembled, normalized intensities across an image typically range from 10^{-4} down to 10^{-10}.

A simple one-step calibration technique would be to image the unocculted star with a short exposure, record its peak, then linearly scale that peak with exposure time and assume stability of the source brightness. However, this would require linearity over $> 10^6$ range of exposure times and would be limited by 1-2% source variability on minutes timescales and $>$ 10% variability over days timescales. The solution used in TPF-C Milestone #2, and in this experiment, is to   perform a calibration of the brightness of a reference region of the coronagraph science plane image relative to the unocculted star brightness, then normalize each subsequent fully assembled coronagraph image to the

occulter-in

occulter-out

normalize to 1.0

reference region
(mean ~ 10^{-5})

Fig. 6.   (LEFT) Unocculted star, (RIGHT) assembled coronagraph image. The reference region is located 25-28 λ/D away from the star, where the DM has little effect. The reference region brightness is calibrated to the unocculted star brightness, then every coronagraph image uses the reference region for normalization.

brightness of the reference region contained in the same image (see fig. 6). Because this reference region is imaged concurrently with the rest of the coronagraph field, the stability of the source brightness and the linearity of exposure times have no effect on the normalization.

The reference region of the image is chosen to be in a location that is bright enough to be well measured, but far enough out in the PSF so that it is affected little by changes in the DM. The features in the unocculted images in the region spanning 25-28 λ/D are dominated by the diffraction rings of the on-axis star, which are exactly the features that the fully assembled coronagraph removes. This means that there are no easily isolated features that are common to both the unocculted and fully assembled coronagraph images to establish the relationship between them.

While the use of a calibrated reference region to normalize subsequent images is the same in this experiment as it was for TPF-C Milestone #2, the method used for initial calibration has changed. The TPF-C Milestone #2 calibration technique relied on a sequence of images, alternating between changing total illumination and changing occulter positions. Each step in that sequence which changed the occulter position relied on source stability to tie together successive exposures; with ~ 1-2% source variability on short timescales, used on ~4 steps, the resulting uncertainty was in the range of 4%. The technique adopted in this experiment eliminates the dependence on source stability, trading it for a dependence on
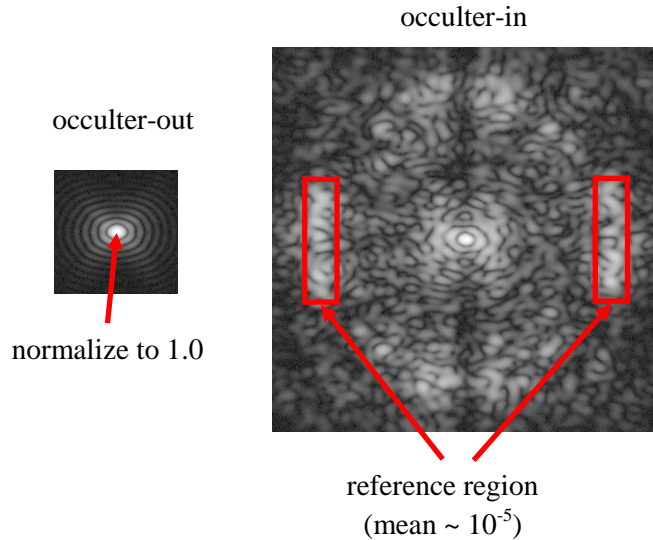
DM linearity and hysteresis. The hysteresis and departures from linearity, while each affecting the DM
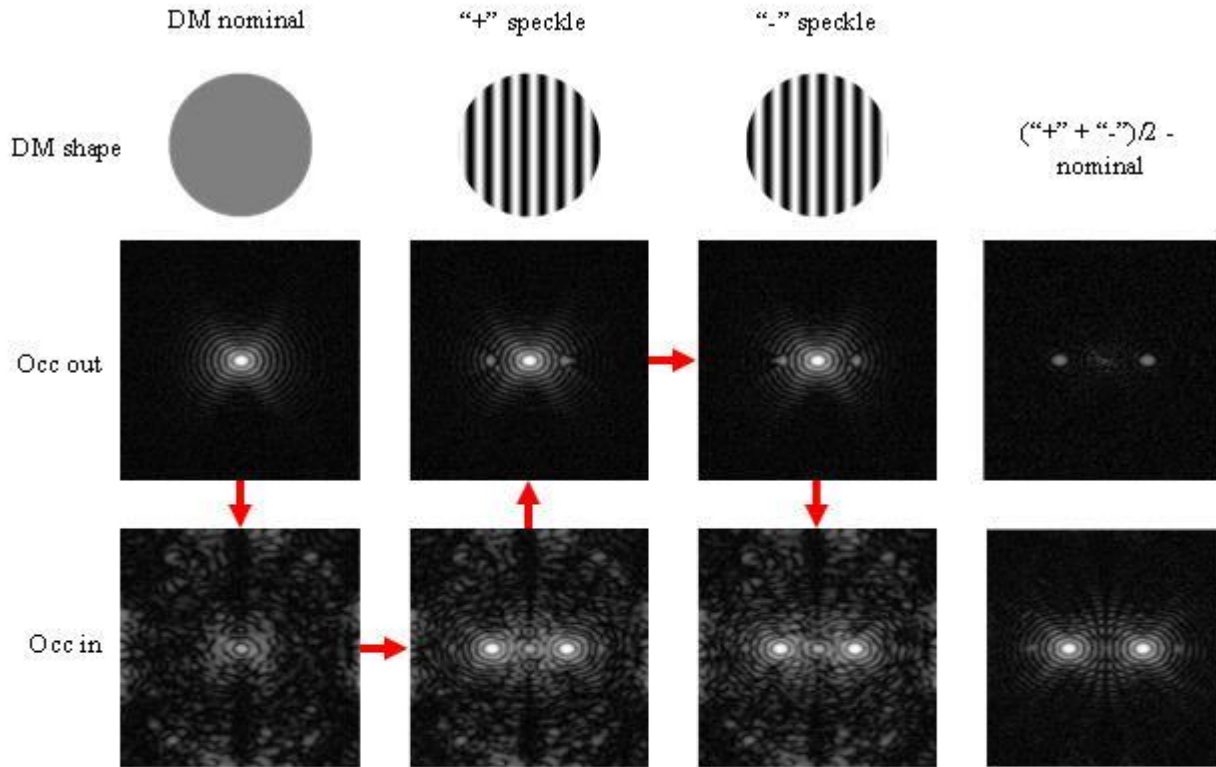

Fig. 7. Sequence of images used to establish photometric relationship between unocculted star and "reference region." All intensity images are log-scaled, and the occulter-in images are ~ 1000× brighter both in integrated source flux and in display stretch. Each image spans ± 25 λ/D in x and y. The sequence begins at the top-left image, with the occulter out and the DM set to a nominal shape. The sequence is established by moving the occulter in or out at each DM setting, then moving to the next DM setting, adding a "+" speckle or a "-" speckle (shown by following the red arrows). The difference images (shown in the right-hand panels) contain, to first order, only the intensity of the dynamic speckle field added by the DM. The occulter-out dynamic speckle field is related to the occulter-in dynamic speckle field by the occulter intensity transmission, which is well measured at these separations (near the transmission maximum).

motion at ~ 4% levels, are expected to result in calibration errors at ~1% levels, as described below. While the accuracies of the previous calibration technique, ~4%, and the current technique, ~1%, are both acceptable, the initial calibration technique adopted in this experiment is preferred.

To perform the initial calibration of the relative brightnesses of the unocculted peak intensity and the reference region of a fully assembled coronagraph image, the DM is used to create a dynamic speckle pattern across a sequence of images (see fig. 7). This speckle pattern is visible both in the unocculted and fully assembled coronagraph images, and by choosing DM patterns with opposite signs (i.e., a "+" pattern and a "-" pattern), the underlying "nominal" intensity pattern has no influence on the difference signal, to limits set by DM hysteresis and nonlinearities. Briefly, at any given point in the unocculted image, if the initial E-field is E_0, the nominal intensity is $|E_0|^2$, and the difference image formed by $(|E_0+\Delta E_{DM}|^2 + |E_0-\Delta E_{DM}|^2)/2 - |E_0|^2 = |\Delta E_{DM}|^2$.. A sample sequence of images is shown in Fig. 7, clearly demonstrating that the features in the left-hand panels are absent from the right-hand panels. The DM hysteresis and

55

nonlinearity re-introduce a sensitivity to E_0 through the cancelled "cross-term" $2\mathrm{Re}\{E_0 \Delta E_{\mathrm{DM}}\}$, which for reasonable errors in the unocculted images come to ~1% of $|\Delta E_{\mathrm{DM}}|^2$. This systematic error is smaller than the typical random error, which in practice comes to about 1.7% rms without any averaging of separate images or sequences.

The difference in observed brightness of a dynamic speckle in the unocculted images and the same speckle observed in the fully assembled coronagraph, is simply the occulter transmission at the location of that speckle. For this reason, the location of the dynamic speckles is chosen to be near the occulter
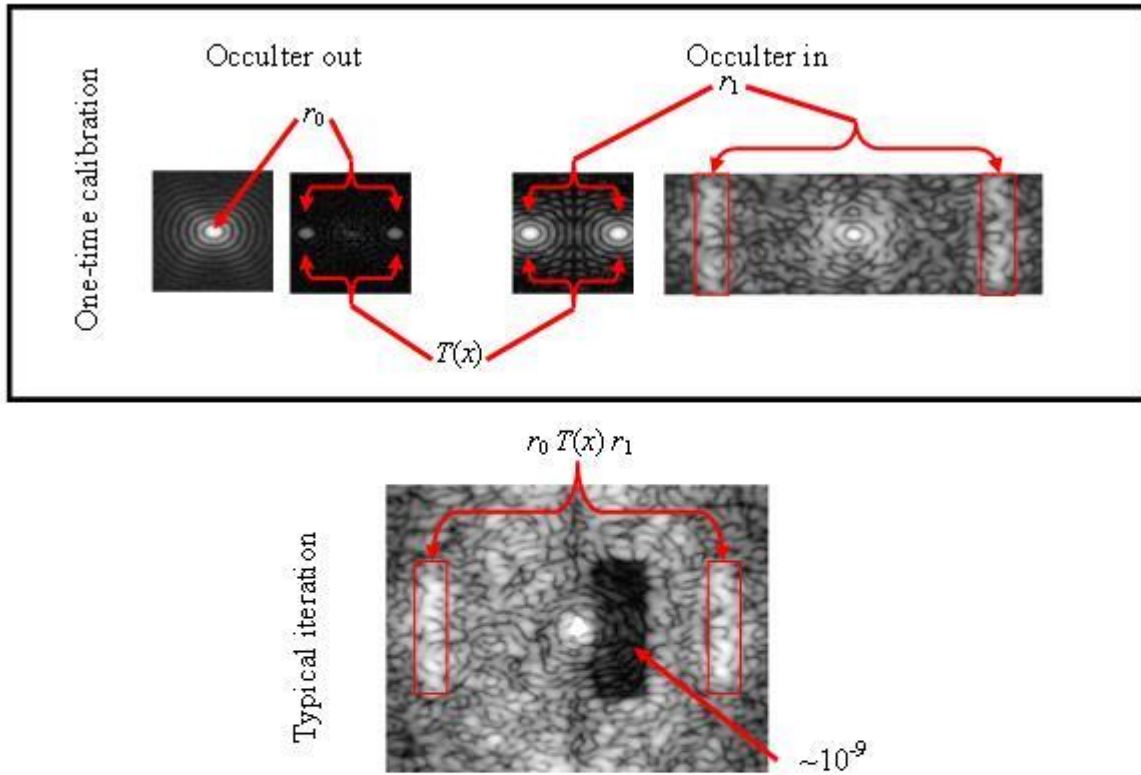

Fig. 8. Photometric calibration relationships and usage. The top panels show steps in the one-time calibration establishing the reference region. The measurement of r_0 and r_1 are ratios of the dynamically added speckles relative to the unocculted peak and reference region brightnesses, respectively, and typically come to 10^{-3} and 10^{-2}. The occulter-out dynamic speckles are related to the occulter-in dynamic speckles by the occulter intensity transmission at the location of the speckles, $T(x) \sim 0.91$ (transmission relative to maximum transmission). In every image afterwards (e.g., bottom panel), the observed reference region brightness is scaled to $r_0 T(x) r_1$, implying an equivalent unocculted peak brightness of 1.

transmission maximum, where uncertainty in the transmission is negligible. The sequence of images that establishes the photometric calibration relies only on relative brightnesses of concurrently measured features (i.e., different locations in the same image) and on knowledge of the occulter intensity transmission at the location of the dynamic speckles.

The photometric calibration bridges the range of intensities from 1.0 at the unocculted peak, to 10^{-3} for the dynamic speckles, to 10^{-5} for the reference region. Once the photometric calibration is established for the reference region, intensities down to the 10^{-9} level can be measured with a SNR $\geq$ 1 per pixel per image, in images that do not saturate the reference region (see fig. 8). By increasing exposure times and allowing the reference region to saturate, and by averaging over multiple exposures, intensities at the 10^{-10} level can be measured with SNR > 1 per pixel. Given the current f/# and an 800 nm center wavelength, $f\lambda/D \sim 6$ pixels, the noise level per resolution element is typically well below 10^{-10}.

XI. Appendix: Published Papers with Milestone 3A Simulations and Results

The following papers have been appended for reference.

Sidick, E., etal, "Studies of the effects of optical system errors on the HCIT contrast performance," Proc. SPIE 8151, 815106 (ed. S. Shaklan) 2011.

Sidick, E., Shaklan., S., and Balasubramanian, K., "HCIT broadband contrast performance sensitivity studies," Proc. SPIE 8520, 85200M (Ed. J. Dolne, T. Karr, V. Gamiz) 2012.

Sidick, E., et al, "HCIT contrast performance sensitivity studies: simulation vs. Experiment," Proc. SPIE 8864, 88640Q (ed. S. Shaklan) 2013.

Sidick, E., et al, "High contrast coronagraph performance in the presence of focal plane mask defects," Proc. SPIE 9143, 914336 (ed. J. Oschmann, M. Clampin, G. Fazio, H. MacEwen) 2014.

Cady, E., and Shaklan, S., "Measurements of incoherent light and background structure at exo_Earth detection levels in the High Contrast Imaging Testbed," Proc. SPIE 9143, 914338 (ed. J. Oschmann, M. Clampin, G. Fazio, H. MacEwen) 2014.

Studies of the Effects of Optical System Errors on the HCIT Contrast Performance

Erkin Sidick*, Stuart Shaklan, Amir Give'on, and Brian Kern

Jet Propulsion Laboratory, California Institute of Technology, 4800 Oak Grove Drive, Pasadena, CA, USA 91109

ABSTRACT

The High Contrast Imaging Testbed (HCIT) at the Jet Propulsion Laboratory employs a broadband wavefront correction algorithm called Electric Field Conjugation (EFC) to obtain the required 10^{-10} contrast. This algorithm works with one deformable mirror (DM) to estimate the electric-field to be controlled, and with one or multiple DM's to create a "dark-hole" in a predefined region of the image plane where terrestrial planets would be found. We have investigated the effects of DM actuator errors and the optic position errors on the efficiency of the EFC algorithm in a Lyot coronagraph configuration. The structural design of the optical system as well as the parameters of various optical elements used in the analysis are drawn from those of the HCIT system that have been implemented with one DM. The simulation takes into account the surface errors of various optical elements. Results of some of these studies have been verified by actual measurements.

Key words: Coronagraphy, adaptive optics, space telescopes, exoplanets

1. INTRODUCTION

High-contrast imaging testbed (HCIT) at JPL is Terrestrial Planet Finder (TPF) Coronagraph's primary platform for experimentation [1-3]. It is used to provide laboratory validation of key technologies as well as demonstration of a flight-traceable approach to implementation. It employs a broadband wavefront correction algorithm called Electric Field Conjugation (EFC) to obtain the required 10^{-10} contrast [4]. This algorithm works with one or multiple deformable mirrors (DM's) to create a "dark-hole" in a predefined region of the image plane where terrestrial planets would be found. It achieves the desired high contrast level in two stages. The first is the reconstruction (or estimation) stage. In this stage, the algorithm provides an estimate of the aberrated complex electric field (e-field) in the image plane based on pairs of images taken at the final image plane using different DM configurations. The second is the correction or EFC stage. In this stage the algorithm generates a correction based on e- field estimated in the first stage. The correction is then applied to the DM actuators to null the image e-field in the predefined dark-hole region.

We have investigated the effects of DM actuator errors and the optic position errors on the efficiency of the EFC algorithm in a Lyot coronagraph configuration. Considered cases include dead actuators, lateral and longitudinal movement of the occulting mask, and the lateral movement of a flat optical surface. The structural design of the optical system as well as the parameters of various optical elements used in the analysis are drawn from those of the HCIT system that have been implemented with one DM. The simulation takes into account the surface errors of various optics. The optical simulation algorithm uses MACOS (Modeling and Analysis for Controlled Optical Systems) as its analytic tool [5]. Hence it is capable of performing full three-dimensional near-field diffraction analysis on HCIT's optical model. Results of some of these studies have been verified by actual measurements.

2. BACKGROUND

2.1 The HCIT Optical System

The schematic diagram of the HCIT layout in the *xz*-plane is shown in Figure 1. Artificial starlight is created by a 5μm pinhole illuminated by an optical fiber. We assume a broadband light source centered at λ_0=800nm and having a bandwidth of ±10%, or $\Delta\lambda$=160nm. An off-axis parabolic mirror (OAP1) collimates the light from the pinhole and

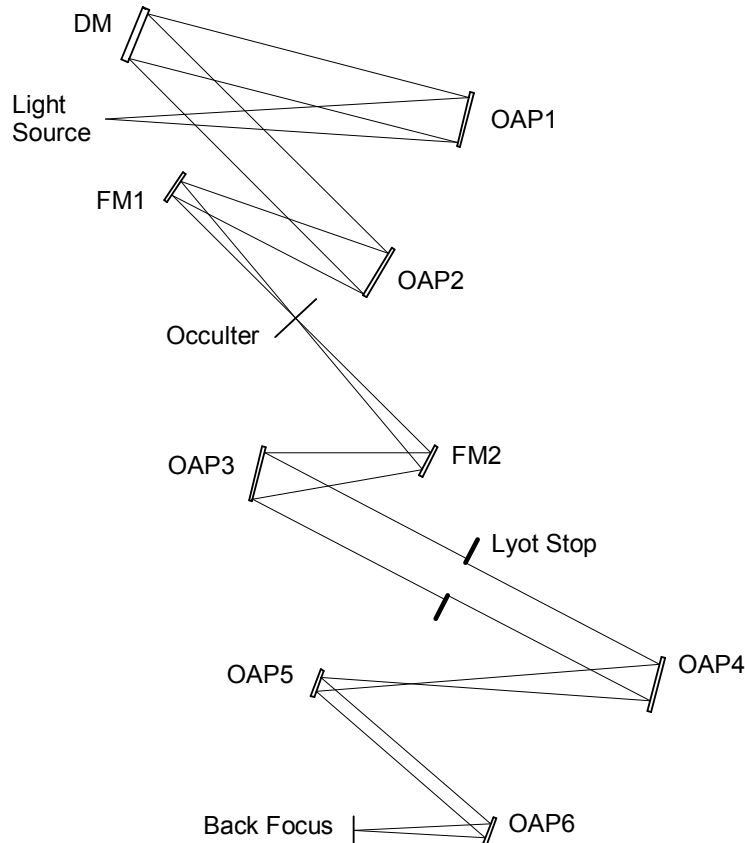*Erkin.Sidick@jpl.nasa.gov; Phone 1 818 393-7585; Fax 1 818 393-9471; www.jpl.nasa.gov

Figure 1. Schematic diagram of the High Contrast Imaging Testbed layout. The light source ("starlight") is a 5μm pinhole illuminated by an optical fiber, and a CCD science camera is located at the back focal plane for detecting the image of the "starlight".

directs it to a high-density, 32x32 actuator deformable mirror (DM), which performs wavefront control. A circular aperture mask on the DM defines the system pupil of the HCIT, and has a diameter of D=30mm. After the DM, the collimated light is re-imaged onto the focal plane of the occulting mask by OAP2 and a flat-mirror (FM1). The occulting mask attenuates the starlight, and almost has no effect on the light of a planet if present. The "back-end" of the system, from the occulting mask to the back focus plane, supports experimentation with diverse coronagraph configurations and apodizations. A flat mirror (FM2) and OAP3 re-collimate the light passing through the occulter mask and form a same-size sharp image of the DM pupil at the Lyot plane. A Lyot stop blocks the ring-like residual light diffracted off the occulting mask while letting most of the planet light through. After OAP4 forms an image from the remaining stellar and planet lights, it is then magnified (M ≈3) by the OAP5-OAP6 pair for proper sampling on the CCD science camera located at the back focal plane. More information on the HCIT and the DM can be found in Refs. [1-3].

2.2 Occulting Mask

In this paper, we use a linear-sinc[2] occulting mask consisting of platinum (Pt) deposited on a fused-silica and compensated with spatially profiled polymethyl methacrylate (PMMA) [6-8]. It has a linear-sinc[2] intensity profile with a one-dimensional transmittance profile $T(x)$ given by:

$$T(x) = \left[1 - \left(\frac{\sin(\pi x / w)}{(\pi x / w)} \right)^2 \right]^2. \tag{1}$$
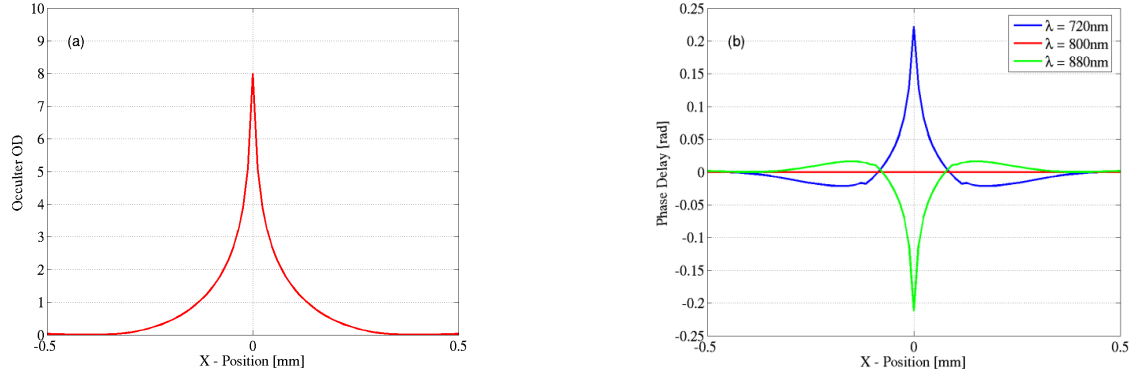
Figure 2. (a) Optical density (OD) and (b) phase profiles of a linear-sinc^2 occulting mask consisting of platinum (Pt) deposited on a fused-silica and compensated with spatially profiled PMMA.

This mask has a constant (zero) phase at λ_0=800nm, but its phase is non-zero and varies with both the optical density (OD) of the occulter and the wavelength, λ. Figures 2(a) shows the OD profile of the occulter as a function of the x-position. The dependence of the OD on λ is negligibly small, therefore, it is ignored in this paper. But we include the dispersion of the occulter phase in our simulations. The profiles of the occulter phase at three different wavelengths are shown in Fig. 2(b). The width of this occulter is $w = 144\mu m$, which gives $T(x) = 0.5$ at $x/f = 4\lambda/D$, where $D = 30mm$ is the diameter of the system clear aperture. The front end F-number (F/#) of this optical system is 25.8.

2.3 Other Optical Components

The DM used on the HCIT has 1024 (32x32) actuators arrayed on a 1mm pitch. Its description is given in detail in Ref. [1], and will not be repeated here.

Our Lyot stop is a simple blackened piece of sheet metal with a sharp edge. Its opening (Lyot stop aperture) has an eye-shape defined by two circles that are shifted with respect to each other in the horizontal direction by a distance of ε in units of D. The value of ε needs to be chosen based on the value of the occulting mask width parameter w, and ε=0.36 in this paper.

In our simulations, we include the surface errors of six OAP's and two FM's shown in Figs. 4(a-h) of Ref. [3]. Some optics on the current HCIT have surface height errors different from the above, and we used them here just to introduce some realistic surface errors into the HCIT optical model.

2.4 Definitions of Half Dark-Hole Area and Contrast

For the current optical system with only one DM, we carry out wavefront control (WFC) over a region Ω_c, where Ω_c is a D-shaped half dark-hole region bound by $x/f = X \geq 4\lambda/D$ and $\sqrt{x^2 + y^2}/f = R = 11\lambda/D$, or $[X,R] = [5,11]\lambda/D$. We will evaluate the performance of the HCIT using either the normalized intensity,

$$I(x,y) = I_o(x,y)/I_{uo\,max} , \tag{2}$$

or the contrast,

$$C(x,y) = I(x,y)[T_0/T(x,y)] = [I_o(x,y)/I_{uo\,max}][T_0/T(x,y)] , \tag{3}$$

where $I_o(x,y)$ is the image intensity of the occulted star, $I_{uo\,max}$ is the maximum value of the unocculted star intensity, $T(x,y)$ is the occulter transmittance, and T_0 is the maximum value of the $T(x,y)$. We will keep track of the following three contrast parameters in this paper: (i) C_b, the mean contrast inside a "Big" D-shaped region Ω_b defined by $[X,R] = [5,10]\lambda/D$. (ii) C_s, the mean contrast inside a "Small" square region Ω_s from $X = 4\lambda/D$ to $5\lambda/D$ and from $y/f = Y = -0.5\lambda/D$ to $0.5\lambda/D$. (iii) C_m, the "Maximum" contrast value inside the small square region Ω_s. Similarly, we use I_b, I_s and I_m to denote the big-region mean, the small-region mean, and the small-region maximum of the

normalized intensity. The nominal contrast values obtained for a narrowband light with $\lambda_0 = 800\text{nm}$ and the error-free optical system without conducting any wavefront control are $C_b = 2.54\text{E}-14$, $C_s = 1.32\text{E}-13$, and $C_m = 2.93\text{E}-13$, respectively. When the phase errors of the eight optics are included in simulation, the above intensity values change to $C_b = 3.98\text{E}-6$, $C_s = 4.88\text{E}-5$, and $C_m = 8.41\text{E}-5$, respectively.

2.5 About the Wavefront Control (WFC) Algorithm

In this paper, we use a control algorithm similar to the "minimum-wavefront and optimal control compensator" described in detail in Ref. [9]. This approach is also called "Actuator regularization" [4]. The WFC algorithm described in Ref. [9] uses the wavefront at the system exit pupil as its input, and calculate the actuator commands as its output. In the present case we set the DM actuators to superpose the negative of the e-field onto the image plane, with a goal to make the image intensity zero on the region Ω_c on the image plane. Therefore, the WFC algorithm uses an e-field column-vector $\vec{\mathbf{e}}$ as its input, where

$$\vec{\mathbf{e}} = \begin{bmatrix} \Re(\vec{\mathbf{E}}) \\ \Im(\vec{\mathbf{E}}) \end{bmatrix}. \tag{4}$$

The joint cost function now becomes as

$$J = \frac{1}{2}\left(\vec{\mathbf{e}}^T \vec{\mathbf{e}} + \gamma_{\text{wu}} \vec{\mathbf{u}}^T \vec{\mathbf{u}}\right), \tag{5}$$

and the gain matrix $\widetilde{\mathbf{G}}$ is obtained from

$$\widetilde{\mathbf{G}} = \left[\widetilde{\mathbf{S}}^T \widetilde{\mathbf{S}} + \gamma_{\text{wu}} \widetilde{\mathbf{I}}\right]^{-1} \widetilde{\mathbf{S}}^T. \tag{6}$$

In Eq. (4), $\vec{\mathbf{E}}$ is the column-vector of the complex e-field on region Ω_c. It is normalized by the maximum value of the reference e-field, the one obtained when no one actuator is actuated, and is formed by stacking the elements of the complex e-field on region Ω_c in a certain order, as was explained in Eq. (1) of Ref. [9]. The $\Re(\vec{\mathbf{E}})$ and the $\Im(\vec{\mathbf{E}})$ are the real and the imaginary parts of $\vec{\mathbf{E}}$, respectively. In Eq. (6), the $\widetilde{\mathbf{S}}$ is the sensitivity matrix consisting of the influence functions of all actuators. The MACOS simulation tool calculates the complex e-field at the final focal plane directly. Therefore, the e-field estimation step is actually not needed in our simulation. However, we will use this step when we evaluate the effects of DM actuator errors for they will have an impact on both the e-field estimation and control processes. The simulation creates a 512x512-pixel image plane, with ~5 pixels per $f\lambda/D$. Considering only the pixels in the dark hole gives an e-field vector, $\vec{\mathbf{e}}$, having a size of 6032x1 pixels. There are a total of 1024 DM actuators in the current 1-DM system, but we exclude the actuators with zero or very weak influences, thus reducing the number of the actuators used to 932.

3. SIMULATION RESULTS

We now describe our simulation results on the effects of dead actuators, lateral and longitudinal movement of the occulting mask, and the lateral movement of a flat optical surface on the contrast performance of the HCIT. We start with the nominal case where only the optical surface errors and the occulter phase are included in the simulation.

3.1 Nominal Case

We use the EFC-based broadband wavefront correction algorithm described Ref. [4] in our simulations. The broadband sensitivity-matrix $\widetilde{\mathbf{S}}$ consists of five monochromatic sensitivity matrices corresponding to wavelengths λ_1=720nm, λ_2=760nm, λ_3=800nm, λ_4=840nm, and λ_1=880nm, respectively. That is, we carry out the WFC at those five wevelengths simultaneously. We calculate the broad-band contrast in the following way: Divide the full bandwidth $\Delta\lambda$=160nm into 4 equal segments with a wavelength increment of $\delta\lambda$=40nm, representing the $\Delta\lambda$=160nm broad-band light with 5 narrow-band (or monochromatic) beams with equal intensity centered at the above five wavelengths. We calculate the final image plane intensity maps at each of these wavelengths separately, rescale them to the pixel size the same as that of $\lambda_3 = \lambda_0 = 800\text{nm}$ beam, and average them to obtain the broad-band image intensity map. We perform

this calculation on the occulted and the unocculted images separately to obtain their broadband images first, then use these averaged images to obtain a broadband contrast map.
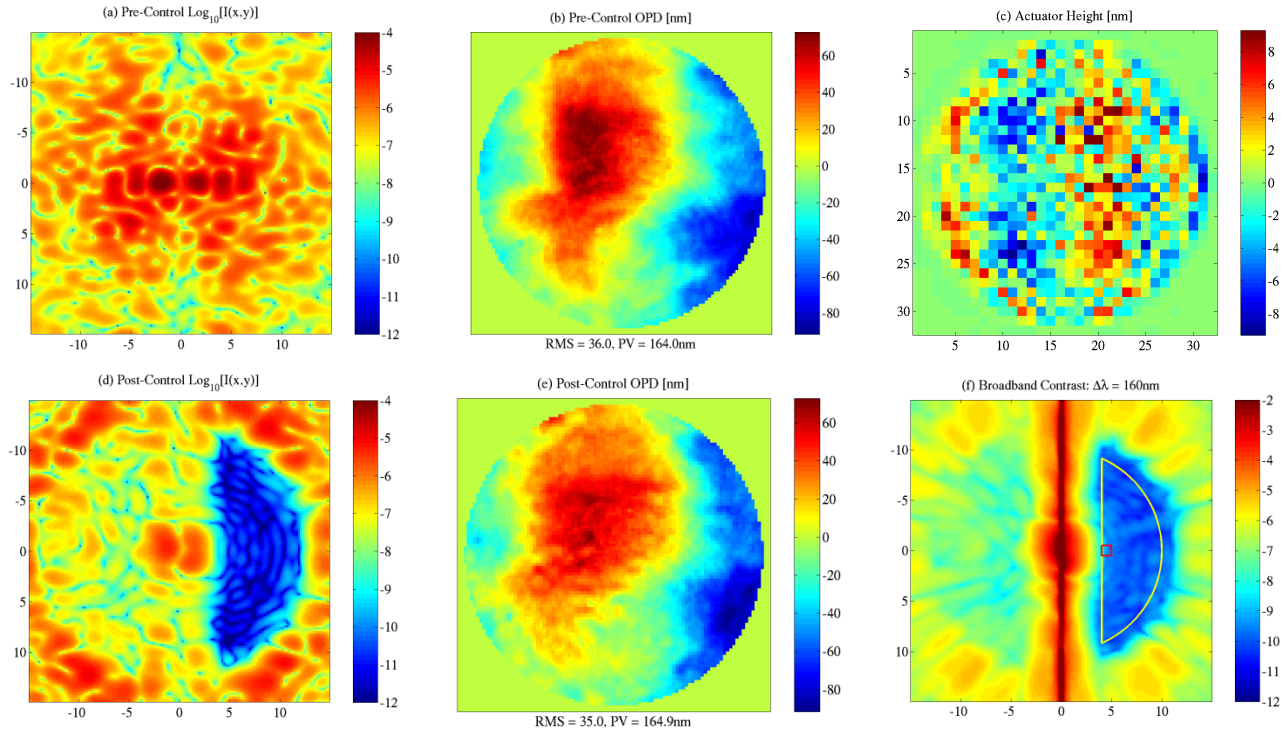

Figure 3. (a) Log-scale PSF before WFC when $\lambda_3 = \lambda_0 = 800$nm, where the units of the horizontal- and the vertical-axes are λ/D. (b) Exit-pupil Optical Path Difference (OPD) before WFC. (c) Actuator-height map obtained at the end of broadband WFC, where the units of the horizontal- and the vertical-axes are mm. (d)-(e) PSF and OPD when $\lambda_3 = \lambda_0 = 800$nm, and the broadband contrast obtained at the end of broadband WFC. The yellow- and the red-lines in part (f) show the boundaries of the regions in which C_b, C_s and C_m are defined. In parts (b) and (e), the "RMS" and the "PV" denote the root-mean-square and the peak-to-valley values of the OPD.
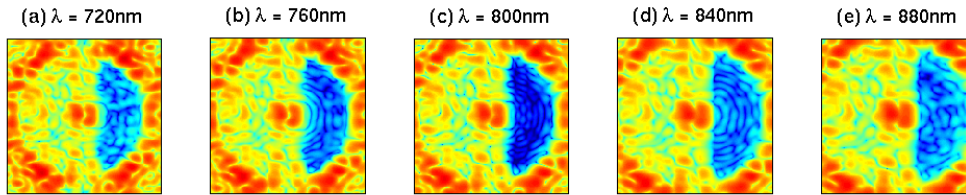
Figure 4. $Log_{10}[I(x,y)]$ at five different wavelengths. The ranges of the horizontal- and the vertical axes are from -15λ/D to $+15\lambda$/D, and the stretch of all the color maps is -12 to -4.

When we include the surface errors of the eight optical surfaces and the occulter phase only, we obtain the $I(x,y)$ and the exit-pupil Optical Path Difference (OPD) as shown in Figs. 3(a-b) at $\lambda_3 = \lambda_0 = 800$nm before WFC. After conducting broadband WFC for 25 iterations, we obtain a DM solution as shown in Fig. 3(c), the $I(x,y)$ and the OPD maps as shown in Figs. 3(d-e), and a broadband contrast map as in Fig. 3(e). The corresponding $I(x,y)$ maps at the five wavelengths are shown in Fig. 4. The three contrast values corresponding to Fig. 3(e) are $C_b = 1.85E-10$, $C_s = 9.92E-10$, and $C_m = 3.20E-9$, respectively. As has been shown before, the WFC (or the EFC) process does not minimize the wavefront error at the exit-pupil, instead re-arranges it to create a dark-hole in the pre-determined region. These results are included here as a baseline to the simulations to be presented in the following sub-sections.

In the above WFC simulation, we used an optimized set of two actuator regularization values, $\gamma_{wu} = [50\ 100]/nm^2$, with the corresponding WFC iteration numbers listed in the same order, $N_{WFC} = [15\ 10]$. That is, the WFC process is completed in two phases with two different γ_{wu} values in the order given above, each with a different WFC iteration number also given above. We didn't use the e-field estimation routine in the current nominal case, instead obtained the complex e-field directly from our MACOS simulation tool. However, we will use the e-field estimation routine whenever the errors introduced have an impact on the process of e-field estimation.

It should be mentioned that the sensitivity matrix $\widetilde{S}$ is obtained for this nominal case, where the initial e-field at $\lambda = \lambda_0 = 800nm$ corresponds to the intensity map shown in Fig. 3(a). Also, the same sensitivity matrix $\widetilde{S}$ is used in all control iterations, that is, the $\widetilde{S}$ is not updated or altered during a WFC process, and the same $\widetilde{S}$ of the current nominal case is used in all other non-nominal cases.

3.2 Dead Actuators

Actuator errors affect both the e-field estimation and control [10]. Therefore, we will obtain the complex e-field on the final image plane using the e-field estimation routine described in Ref. [4]. The four probe DM settings used in our e-field estimation calculation are obtained with $\theta = 0$, $\pi/2$, π and $3\pi/2$, respectively. The DM height maps of the first two settings are shown in Figs. 5(a-b) for $P = 5nm$.
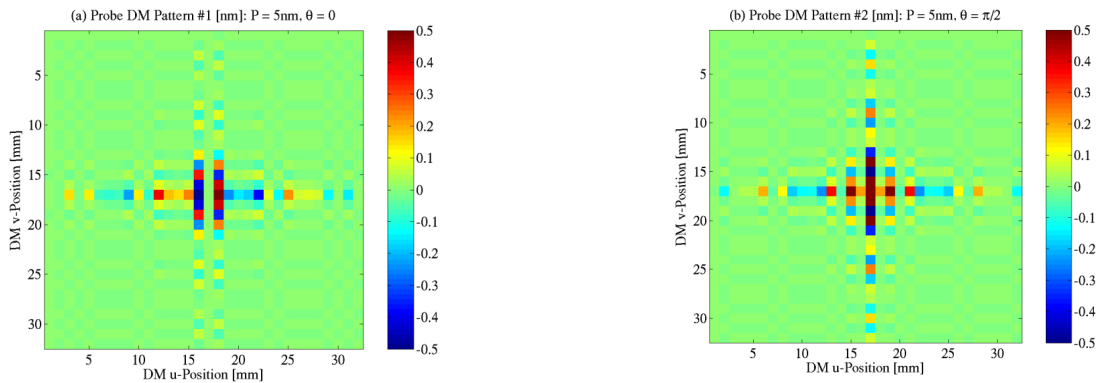

Figure 5. Actuator height maps of two probe DM settings with (a) $\theta = 0$ and (b) $\theta = \pi/2$, respectively. The other two settings have $\theta = \pi$ and $3\pi/2$, and are not shown here.

The first error we examined is the case where two actuators on row $v = 17mm$ and are separated by 2mm (or interleaved by one actuator) are not responsive to the applied commands, and remain fixed at the mid-point of their control range. We call such actuators "dead actuators" in this paper. In the current simulations, for the optical system with all eight phase errors, we obtained probe actuator command patterns as usual, but set the command values of the selected actuators to 0nm (the mid-point of the -200nm to 200nm range) when performing each e-field estimation calculation. We did the same to the actuator command solutions obtained in each WFC iteration: The sensitivity matrix $\widetilde{S}$ is kept the same, but the command values of the dead actuators are set to 0nm. The dead actuators selected are shown on the map of actuator positions in Fig. 6(a), where each of the different pairs of the dead-actuators are marked with the same color and the same shape. When there is no dead-actuator in the system, we obtain I_b as a function of control iteration number and wavelength as shown in Fig. 6(b). It displays the efficiency of e-field estimation and control achieved at the end of each control iteration. Figure 6(c) shows the similar result when the two actuators on columns $u = 9,11mm$ are dead. As compared to the case of Fig. 6(b), the contrast performance becomes worse in this case as expected. Figure 6(d) compares the values of $I_b(\lambda=800nm)$ of all the cases considered. As expected, the final value of $I_b(\lambda=800nm)$ moves higher as the dead-actuators move closer to the DM center, but the process of e-field estimation and control does not completely fail in any case considered. That is, this simulation predicts that if any two actuators separated by 2mm die, the process of e-field estimation and control either does not get affected or lose some efficiency, but still yields acceptable contrast values.

Next, we investigated the cases where three actuators separated by 2mm (interleaved by one actuator) are dead. Figure 7(a) compares the values of $I_b(\lambda=800nm)$ for six groups of dead actuators on row $v = 17mm$. As we can see, the e-field
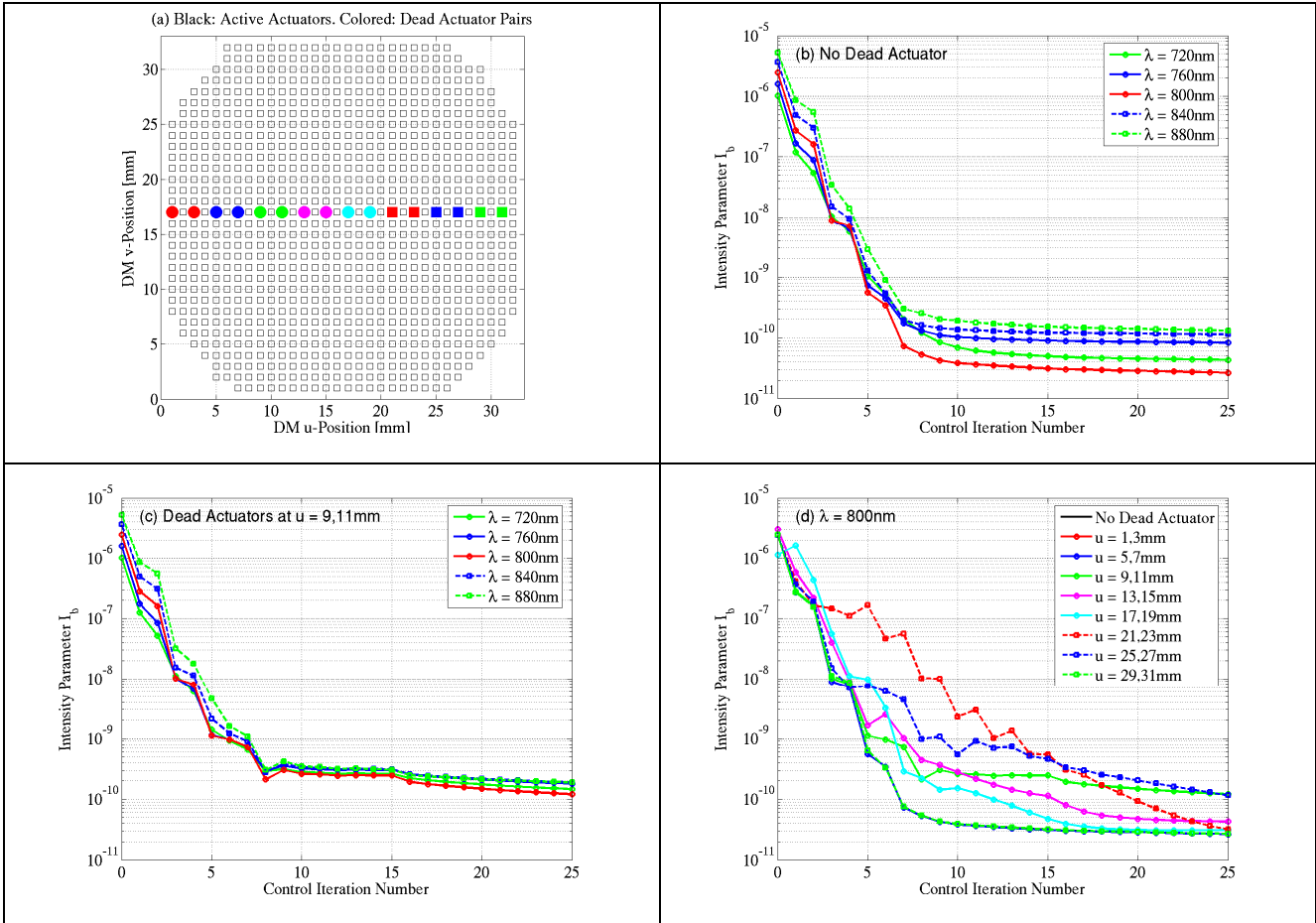
Figure 6. (a) Locations of the different dead actuator pairs on the actuator position map. The different dead actuator pairs are marked with the different colors and/or the different shapes. (b) I_b versus control iteration number when there is no any dead actuator. (c) I_b versus control iteration number when the two actuators at $u = 9,11$mm are dead. (d) Comparison of $I_b(\lambda=800$nm) versus control iteration number curves obtained for different pairs of dead actuators whose u-positions are indicated in the figure legend.
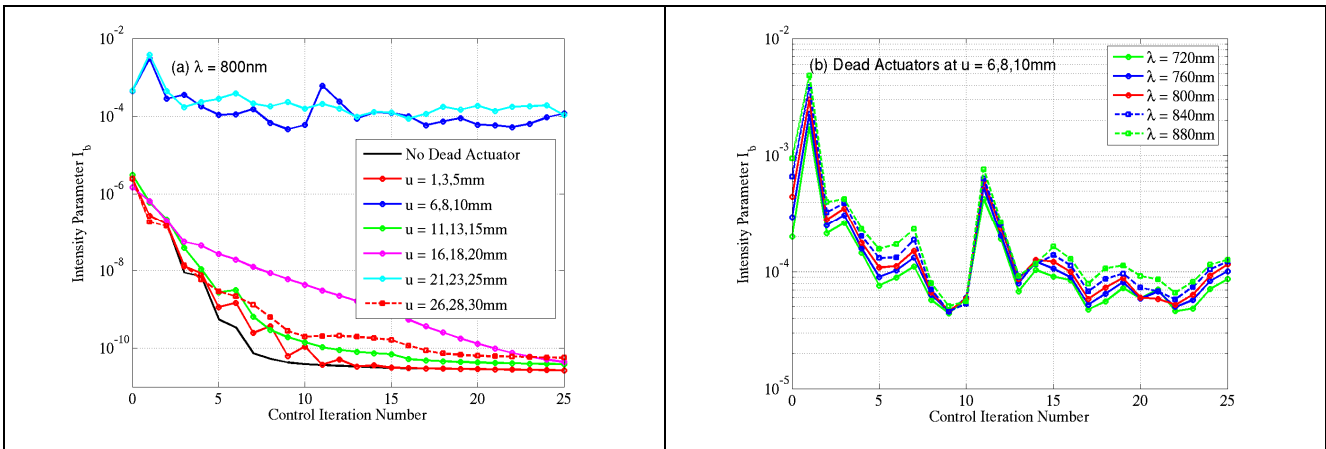
Figure 7. (a) Comparison of $I_b(\lambda=800$nm) versus control iteration number curves obtained for different groups of three dead actuators on row $v = 17$mm and on u-positions indicated in the figure legend. (b) I_b versus control iteration number when the three actuators at $u = 6,8,10$mm are dead.
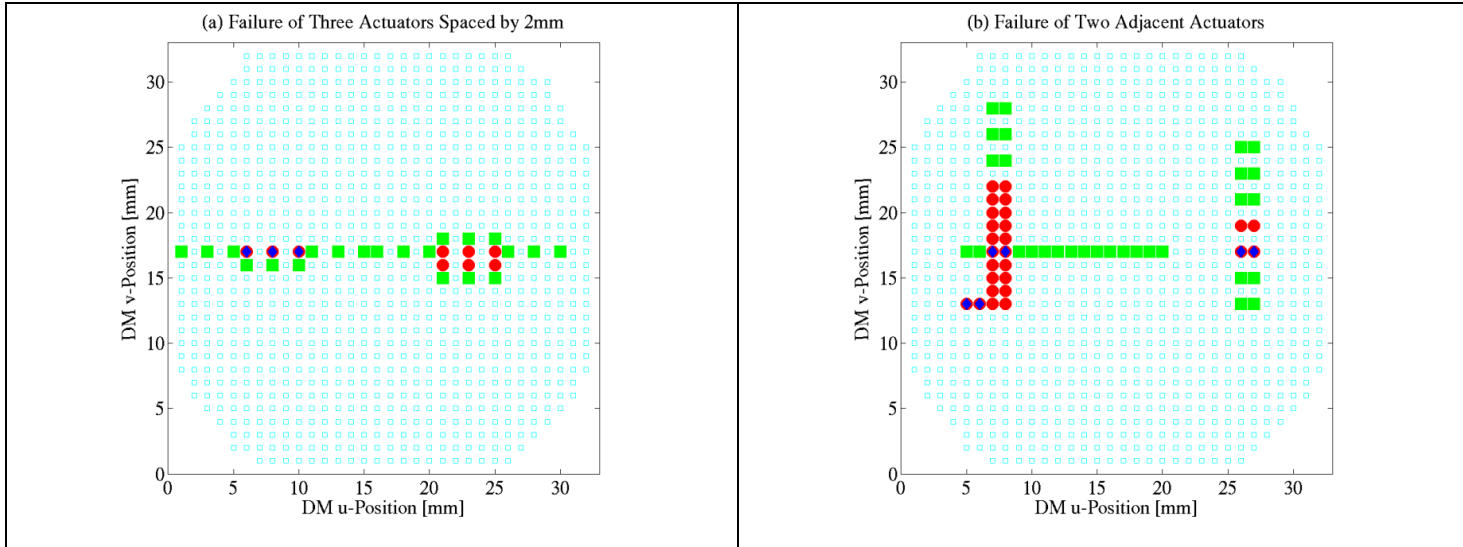
Figure 8. Locations of the dead actuators on the actuator position map. (a) Cases of 3-dead-actuators separated by 2mm (interleaved by one actuator), and (b) cases of 2-adjacent actuators dead. The green-color indicates the dead-actuators groups that work, the red-color indicates the groups that fail, and the blue-color on top of the read-color indicates the group which fails when conducting e-field estimation but works without it.
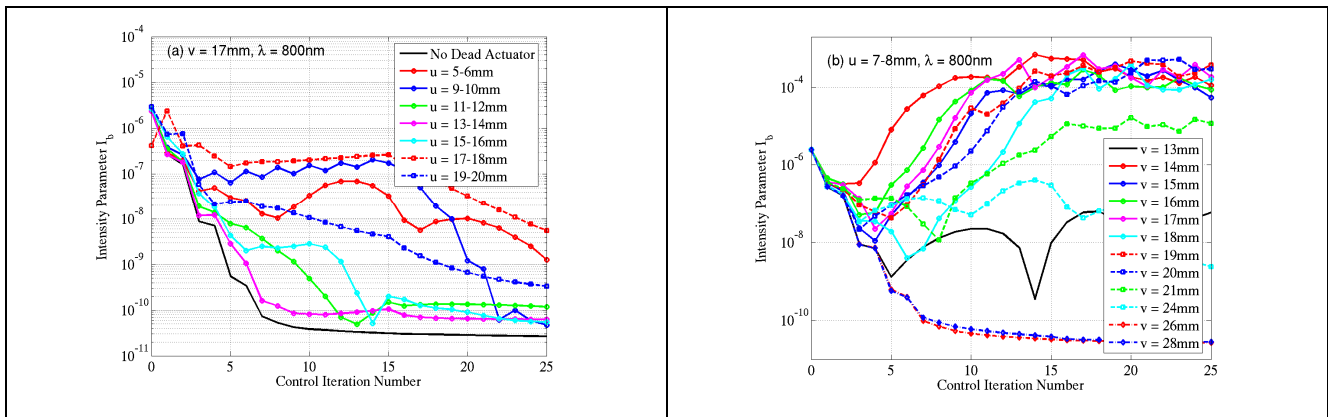

Figure 9. Comparison of $I_b(\lambda=800nm)$ versus control iteration number curves obtained for the cases of two adjacent actuators dead. (a) For actuators on row $v = 17$mm and on u-positions indicated in the figure legend. (b) For actuators on columns $u = 7,8$mm and on v-positions indicated in the figure legend.

estimation and control processes do not fail in all cases except those where the dead actuators are located at $u = 6,8,10$mm and $u = 21,23,25$mm, respectively. The I_b of the case where the dead actuators are located at $u = 6,8,10$mm is shown as a function of control iteration number and the wavelength in Fig. 7(b). We have also examined several other dead actuator groups located on rows $v = 15, 16$ and 18mm. For the case where the dead actuators are located at $v = 17$mm and $u = 6,8,10$mm, we tested our WFC algorithm without performing e-field estimation, that is, by obtaining the e-field from our MACOS simulation tool directly, and found that the WFC process still works in this case. That is, the failure of this case is caused by the failure of the e-field estimation process, not by the WFC process. The "pass/fail" results of all the investigated cases with three dead actuators are shown on the actuator position map of Fig. 8(a), where the green-color indicates the 3-dead-actuators groups that work, the red- color indicates the groups that fail, and the blue-color on top of the read-color indicates the group which fails when conducting e-field estimation but works without it.

The last actuator errors we investigated are the cases where two adjacent actuators are dead at a time. The locations of the actuators considered are shown in Fig. 8(b), where the meanings of the different actuator colors are the same as in Fig. 8(a). We found that the e-field estimation and control processes are much more sensitive to the dead actuators located on two columns $u = 7$-8mm and are on or close to row $v = 17$mm than the other pairs considered. Again, three

pairs of actuators that originally failed worked fine when not using the e-field estimation process. Figure 9(a) compares the $I_b(\lambda=800\text{nm})$ versus control iteration number curves of the cases where $v = 17\text{mm}$ (the result of the case where $u = 7$-8mm is shown in part (b)), and Fig. 9(b) compares the same for the dead actuator pairs located on columns $u = 7$-8mm.

In Ref. [10], we also investigated the effects of one, two or three randomly selected dead actuators on the four-probe e-field estimation and the EFC-based WFC performance of the High Contrast Imaging Testbed Phase Induced Amplitude Apodization (HCIT/PIAA) coronagraph system at JPL. It was shown that the effect of the one, two or three dead actuators, at least for the most cases considered there, is to slow down the process of WFC. The majority of realizations gave acceptable contrast values below 10^{-9} in 50 WFC iterations.

Although we haven't conducted an exhaustive search on the number and the distribution of the dead actuators that can be tolerated, the above results show that the HCIT Lyot coronagraph system is fairly robust for the 1-3 dead actuators. Even when 1-3 "critical" actuators is or are dead, we still have the option to rotate the DM, move the DM, or move the probe DM patterns such that those dead actuators no longer become critical. This is one of the significant findings of this study.

3.3 Lateral Translation of a Flat Optic

In order to estimate the sensitivity of the HCIT's monochromatic contrast on the lateral movement of a flat optic, we translated FM1 along the x-axis by T_x after WFC, and evaluated the changes in the normalized intensity parameters. In Fig. 1, positive T_x moves the FM1 into the paper (and towards the dark-hole). In this part of our simulations, we didn't use the e-field estimation algorithm because the errors introduced (x-translation of FM1) do not affect the process of e-field estimation. If we introduce a sinusoidal surface error into FM1 as shown in Fig. 10(a) and "turn off" all of the other surface errors, carry out WFC to create a dark-hole for a monochromatic beam with $\lambda = 800\text{nm}$ and $T_x = 0$, and finally find the changes in normalized intensity parameters, $\Delta I(x, y)$, as a function of FM1- T_x, we obtain the curves in Fig. 10(b). In this figure, the "True (solid)" and the "Predicted (dashed)" results were obtained from

$$\text{True}: \Delta I(x,y) = \left|E(x - T_x, y) - E(x,y)\right|^2 / I_{uo\max}$$
$$\text{Predicted}: \Delta I(x,y) = (\pi / \lambda)^2 [PV(\Delta OPD)/2]^2 \left|M(x - N_x \lambda f / D, y)E(x',y')\right|^2 / I_{uo\max}$$

(7)

where $E(x, y)$ is the complex e-field, $PV(\Delta OPD)$ is the Peak-to-Valley value of the change in the exit-pupil OPD, $\Delta OPD = OPD(T_x) - OPD(0)$, $M(x, y)$ is the complex transmission coefficient of the occulting mask, and N_x is the spatial-frequency of the sinusoidal surface error of the FM1 in cyc/aper. The origin of the (x, y) coordinate frame is at $(N_x \lambda f / D, 0)$, and that of the (x', y') frame is at $(0,0)$. In Fig.10(b), the root-mean-square (RMS), the average (Mean), and the maximum (Max) values of $\Delta I(x, y)$ are evaluated over a square region having a width of $a = 1 f \lambda / D$. As we can see from Fig. 10(b), the "True" and the "Predicted" values of the $\Delta I(x, y)$ parameters agree well in this case.
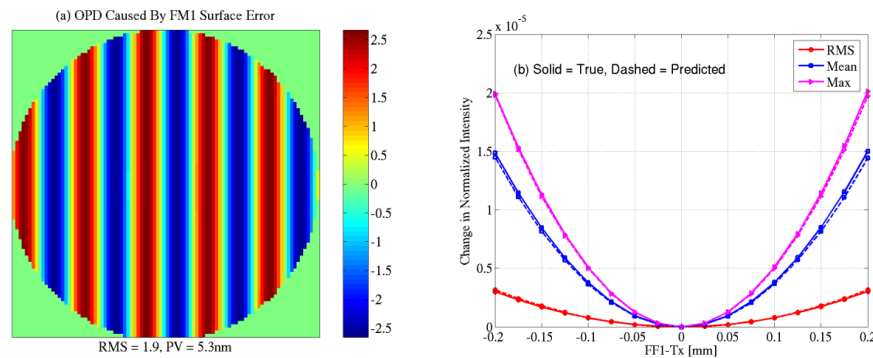

Figure 10. (a) Exit-pupil OPD caused by a sinusoidal surface error of FM1. (b) Change in normalized intensity parameters, root-mean-square (RMS), average (Mean), and maximum (Max), as a function of FM1- T_x.

We also investigated the case where the surface error of FM1 is not sinusoidal. When the "true" surface error of only the FM1 used in the previous sub-sections is included in our model, we obtain an exit-pupil OPD map as shown in Fig. 11(a). If we include the surface errors of all eight optics, the $OPD(0)$ becomes the same as shown in Fig. 3(b). When T_x
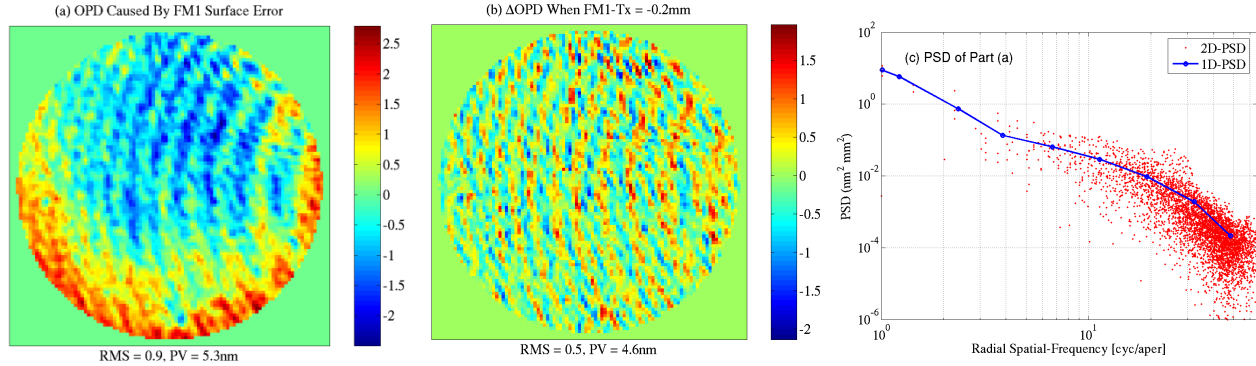
Figure 11. (a) Exit-pupil OPD caused by the FM1 "true" surface error only. (b) Change in exit-pupil OPD when FM1 is translated by T_x = -0.2mm. (c) Two-dimensional (2D) PSD of the OPD in part (a) and its radially-averaged 1-D version versus radial spatial-frequency.
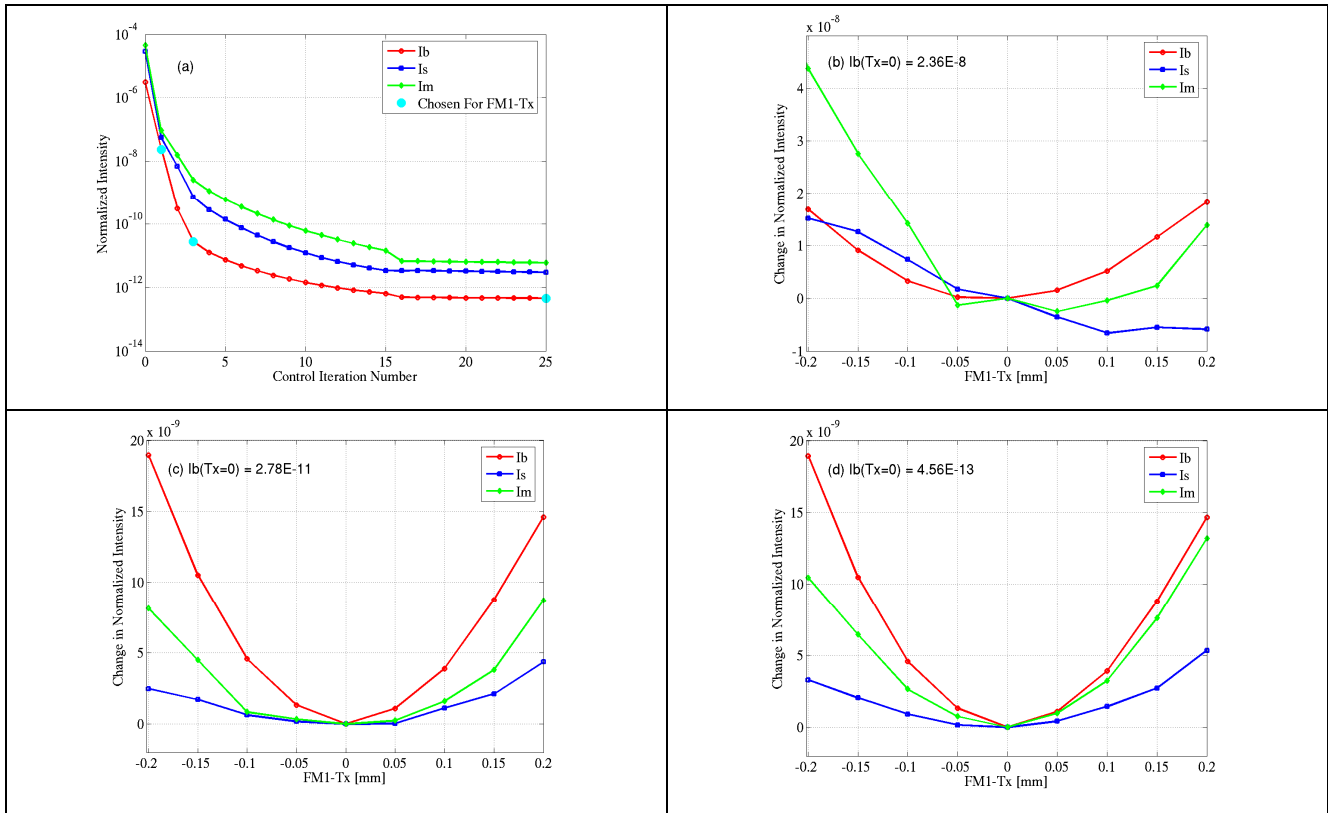

Figure 12. (a) Normalized intensity parameters versus control iteration number obtained for a monochromatic beam with λ=800nm. The surface errors of all eight optics are included in the simulation. (b)-(d) Variation of the normalized intensity parameters as a function of FM1- T_x (translation of FM1 along the x-axis) corresponding to three different contrast levels. The value of I_b when T_x = 0 is given as an insert along with the figure number.

= -0.2mm, we obtain a ΔOPD map as shown in Fig. 11(b), and its PSD as shown in Fig. 11(c), where the blue-curve is the 1-D (one-dimensional) version of the 2D-PSD calculated using the method described in Ref. [11]. For this case, we first carried out WFC for T_x = 0, and obtained the normalized intensity versus control iteration number result as shown in Fig. 12(a). Then, for the three different contrast levels shown by the cyan-color filled circles in Fig. 12(a), we calculated the changes in the values of the three normalized intensity parameters, I_b, I_s, and I_m, as a function of FM1- T_x, and obtained the results shown in Figs. 12(b-d). As we can see, none of the I_i –curves, where $i = b$, s or m, is symmetric with

respect to T_x , and they become more irregular when the darkness of the dark-hole reduces. Also, the sensitivity of contrast to FM1- T_x becomes stronger when the darkness of the dark-hole achieved is weaker. For this case, we found it difficult to do exact predictions as in the case of FM1 sinusoidal surface error shown in Fig. 10(b). This is because in the current case a spatial-frequency component of the ΔOPD is not well defined and $\Delta I(x,y)$ in the vicinity of $(N_x \lambda f / D, 0)$ is the combined product of all the spatial-frequency components of the ΔODP.

3.4 Translation of Occulter along the x- and z-Directions

We conducted an experiment on the HCIT to measure the sensitivity of narrow-band contrast on the x- (de-centering, T_x) and the z- (de-focusing, T_z) translations of the occulter. We carried out simulations on the same situation to find out how well the model predictions match with the experimental findings. The HCIT setup used for this experiment is slightly different from what was described in Section 2. That is, in this setup, $D = 48\text{mm}$, $\varepsilon = 0.4$, the front end F/# = 31.25, and the occulter is a thin-film Ni occulter deposited on a glass. This occulter has an OD-dependent phase profile similar to the blue-curve in Fig. 2(b) with a peak value of ~1.2 radians at the operating wavelength of $\lambda = 800\text{nm}$. We matched our optical model to this HCIT setup by using the same OD- and phase-profiles (designed, not measured) for the occulter while adjusting its width so that $T(x) = 0.5$ at $x/f = 3.3\lambda/D$, the same as on the testbed. No attempt has been made to match the magnitude and the registration of the optical surface errors between the experimental setup and the model— The same surface errors of the eight optics used in the simulations of the previous sub-sections were used for this simulation.
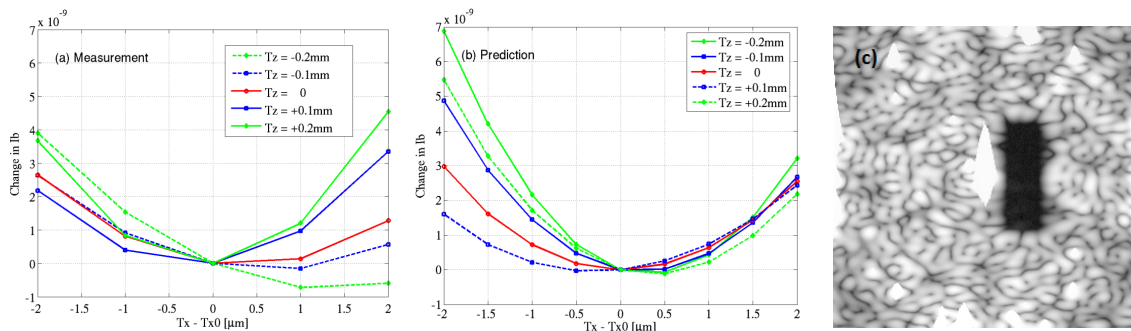

Figure 13. Sensitivity of I_b to occulter T_x and T_z. (a) Measured, and (b) simulated. (c) Normalized intensity map measured when $T_x = T_z = 0$, where $I_b = 2.91\text{E-9}$.

In the experiment, a rectangle-shaped half dark-hole was first created with the occulter at its nominal position ($T_x = T_z = 0$) in two WFC steps. In the first step, the exit-pupil wavefront was minimized through a normal, wavefront-based control procedure. In the next step, a dark-hole was created using the EFC-based correction procedure. Then the occulter T_x - and T_z -sensitivities of the contrast were measured with the following steps: (1) Move the occulter by T_z = -0.2mm (the occulter moves towards FM1). (2) Removing the Lyot Stop, scan the occulter along the x-axis (positive T_x moves the occulter towards the dark-hole), and find $T_x = T_{x0}$ at which the two symmetric side-lobes of the measured point-spread function (PSF) have the same intensity values. (3) Move the occulter from $T_x = T_{x0}$ -2μm to $T_x = T_{x0}$ +2μm in an increment of ΔT_x=1μm, and record the I_b values. (4) Repeat Steps 1-3 for T_z =-0.1, 0, 0.1, and 0.2mm. (5) Plot the change in I_b , or $I_b(T_x) - I_b(T_{x0})$, as a function of T_x - T_{x0}. The experimental result is shown in Fig. 13(a), and the one predicted by the model is shown in Fig. 13(b). Figure 13(c) shows an example of measured normalized intensity map. There are uncertainties and difference between the measurement and the simulation at least in the following several areas: (1) A monochromatic beam with λ = 808nm was used in the experiment, but the simulation was carried out with λ = 800nm. (2) Both the magnitudes and the registration of the surface error maps used in the simulation are different from what the propagating beam sees on the testbed. (3) The simulation uses the designed OD and phase profiles of the occulter, and they can be different on the testbed. (4) WFC was carried out over a rectangular area in the experiment, but on a D-shaped region in the simulation. (5) The darkness of the dark-hole achieved for the nominal case on the testbed and in the simulation is different. As we can see from Fig. 13(a-b), the measured and the predicted sensitivities are comparable even under the above-mentioned uncertainties and difference between the measurement and the simulation. Although not presented here, we found that the contrast sensitivity to the occulter's lateral and axial motions varies with, among other things, the darkness of the dark-hole achieved for the nominal case, just like in the case of FM1 x-motion.

4. CONCLUSION

One of the important milestones of the TPF Coronagraph project is to demonstrate the ability to predict the performance sensitivities of the system at levels consistent with exoplanet detection requirement. In order to gain some general understanding about the potentials and the limitations of the current single-DM HCIT system, we have examined through modeling and simulations the effects of some common errors on the estimation and the EFC-based control of the e-field over a half dark-hole region. Considered cases include two or three dead actuators, lateral and longitudinal movement of the occulting mask, and the lateral movement of a flat optical surface. We have shown that, when two or three actuators die at a time, one of the following four things can happen: (1) The e-field estimation and control algorithms work as usual; (2) the two algorithms become less efficient, but ultimately yield the same level of contrast as obtained when there is no any dead actuator; (3) both the efficiency of the algorithms and the ultimate contrast level get reduced; (4) the algorithms fail completely. The locations of the dead actuators determine which of the above four situations will occur, and we have identified through modeling and simulations some actuators that play crucial role in the e-field estimation and control processes on the HCIT. We have also shown that the lateral movement of a flat optic after WFC degrades the contrast slightly differently in the positive and the negative (towards or away from the dark-hole) directions, and the level of such degradation is strongly dependent on the darkness of the dark-hole achieved before introducing an error to the position of an optical component. The same is true for the de-centering and the defocus of the occulting mask. For this latter case, we compared the model predictions with the experimental results and obtained reasonable agreement between the two.

This work was carried out at the Jet Propulsion Laboratory, California Institute of Technology, under contract with the National Aeronautics and Space Administration.

REFERENCES

1. John T. Trauger, Chris Burrows, Brian Gordon, Joseph J. Green, Andrew E. Lowman, Dwight Moody, Albert F. Niessner, Fang Shi, and Daniel Wilson, "Coronagraph contrast demonstrations with the high-contrast imaging testbed," Proc. SPIE, **5487**, 1330, 2004.
2. Andrew E. Lowman, John T. Trauger, Brian Gordon, Joseph J. Green, Dwight Moody, Albert F. Niessner, and Fang Shi, "High-contrast imaging testbed for the Terrestrial Planet Finder coronagraph," Proc. SPIE, **5487**, 1246, 2004.
3. Erkin Sidick, Fang Shi, Scott Basinger, Dwight Moody, Andrew E. Lowman, Andreas C. Kuhnert, and John T. Trauger, "Performance of TPF's High-Contrast Imaging Testbed: Modeling and simulations, "Proc. SPIE, **6265**, 62653L, 2006.
4. Amir Give'on *et al*, "Broadband wavefront correction algorithm for high-contrast imaging system," Proc. SPIE, **6691**, 66910A (2007).
5. *Modeling and Analysis for Controlled Optical Systems User's Manual*, Jet Propulsion Laboratory, California Institute of Technology, Pasadena, CA.
6. Kunjithapatham Balasubramanian, Daniel W. Wilson, Brian D. Kern, Erkin Sidick, "Thickness-dependent optical properties of metals and alloys applicable to TPF coronagraph image masks," Proc. SPIE vol. 6693, pp. 66930Z, Aug. 2007..
7. Erkin Sidick and Kunjithapatham Balasubramanian, "Effects of optical-density and phase dispersion of an imperfect band-limited occulting mask on the broadband performance of a TPF coronagraph," *Proc. SPIE* vol. 6693, pp. 66931C, Aug. 2007..
8. Erkin Sidick, "Requirements on optical-density and phase dispersion of imperfect band-limited occulting masks in a broadband coronagraph," *Applied Optics,* vol. 26, pp. 7485-7493, Oct. 20, 2007.
9. Erkin Sidick, Scott A. Basinger, and David C. Redding, "An improved wavefront control algorithm for large space telescopes," Proc. SPIE, **7015**, 70154P (2008).
10. E. Sidick, S. Shaklan, A. Give'on, and B. Kern, "Studies of the effects of actuator errors on the HCIT/PIAA contrast performance ," *Proc. SPIE,* vol. 7731, pp.7731-4T, June 2010.
11. Erkin Sidick, " Power spectral density specification and analysis of large optical surfaces ," *Proc. SPIE*, vol. 7390, pp. 73900L, June 2009.

HCIT Broadband Contrast Performance Sensitivity Studies

Erkin Sidick*, Stuart Shaklan, Kunjithapatham Balasubramanian

Jet Propulsion Laboratory, California Institute of Technology, 4800 Oak Grove Drive, Pasadena, CA 91109, USA

ABSTRACT

The High Contrast Imaging Testbed (HCIT) at the Jet Propulsion Laboratory employs a broadband wavefront correction algorithm called Electric Field Conjugation (EFC) to obtain the required 10^{-10} contrast. This algorithm works with one deformable mirror (DM) to estimate the electric-field to be controlled, and with one or multiple DM's to create a "dark-hole" in a predefined region of the image plane where terrestrial planets would be found. We have investigated the effects of absorbing dust particles on a flat optic, absorbing spots on the occulting mask, dead actuators on the DM, and the effects of control bandwidth on the efficiency of the EFC algorithm in a Lyot coronagraph configuration. The structural design of the optical system as well as the parameters of various optical elements used in the analysis is drawn from those of the HCIT system that have been implemented with one DM. The simulation takes into account the surface errors of various optical elements. Results of some of these studies have been verified by actual measurements.

Key words: Coronagraphy, adaptive optics, space telescopes, exoplanets

1. INTRODUCTION

The High-contrast imaging testbed (HCIT) at JPL is the Exoplanet Exploration Program's primary platform for experimentation [1-3]. It is used to provide laboratory validation of key technologies as well as demonstration of a flight-traceable approach to implementation. It employs a broadband wavefront correction algorithm called Electric Field Conjugation (EFC) to obtain the required 10^{-10} contrast [4]. This algorithm works with one or multiple deformable mirrors (DM's) to create a "dark-hole" in a predefined region of the image plane where terrestrial planets would be found. It achieves the desired high contrast level in two stages. The first is the estimation stage. In this stage, the algorithm provides an estimate of the aberrated complex electric field (e-field) in the image plane based on pairs of images taken at the final image plane using different DM surface configurations. The second is the correction or EFC stage. In this stage the algorithm generates a correction based on the e-field estimated in the first stage. The correction is then applied to the DM actuators to null the image e-field in the predefined dark-hole region.

We have investigated the effects of absorbing particles/spots, dead actuators and control bandwidth on the system performance and the efficiency of the EFC algorithm in a Lyot coronagraph configuration. Considered cases include absorbing particles on the surface of a flat optic, i.e., a fold-mirror, absorbing spots on the surface of the occulting mask, dead actuators on the DM, and varying control bandwidths. The structural design of the optical system as well as the parameters of various optical elements used in the analysis is drawn from those of the HCIT system that have been implemented with one DM. The simulation takes into account the surface errors of various optics. The optical simulation algorithm uses MACOS (Modeling and Analysis for Controlled Optical Systems) as its analytic tool [5]. Hence it is capable of performing full three-dimensional near-field diffraction analysis on HCIT's optical model. Results of some of these studies have been verified by actual measurements. Other types of errors were investigated and reported earlier [6].

2. BACKGROUND

2.1 The HCIT Optical System

The schematic diagram of the HCIT layout in the *xz*-plane is shown in Figure 1. Artificial starlight is created by a 5μm pinhole illuminated by an optical fiber. We assume a broadband light source centered at wavelength λ=800nm and having a bandwidth of ±5%, or Δλ=80nm. An off-axis parabolic mirror (OAP1) collimates the light from the pinhole

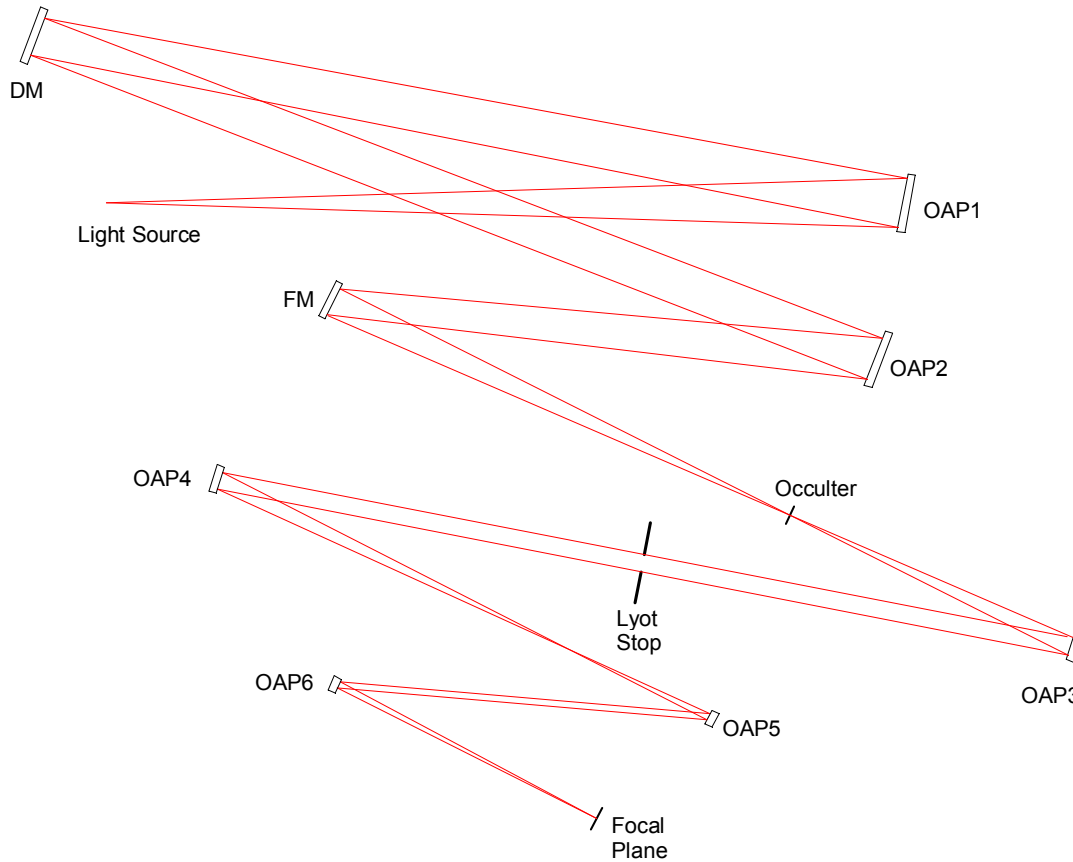*Erkin.Sidick@jpl.nasa.gov; Phone 1 818 393-7585; Fax 1 818 393-9471; www.jpl.nasa.gov

Figure 1. Schematic diagram of the High Contrast Imaging Testbed (HCIT) layout. The light source ("starlight") is a 5μm pinhole illuminated by an optical fiber, and a CCD science camera is located at the back focal plane for detecting the image of the "starlight".

and directs it to a high-density, 64x64 actuator deformable mirror (DM), which performs wavefront control. A circular aperture mask on the DM defines the system pupil of the HCIT, and can have a diameter of up to D=64mm. However, the current HCIT was implemented with D=48mm inscribed in an area covered by 48x48 actuators, so we will use this D value in the simulations of this paper. After the DM, the collimated light is imaged onto the focal plane of the occulting mask by OAP2 and a flat-mirror (FM). The occulting mask attenuates the starlight, and almost has no effect on the light of a planet if present. The "back-end" of the system, from the occulting mask to the back focal plane, supports experimentation with diverse coronagraph configurations and apodizations. OAP3 re-collimates the light passing through the occulter mask and forms a same-size sharp image of the DM pupil at the Lyot plane. A Lyot stop blocks the ring-like residual light diffracted off the occulting mask while letting most of the planet light through. After OAP4 forms an image from the remaining stellar and planet lights, it is then magnified (M ≈3) by the OAP5-OAP6 pair for proper sampling on the CCD science camera located at the back focal plane. More information on the HCIT and the DM can be found in Refs. [1-3].

2.2 Occulting Mask

The HCIT uses a modified one-dimensional band-limited occulter whose OD profile at wavelength λ = 800nm is truncated and smoothed by convolution with a Gaussian function. This smoothed pattern is described in detail in Refs. [7-8]. Specifically, the sinc^2 intensity transmission profile is $T_{\text{sinc}}(x) = \{1-[\sin(\pi x/w)/(\pi x/w)]^2\}^2$, $\text{OD}_{\text{sinc}}(x) = -\log_{10} T_{\text{sinc}}(x)$, with $w = 142$μm. The truncation and smoothing gives $\text{OD}_{\text{rel}}(x) = \min[\text{OD}_{\text{sinc}}(x), 8] \otimes G(x)$ with $G(x) = (2\pi\sigma^2)^{-1/2} \exp[-x^2/(2\sigma^2)]$, σ = 9μm. For practical reasons, the maximum transmission is often less than unity, so the final transmission is $T(x) = T_0\, 10^{-\text{ODrel}(x)}$, for some maximum transmission T_0. The above two OD profiles are shown graphically in Fig. 2(a). The spatially-varying transmission profile is optically realized by spatially varying the thicknesses of Ni layers, deposited on a fused quartz substrate. Because Ni has a large index of refraction ($n \sim 2.5$ at

800nm), regions of the occulter with higher OD (lower transmission, thicker Ni) also have a greater optical path length in transmission than low OD regions. The spatially-varying transmitted e-field is therefore complex-valued. In addition to the spatial variations in OD and phase, the OD and phase also vary with wavelength. Ni was chosen for this application because its OD and phase vary less with wavelength than other practical materials, as described in Ref. [9]. We will include the dispersion of both occulter OD and phase in our simulations. The profile of the occulter phase at λ=800nm, $\phi(800)$ is also shown in Fig. 2(a) in radians. Figure 2(b) shows the variation of the occulter OD at five wavelength values relative to that at λ=800nm, or the OD dispersion. The occulter phase dispersion is weaker than the OD dispersion, and the $\phi(\lambda) - \phi(800)$ has the largest value of -0.012 radians at the center of occulter and at λ = 768nm. For this occulter, $T(x) = 0.5$ at $x/f = 3.3\lambda/D$, where $D = 48$mm is the diameter of the system clear aperture and f is the focal length. The front end F-number (F/#) of this optical system is 31.25.
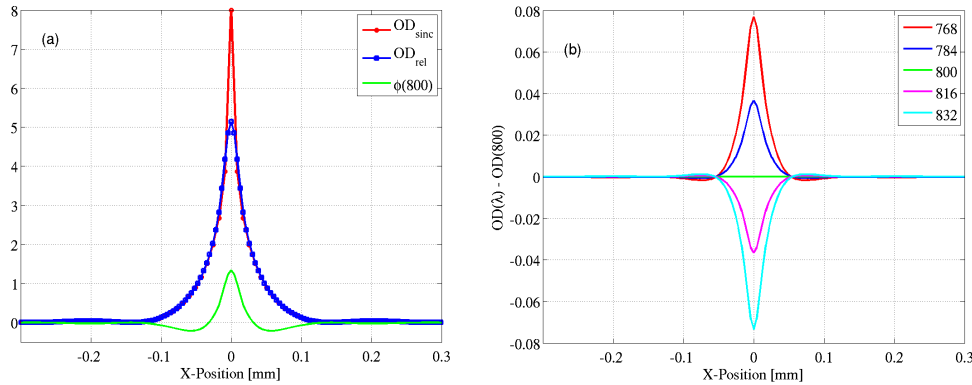

Figure 2. (a) The x-profiles of occulter Optical Densities, OD_{sinc} and OD_{rel}, as well as transmitted occulter phase at λ = 800nm, $\phi(800)$, where the latter is given in radians. (b) Occulter OD dispersion, where the figure legend shows five wavelength values in nm. These parameters correspond to a linear-sinc^2 occulting mask consisting of Ni deposited on a fused quartz substrate. .
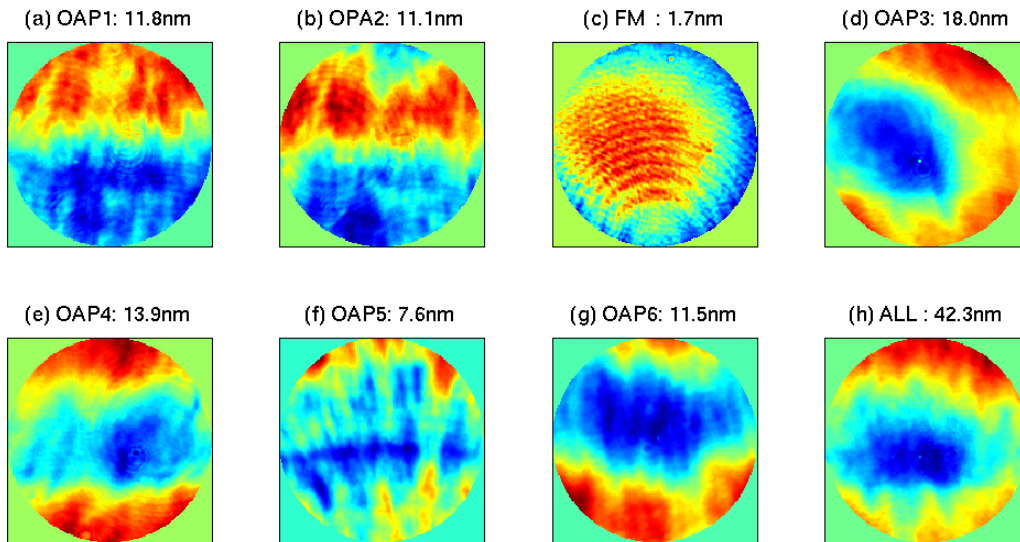

Figure 3. Surface height errors of various optics exhibited as OPD (Optical Path Difference) at the exit-pupil. The part (h) is the OPD when the surface height errors of all seven optics are included. The number included in each figure's title is the RMS (root-mean-square) value of the corresponding OPD map.

2.3 Other Optical Components

The DM used on the HCIT has 64x64 actuators arrayed on a 1mm pitch. Its description is similar to the 32x32 actuator DM described in detail in Ref. [1], and will not be repeated here.

Our Lyot stop is made from a simple blackened piece of sheet metal with a sharp edge. Its opening (Lyot stop aperture) has an eye-shape defined by two circles that are shifted with respect to each other in the horizontal direction by a distance of ε in units of D. The value of ε needs to be chosen based on the value of the occulting mask width parameter w, and $\varepsilon=0.36$ in this paper.

In our simulations, we include the surface errors of the six OAP's and the FM shown in Figs. 3(a-g). These are OPD (Optical Path-Difference) maps obtained at the system exit pupil by "turning-on" one surface height error map at a time. The part (h) is the total OPD at the exit-pupil obtained when the surface height errors of all seven optics are included in the simulation. Some optics on the current HCIT have surface height errors different from the above, and we used them here just to introduce some realistic surface errors into the HCIT optical model.

2.4 Definitions of Half Dark-Hole Area and Contrast

For the current optical system with only one DM, we carry out wavefront control (WFC) over a region Ω_c, where Ω_c is a rectangular half dark-hole region bound by $[X_1 \; X_2 \; Y_1 \; Y_2] = [3.5 \; 12 \; -12 \; 12]\lambda/D$, $X = x/f$, $Y = y/f$, and x and y are the horizontal and the vertical position variables on the corresponding image-plane. We will evaluate the performance of the HCIT using either the normalized intensity,

$$I_n(x, y) = I(x, y)/I_0, \tag{1}$$

or the contrast,

$$C(x, y) = I_n(x, y)[T_0/T(x, y)] = [I(x, y)/I_0][T_0/T(x, y)], \tag{2}$$

where $I(x, y)$ is the image intensity of the occulted star, and I_0 is the maximum value of the un-occulted star intensity, $T(x, y)$ is the occulter transmittance, and T_0 is the maximum value of the $T(x, y)$. We will keep track of the following three contrast quantities in this paper: (i) C_b, the mean contrast inside a "Big" rectangular region Ω_b defined by $[X_1 \; X_2 \; Y_1 \; Y_2] = [4 \; 11 \; -11 \; 11]\lambda/D$. (ii) C_s, the mean contrast inside a "Small" square region Ω_s defined by $[X_1 \; X_2 \; Y_1 \; Y_2] = [4 \; 5 \; -0.5 \; 0.5]\lambda/D$. (iii) C_m, the "Maximum" contrast value inside the small square region Ω_s. Similarly, we also use I_b, I_s and I_m to denote the big-region mean, the small-region mean, and the small-region maximum of the normalized intensity $I_n(x, y)$. The nominal Intensity values obtained for a narrowband light with $\lambda_0 = 800$nm and the error-free optical system (even the occulter phase is set to zero) without conducting any wavefront control are $[I_b \; I_s \; I_m] = [0.37 \; 2.8 \; 3.8] \times 1E-8$, respectively. When the phase errors of the seven optics as well as the occulter phase are included in simulation, the above intensity values change to $[0.39 \; 4.7 \; 9.3] \times 1E-5$, respectively. If we use the designed transmission profile $T_{\text{sinc}}(x)$ of the occulter, we obtain much better contrast values: $[0.77 \; 8.7 \; 11.9] \times 1E-12$. This is similar to what we reported in Ref. [6]. This is because $OD_{\max} = 8$ for $T_{\text{sinc}}(x)$ at the center of the occulter, while $T(x)$ has only $OD_{\max} = 5.14$.

2.5 About the Wavefront Control (WFC) Algorithm

In this paper, we use a control algorithm similar to the "minimum-wavefront and optimal control compensator" described in detail in Ref. [10]. This approach is also called "Actuator regularization" [4]. The WFC algorithm described in Ref. [10] uses the wavefront at the system exit pupil as its input, and calculates the actuator commands as its output. In the present case we set the DM actuators to superpose the negative of the e-field onto the image plane, with a goal to make the image intensity zero on the region Ω_c. Therefore, the WFC algorithm uses an e-field column-vector $\vec{\mathbf{e}}$ as its input, where

$$\vec{\mathbf{e}} = \begin{bmatrix} \Re(\vec{\mathbf{E}}) \\ \Im(\vec{\mathbf{E}}) \end{bmatrix}. \tag{3}$$

The joint cost function now becomes as

$$J = \frac{1}{2}\left(\vec{\mathbf{e}}^T \vec{\mathbf{e}} + \gamma_{wu} \vec{\mathbf{u}}^T \vec{\mathbf{u}}\right),$$

(4)

and the gain matrix $\widetilde{\mathbf{G}}$ is obtained from

$$\widetilde{\mathbf{G}} = \left[\widetilde{\mathbf{S}}^T \widetilde{\mathbf{S}} + \gamma_{wu} \widetilde{\mathbf{I}}\right]^{-1} \widetilde{\mathbf{S}}^T.$$

(5)

In Eq. (3), $\vec{\mathbf{E}}$ is the column-vector of the complex e-field on region Ω_c. It is formed by stacking the elements of the complex e-field on region Ω_c in a certain order, as was explained in Eq. (1) of Ref. [10]. The $\Re(\vec{\mathbf{E}})$ and the $\Im(\vec{\mathbf{E}})$ are the real and the imaginary parts of $\vec{\mathbf{E}}$, respectively. In Eq. (5), the $\widetilde{\mathbf{S}}$ is the sensitivity matrix consisting of the influence functions of all actuators. The MACOS simulation tool calculates the complex e-field at the final focal plane directly. Therefore, the e-field estimation step is actually not needed in our simulation and we will not use it in this paper. The simulation creates a 512x512-pixel image map, with ~4 pixels per $f\lambda/D$. Considering only the pixels in the dark hole gives an e-field vector, $\vec{\mathbf{e}}$, having a size of 3521x1 pixels per wavelength on the average. There are a total of 2304 DM actuators in the current 1-DM system, but we use only 1907 (~83%) actuators excluding those with zero or very weak influences.

3. SIMULATION RESULTS

We now describe our simulation results. We start with the nominal case where only the optical surface errors and the occulter phase are included in the simulation.
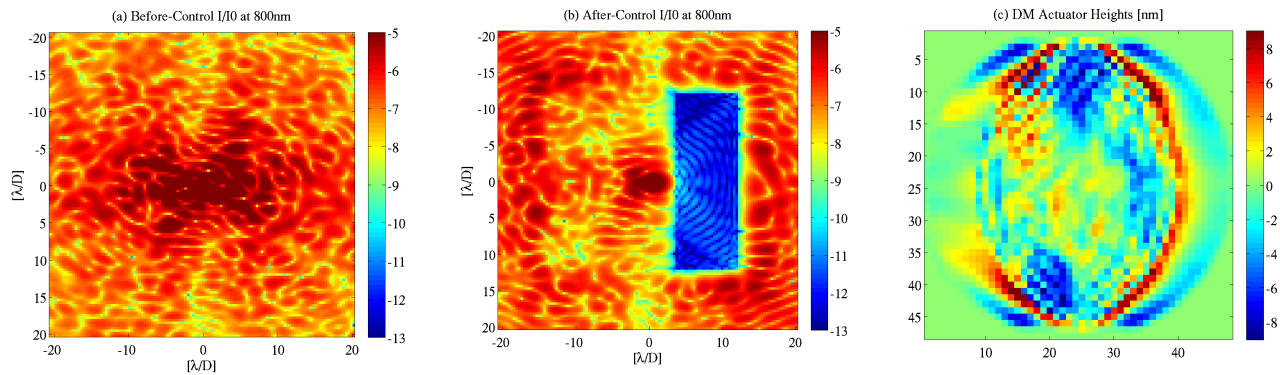

Figure 4. Log-scale PSF (a) before WFC and (b) after 30-iterations WFC at $\lambda_3 = 800$nm, where the units of the horizontal- and the vertical-axes are λ/D. (c) Actuator-height map obtained at the end of broadband WFC, where the units of the horizontal- and the vertical-axes are mm.

3.1 Nominal Case

We use the EFC-based broadband wavefront correction algorithm described in Ref. [4] in our simulations. The broadband sensitivity-matrix $\widetilde{\mathbf{S}}$ consists of three monochromatic sensitivity matrices corresponding to wavelengths λ=768, 800nm and 832nm, respectively. That is, we carry out the WFC at the above three wavelengths simultaneously, by obtaining one set of DM solutions from the e-fields corresponding to the three wavelengths. These wavelengths correspond to the center wavelengths of three of the five 2% bandpass filters [8] employed on the HCIT and centered at λ = 768, 784, 800, 816 and 832nm, respectively. To obtain a 8%-broadband $I_n(x,y)$ map, we calculate the final image plane intensity maps at the above five wavelengths separately first, then average them to obtain the broadband image intensity map. To calculate the 10%-broadband contrast, we add two new wavelengths to the above list, λ=760 and 840nm, and average the resulting seven intensity maps.
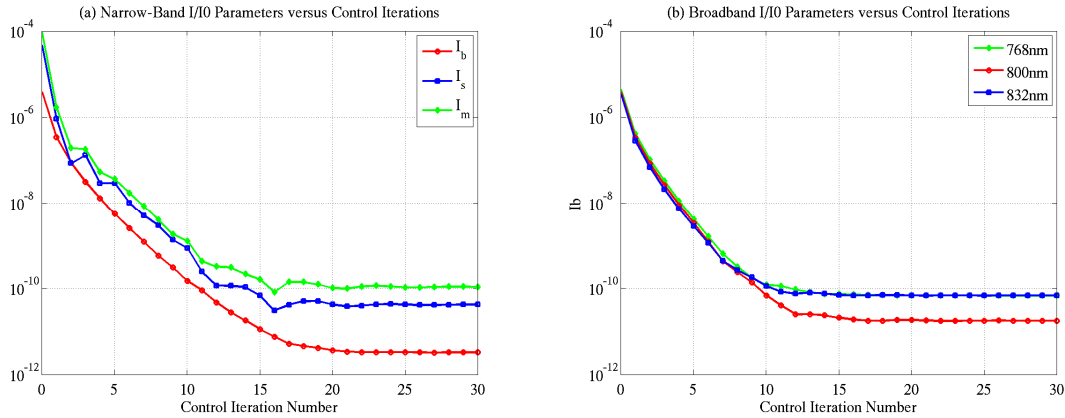
Figure 5. I_b, I_s and I_m versus control iteration number. (a) Monochromatic I_b, I_s and I_m at λ_3=800nm. (b) I_b at three different wavelengths obtained with a single set of DM solutions.
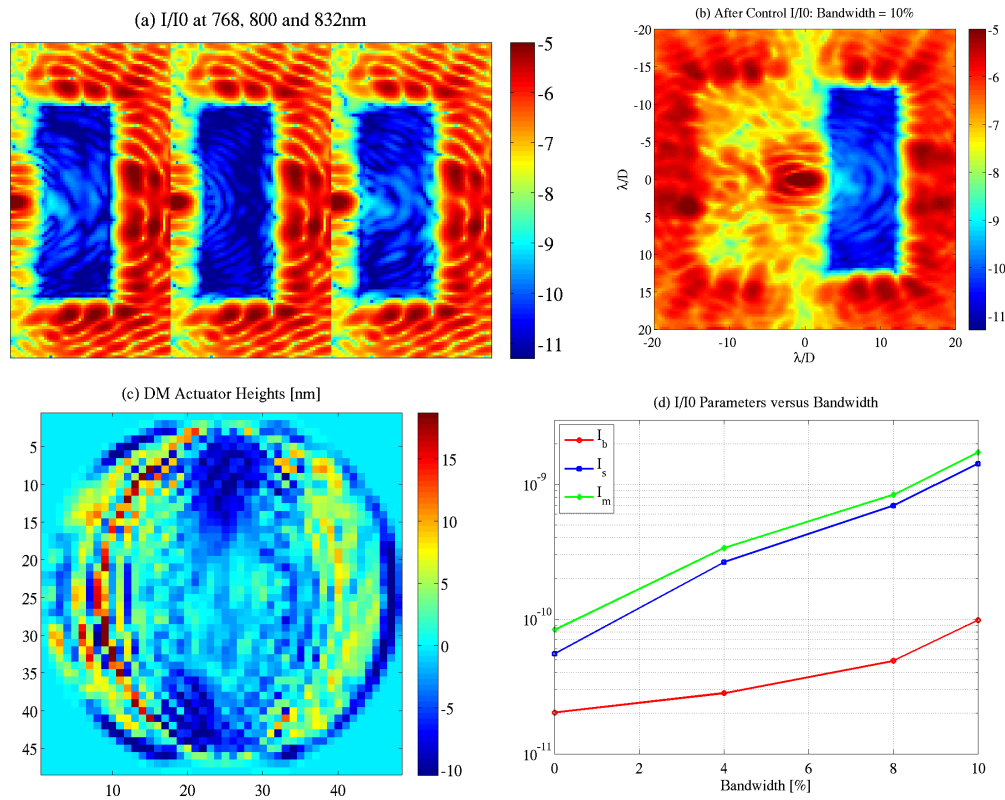

Figure 6. (a) Log-scale $I_n(x,y)$ maps obtained after 30-iterations of broadband-WFC at three wavelengths. (b) Log-scale 10%-broadband $I_n(x,y)$ map corresponding to part (a). (c) DM heights leading to the $I_n(x,y)$ maps in parts (a) and (b). (d) Normalized intensities versus bandwidth.

When we include the surface errors of the seven optics and the occulter phase only, we obtain a monochromatic $I_n(x,y)$ map as shown in Fig. 4(a) at λ = 800nm before WFC. After conducting monochromatic WFC for 30 iterations, we obtain a new $I_n(x,y)$ map as shown in Fig. 4(b) with the DM solution shown in Fig. 4(c). The three normalized intensities of this case are shown as a function of control iteration number in Fig. 5(a). If we carry out broadband WFC for the same case, we obtain I_b versus control iteration number curves as shown in Fig. 5(b) at the three wavelengths used. The $I_n(x,y)$ maps at the end of 30 control iterations, the 10%-broadband $I_n(x,y)$ map, and the corresponding DM solution used are shown in Figs. 6(a-c). Also, the broadband normalized intensities are shown as a function of control

bandwidth in Fig. 6(d). As we can see, we can obtain $I_b \approx 1\text{E} - 10$ with a bandwidth of 10% in this system. These results are included here as a baseline to the simulations to be presented in the following sub-sections.

In the above WFC simulation, we used an optimized set of four actuator regularization values, $\gamma_{\text{wu}} = [0.1\ 1\ 10\ 100]/\text{nm}^2$, with the corresponding WFC iteration numbers listed in the same order, $N_{\text{WFC}} = [5\ 10\ 10\ 5]$. That is, the WFC process is completed in four phases with four different γ_{wu} values in the order given above, each with a different WFC iteration number also given above.

It should be mentioned that the sensitivity matrix $\widetilde{\mathbf{S}}$ is obtained by including the occulter phase error but setting the surface height errors of the seven optics to zero. Also, the same sensitivity matrix $\widetilde{\mathbf{S}}$ is used in all control iterations, that is, the $\widetilde{\mathbf{S}}$ is not updated or altered during a WFC process, and the same $\widetilde{\mathbf{S}}$ is used in all simulation cases.

3.2 Absorbing Particles on the Flat-Mirror (FM)

The first defect we investigated is the case of absorbing particles on the FM. We assumed 1, 3 and 6 particles having a square shape of width 114μm and heights varying between 10 and 100μm. All particles exhibit the same amount of absorption at a given wavelength, but differing amounts of reflected phase-delays due to different heights. Also, both the reflection coefficient and the phase-delay of those particles change with wavelength. The size of the propagation matrix, 512x512, used in our MACOS simulation tool gives a pixel size of 114μm for the FM, therefore, we chose the smallest possible particle size, varying only the heights, for this category of simulations. The values of the reflection coefficient and the phase-delay of the 6 particles at five different wavelengths are listed in Table 1.

Table 1. Reflection coefficient $r(\lambda)$ and phase-delay $\varphi(\lambda)$ of six absorbing particles on the FM. The optical constants n and k of the particles at 800nm are assumed to be 2.3 and 0.3, respectively.

	Spot #	768nm	784nm	800nm	816nm	832nm
$r(\lambda)$	All	0.4105	0.4065	0.4028	0.3994	0.3963
$\varphi(\lambda)$ [waves]	1	-0.3541	0.3366	-0.0402	-0.4805	0.0193
	2	0.4323	0.0661	-0.3253	0.2596	-0.1779
	3	-0.2695	-0.2744	-0.479	0.1285	-0.4411
	4	0.3652	-0.2036	0.0904	0.2554	0.2987
	5	-0.3825	0.1659	-0.3874	-0.0366	0.2239
	6	-0.0111	0.3869	-0.3509	-0.2165	-0.2025

The MACOS simulation tool does not allow us to place partially-absorbing particles on a reflector. Therefore, we placed the particles on a transparent (transmission-coefficient $t = 1$ everywhere) virtual surface just before the FM as partially-absorbing spots whose transmission-coefficient is described by $t(x,y;\lambda) = |r(\lambda)| \exp[j\varphi(x,y;\lambda)]$, where the values of $r(\lambda)$ and $\varphi(x,y;\lambda)$ are those listed in Table 1. Figure 7(a) shows the locations of the six particles. The locations are chosen randomly and divided into three groups: One-particle (red), three-particles (red and blue), and six-particles (all colors). We carried out 8%-broadband WFC for these 3 cases, and obtained the 10%-broadband contrast values shown in Fig. 7(b). As a comparison, we included the contrast values of the nominal case where no particle is placed on the FM. The corresponding 10%-broadband $I_n(x,y)$ maps obtained at the end of 30-iterations broadband WFC are shown in Fig. 8(a). To obtain these $I_n(x,y)$ maps, we evaluated the single set of DM solutions at 41 wavelengths, ranging from 760nm to 840nm in increments of 2nm, so that phase excursions within the increments are captured by employing smaller steps. As we can see from Fig. 7(b), placing just one particle on the FM greatly degrades the broadband contrast, and increasing the number of particles from one to three and six does not make too much difference

on the broadband contrast. The scatter from a particle is a function of the illumination, in particular the Airy rings that evolve radially with wavelength. Thus a particle will appear bright at wavelengths where the Airy ring crosses it, and dimmer at other wavelengths. We are currently investigating the additive effects of the particles. As mentioned above, the single set of DM solutions was obtained through a broadband WFC carried out at only three discrete wavelengths. When that set of DM solutions is evaluated at other wavelengths, the particles exhibit completely different phase-delays at the new wavelengths, giving rise to a lot of scattered light inside the dark-hole region.

We also examined a case where no particle is placed on the FM when the initial 30-iterations WFC was carried out, then one particle is placed on the FM, and after that another 30-iterations WFC was conducted. The $I_n(x, y)$ maps at the end of those three steps are shown in Fig. 8(b). In this figure, the left-most $I_n(x, y)$ map has $\begin{bmatrix} C_b & C_s & C_m \end{bmatrix}$ = $\begin{bmatrix} 0.49 & 6.9 & 8.3 \end{bmatrix} \times 1E-10$, the middle map $\begin{bmatrix} 8.6 & 9.0 & 9.5 \end{bmatrix} \times 1E-9$, and the right-most map $\begin{bmatrix} 1.5 & 1.9 & 2.2 \end{bmatrix} \times 1E-9$, respectively. The last contrast values are very close to the 8%-broadband contrasts of $\begin{bmatrix} 1.5 & 2.5 & 3.5 \end{bmatrix} \times 1E-9$ of the Particle # = 1 case shown in Fig. 7(b) but obtained by evaluating the DM solutions with five wavelengths.
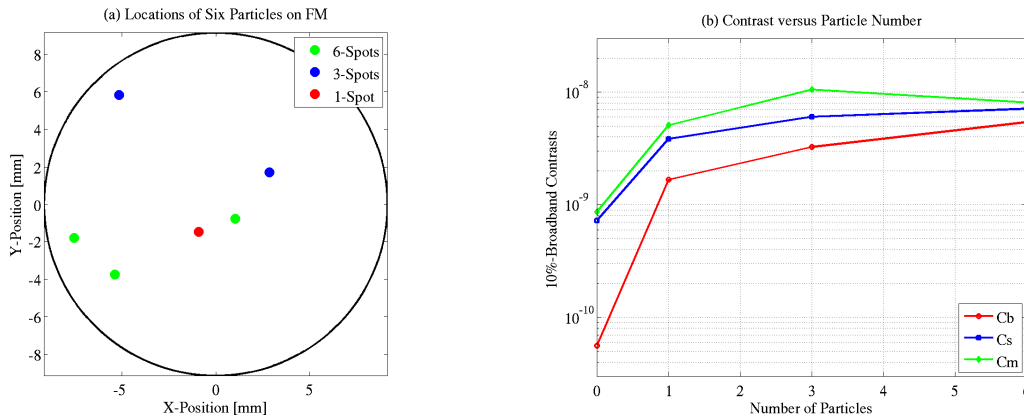

Figure 7. (a) Locations of the six particles on FM. The black-circle indicates the boundary of the FM's illuminated area. (b) 10%-broadband contrasts versus particle number.
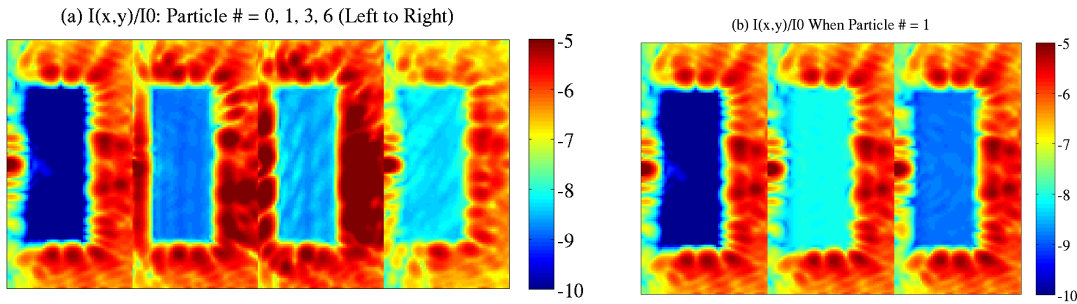

Figure 8. (a) Log-scale 10%-broadband $I_n(x,y)$ maps when the number of the particles placed on FM is 0, 1, 3 and 6, respectively. (b) Log-scale 8%-broadband $I_n(x,y)$ maps when no particle is placed on FM (left), one particle is placed on the FM of the system that achieved the $I_n(x,y)$ map on the left (middle), and after carrying-out another 30-iterations WFC (right).

3.3 Defects on the Occulter Surface

Figure 9(a) shows a portion of the measured image of an occulter fabricated at JPL. A narrow 20µm wide moving slit in close proximity to the substrate surface was employed in a vacuum deposition chamber to coat a thickness profiled layer of Ni on a fused silica substrate. By controlling the dwell time of the slit at a given location, the total thickness of the layer at a given spot to obtain chosen optical density was achieved. Careful thickness calibration runs and multiple passes of the procedure ensured minimum error in fabricating the mask per design as detailed in Refs. [7,12]. However, defects do occur on the occulter as shown in Figure 9(a). In order to understand how the defects on the surface of an actual occulter will affect the broadband contrast of the HCIT, we did the following: (1) Divided the occulter image shown in Fig. 9(a) by its horizontal profile obtained by vertically averaging the same image. (2) Replaced its central,

$\Delta x \sim 280 \mu m$-wide region with a value of one. We call the resultant map the Occulter Multiplier. (3) Selected two areas from this Occulter Multiplier, a "good" and a "bad" areas, as indicated by the red- and the yellow-rectangles in Fig. 9(a), and obtained the Occulter Multipliers A and B shown in Figs. 9(b-c), respectively. (4) Multiplied the model Occulter transmittance by those two multipliers, one at a time, and evaluated the resultant 8%-broadband contrast after conducting 30-iterations broadband WFC. That is, we altered the Occulter transmission coefficient by multiplying it with the square-root of the map of Fig. 9(b) or 9(c), but left the Occulter phase unchanged. The resulted $I_n(x,y)$ maps at five different wavelengths (indicated in the figure title) and their average (the right-most part) are shown in Fig. 10. In this figure, the top-row corresponds to the Occulter Multiplier A, and has $\begin{bmatrix} C_b & C_s & C_m \end{bmatrix} = \begin{bmatrix} 0.16 & 1.0 & 1.4 \end{bmatrix} \times 1E-9$. The bottom-row corresponds to the Occulter Multiplier B, and has $\begin{bmatrix} C_b & C_s & C_m \end{bmatrix} = \begin{bmatrix} 0.50 & 1.2 & 1.6 \end{bmatrix} \times 1E-9$. With these two new occulters, the broadband contrast gets degraded as compared to the nominal case, Figs. 6(a-d), where $\begin{bmatrix} C_b & C_s & C_m \end{bmatrix} = \begin{bmatrix} 0.49 & 6.9 & 8.3 \end{bmatrix} \times 1E-10$, and such degradation is more severe with the Occulter B than the Occulter A, as expected. The broadband contrast of HCIT utilizing an occulter similar to Occulter B has been measured by a different group of researchers at JPL, and their measured contrast map has a feature very similar to those of the bottom-row in Fig. 10.
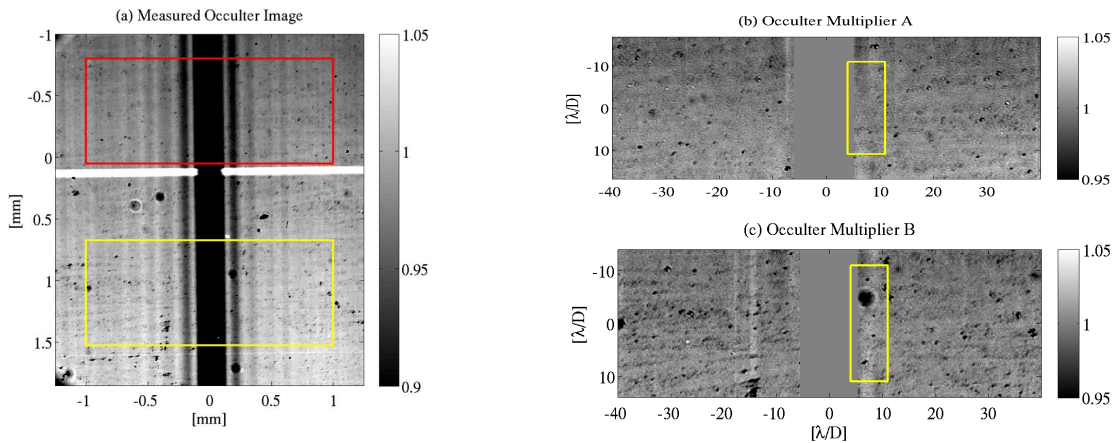

Figure 9. (a) Measured transmittance of an occulter fabricated at JPL. The red- and the yellow-rectangles show a "good" and a "bad" areas on the occulter surface, respectively. (b) An occulter multiplier map obtained from the area of red-rectangle in part (a). The occulter transmission coefficient is multiplied by the square-root of this map to simulate a realistic "good" occulter area. (c) Same as part (b), except that this map is for a "bad" occulter area. Mask Transmittance was measured by Brian Kern at JPL.
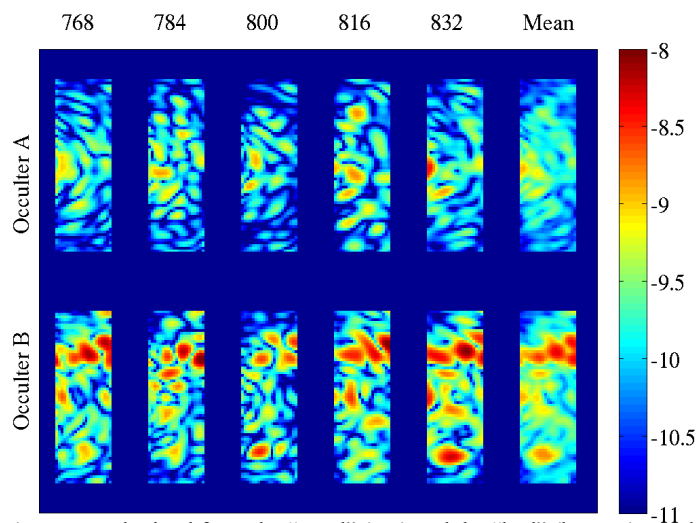

Figure 10. Log-scale $I_n(x,y)$ maps at obtained from the "good" (top) and the "bad" (bottom) occulter areas, respectively. The five left parts of each row correspond to five different wavelengths, and the right-most part is their mean or 8%-broadband $I_n(x,y)$ maps.

3.4 Dead Actuators

Actuator errors affect both the e-field estimation and control. However, there are 2.25 times more actuators in the current HCIT system as compared to those studied in Ref. [6], thus one can expect that the current system is much less sensitive to dead actuators. To confirm this point, we examined the effects of dead actuators on the EFC efficiency only. We chose three cases of dead actuators as shown in Fig. 11(a), where the number of dead actuators, N_{dead}, is equal to 200 (green), 400 (green + blue) and 600 (all colors), respectively. The dead actuators are chosen randomly among the 1907 actuators used. They are not responsive to the applied commands, and remain fixed at the mid-point of their control range. In the current simulations, for the optical system with all seven phase errors, we set the command values of the selected actuators to 0nm (the mid-point of the -200nm to 200nm range) when performing each control iteration. The sensitivity matrix $\widetilde{\mathbf{S}}$ is kept the same, but the command values of the dead actuators are set to 0nm.
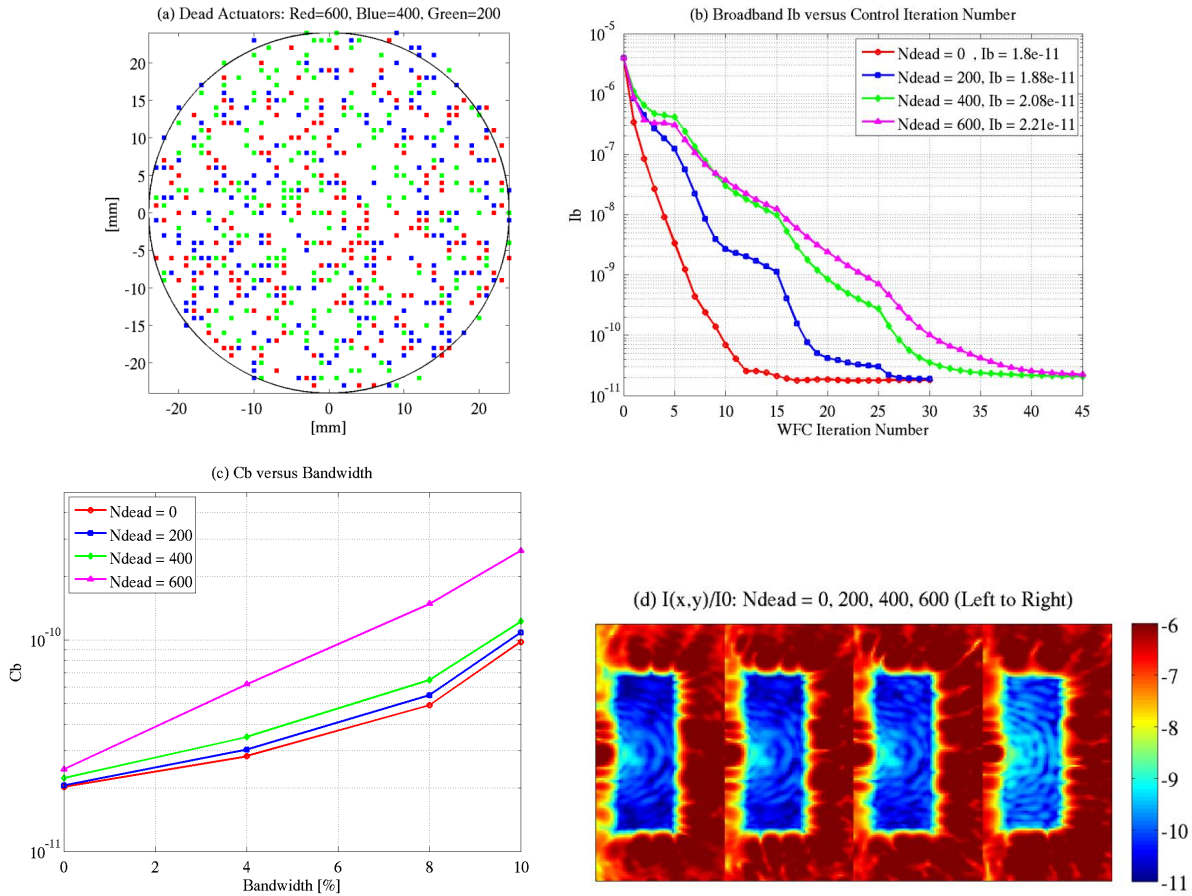
Figure 11. (a) Three groups of dead actuators selected: N_{dead} = 200 (green), 400 (green + blue), and 600 (all colors). (b) I_b versus control iteration number during a 8%-broadband WFC process with N_{dead} as a parameter. Also listed in the figure legend are the I_b values corresponding to the last control iterations. (c) C_b as a function of bandwidth with N_{dead} as a parameter. (d) 10%-broadband $I_n(x,y)$ maps corresponding from the left to the right to N_{dead} = 0, 200, 400, and 600, respectively.

Figure 11(b) compares the WFC efficiency of the following four cases: N_{dead} = 0 (nominal case), 200, 400 and 600. Although what was carried out is 8%-broadband control as in Fig. 5(b), we showed here only I_b as an example. The WFC process becomes less efficient with increasing N_{dead} as expected, but the final value of I_b differs only slightly

among the four cases considered. The same is true for C_b versus bandwidth as shown in Fig. 11(c), except the case of $N_{dead} = 600$ where C_b worsens faster with increased bandwidth than the other three cases. This result is obtained from the 8%-broadband DM solutions corresponding to the last data points in Fig. 11(b). The same DM solutions are used to obtain the 10%-broadband $I_n(x,y)$ maps shown in Fig.11(d). Again, the first three $I_n(x,y)$ maps are almost identical. That is, as much as 400 dead-actuators do not cause any meaningful reduction in the obtainable 10%-broadband contrast. This is one of the most significant findings of this study. In future work, we will study the effects of actuators that are stuck at one end of their range, as well as actuators that fail in local groups.

3.5 Effects of Control Bandwidth

Carrying-out WFC with a larger bandwidth yields better 10%-broadband contrast, but it takes a longer time to achieve the best level of dark-hole. In order to gain an understanding on the trade-off between the control bandwidth and the best 10%-broadband contrast achievable, we carried out control for the nominal case (all seven phase errors and occulter phase are included) at 0 (monochromatic), 2% and 8% bandwidths, each for 35 iterations, then evaluated the obtained DM solutions at 0, 4, 8 and 10% bandwidths. The 2%-broadband control and the 2%-broadband $I_n(x,y)$ evaluation are done in the same way as the 8%-broadband ones, but with wavelengths of 792, 800 and 808nm, respectively. The results of C_b are shown in Fig. 12(a), and the $I_n(x,y)$ maps at 10%-bandwidth are shown in Fig. 12(b). As we can see from Fig. 12(a), at contrast bandwidth of 10%, C_b of control bandwidth = 0 is about 20 times worse, and that of control bandwidth = 2% is about 2 times worse than the C_b of the control bandwidth = 8%. In the cases of control bandwidth = 2 and 8%, increasing the control bandwidth by a factor of 4 improves C_b by a factor of 2.
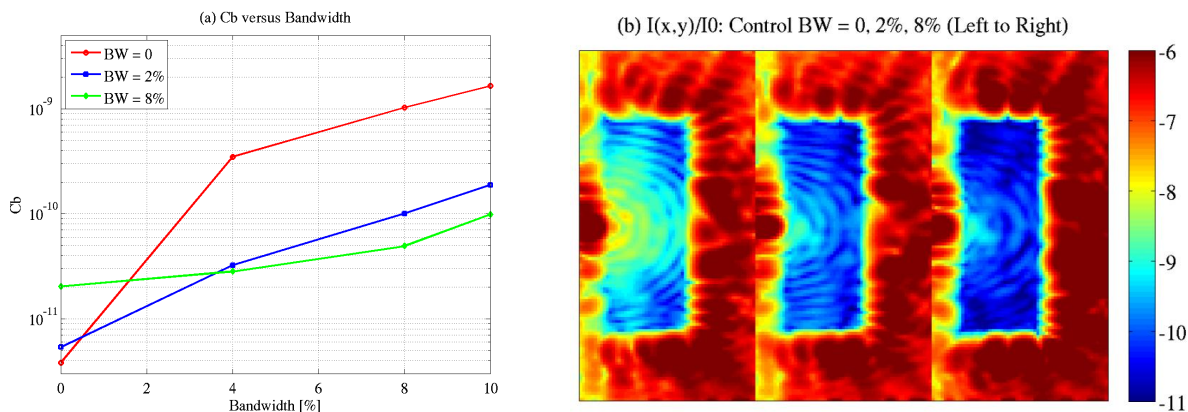

Figure 12. (a) Contrast C_b as a function of contrast bandwidth with control bandwidth (BW in the figure legend) as a parameter. (b) 10%-broadband $I_n(x,y)$ maps corresponding from the left to the right to control bandwidth = 0, 2%, 8%, respectively.

4. CONCLUSION

One of the important milestones of the TPF Coronagraph project is to demonstrate the ability to predict the performance sensitivities of the system at levels consistent with exoplanet detection requirement. In order to gain some general understanding about the potentials and the limitations of the current single-DM HCIT system, we have examined through modeling and simulations the effects of some common errors on the EFC-based control of the e-field over a half dark-hole region. Considered cases include partially-absorbing spots on a flat mirror, defects on the occulting mask surface, and dead actuators of the DM. We have also examined how the control bandwidth affects the 10%-broadband contrast. We have shown that, a single 114μm particle alters both the reflected amplitude and phase of the propagating beam and scatters light into the dark-hole. The resulting speckles can only be nulled partially, and it is impossible to obtain 10%-broadband contrast better than 1E-9 in the presence of one or more such particles. Some defects found on the surface of a fabricated occulter can be very detrimental to the broadband contrast and should be avoided whenever possible. At JPL, a HCIT team has mitigated such a problem by moving the beam center to a "clean" area on the occulter. Current HCIT system utilizing a 48x48 actuators DM is very robust in terms of dead actuators, and up to 400 dead actuators randomly selected did not cause any meaningful degradation to the 10%-broadband contrast. Increasing

the control bandwidth does improve the contrast bandwidth. It was found that increasing the control bandwidth from 2% (one 2% bandpass filter) to 8% (three 2% bandpass filters) improves the 10%-broadband contrast by a factor of two at the cost of longer control time.

REFERENCES

1. John T. Trauger, Chris Burrows, Brian Gordon, Joseph J. Green, Andrew E. Lowman, Dwight Moody, Albert F. Niessner, Fang Shi, and Daniel Wilson, "Coronagraph contrast demonstrations with the high-contrast imaging testbed," *Proc. SPIE*, **5487**, 1330 (2004).
2. Andrew E. Lowman, John T. Trauger, Brian Gordon, Joseph J. Green, Dwight Moody, Albert F. Niessner, and Fang Shi, "High-contrast imaging testbed for the Terrestrial Planet Finder coronagraph," *Proc. SPIE*, **5487**, 1246 (2004).
3. Erkin Sidick, Fang Shi, Scott Basinger, Dwight Moody, Andrew E. Lowman, Andreas C. Kuhnert, and John T. Trauger, "Performance of TPF's High-Contrast Imaging Testbed: Modeling and simulations, " *Proc. SPIE*, **6265**, 62653L (2006).
4. Amir Give'on *et al*, "Broadband wavefront correction algorithm for high-contrast imaging system," *Proc. SPIE*, **6691**, 66910A (2007).
5. *Modeling and Analysis for Controlled Optical Systems User's Manual*, Jet Propulsion Laboratory, California Institute of Technology, Pasadena, CA.
6. Erkin Sidick, Stuart Shaklan, Amir Give'on, and Brian Kern, " Studies of the effects of optical system errors on the HCIT contrast performance," *Proc. SPIE*, **8151**, 8151-06 (2011).
7. D. C. Moody and J. T. Trauger, "Hybrid Lyot coronagraph masks and wavefront control for improved spectral bandwidth and throughput," *Proc. SPIE*, 6693, 6693I1-9 (2007).
8. "Exoplanet Exploration Coronagraph Technology: Technology Milestone #2 Report," Brian Kern, Andreas Kuhnert and John Trauger, editors, 8 Aug. 2008, http://exep.jpl.nasa.gov/TPF-C/HCIT-Milestone2Signed-2008-08-08.pdf.
9. K. Balasubramanian, "Band-limited image plane masks for the Terrestrial Planet Finder coronagraph: materials and designs for broadband performance," *Appl. Opt*. 47, pp.116-125 (2008).
10. Erkin Sidick, Scott A. Basinger, and David C. Redding, "An improved wavefront control algorithm for large space telescopes," Proc. SPIE, **7015**, 70154P (2008).
11. E. Sidick, S. Shaklan, A. Give'on, and B. Kern, "Studies of the effects of actuator errors on the HCIT/PIAA contrast performance ," *Proc. SPIE*, **7731**, 7731-4T (2010).
12. D.C. Moody, B.L. Gordon, J.T. Trauger, "Design and demonstration of hybrid Lyot coronagraph masks for improved spectral bandwidth and throughput," *Proc SPIE,* **7010**, 70103P1-9 (2008).

HCIT Contrast Performance Sensitivity Studies: Simulation versus Experiment

*Erkin Sidick, Stuart Shaklan, John Krist, Eric J. Cady, Brian Kern, and Kunjithapatham Balasubramanian

Jet Propulsion Laboratory, California Institute of Technology, 4800 Oak Grove Drive, Pasadena, CA 91109, USA

ABSTRACT

Using NASA's High Contrast Imaging Testbed (HCIT) at the Jet Propulsion Laboratory, we have experimentally investigated the sensitivity of dark hole contrast in a Lyot coronagraph for the following factors: 1) Lateral and longitudinal translation of an occulting mask; 2) An opaque spot on the occulting mask; 3) Sizes of the controlled dark hole area. Also, we compared the measured results with simulations obtained using both MACOS (Modeling and Analysis for Controlled Optical Systems) and PROPER optical analysis programs with full three-dimensional near-field diffraction analysis to model HCIT's optical train and coronagraph.

Key words: Coronagraphy, adaptive optics, space telescopes, exoplanets

1. INTRODUCTION

This paper presents both simulated and measured results on the sensitivity of broadband contrast of a Lyot coronagraph on the High-Contrast Imaging Testbed (HCIT) at NASA's Jet Propulsion Laboratory (JPL). This testbed is the Exoplanet Exploration Program's primary platform for experimentation [1-3]. It is used to provide laboratory validation of key technologies as well as demonstration of a flight-traceable approach to implementation. It employs a 48x48 actuators deformable-mirror (DM) and a broadband wavefront correction algorithm called Electric Field Conjugation (EFC) to obtain the required 10^{-10} contrast [4]. We have investigated the effects of the following factors on the system performance and the efficiency of the EFC algorithm: Lateral and longitudinal translation of the occulter, an opaque spot on the occulter, and the size of the controlled dark-hole area. The laboratory testing was carried out with either a 2%-narrowband or a 10%-broadband light. The simulations were conducted with both MACOS (Modeling and Analysis for Controlled Optical Systems) [5] and PROPER [6], and their results were compared with measurements. We got fairly good agreement between the measurement and the simulation. In an earlier paper we reported on model sensitivities for the number and position of dead actuators, and beam walk due to translation of a flat optic in the beam [7].

2. BACKGROUND

2.1 The HCIT Optical System

The schematic diagram of the HCIT layout in the *xz*-plane is shown in Figure 1. Artificial starlight is created by a 5µm pinhole illuminated by an optical fiber. We use a broadband light source centered at wavelength λ=800nm in combination with five 2%-bandpass filters whose passbands are centered at 768, 784, 800, 816 and 832nm, respectively. For some experiments only the 768, 800 and 832nm filters were employed. An off-axis parabolic mirror (OAP1) collimates the light from the pinhole and directs it to a high-density, 64x64 actuator DM, which performs wavefront control. A circular aperture mask on the DM defines the system pupil of the HCIT, and can have a diameter of up to *D*=64mm. However, the current HCIT was implemented with *D*=48mm inscribed in an area covered by 48x48 actuators, and we use this same *D* value in the simulations of this paper. After the DM, the collimated light is imaged onto the focal plane of the occulting mask by OAP2 and a flat-mirror (FM). The occulting mask attenuates the starlight, and has little effect on the light of a planet if present. The "back-end" of the system, from the occulting mask to the back focal plane, supports experimentation with diverse coronagraph configurations and apodizations. OAP3 re-collimates

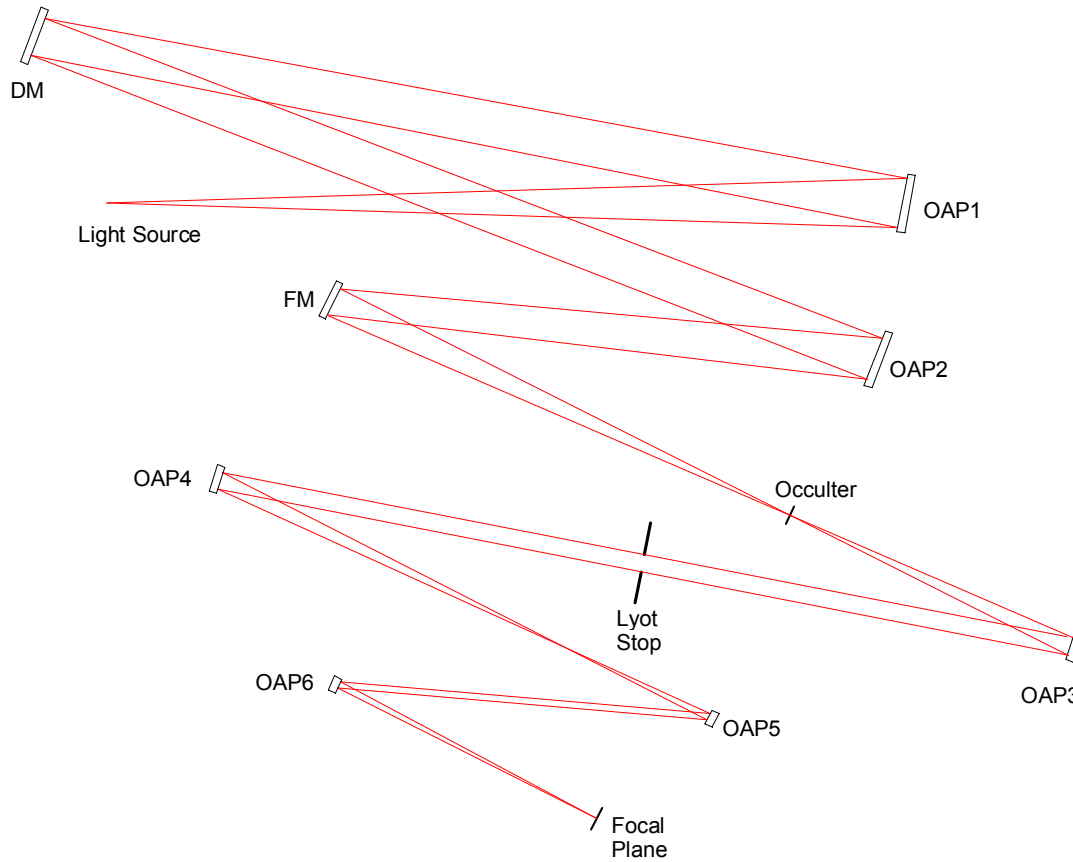*Erkin.Sidick@jpl.nasa.gov; Phone 1 818 393-7585; Fax 1 818 393-3290; www.jpl.nasa.gov

Figure 1. Schematic diagram of the High Contrast Imaging Testbed (HCIT) layout. The light source ("starlight") is a 5μm pinhole illuminated by an optical fiber, and a CCD science camera is located at the back focal plane for detecting the image of the "starlight".

the light passing through the occulter mask and forms a sharp image of the DM pupil at the Lyot plane. A Lyot-stop blocks the ring-likeresidual light diffracted off the occulting mask while letting most of the planet light and aberrated starlight through. After OAP4 forms an image from the remaining stellar and planet lights, it is then magnified (M ≈3) by the OAP5-OAP6 pair for proper sampling on the CCD science camera located at the back focal plane. More information on the HCIT and the DM can be found in Refs. [1-3].

2.2 Optical Components

The DM used on the HCIT has 64x64 actuators arrayed on a 1mm pitch. Its description is similar to the 32x32 actuator DM described in detail in Ref. [1], and will not be repeated here.

Our Lyot-stop is made from a simple blackened piece of sheet metal with a sharp edge. Its opening (Lyot-stop aperture) has an eye-shape defined by two circles that are shifted with respect to each other in the horizontal direction by a distance of ε in units of D. The value of ε needs to be chosen based on the value of the occulting mask width parameter w, and $\varepsilon=0.36$ in this paper.

In the experiment, the phase error at the system exit pupil was flattened by iterative phase estimation and DM adjustments before the data to be shown later were taken. Therefore, in our simulations, we did not include the surface height errors of the six OAP's and the FM. But we included the phase error, the optical density (OD) dispersion and the phase dispersion of the occulter. Details of the occulter used and electric-field conjugation method are described in Ref. [8].

2.3 Definitions of Half Dark-Hole Area and Contrast

For the current optical system with only one DM, we carry out wavefront control (WFC) over a region Ω_c, where Ω_c is either a D-shaped dark-hole region bound by $X \geq X_{\min}$ and $R \leq R_{\max}$, or a rectangular region bound by $[X_{\min}\ X_{\max}\ Y_{\min}\ X_{\max}]$, with $X = x/f$, $Y = y/f$, $R = \sqrt{X^2 + Y^2}$, x and y are the horizontal and the vertical position variables on the corresponding image-plane, and f is the focal length. For the x- and the y-translations of the occulter, we used an Ω_c with $[X_{\min}, R_{\max}] = [3.5\ 12] \lambda/D$. For the opaque spots on the occulter, we used $[X_{\min}, R_{\max}] = [3.5\ 11] \lambda/D$. In the investigation on the effect of dark hole size, we used several sizes of rectangular areas to be described later. We evaluate the performance of the HCIT using either the normalized intensity,

$$I_n(x,y) = I(x,y)/I_0 , \tag{1}$$

or the contrast,

$$C(x,y) = I_n(x,y)[T_0/T(x,y)] = [I(x,y)/I_0][T_0/T(x,y)] , \tag{2}$$

where $I(x,y)$ is the image intensity of the occulted star, and I_0 is the maximum value of the un-occulted star intensity, $T(x,y)$ is the occulter transmittance, and T_0 is the maximum value of the $T(x,y)$. We keep track of the following three contrast quantities in this paper: (i) C_b, the mean contrast inside a "Big" region Ω_b defined by $[X_{\min}, R_{\max}] = [4\ 10] \lambda/D$ for the occulter translations and $[X_{\min}, R_{\max}] = [3.5\ 11] \lambda/D$ for the opaque occulter spots. (ii) C_s, the mean contrast inside a "Small" square region Ω_s defined by $[X_{\min}\ X_{\max}\ Y_{\min}\ X_{\max}] = [4\ 5\ -0.5\ 0.5] \lambda/D$. (iii) C_m, the "Maximum" contrast value inside the small square region Ω_s. Similarly, we also use I_b, I_s and I_m to denote the big-region mean, the small-region mean, and the small-region maximum of the normalized intensity $I_n(x,y)$ ..

3. WAVEFRONT CONTROL RESULTS

The sensitivity study of coronagraph performance on various system errors, light bandwidth, and control and score dark-hole areas is an on-going process. Some results of this study have been reported before [7], and some will be reported in the future. In this paper, we report our results for three areas: Lateral and longitudinal translation of occulter, an opaque spot on the occulter, and different dark hole sizes. Before we present our measured and simulated results on the above topics, we first provide a comparison between the MACOS and the PROPER simulation tools.

3.1 Comparison of PROPER with MACOS

We have used either MACOS or PROPER [6, 9] in many studies of Lyot and other coronagraphs. In this sub-section, we present a brief comparison of the two approaches when applied to a Lyot coronagraph on the HCIT. Figure 2 shows a comparison of the normalized intensity results obtained with the Lyot-stop taken out, and when the occulter is placed in three different longitudinal locations: $T_z = -0.6\,\text{mm}$ (the occulter is moved away from the DM), 0mm, and 0.6mm relative to design or nominal position. The top-row shows the normalized intensity maps obtained with PROPER, and bottom-row are their x-profiles obtained with both PROPER and MACOS. The two simulation tools use different sampling intervals in the image-plane: 0.15λ/D per pixel in PROPER, and 0.34λ/D per pixel in MACOS. As we can see from Figs. 2(d-e), the results of PROPER and MACOS agree to a few percent over a wide range of intensity and out to at least to 30λ/D. We repeated the above simulations by putting back in the Lyot-stop with $T_z = -0.8$, 0, and 0.8mm, respectively. The results are shown in Figs. 3(a-f). Again, the two approaches agree to several percent over several orders of magnitude of intensity. We believe the small discrepancy between the two methods comes from the fact that, although PROPER does full diffraction analysis between all elements, it does so with an unfolded optical system and does not account for diffraction being off axis. Whereas MACOS simulates the full optical system depicted in Fig. 1. Another factor contributing to the small discrepancy is the difference in the sampling sizes. The courser sampling in MACOS results in some differences in the peaks and the valleys of the PSF cross-sections shown in Figs. 2(d-f) and Figs. 3(d-e). We conclude from these simulations that
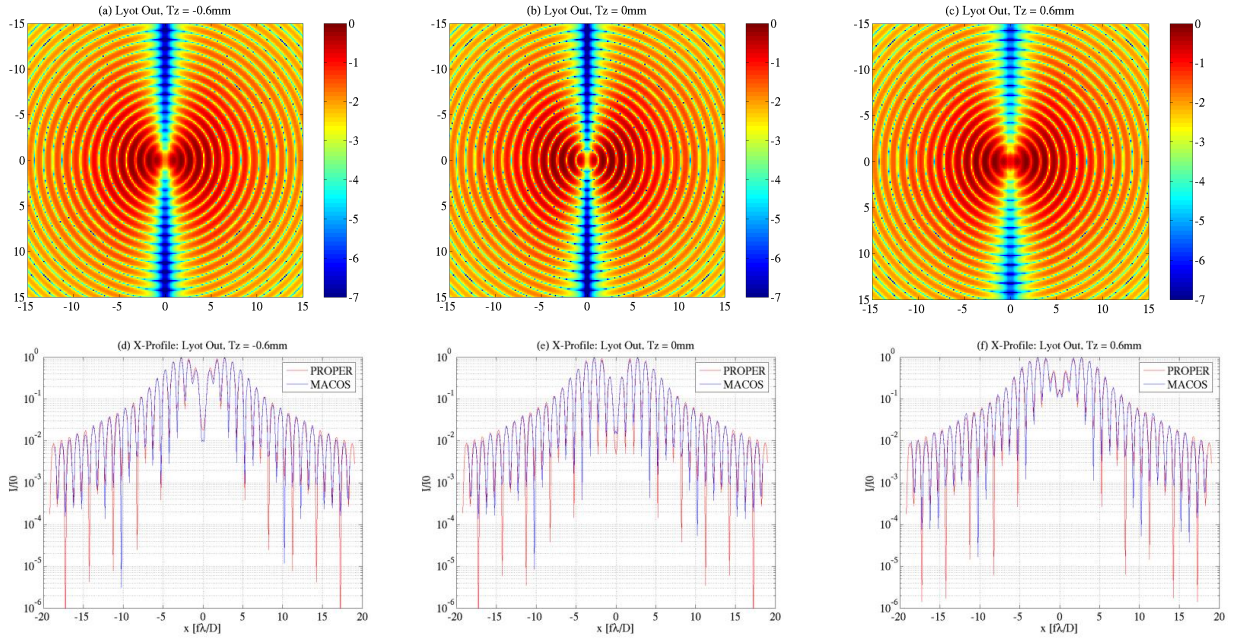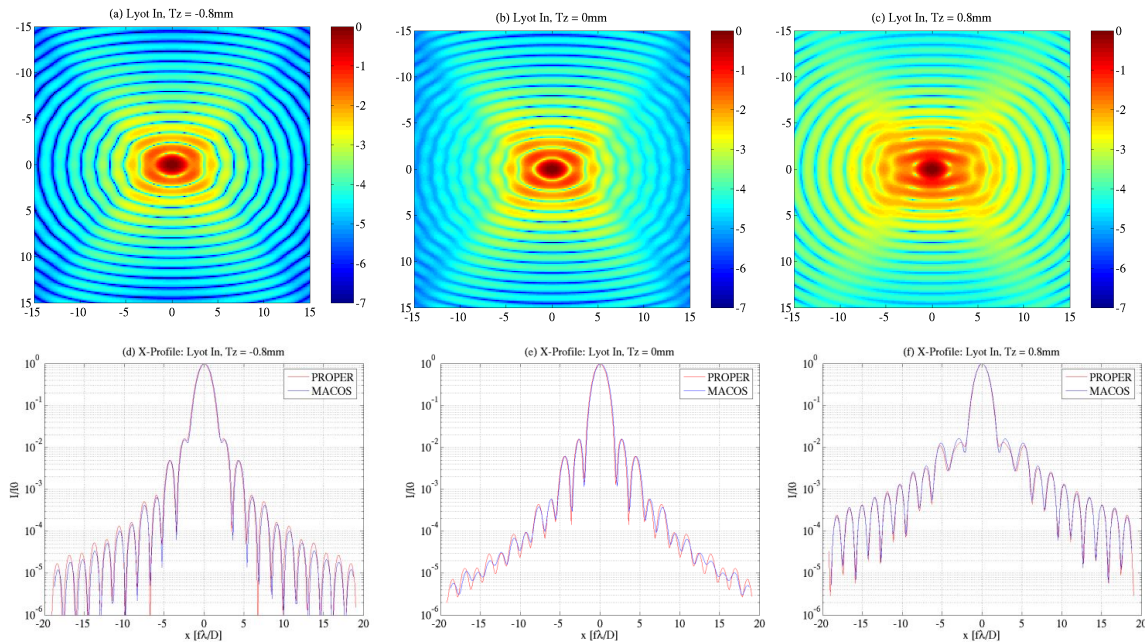
Figure 2. Normalized intensities, $I(x,y)/I_0$, when the Lyot-Stop are taken out. Top-row: $I(x,y)/I_0$ maps obtained using PROPER with the occulter z-translation values of T_z=-0.6mm (occulter is moved away from the DM), 0mm, and 0.6mm (occulter is moved towards the DM), respectively. The units of the x- and the y-axes are λ/D. Bottom-row: The x-cross-section of $I(x,y)/I_0$ maps obtained using PROPER and MACOS with three T_z –values used in the top-row. The sampling is different for PROPER and MACOS.

Figure 3. Normalized intensities, $I(x,y)/I_0$, when the Lyot-Stop are put back in. Top-row: $I(x,y)/I_0$ maps obtained using PROPER with the occulter z-translation values of T_z=-0.8mm (occulter is moved away from the DM), 0mm, and 0.8mm (occulter is moved towards the DM), respectively. The units of the x- and the y-axes are λ/D. Bottom-row: The x-cross-section of $I(x,y)/I_0$ maps obtained using PROPER and MACOS with three T_z –values used in the top-row. The sampling is different for PROPER and MACOS.

PROPER and MACOS models are consistent to a few percent over a wide range of intensity and an area that exceeds the dark holes formed in HCIT.

3.2 Longitudinal and Lateral Translation of occulter

The studies whose results will be reported in the next three sub-sections are part of the work of Exoplanet Exploration Coronagraph Technology Milestone Number 3A: Coronagraph starlight suppression: Model validation [10]. The goal of Milestone 3A is to demonstrate the ability to predict the performance sensitivities of a high-contrast imaging system at levels consistent with exoplanet detection requirements. Milestone 3A data was collected in HCIT between January and March, 2013, beginning with longitudinal and lateral occulter translation tests. We denote the amounts of these two types of translation by T_z and T_x, respectively. The experiment and the corresponding simulations of this part were carried out in the following steps:
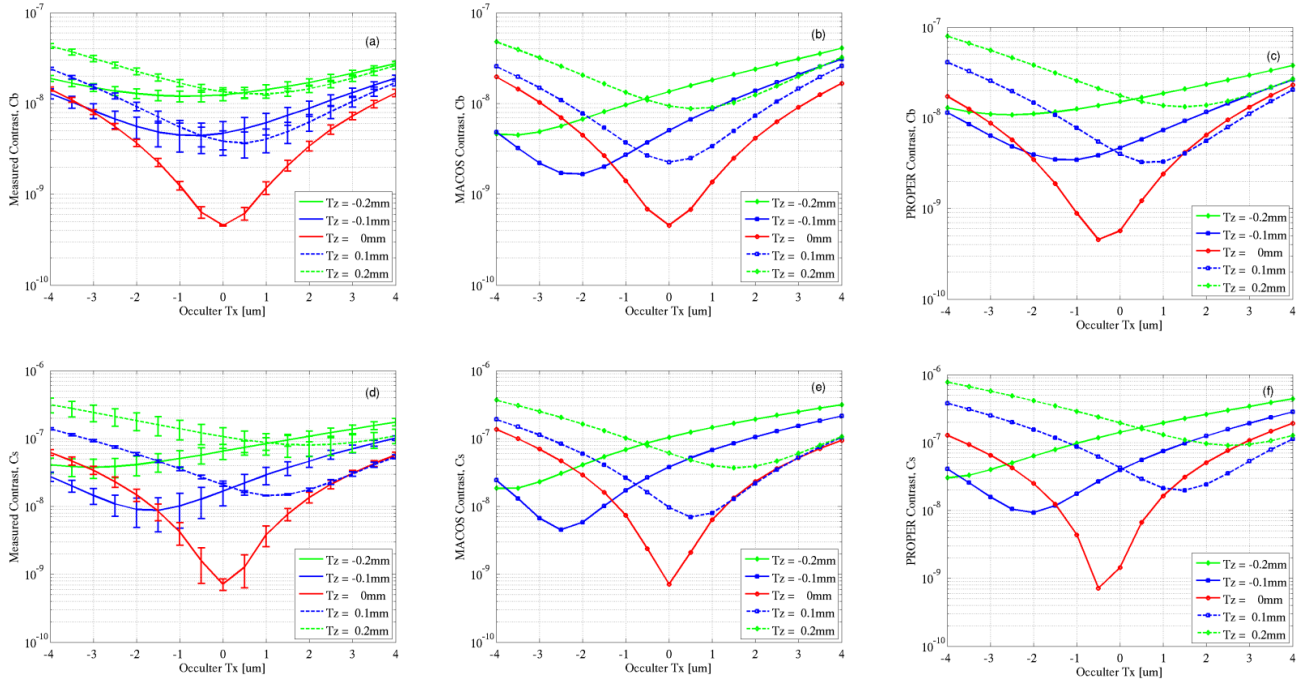
Figure 4. Contrast as a function of occulter lateral translation, T_x, and with longitudinal translation, T_z, as a parameter. The T_x and T_z are defined in the local coordinates of the occulter with T_z parallel to the direction of the chief-ray. (a) Three-day average of the measured C_b. The error bars correspond to the standard deviation (STD) of the three sets data. (b-c) C_b calculated using MACOS and PROPER, respectively. Parts (d-f) are the same as parts (a-c) and show the values of C_s (small box) in place of C_b.

1. Before conducting wavefront control, an occulter T_z-scan was carried out to determine $T_z = T_{z0}$ where the peak intensity at the final focal plane becomes minimum. We found $T_{z0} = 0.8$mm, where positive T_z (or T_{z0}) moves the occulter towards the DM. This shift is caused by the phase transmission profile of the variable thickness nickel on the mask, and is predicted by models to be also ~0.8 microns.

2. Carried-out 2% narrow-band wavefront control with the occulter positioned at this new location, $T_{z0} = 0.8$mm and set to the DM to form a dark-hole. For simulations, we tried both monochromatic and 2% narrow-band beams, and got very similar results. For the translation tests, we present the results obtained with the monochromatic model only.

3. Because the mechanical translation axis was not necessarily aligned to the optical axis, we had to determine a lateral zero point for each axial position. We did this by first setting the DM actuators to the heights obtained in Step 2, removing the Lyot-Stop, then moving the occulter longitudinally to a new position $T_z' = T_z + T_{z0}$ before carrying out an occulter T_x–scan. We then determined the value of $T_x = T_{x0}$ at which the intensities of the first

Airy-ring side-lobes on either side of the center of the image were equal. This step was repeated for five values of T_z, that is, T_z = -0.2, -0.1, 0, 0.1 and 0.2mm.

4. We then reinstalled the Lyot Stop and scanned te occulter in x for each T_z-value, that is, the occulter was translated laterally by $T_x' = T_x + T_{x0}$, and we recorded the values of C_b and C_s. We repeated this step for all five values of T_z.

The same procedure was followed in the simulations. We did not keep track of the T_{x0}-values obtained in the experiment, and they may be different from what we got in the simulations.

In Figs. 4(a-f), we plot C_b and C_s as a function of T_x with T_z as a parameter. As expected, simulation yields contrast values better than the measured ones because the simulations do not account for any experimental floor (e.g. incoherent scattered light). Therefore, for the purpose of comparison, we set as the minimum for all model curves the contrast at T_x = T_z = 0 and added this value to all the simulated data.

Figures 5(a-d) show the percentage errors between the measured and the calculated C_b and C_s values, where the error is defined as (Calculated – Measured) / Calculated (including the contrast floor). The predicted C_b and C_s curves exhibit similar behaviors as those of the measured ones, but the valleys of the $T_z \neq 0$ curves take place at T_x -values slightly different than those of the measured ones. Overall, the results of PROPER agree with the measurement better than those of MACOS. Also, most predicted data points differ from the measurements with a factor of 2. The exact reasons that cause the difference observed between the prediction and the measurement for these tests is still under investigation.
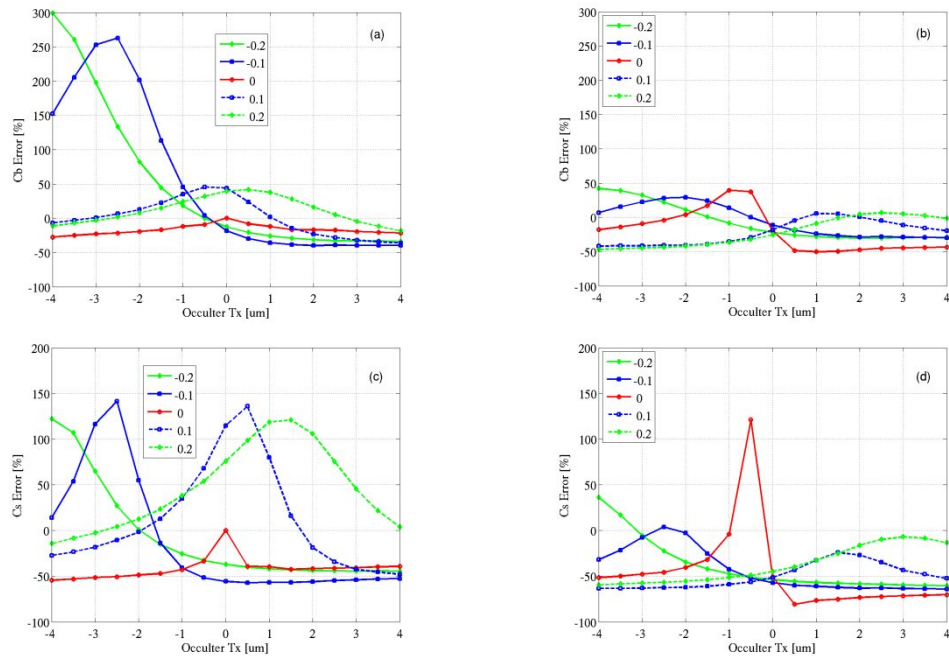

Figure 5. Percentage contrast error, defined as 100×(Calculated – Measured) / Calculated, as a function of occulter lateral translation, T_x, with longitudinal translation, T_z, as a parameter. (a) C_b error: MACOS versus measured. (b) C_b error: PROPER versus measured. (c) C_s error: MACOS versus measured. (d) C_s error: PROPER versus measured. Shown on the figure legends are T_z-values in mm.

The dependence of contrast leakage in the dark hole is approximately quadratic in the lateral translation parameter. If we fit a second-order polynomial to the curves in Figs. 4(a-c) in the form of

$$C_b = a(T_z)[T_x - x_0(T_z)]^2 + b(T_z), \qquad (1)$$

we obtain the fitting parameter values listed in Table 1. The values of $a(T_z)$, $x_0(T_z)$ and $b(T_z)$ are plotted as a function of T_z in Figs. 6(a-c) respectively. These data are useful in predicting the sensitivity of a Lyot coronagraph's narrow-band contrast to the occulter position.
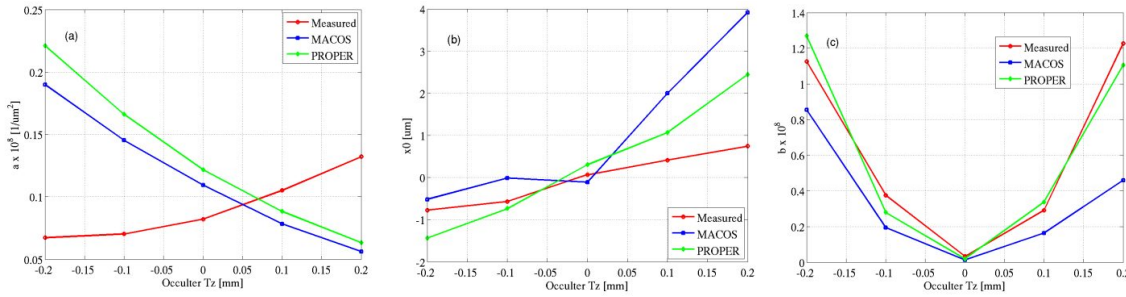

Figure 6. Fitting parameters defined in Eqn. (1) and listed in Table 1.

Table 1. Values of the fitting parameters defined in Eqn. (1).

Tz [mm]	Measured			MACOS			PROPER		
	$ax10^8$ [$1/um^2$]	x_0 [um]	$bx10^8$	$ax10^8$ [$1/um^2$]	x_0 [um]	$bx10^8$	$ax10^8$ [$1/um^2$]	x_0 [um]	$bx10^8$
-0.2	0.0672	-0.7733	1.1261	0.1900	-0.5199	0.8539	0.2210	-1.4394	1.2688
-0.1	0.0702	-0.5677	0.3757	0.1453	-0.0119	0.1939	0.1661	-0.7386	0.2789
0	0.0821	0.0641	0.0328	0.1094	-0.1123	0.0133	0.1217	0.3032	0.0187
0.1	0.1052	0.4132	0.2915	0.0784	1.9982	0.1638	0.0882	1.0678	0.3374
0.2	0.1322	0.7453	1.2267	0.0561	3.9111	0.4600	0.0634	2.4388	1.1043

3.3 Opaque Spot on the occulter Surface

The next topic of our report is the effect of an opaque spot on 10% broadband contrast. In order to evaluate the effect of small extraneous inclusions such as a dust particle or a coating defect on the performance of the occulter, we added a few marks at chosen locations on the mask. The occulting mask was originally fabricated by a vacuum deposition process for the TDEM Milestone 2 demonstration [11]. This is a linear mask, i.e., the mask profile is along one dimension with the other dimension ideally constant. The mask profile is described elsewhere [8] and is made with varying thickness of a nickel layer to obtain the required transmission profile. We added square shaped marks of platinum on this mask at chosen locations as shown in Fig. 7. Figure 8(a) shows one of the marks under SEM. The rectangular shape under SEM is due to the 52 deg tilted observation of square mark. The debris field seen was present on the mask before the marks were written by focused ion beam (FIB) technique. A dual beam SEM/FIB system (NOVA 600-D24 from FEI Company) at Caltech was employed for writing these Pt marks of required thickness and area. Mark C3 shown on Fig. 8(b) is about 170nm tall with optical density ~8. Similarly, the mark C4 in Fig. 8(c) is about 150nm
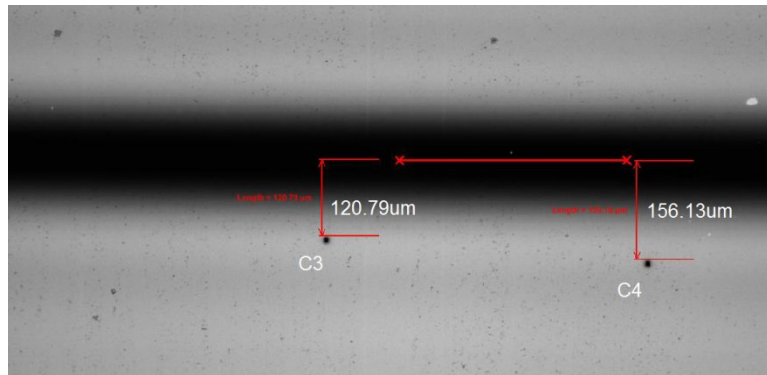

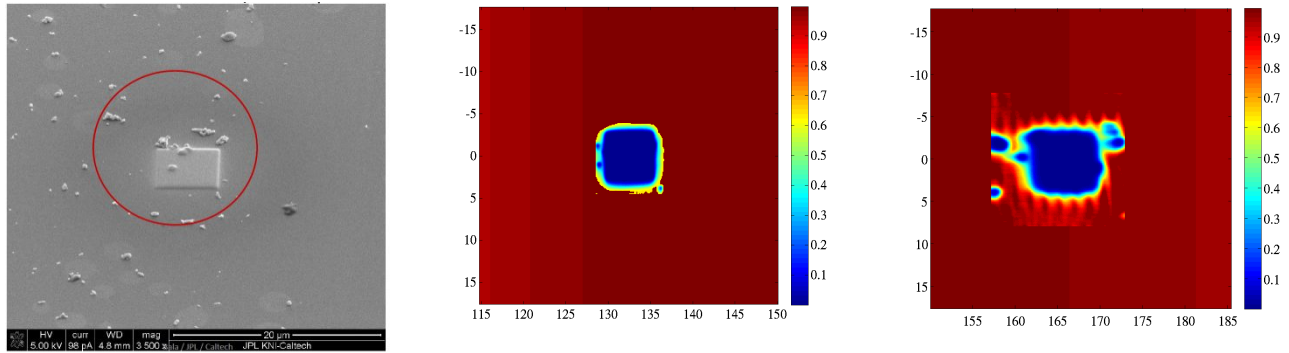Figure 7. Optical microscope image of the C3- and the C4-spot areas on the occulting mask.

Figure 8. (a) SEM image of the C3-spot area on the occulting mask. (b) Measured C3-spot transmission map superimposed into the occulter transmission model. The pixel size is 0.0984μm. (c) Measured C4-spot transmission map superimposed into the occulter transmission model. The pixel size is 0.1228μm. These two occulter transmission maps are re-sampled to a pixel size of 8.492μm in MACOS model. In parts (b) and (c), the horizontal and the vertical axis labels are positions in μm.
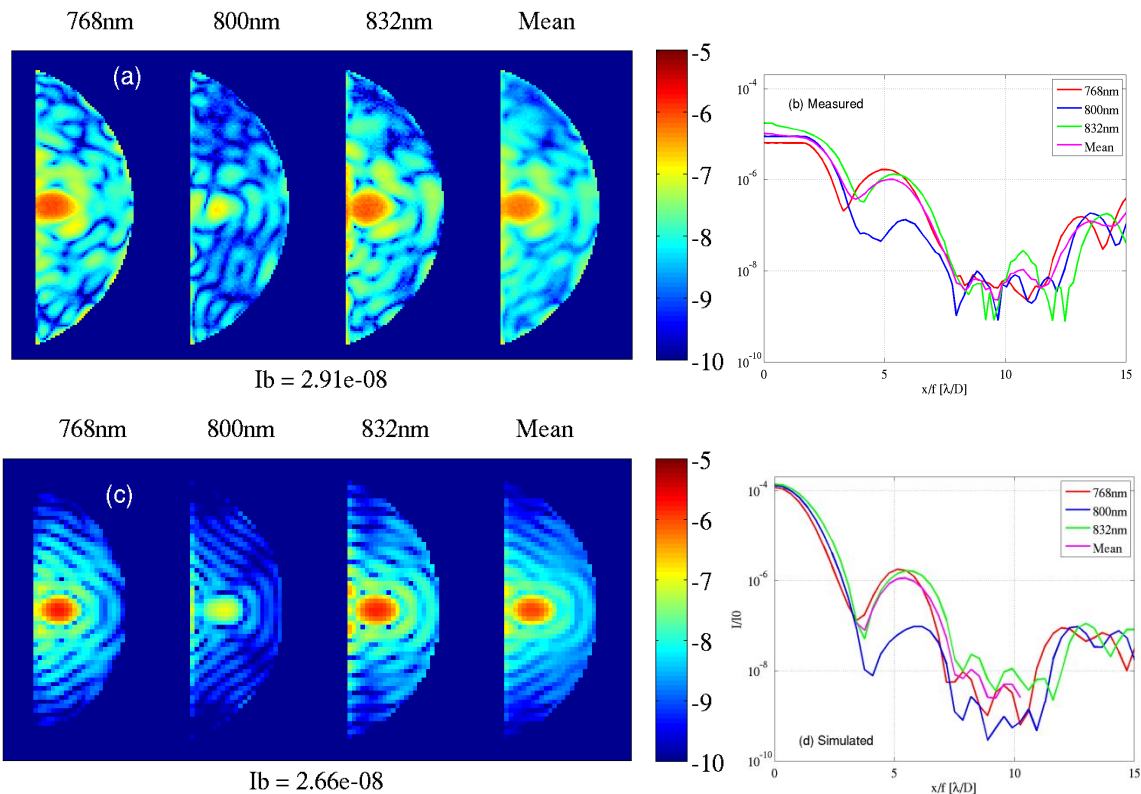
Figure 9. Log-scale normalized intensity, $I_n(x,y)$, maps obtained with the C3-spot occulter area. The top row shows the measured data, and the bottom row shows the corresponding simulated results. The first three maps in parts (a) and (c) correspond to three different 2%-filters, and the fourth parts are their mean values or 8%-broadband $I_n(x,y)$ maps. Parts (b) and (d) show the x-cross sections of the four corresponding $I_n(x,y)$ maps. The I_b –values listed in the bottoms of parts (a) and (c) are the broadband normalized intensities.

tall with optical density ~6. These marks are about 6um squares as measured by AFM and SEM. Two dimensional optical transmission profiles of these marks were calculated based on 2-D maps of the marks from AFM and using known optical constants of Pt. Figure 8(b) shows the part of the occulter transmission coefficient (amplitude) map on which the fine-sampled C3-spot is superimposed, and Fig. 8(c) shows the same for C4-spot. After an opaque spot is added to the occulter transmission amplitude in this way, the occulter map is down-sampled to its normal MACOS pixel-size of 8.492μm, and wavefront control simulation is carried out with this modified occulting mask.
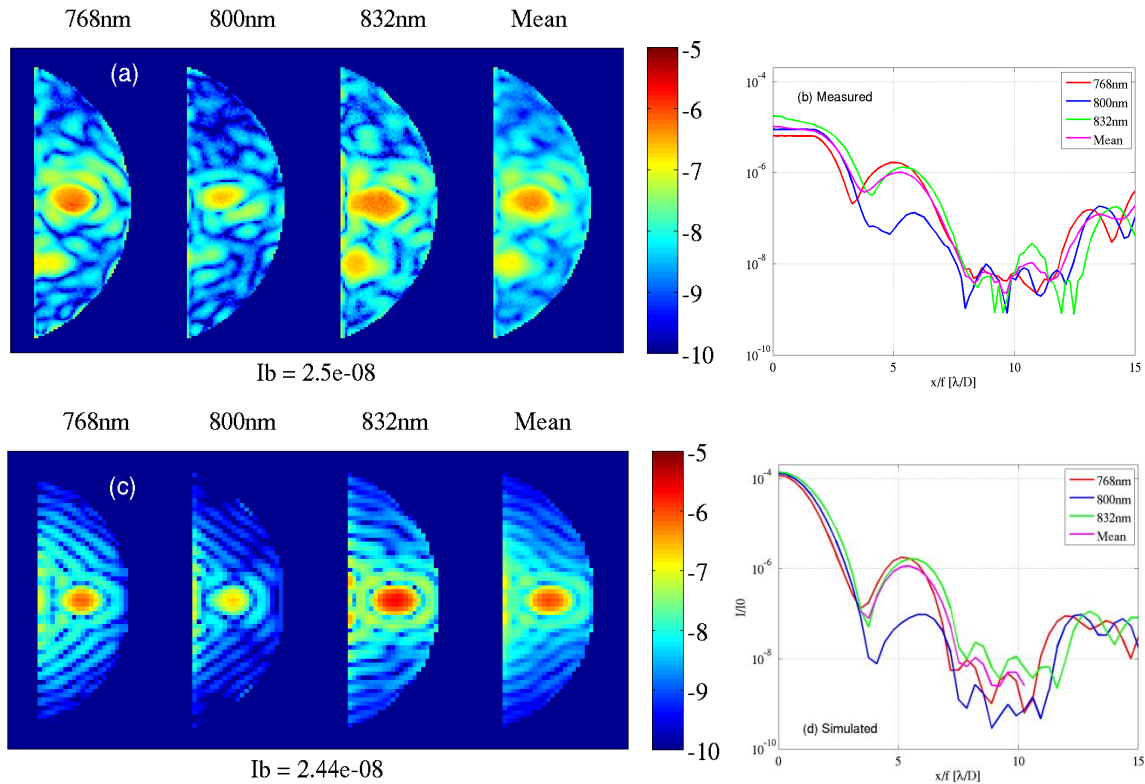
Figure 10. Same as Fig. (9) for the C4-spot area of the occulter.

Table 2. Measured and predicted 2% and 8% (Mean) normalized intensities, or I_b-values, and the measured-to-predicted ratios obtained from the C3- and C4-post areas of the occulter. The simulated results were obtained assuming monochromatic beam.

Box Size	Spot Name	Contrast Type	768nm	800nm	832nm	Mean
Dark-Hole Area	C3-Spot	Measured, x10^{-8}	4.17	0.61	3.96	2.91
		Simulated, x10^{-8}	3.55	0.27	4.17	2.66
		Ratio: Meas/Simul	1.17	2.25	0.95	1.09
	C4-Spot	Measured, x10^{-8}	2.81	0.92	3.78	2.50
		Simulated, x10^{-8}	1.57	0.48	5.28	2.44
		Ratio: Meas/Simul	1.79	1.91	0.72	1.03
2λ/D-Wide Spot Area	C3-Spot	Measured, x10^{-6}	1.49	0.08	1.06	0.88
		Simulated, x10^{-6}	0.86	0.05	0.89	0.60
		Ratio: Meas/Simul	1.73	1.67	1.19	1.46
	C4-Spot	Measured, x10^{-6}	0.91	0.16	0.93	0.67
		Simulated, x10^{-6}	0.34	0.09	1.10	0.51
		Ratio: Meas/Simul	2.69	1.82	0.85	1.31

Figures 9(a-d) compare the predicted maps of the normalized intensity with the measured ones for the C3 occulter spot, and Figs. 10(a-d) show the same results for C4 occulter spot. Among them, part (a) shows the measured individual and the averaged intensity maps, and part (b) shows their x-profiles at $Y = 0$. Parts (c-d) show the corresponding simulated results. The measurements and the predictions come close in this case, especially the broadband I_b−values listed in the bottom of each intensity map plot. The residual Airy-rings are visible in the predicted maps, but they were washed out in the measured ones. One reason causing such a difference is that some residual exit-pupil phase error still exists in the experiment, but it was not included in the simulation. The measured normalized intensities in Fig. 10(a) display an evidence of the second occulting defect near C4-spot. That spot was not intentional and was not included in our

simulations In Table 2, we listed the I_b–values of the measured and the simulated normalized intensities at three individual wavelengths as well as their average values. As we can see from this table, the agreement between the measurement and the prediction is typically between a factor of 0.7 and 2.

3.4 Different Dark-Hole Sizes

The last topic that we are going to cover is the dependency of the broadband control efficiency on the dark-hole size. In theory, a 48x48 actuators DM can control a region up to $R_{max} = 24\lambda/D$ when the exit-pupil covers the whole diameter of the DM. In order to understand the dependency of broadband wavefront control efficiency on the dark-hole region, we carried out control experiments and simulations for three dark-hole sizes with $[X_{min}, R_{max}] = [3.5\ 15]$ and $[3.5\ 20]\lambda/D$ in the first two cases and with $[X_{min}, X_{max}, Y_{min}, Y_{max}] = [3.5, 24, -10, 10]\lambda/D$ in the last one. The experiments were carried out in the 768, 800, and 832 nm filters, with the resulting images combined to form a composite broad-band image. The I_b and I_s results of all four cases are summarized in Table 3, and the measured and the simulated $I_n(x,y)$ maps of the three cases with increased dark-hole sizes are shown in Fig. 11. The data includes several defects that correspond to particulate contamination of the mask, especially near the lower right side of the dark hole. The data show that indeed we could control the dark hole out to the theoretical limit of the DM with a factor of 3 loss of contrast (vs. a predicted factor of two loss from the simulation) at the inner working angle (the I_s box). The predicted contrast within the I_s box was within a factor of 2 of the measured contrast for the 15 λ/D and 20 λ/D cases, while it was off by a factor of 2.3 for the 24 λ/D case. We also observed that the average contrast in the full dark hole *improved* as the dark hole grew larger. We believe this is because the Airy rings are less pronounced at larger radii, so the DM does not have to work as hard to achieve high contrast at these angles. However, the simulation did not bear this out and predicted a slight increase (from 4.9e-11 to 6.9e-11) in overall contrast. In the above simulations, we included the phase-error estimated at the exit-pupil of the current optical system. When that phase-error was not included, our simulation yielded $I_b = 4.75\times10^{-11}$, 4.41×10^{-11} and 5.57×10^{-11} for the three different dark-hole sizes, respectively. That is, the exit-pupil phase-error did not introduce any meaningful change to the simulated final big-box mean contrast values.

Table 3. Broadband I_b-values corresponding to four different dark-hole sizes. The experiments were carried out with three 2%-bandpass filters centered at 768, 800 and 832nm, but those three beams were modeled as monochromatic beams in simulations. The dark-hole size parameters are $[X_{min}, R_{max}]$ in the first three cases, and $[X_{min}, X_{max}]$ in the last one.

Dark-Hole Size		3.5 to 15λ/D	3.5 to 20λ/D	3.5 to 24λ/D
I_b	Measured	1.32×10^{-9}	1.02×10^{-9}	9.91×10^{-10}
	Simulated	4.91×10^{-11}	5.59×10^{-11}	6.90×10^{-11}
I_s	Measured	1.61×10^{-9}	2.37×10^{-9}	4.36×10^{-9}
	Simulated	9.93×10^{-10}	1.71×10^{-9}	1.87×10^{-9}

4. CONCLUSION

We have shown that our models are predicting contrast sensitivity to within a factor of 2 for contrast levels in the 1e-9 to 1e-8 region, for mask motion, mask defects, and contrast at the IWA for different dark hole sizes. We have formed dark holes out to the theoretical limit of our 48x48 illuminated deformable mirrors.

Our work suggests that in predicting coronagraph contrast performance, e.g. sensitivity-based predictions such as Ref. 12, a factor of 2 should be carried for the model uncertainty factor. In future work we will report on model and data agreement for different wavelength control bandwidths, non-functional DM actuators, and the ability to discriminate instrument-induced speckles from other background sources. These experimental validations of key coronagraph sensitivity factors will additionally contribute to the confidence in performance prediction models for future flight systems.
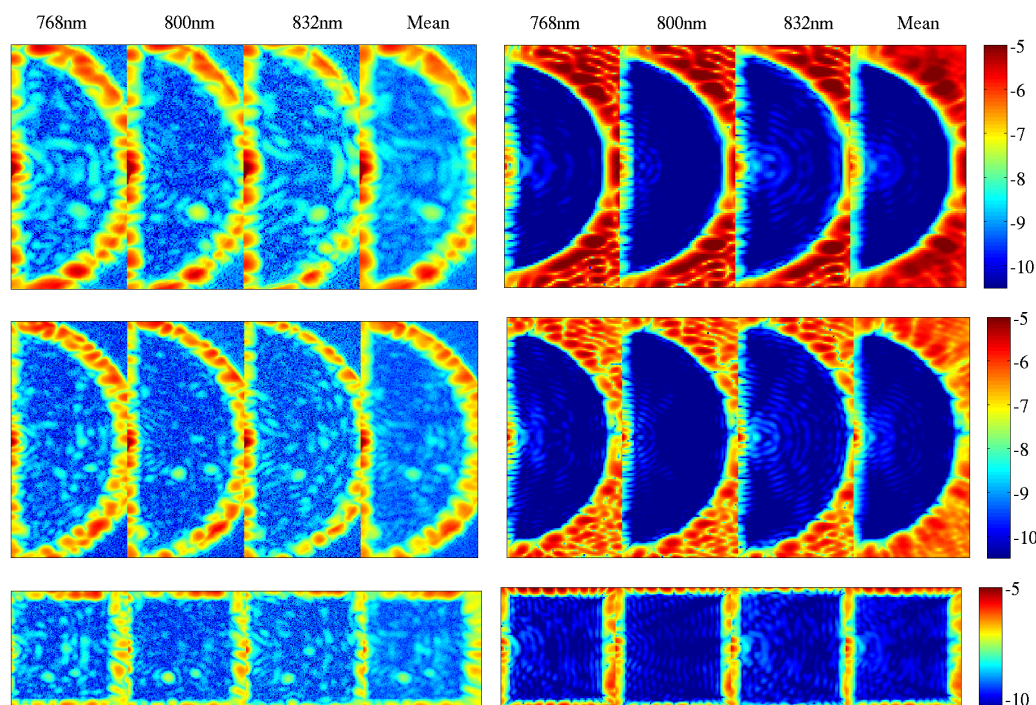
Figure 11. Left-column: Measured $I_n(x,y)$ maps at three 2%-bands and their mean corresponding to two D-shaped dark-hole areas with $[X_{min}, R_{max}] = [3.5\ 15]$, and $[3.5\ 20]\lambda/D$, and one rectangular area with $[X_{min}, X_{max}, Y_{min}, Y_{max}] = [3.5, 24, -10, 10]\lambda/D$. Right-column: The corresponding simulated $I_n(x,y)$ maps obtained with monochromatic beams. The corresponding I_b and I_s values are listed in Table 3.

REFERENCES

[1] John T. Trauger, Chris Burrows, Brian Gordon, Joseph J. Green, Andrew E. Lowman, Dwight Moody, Albert F. Niessner, Fang Shi, and Daniel Wilson, "Coronagraph contrast demonstrations with the high-contrast imaging testbed," *Proc. SPIE*, **5487**, 1330 (2004).

[2] Andrew E. Lowman, John T. Trauger, Brian Gordon, Joseph J. Green, Dwight Moody, Albert F. Niessner, and Fang Shi, "High-contrast imaging testbed for the Terrestrial Planet Finder coronagraph," *Proc. SPIE*, **5487**, 1246 (2004).

[3] Erkin Sidick, Fang Shi, Scott Basinger, Dwight Moody, Andrew E. Lowman, Andreas C. Kuhnert, and John T. Trauger, "Performance of TPF's High-Contrast Imaging Testbed: Modeling and simulations, " *Proc. SPIE*, **6265**, 62653L (2006).

[4] Amir Give'on *et al*, "Broadband wavefront correction algorithm for high-contrast imaging system," *Proc. SPIE*, **6691**, 66910A (2007).

[5] *Modeling and Analysis for Controlled Optical Systems User's Manual*, Jet Propulsion Laboratory, California Institute of Technology, Pasadena, CA.

[6] John E. Krist, "PROPER: an optical propagation library for IDL," *Proc. SPIE*, **6675**, 66750P-1 (2007).

[7] Erkin Sidick, Stuart Shaklan, Amir Give'on, and Brian Kern, " Studies of the effects of optical system errors on the HCIT contrast performance," *Proc. SPIE*, **8151**, 8151-06 (2011).

[8] Erkin Sidick, Stuart Shaklan, Kunjithapatham Balasubramanian, "HCIT Broadband Contrast Performance Sensitivity Studies", *Proc. SPIE*, 8520, 85200M-1 (2012).

[9] John E. Krist, Ruslan Belikov, Laurent Pueyo, Dimitri P. Mawet, Dwight Moody, John T. Trauger, Stuart B. Shaklan, "Assessing the performance limits of internal coronagraphs through end-to-end modeling: a NASA TDEM study," *Proc. SPIE*, **8151**, 81510E-1 (2011).

[10] "Exoplanet Exploration Coronagraph Technology: Technology Milestone #3 White Paper," Stuart Shaklan editor, 5 Jan. 2009,
http://exep.jpl.nasa.gov/files/exep/ExEPC%20Milestone%203%20white%20paper%20signed.pdf.

[11] "Exoplanet Exploration Coronagraph Technology: Technology Milestone #2 Report," Brian Kern, Andreas Kuhnert and John Trauger, editors, 8 Aug. 2008, http://exep.jpl.nasa.gov/TPF-C/HCIT-Milestone2Signed-2008-08-08.pdf.

[12] S. Shaklan, L. Marchen, J. Krist, and M. Rud, "Stability error budget for an aggressive coronagraph on a 3.8 m Telescope," *Proc. SPIE*, **8151**, 815109-1 (2011).

High-Contrast Coronagraph Performance in the Presence of Focal Plane Mask Defects

*Erkin Sidick, Stuart Shaklan, Kunjithapatham Balasubramanian, and Eric Cady

Jet Propulsion Laboratory, California Institute of Technology, 4800 Oak Grove Drive, Pasadena, CA 91109, USA

ABSTRACT

We have carried out a study of the performance of high-contrast coronagraphs in the presence of mask defects. We have considered the effects of opaque and dielectric particles of various dimensions, as well as systematic mask fabrication errors and the limitations of material properties in creating dark holes. We employ sequential deformable mirrors to compensate for phase and amplitude errors, and show the limitations of this approach in the presence of coronagraph image-mask defects.

Key words: Coronagraphy, adaptive optics, high-contrast imaging, space telescopes, exoplanets

1. INTRODUCTION

This paper presents both simulated and measured results on the sensitivity of broadband contrast to the defects of an occulting mask in a Lyot coronagraph implemented on the High-Contrast Imaging Testbed (HCIT) at NASA's Jet Propulsion Laboratory (JPL). This testbed is the Exoplanet Exploration Program's primary platform for experimentation [1-3]. It is used to provide laboratory validation of key technologies as well as demonstration of a flight-traceable approach to implementation. It employs a 48x48 actuator deformable-mirror (DM) and a broadband wavefront correction algorithm called Electric Field Conjugation (EFC) to obtain the required 10^{-10} contrast [4]. In an effort to be able to predict the measured contrast performance of the coronagraph, we have investigated the following defects of the occulting mask: randomly distributed opaque spots on the occulter, occulters with asymmetric optical-density (OD) profiles, and occulter profile with reduced OD peak. We have also carried out simulations by using the measured microscope image of an occulter's transmittance while keeping its phase the same as that of the model, as well as adding some phase values to the measured occulter spots. The laboratory testing was carried out with either a 2%-narrowband or a 10%-broadband light. The simulations were conducted with MACOS (Modeling and Analysis for Controlled Optical Systems) [5], and their results were compared with measurements. We achieved good agreement between the measurement and the simulation in some of the cases investigated. In three earlier papers we reported on the broadband contrast sensitivity of the number and position of dead actuators, beam walk due to translation of a flat optic in the beam, as well as on the effects of occulter displacement, an opaque spot on the occulter, and the controlled dark-hole dimensions[6-8].

2. DEFINITION OF DARK-HOLE AREA AND MEASURED CONTRAST MAPS

The detailed background information of the Lyot coronagraph used in this study is given in Ref. [7] and is not repeated here. For the current optical system with only one DM, we carry out wavefront control (WFC) over a region Ω_b, where Ω_b is a D-shaped dark-hole region bound by $X \geq X_{min}$ and $R \leq R_{max}$, with $X = x/f$, $Y = y/f$, $R = \sqrt{X^2 + Y^2}$, x and y are the horizontal and the vertical position variables on the corresponding image-plane, and f is the focal length. In this paper we used $[X_{min}, R_{max}] = [3.5\ 11]\lambda/D$ for Ω_b. We evaluate the performance of the HCIT using the normalized intensity,

$$I_n(x,y) = I(x,y)/I_0, \tag{1}$$

*Erkin.Sidick@jpl.nasa.gov; Phone 1 818 393-7585; Fax 1 818 393-3290; www.jpl.nasa.gov

where $I(x, y)$ is the image intensity of the occulted star, and I_0 is the maximum value of the un-occulted star intensity. We keep track of I_b, the mean value of $I_n(x, y)$ inside a "Big" region Ω_b defined above.

3. MEASURED CONTRAST RESULTS

The main goal of this paper is to find an explanation for the measured normalized intensity floor observed in an HCIT experiment carried out in the spring of 2013. The measured data, which is the total residual light in the dark hole, is shown in Fig. 1(a) while the estimated coherent parts of the intensity are shown in Fig. 1(b). Each of these plots shows $I_n(x, y)$ maps measured using 5 different bandpass filters each with a passband of 2%, and their mean normalized intensity value, as indicated in the figure. The rightmost mean intensity map corresponds to the 10%-broadband contrast. The top-row is the intensity map measured directly with the science camera first then normalized by the unocculted intensity peak when the 5 bands are equally weighted. The bottom-row shows the estimated coherent part of the intensity; this is the part that responds to multiple probe intensity measurements [4] created by setting the DM to 4 preset phases. The top-row, which is the total measured signal, corresponds to the combination of the coherent and the incoherent light, and the bottom one to the estimate of the coherent light only. In the next section, we compare our simulated $I_n(x, y)$ maps with those shown in Fig. 1(b).

(a) Coherent + Incoherent: Ib = 1.4e-09

(b) Coherent Only: Ib = 7.47e-10
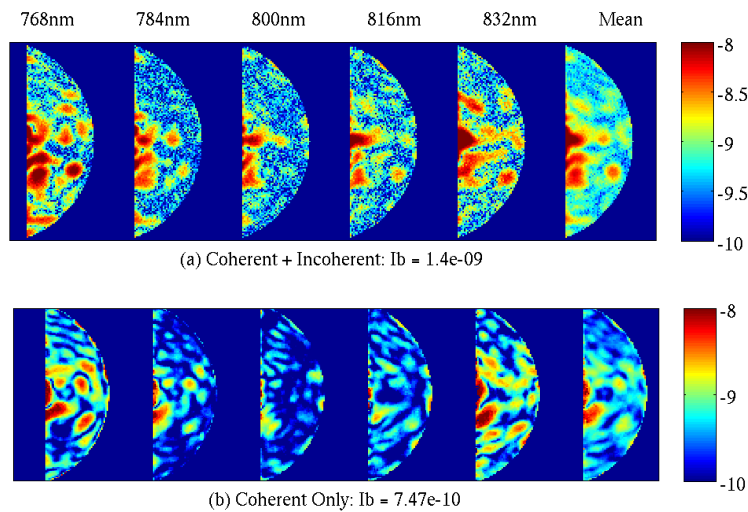
Figure 1. Measured $I_n(x, y)$ maps at 5 individual wavelengths listed at the figure title and their mean. The mean $I_n(x, y)$ corresponds to a 10%-broadband contrast map. (a) Coherent plus incoherent parts. (b) Coherent part only.

4. SIMULATED RESULTS

In this section, we present the results of simulated contrast maps corresponding to a nominal case as well as the several cases of occulter defects, and compare them with the measured intensity maps in Fig. 1(b).

The HCIT uses a modified one-dimensional band-limited occulter whose OD profile at wavelength $\lambda = 800$nm is truncated and smoothed by convolution with a Gaussian function. This smoothed pattern is described in detail in Refs. [9-10]. Specifically, the sinc^2 intensity transmission profile is $T_{\text{sinc}}(x) = \{1 - [\sin(\pi x/w)/(\pi x/w)]^2\}^2$, $\text{OD}_{\text{sinc}}(x) = -\log_{10} T_{\text{sinc}}(x)$, with $w = 142$μm. The truncation and smoothing gives $\text{OD}_{\text{rel}}(x) = \min[\text{OD}_{\text{sinc}}(x), 8] \otimes G(x)$ with $G(x) = (2\pi\sigma^2)^{-1/2} \exp[-x^2/(2\sigma^2)]$, where $\sigma = 9$μm. For practical reasons, the maximum transmission is often less than unity, so the final transmission is $T(x) = T_0 \, 10^{-\text{OD}_{\text{rel}}(x)}$, for some maximum transmission T_0. The two OD profiles, OD_{sinc} and OD_{rel}, are shown graphically in Fig. 2(a). The spatially-varying transmission profile is optically realized by spatially varying the thicknesses of Ni layers deposited on a fused quartz substrate. Because Ni has a large index of refraction ($n \sim 2.5$ at 800nm), regions of the occulter with higher OD (lower transmission, thicker Ni) also have a greater optical path length in transmission than low OD regions. The spatially-varying transmitted E-field is therefore complex-valued. In addition to the spatial variations in OD and phase, the OD and phase also vary with wavelength. Ni was chosen for this application because its OD and phase are less dispersive than other practical materials, as described in Ref. [11]. We

include the dispersion of both occulter OD and phase in our simulations. The profile of the occulter phase at λ=800nm, ϕ(800) is also shown in Fig. 2(a) in radians. Figure 2(b) shows the OD dispersion at five wavelength values relative to that at λ=800nm. The occulter phase dispersion is weaker than the OD dispersion, and the ϕ(λ) - ϕ(800) has the largest value of -0.012 radians at the center of occulter and at λ = 768nm. For this occulter, $T(x) = 0.5$ at $x/f = 3.3\lambda/D$, where $D = 48mm$ is the diameter of the system clear aperture and f is the focal length. The front end F-number (F/#) of this optical system is 31.25.
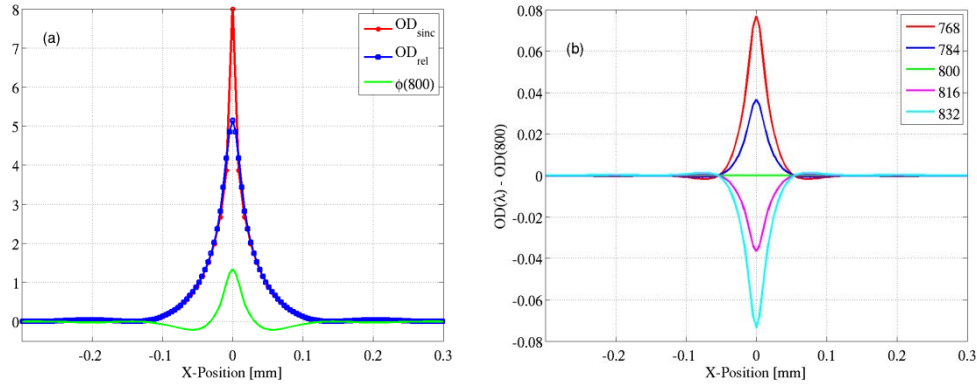
Figure 2. (a) The x-profiles of occulter Optical Densities, OD$_{sinc}$ and OD$_{rel}$, as well as transmitted occulter phase at λ = 800nm, ϕ(800), where the latter is given in radians. (b) Occulter OD dispersion, where the figure legend shows five wavelength values in nm. These parameters correspond to a linear-sinc^2 occulting mask consisting of Ni deposited on a fused quartz substrate. The OD$_{rel}$ corresponds to the OD of the occulter used on the testbed.

4.1 Nominal Case

As a base-line, we carried out a set of broadband wavefront-control (WFC) simulations using the nominal, modeled transmission coefficient and phase-delay of the occulter. In the experiment, the phase error at the system exit pupil was flattened by iterative phase estimation and DM adjustments before the dark-hole was generated. Therefore, in our simulations, we did not include the surface height errors of the various optics. Thus, the only error affecting the contrast of the current system is the parasitic phase-delay of the occulting mask. This phase was not accounted for in the mask design, though later generations of masks do take this into account [9]. Figures 3(a) and 3(b) are the 10%-broadband (760-840 nm) $I_n(x,y)$ maps before and after control, respectively. They are the full-view of the normalized PSFs
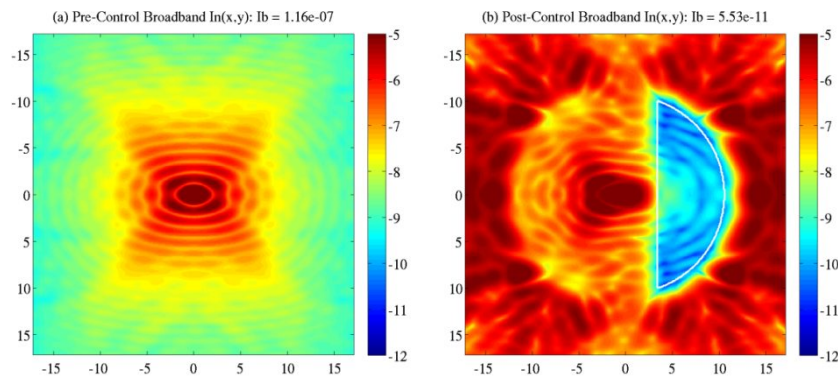

Figure 3. Normalized intensities, $I_n(x,y)$, of the nominal case. (a) Before control, and (b) after control. The units of the x- and the y-axes are λ/D.

inside a 30 x 30 λ/D square area. The post-control $I_n(x,y)$ maps are shown in Figs. 4(a) and 4(b) in the same form as the measured data in Figs. 1(a-b), where the only difference between the top and the bottom rows is the color-stretch.

The fine features of the $I_n(x,y)$ maps in Figs. 4 are quite different from that of the Fig. 1(b) , and the simulated broadband contrast ($I_b = 5.53e^{-11}$) is more than an order of magnitude better than the measured data ($I_b = 7.47e^{-10}$). In spite of the residual occulter phase, the EFC algorithm was able to converge to an intensity level well below the minimum level experienced in the laboratory. The efficiency of the broadband WFC process is shown in Fig. 5(a), where I_b is shown as a function of control iteration. The final actuator commands yielding the present post-control results are shown in Fig. 5(b). The small discontinuity in the I_b versus control-iteration curve took place when we changed the actuator regularization factor from 0.1 to 1.0 after 10 control iterations.
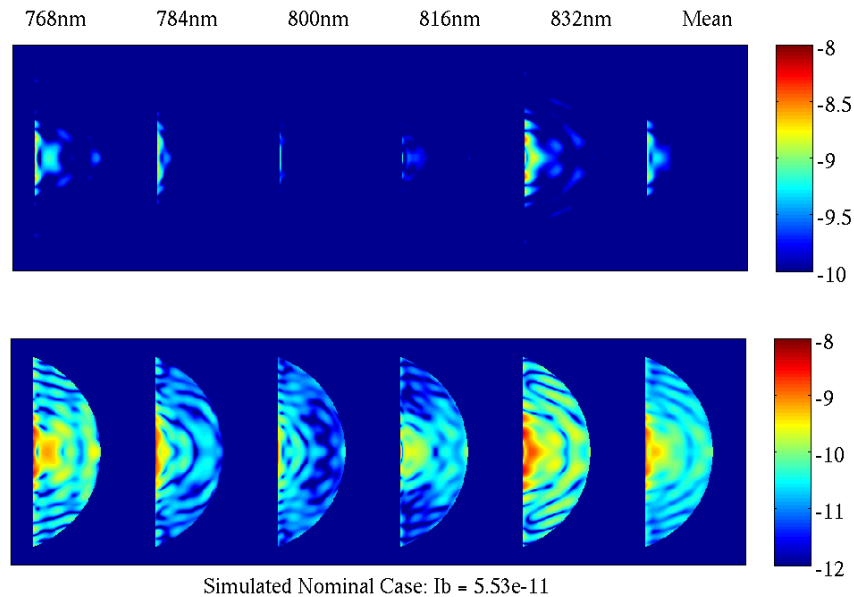
Figure 4. Post-control normalized intensities, $I_n(x,y)$, of the nominal case. The top- and the bottom-rows show the same data plotted with different color-stretches.
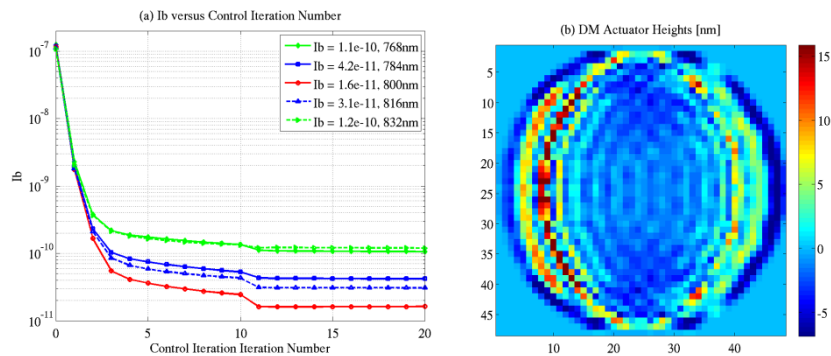
Figure 5. (a) Normalized mean intensity, I_b, versus control iteration number. The five curves correspond to 5 different individual wavelengths indicated in the figure legend. The I_b –values at the end of 20 control iterations are also listed in the figure legend. The discontinuity after 10 control iterations took place when the actuator regularization factor is increased from 0.1 to 1.0. (b) DM actuator heights obtained at the end of 20 WFC iterations as shown in part (a).

4.2 Opaque Particles

Next, we introduced 140 opaque, square-shaped particles randomly distributed inside an annular region bounded by 2 to 12λ/D on the occulter surface as shown in Fig. 6. We assumed the particles would alter only the transmission amplitude of the occulter, making it equal to zero at positions where the particles are located. We considered two values for

particle widths, 2.8 and 2.0μm, and obtained the after-control $I_n(x,y)$ maps shown in Figs. 7(a) and 7(b), respectively. The measured I_b value (Fig. 1(b)) fell in between the two values of the current simulations. The morphology of the $I_n(x,y)$ map in Fig. 7(b) is somewhat comparable to Fig. 1(b); given equal weighting of each wavelength band, the contrast was best in the central band and worst at the extrema. This is an indicator, though by no means proof, that the measured coherent contrast maps of Fig. 1(b) is caused by opaque spots on the occulter. For this case, we did not carry out an exhaustive search for opaque spots whose distribution on the occulter surface would give rise to the contrast maps observed in Fig. 1(b), for reasons to be explained later in this paper.
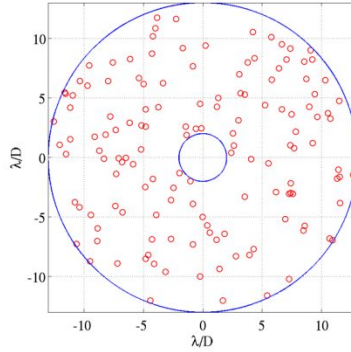
Figure 6. Locations of 140 particles randomly distributed inside an annular region bounded by 2 to 12λ/D on the occulter surface.
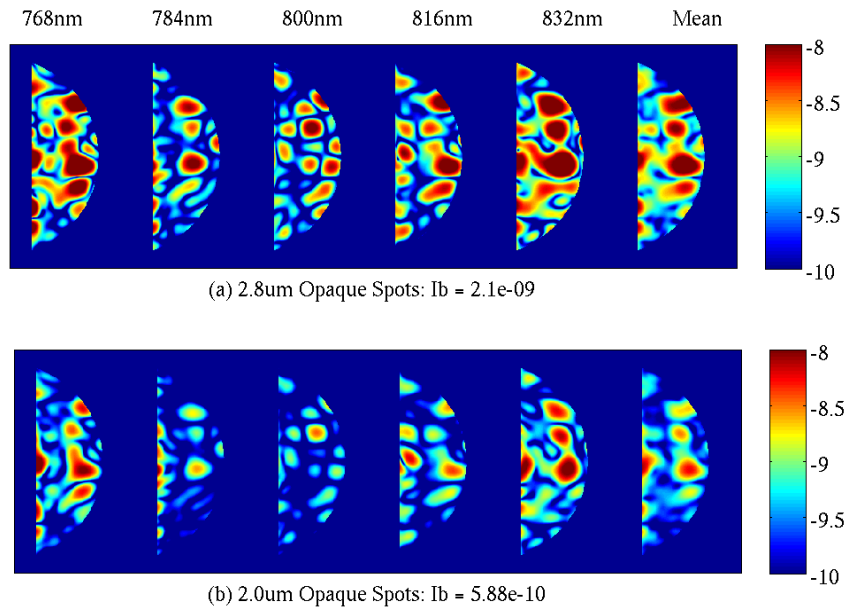
Figure 7. Post-control normalized intensities, $I_n(x,y)$. Top: 140 opaque, square spots with $a = 2.8$μm (width) were introduced to occulter transmission amplitude. The phase-delay of the occulter is kept the same. Bottom: Same as Top except $a = 2.0$μm.

4.3 Asymmetric and Reduced OD

In this sub-section, we introduced the following types of distortions to the occulter OD profile: (1) In a region where $x \geq 0$ and $OD_{max} \geq OD \geq 1$, where $OD_{max} = 5.1378$, we reduced the OD values linearly as

$$OD' = 0.6042 \times OD + 0.3958 \qquad (1)$$

such that the peak of the new OD, or OD', is 3.5. In a region where $x < 0$ and $OD > 3.5$, we truncated the OD values to 3.5. This case is shown graphically in Fig. 8(a). The phase versus OD relationship is kept the same as before, that is, when the OD value is reduced, the phase value is also adjusted according to the original phase versus OD relationship. (2) In a region where $OD > 1$, we symmetrically reduced the OD values linearly using Eqn. (1) so that the peak of the new OD, or OD', is 3.5. This is shown graphically in Fig. 8(b). The occulter phase is treated in the same way as in the previous case. (3) The OD profile is skewed to the left as compared to the nominal case, which also led to some reduction of the OD peak, as shown in Fig. 8(c). The occulter phase profile is also skewed in the same way as OD. This is done in the following way: Assume the 1-D OD profile is given by $od = f(n_v)$, where $n_v = -512, -511, ..., 511$ is an 1x1024pix array. Now we construct a new array,

$$n_v' = \text{sign}(n_v - n_0) \times \sqrt{(n_v - n_0)^2 + n_v^2} / \sqrt{2} \qquad (2)$$

and map $f(n_v)$ onto n_v' by 1-D interpolation, where $\text{sign}(x) = -1$ when $x < 0$ and $\text{sign}(x) = 1$ when $x > 0$. In Fig. 8(c), we used $n_0 = -5.5$. Figures 9(a-c) show the $I_n(x, y)$ maps corresponding to the above 3 types of occulter OD errors. The I_b values worsen as compared to the nominal case as expected, but are still much better than the measured one. Also, the regularly-spaced Airy-rings are preserved in all 3 cases to some levels, resulting in $I_n(x, y)$ morphology that does not match with the measured data. That is, these types of occulter errors cannot explain the observed contrast behavior of the current system.
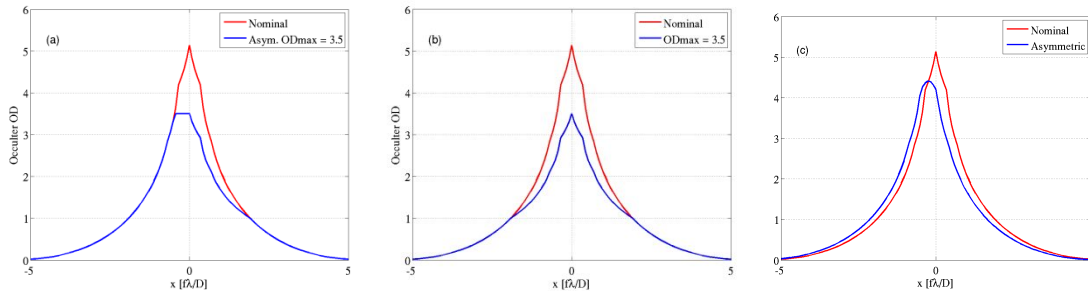

Figure 8. Occulter OD x-profiles versus x-position. (a) Occulter with asymmetric and reduced OD_{max} profile. (b) Occulter with reduced OD_{max} profile. (c) Occulter with skewed OD profile.
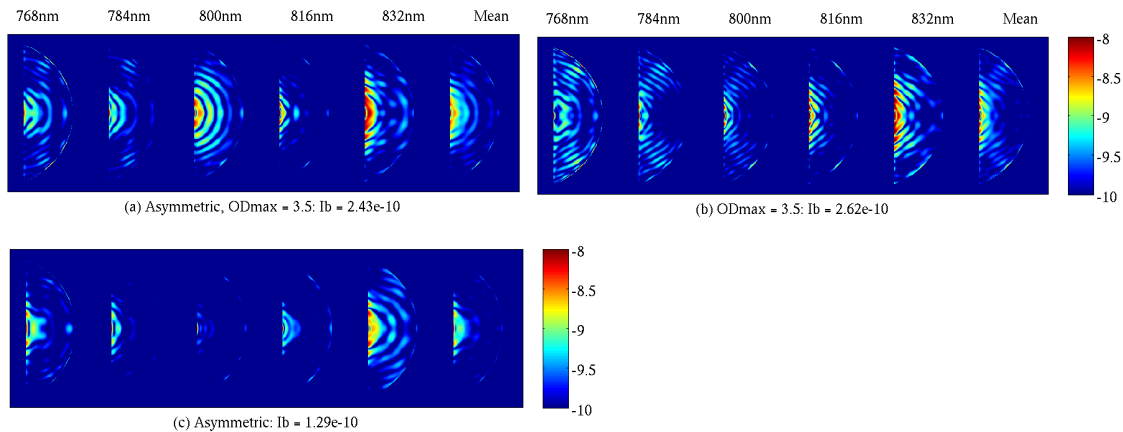

Figure 9. After-control normalized intensities corresponding to the blue-curves in Figs. 8(a-c).

4.4 Increased Occulter Phase

We also examined a case where the occulter phase is doubled everywhere as compared to the nominal case, as shown in Fig 10(a), where the red-curve shows the nominal phase at λ = 800nm and the blue one is equal to 2x of that. We do not

know of a physical phenomenon that would cause such a large phase dependence, but differences between the catalog values of the bulk material properties and the applied thin film could lead to a similar, though smaller phenomenon. The corresponding $I_n(x, y)$ results are shown in Fig. 10(b). The $I_n(x, y)$ maps exhibit features that are very different from those of the measured data in this case; that is, a large central lobe and a bright secondary lobe near the outer part of the dark hole dominate the residual light. The residual intensity due to a proportional phase error does not resemble the coherent scatter in the experiment (Fig. 1(b)).
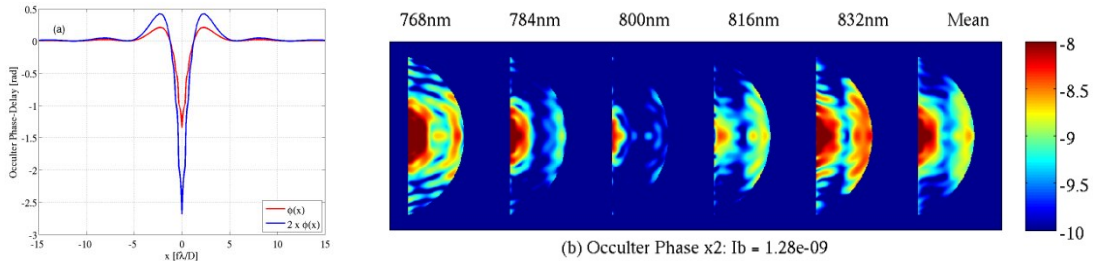
Figure 10. (a) Occulter phase-delay at λ = 800nm. (b) After-control normalized intensities corresponding to the blue-curve in part (a).

4.5 Using Measured Occulter Transmission Images

The speckly nature of the observed coherent dark hole floor, and the simple particle distribution model that produces a similar result, indicate that localized mask errors are the likely cause of the contrast floor. We have measured the transmission (amplitude only, not phase) of the occulter using high resolution (10x magnification, 0.97μm resolution) microscope images to inform a model and see if a mask characterization can be used to predict dark hole contrast. Figure 11(a) is the transmission image of the front side of the occulter with the mask written on it. The back side of the 2 mm thick substrate is not in focus using the NA = 0.3 objective. This is the composite of 10 images taken to average local fringing and detector noise. The vertical red-line is at x = 3.5fλ/D, the red-circle has a radius of r = 10fλ/D; this image roughly corresponds to the area of the occulter used in our experiments. We also took 10 images of the back side of the occulter, averaged them to obtain a single image, and multiplied the resulting image with Fig. 11(a) to obtain a "composite-image" of the front and the back sides of the occulter shown in Fig. 11(b). The HCIT optical system F-
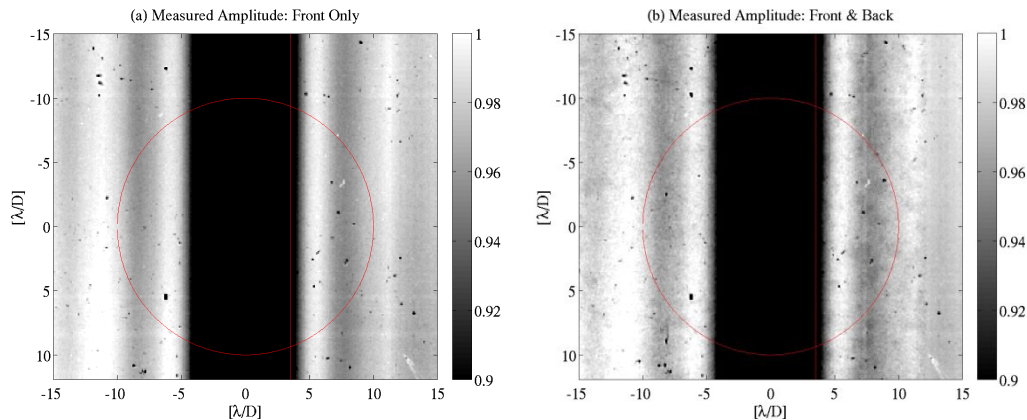

Figure 11. Transmitted amplitude images of the occulter. (a) Front (occulter) side only. (b) Combined image of the front and the back sides.

number at the occulter plane is 31.25, so the E-field changes very little when the beam propagates through the occulter glass. Thus, to a good approximation, the composite image in Fig. 11(b) can be used to account for the spots on both the front and the back sides of the occulter glass without modeling the propagation through the substrate. The microscope used in this measurement does not have enough dynamic range to measure the transmittance of the central dark area of the occulter. Therefore, we replaced the transmittance of the central ~4λ/D-wide area with the model data forming a

composite model. Figure 12 is an example of the x-profiles of the occulter amplitude function. The red- and the blue-curves correspond to the original and composite data, respectively, and the green dashed-curve is the as-designed mask model. In the plot, 1pixel corresponds to 2.1μm. We used the modeled data for the occulter phase and its dispersion for both the corresponding to the measured and composite OD.

Figures 13(a) and 13(b) are the after-control $I_n(x, y)$ maps obtained with the occulter amplitude function shown in Figs. 11(a) and 11(b), respectively. The dark hole floor is ~3x below the measured floor. We have repeated these simulations for different areas of the occulter (moving along the central lobe in Fig. 11), but failed to achieve a result that matches both qualitatively and quantitatively the measured data. That is, the fine-features of the $I_n(x, y)$ maps are not quite similar to those of the measured data, and the I_b values of the simulations are several times better than the measured one.
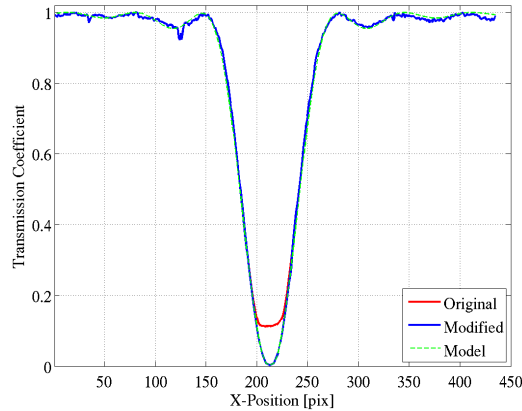

Figure 12. An example of the x-profile of the occulter transmission. The red- and the blue-curves correspond to the original and the modified measured data, and green dashed-curve is the model.
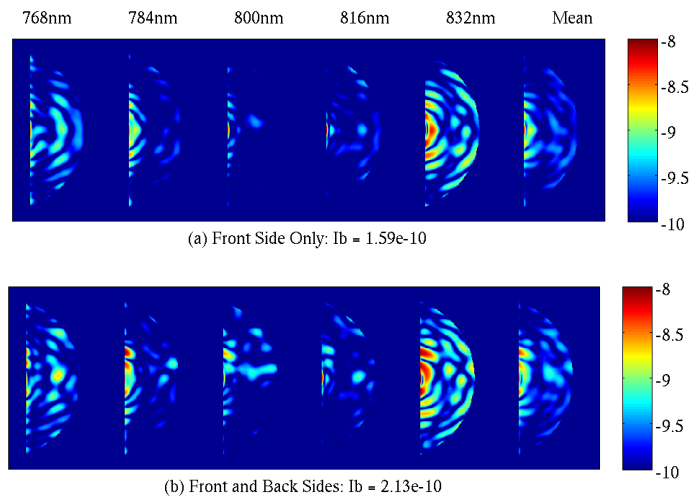

Figure 13. After-control normalized intensities obtained using the two occulter images in Figs. 11(a) and 11(b), respectively.

4.6 Adding Phase to Measured Occulter Spots

As noted above, we were able to measure the amplitude transmission, but not the phase, through the mask. We have artificially added phase to the spots to test the importance of phase and to motivate characterization by other means. Figure 14 is a surface plot of the measured optical density of the dark-hole side of the occulter surface after removing the

linear-sinc[2] occulter pattern. The x- and the y-axes are in units of λ/D, and the z-axis is OD. In this plot, the original OD value is multiplied by 50 for the sake of better visibility.

We have added additional phase to the occulter transmission function in the form of $\varphi_{spot} \approx \pi \times F_{spot} OD_{spot}$. Where F_{spot} is a multipler we tested at values 0, 0.25, 0.5, 0.75, and 1. At or near the optical resolution limit of the microscope objective, quantitative measure of the transmitted intensity through small spots / particulates is subject to large errors. Phase measurements by non contact methods with standard interferometers is also subject to large errors at the resolution of interest.
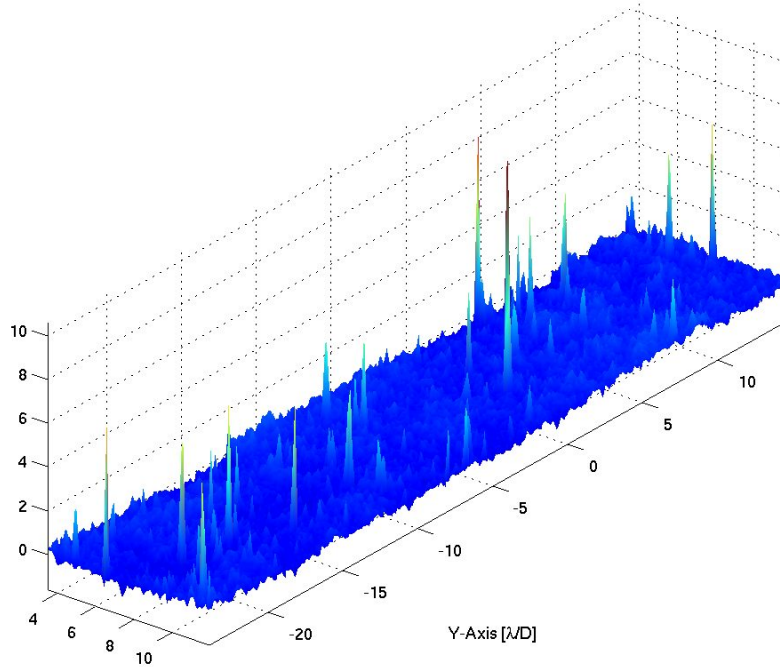

Figure 14. Values of the spot OD in the dark-hole side of the occulter. The OD value is multiplied by 50 for a better visibility.
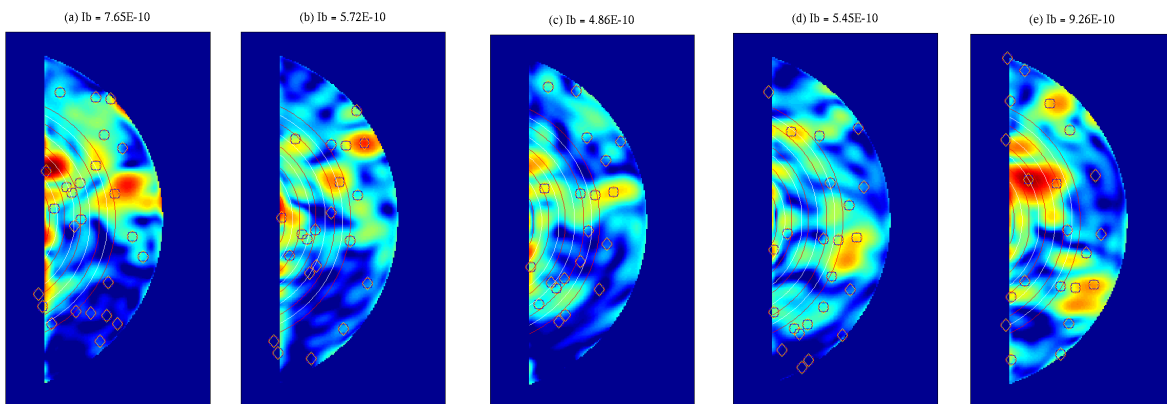

Figure 15. Change in $I_n(x, y)$ map when the Occulter is moved downward in a step of ~21μm. The red and the white arc lines indicate the positions of the Airy-ring peaks and valleys at the occulter plane. The markers indicate the locations of the major occulter spots.

Figures 15(a-e) show the after-control 10%-broadband $I_n(x,y)$ maps corresponding to 5 different locations when the occulter is moved downward in an increment of ~21µm. We used $F_{spot} = 1$ in these simulations. The red- and the white-circular lines indicate the locations of the peaks and the valleys of the Airy-rings at the occulter plane, and the markers indicate the locations of the major measured particles (or low transmission areas) on the occulter. Given in each sub-plot title is the corresponding I_b-value. We found that the contrast map features do not track in a predictable way as the occulter is moved downward. This means that it is meaningless to associate the colored-features of the
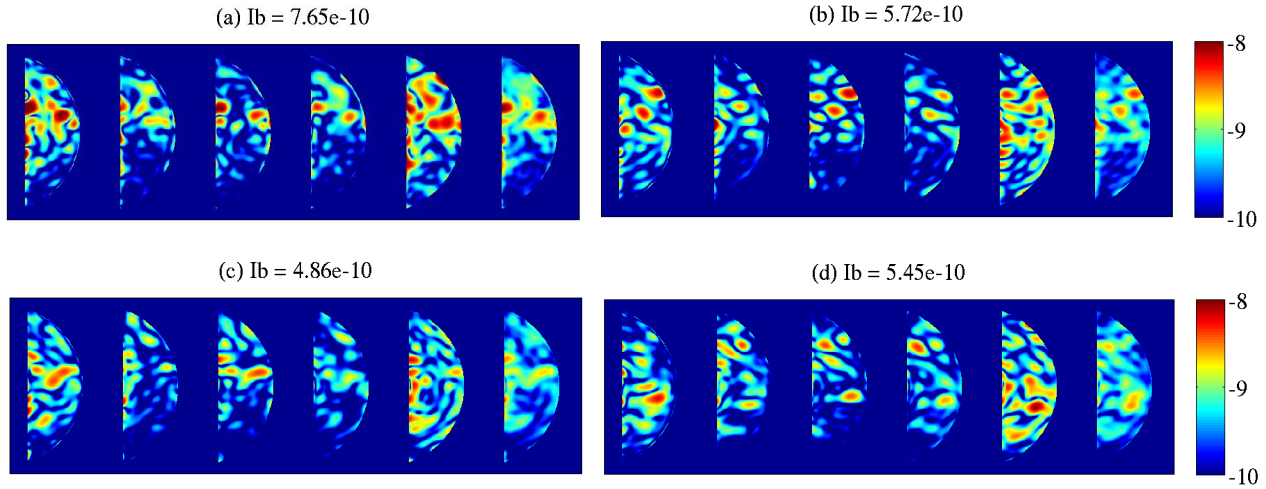

(a) Ib = 7.65e-10   (b) Ib = 5.72e-10

(c) Ib = 4.86e-10   (d) Ib = 5.45e-10

Figure 16. Simulated $I_n(x,y)$ maps corresponding to 4 different occulter positions. The occulter positions are the same as those used to obtain the first 4 broadband $I_n(x,y)$ maps in Fig. 15. As in Figs. 1(a-b), the leftmost images in each frame are for λ = 768, 784, 800, 816, and 832nm, respectively, and the rightmost images are their mean representing the 10% broadband $I_n(x,y)$ map.
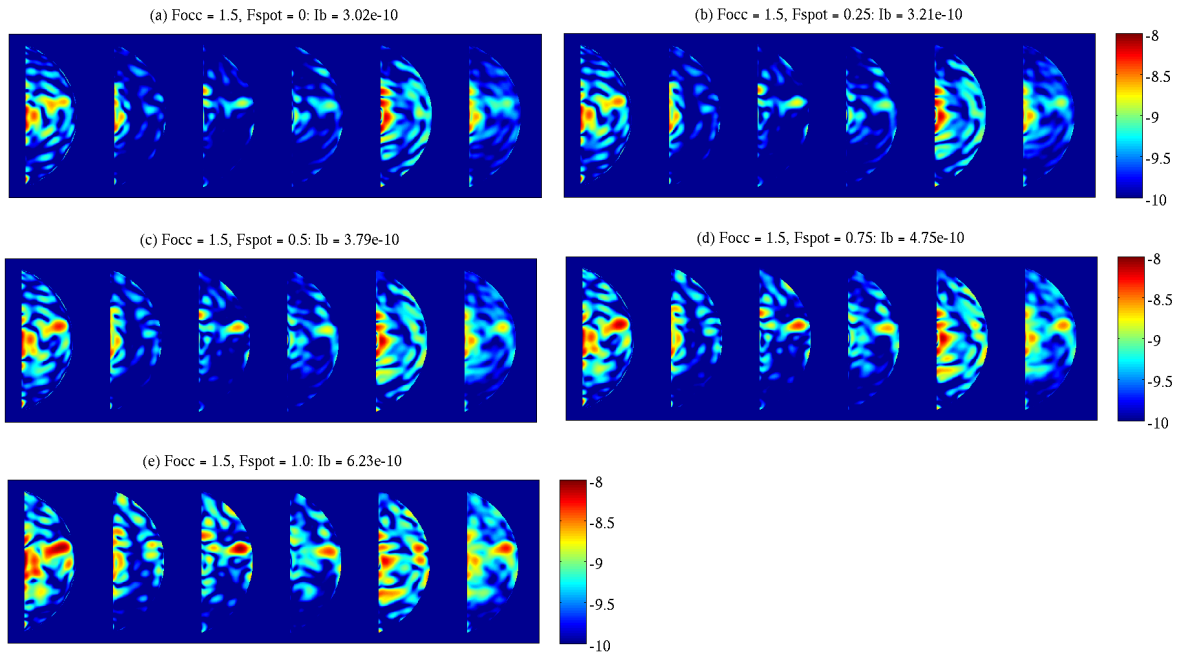

(a) Focc = 1.5, Fspot = 0: Ib = 3.02e-10   (b) Focc = 1.5, Fspot = 0.25: Ib = 3.21e-10

(c) Focc = 1.5, Fspot = 0.5: Ib = 3.79e-10   (d) Focc = 1.5, Fspot = 0.75: Ib = 4.75e-10

(e) Focc = 1.5, Fspot = 1.0: Ib = 6.23e-10

Figure 17. Simulated $I_n(x,y)$ maps similar to Fig. 16(c), except that the parasitic occulter is multiplied by x1.5 ($F_{occ} = 1.5$), and F_{spot} is varied from 0 to 1.0 with an increment of 0.25.

measured contrast maps with the locations of the actual spots of the occulter. This is one of the most important findings of this study. Figures 16(a-d) show the individual and the averaged after-control $I_n(x, y)$ maps corresponding to Figs. 15(a-d). We can see that both the I_b-values and the $I_n(x, y)$ map features of these simulated results are comparable to the measured data. However, we did not find a mask position where the measured speckles resemble one-for-one the model speckles.

Figures 17(a-e) are the same as Fig. 16(c) except that we multiplied the parasitic occulter phase by x1.5 ($F_{occ} = 1.5$) and varied F_{spot} from 0 to 1.0 with an increment of 0.25. That is, a fairly big range of spot phases can yield I_b-values that are within a factor of 2 of the measured I_b-value.

5. CONCLUSION

We have shown that the observed contrast performance of our HCIT testbed cannot be predicted by introducing certain defects to the occulter OD profile, such as reducing the maximum OD value, making the OD profile asymmetric, or by skewing the OD profile. Neither can it be predicted by increasing the parasitic phase of the occulter. These kinds of changes in occulter characteristics still preserve the fairly regularly spaced Airy-ring pattern of the final focal-plane PSF, which is something not observed in the measured data. These findings indicate that the Lyot coronagraph design implemented on the HCIT is fairly tolerant to fabrication errors in the OD profile and the phase of the occulter. We found two kinds of situations where the predicted contrast maps become comparable to the measured data in terms of the mean contrast value and the contrast map features. They are: (1) When we introduce randomly distributed opaque spots having widths of ~2.5μm to occulter transmission amplitude function. (2) When we use the measured occulter transmittance image with actual spots on it and after introducing additional phase values to all major occulter spots. Both of these conditions are possible in the real world, but we did not carry out an exhaustive study to find an exact match between the measured data and our prediction.

Our work suggests that the observed "hot spots" on the contrast maps cannot be predicted based on the actual locations of the occulter spots unless the occulter spot is fairly large, such as in Figs. 9(a-b) of Ref. [7], where an occulter spot leads to $I_b > 10^{-8}$. That is because the "hot spots" on the contrast maps are a delicate function of the EFC algorithm and possibly a function of the interaction between the spots and the incident Airy rings.

In future work we will report on model and data agreement for different wavelength control bandwidths, non-functional DM actuators, and the ability to discriminate instrument-induced speckles from other background sources. These experimental validations of key coronagraph sensitivity factors will additionally contribute to the confidence in performance prediction models for future flight systems.

REFERENCES

[1] John T. Trauger, Chris Burrows, Brian Gordon, Joseph J. Green, Andrew E. Lowman, Dwight Moody, Albert F. Niessner, Fang Shi, and Daniel Wilson, "Coronagraph contrast demonstrations with the high-contrast imaging testbed," *Proc. SPIE*, **5487**, 1330 (2004).
[2] Andrew E. Lowman, John T. Trauger, Brian Gordon, Joseph J. Green, Dwight Moody, Albert F. Niessner, and Fang Shi, "High-contrast imaging testbed for the Terrestrial Planet Finder coronagraph," *Proc. SPIE*, **5487**, 1246 (2004).
[3] Erkin Sidick, Fang Shi, Scott Basinger, Dwight Moody, Andrew E. Lowman, Andreas C. Kuhnert, and John T. Trauger, "Performance of TPF's High-Contrast Imaging Testbed: Modeling and simulations, " *Proc. SPIE*, **6265**, 62653L (2006).
[4] Amir Give'on *et al*, "Broadband wavefront correction algorithm for high-contrast imaging system," *Proc. SPIE*, **6691**, 66910A (2007).

[5] *Modeling and Analysis for Controlled Optical Systems User's Manual*, Jet Propulsion Laboratory, California Institute of Technology, Pasadena, CA.

[6] Erkin Sidick, Stuart Shaklan, Amir Give'on, and Brian Kern, " Studies of the effects of optical system errors on the HCIT contrast performance," *Proc. SPIE*, **8151**, 8151-06 (2011).

[7] Erkin Sidick, Stuart Shaklan, John Krist, Eric J. Cady, and Brian Kern, "HCIT contrast performance sensitivity studies: Simulation versus experiment ," *Proc. SPIE,* vol. 8864, pp. 88640Q-1 (2013).

[8] Erkin Sidick, Stuart Shaklan, and Kunjithapatham Balasubramanian, "HCIT Broadband Contrast Performance Sensitivity Studies", *Proc. SPIE*, 8520, 85200M-1 (2012).

[9] D. C. Moody and J. T. Trauger, "Hybrid Lyot coronagraph masks and wavefront control for improved spectral bandwidth and throughput," *Proc. SPIE*, 6693, 6693I1-9 (2007).

[10] "Exoplanet Exploration Coronagraph Technology: Technology Milestone #2 Report," Brian Kern, Andreas Kuhnert and John Trauger, editors, 8 Aug. 2008, http://exep.jpl.nasa.gov/TPF-C/HCIT-Milestone2Signed-2008-08-08.pdf.

[11] K. Balasubramanian, "Band-limited image plane masks for the Terrestrial Planet Finder coronagraph: materials and designs for broadband performance," *Appl. Opt*. 47, pp.116-125 (2008).

Measurements of incoherent light and background structure at exo-Earth detection levels in the High Contrast Imaging Testbed

Eric Cady[a]*, Stuart Shaklan[a]

[a] Jet Propulsion Laboratory, California Institute of Technology, Pasadena, CA, 91109 USA

ABSTRACT

A major component of the estimation and correction of starlight at very high contrasts is the creation of a dark hole: a region in the vicinity of the core of the stellar point spread function (PSF) where speckles in the PSF wings have been greatly attenuated, up to a factor of 10^{10} for the imaging of terrestrial exoplanets. At these very high contrasts, removing these speckles requires distinguishing between light from the stellar PSF scattered by instrument imperfections, which may be partially corrected across a broad band using deformable mirrors in the system, from light from other sources which generally may not. These other sources may be external or internal to the instrument (e.g. planets, exozodiacal light), but in either case, their distinguishing characteristic is their inability to interfere coherently with the PSF. In the following we discuss the estimation, structure, and expected origin of this "incoherent" signal, primarily in the context of a series of experiments made with a linear band-limited mask in Jan-Mar 2013. We find that the "incoherent" signal at moderate contrasts is largely estimation error of the coherent signal, while at very high contrasts it represents a true floor which is stable over week-timescales.

1. INTRODUCTION

The direct imaging of terrestrial exoplanets orbiting nearby stars is a challenging endeavor, due both to the large ($\sim 10^{10}$) flux ratio between the star and planet and the small (~ 100mas) angular separation between star and planet. There exists an entire family of instruments—coronagraphs—whose purpose is to attenuate the starlight in regions of the image plane where planets may be detected. However, these regions of high image-plane contrast ("dark holes") require iterative correction from a wavefront control system to compensate for imperfections in the optical system down to sub-nm scales.

To effect this correction, we must first estimate the amplitude and phase of the starlight across the dark hole. At the High Contrast Imaging Testbed (HCIT) at NASA/JPL, we use primarily a pairwise-estimation scheme which modulates the electric field by applying known offsets to the deformable mirror settings. A comprehensive description is given in [1]. (Subsequent correction is an orthogonal problem; the HCIT control software uses electric field conjugation[2], but other methods, such as speckle nulling[3], could used without requiring any changes.)

In addition to determining the complex electric field associated with the starlight, the pairwise method also makes an estimate of the components of the signal which do not modulate with the DM and thus are not coherent with the star. This signal has been termed the "incoherent" part of the wavefront. This is a something of a misnomer; as will be shown later, some parts are errors in estimating the field which interferes with the DM probes, and some components do genuinely not interfere with the probes. Nonetheless, it has stuck. In a science image this would include the signals from any planets or disks in orbit about the star.

The incoherent signal was initially viewed as a nuisance, as it represented background that could not be used in the correction and had to be subtracted off prior to control. However, it also represents an opportunity, as treating the *starlight* as the nuisance and subtracting the coherent signal off can serve as a post-processing technique that does not rely on angular or spectral diversity. To show this can work, though, we need to show that 1) an incoherent signal can be shown to exist—i.e. the measurement is not an artifact—and 2) that it can be reliably separated from the starlight.

---

* eric.j.cady@jpl.nasa.gov

Table 1. List of broadband control tests performed

Test #	Date	768 nm	784 nm	800 nm	816 nm	832 nm	Contrast
1	1/22			x			1.420×10^{-10}
2	1/22	x				x	2.191×10^{-9}
3	1/22	x					1.775×10^{-10}
4	1/23					x	2.650×10^{-10}
5	1/23	x				x	2.776×10^{-9}
6	1/25	x	x	x	x	x	1.285×10^{-9}
7	1/27			x			1.329×10^{-10}
8	1/28			x			1.990×10^{-10}
9	1/28	x					1.855×10^{-10}
10	1/28	x				x	1.997×10^{-9}
11	1/28		x	x	x		5.922×10^{-10}
12	1/29	x					2.147×10^{-10}
13	1/29					x	3.299×10^{-10}
14	2/1		x	x	x		5.276×10^{-10}

Data collected as part of a separate analysis was found to be well-suited to investigate the origin of the incoherent signal for that coronagraphic system. Section 2.1 describes the data origin, while Section 2.2 details the filtering and post-processing applied to the data to make it usable for this analysis. The resulting analysis appears in Section 3.

2. DATA AND DATA PROCESSING

2.1 Test background

The original test plan[4] for the Terrestrial Planet Finder Coronagraph (TPF-C) telescope included a set of three technology milestones to be demonstrated prior to the start of Phase A for TPF-C. Milestones 1 and 2 were contrast demonstrations, while Milestone 3 was a two-part model-validation effort. Despite the cancellation of TPF-C, Milestones 1 and 2 were completed in 2006[5] and 2008[6], respectively, to advance coronagraphic technology.

Testing[7] for Milestone 3A, the first half of Milestone 3, was done over a period of three months from January-March 2013. (Results from this work have been presented elsewhere; see [8, 9].) As one part of this work, a number of wavefront control sequences were run with the band-limited Lyot mask used in Milestone 2 testing. Each of these corrected in one or more 2% filters, over 3.5-11 λ/D, and repeated at least 3 tests of these runs 3 times on different days. (Some additional tests were also run twice or once.) A full list of tests appears in Table 1. Iterations continued until the measured contrast over 9 iterations had a slope per iteration of less than 2×10^{-12}—a milestone requirement termed the "stopping condition".

This particular series of tests was meant to examine repeatability of correction as part of model validation, but also serendipitously happened to give a good data set for looking at structure in the "incoherent" signal—the part that does not interfere with the DM probes. In particular, the extended series of iterations prior to the stopping condition allow the variation of the incoherent signal to be examined both as a function of coherent intensity (as the contrast is being pushed lower) and from iteration to iteration (in the region where convergence has stalled). Long-term stability can also be examined by using the three tests of the same case over three days.

2.2 Filtering/post-processing

To estimate the electric field at the science camera using the science camera itself, we use a set of 5 images per narrowband filter, taken with different DM settings. These settings are selected in accordance with the procedure suggested in [1], using two positive and negative versions of two independent probe settings and a fifth unprobed image. The appendix to this paper also describes the methodology, though it does not delve into the motivation as [1] does.

The primary noise sources in the five images in each probe set are read noise (from the detector) and shot noise (from the light source). The unprobed image in particular suffers heavily from these effects, as the residual signal after correction tended to be only a few counts per pixel.

A number of approaches were tested to remove the read-noise/shot-noise contamination without removing the underlying structure, including median filtering, Wiener filtering, and the *à trous* wavelet filter [10]. A Wiener filter using a 3x3 subregion size proved both simple and most effective; while both median and wavelet filters could remove the noise, median filtering tended to produce swatches of intensity with the same count value and the wavelet filter did not prove effective at retaining fine-scale structure. Fig. 1 shows two sets of incoherent estimates, taken with and without filtering.

Even after filtering, the mean and standard deviation are quite noisy, as these statistics assume normality of the underlying data and are sensitive to a small number of outliers. Fig. 2 shows a representative QQ plot[11] of the filtered intensities versus a standard normal distribution for a single wavelength at one iteration. Significant deviation from normality exists near the tails, indicating a sizable outlier population; while most points in this image are on the order of 10^{-9}-10^{-10}, a few are as high as 10^{-7} or as low as a (non-physical) -3.5×10^{-7}.

Rather than hand-massage the data to exclude these—a questionable procedure, as some outliers may be legitimate bright spots, e.g. adjacent to the edges of the dark hole—we first substitute robust estimators of photometric level and variation, and then investigate some of the outliers in the data set to better ascertain their causes.

We estimate the spread of the data using the median in place of the mean, and the "median absolute deviation, normalized" (MADN) in place of the standard deviation. The MADN for a set of data x is defined as [11]:

$$MADN(x) = 1.4826 \, \mathrm{median}(|x - \mathrm{median}(x)|) \tag{1}$$

with the constant chosen such that data drawn from the standard normal distribution is expected to have MADN $= 1$, as the standard deviation does. Both the median and the MADN are robust estimators: while they produce a slightly less efficient estimation of the location and spread of a distribution than mean and standard deviation when the data is normally distributed, they maintain their performance even in the presence of a large outlier population. (More efficient estimators require less sample data to achieve the same confidence level in the estimation of a parameter.) Fig. 3 shows the relative performance—median and MADN are very effective at suppressing the spurious spikes in the data.

3. ANALYSIS

In curves such as the ones in Fig. 3, we see two distinct regimes of behavior, which depend on the coherent contrast level. In the first, which we can see in Fig. 4, the incoherent signal tracks the coherent signal at a nearly-constant level, with the incoherent down by a factor of 2-3, depending on wavelength. In the second, shown in Fig. 5, the coherent signal crosses below the incoherent signal, and the incoherent signal reaches a floor in the vicinity of 2×10^{-10}. The exact number has some chromatic dependence, and decorrelates from the coherent signal entirely. (This behavior was also noted in [1].)

This behavior strongly suggests that above a median coherent intensity of $\approx 6 \times 10^{-10}$, the primary component of the incoherent signal is coherent light that has been incorrectly categorized as not interacting with the starlight.

The cases of the corrections in test #5 and test #12 are instructive in informing this conclusion. Test #5 was performed on two filters at opposite ends of a 10% bandpass (768nm and 832nm). As an initial condition, it used a DM flattened by phase retrieval, with no prior attempt at a dark hole. After 12 iterations, the coherent signal had dropped below 10^{-8}, and continued to decrease until the end of the run. Fig. 4 shows the performance across 77 iterations (top). The bottom shows the ratio between the medians of the coherent and incoherent signal, which track at a nearly constant level after the initial corrections.

Fig. 6 and Fig. 7 show the coherent and incoherent signal in the 768nm band, using every third iteration. While the coherent (and incoherent) drop steadily, the coherent signal maintains a consistent morphology that is only slowly corrected. Note that the values corresponding to plot colors are scaled down by a factor of three from the coherent to incoherent plots, to illustrate the trend from the lower half of Fig. 4.

Conversely, test #12 was performed over a single 2% bandpass (centered at 768nm), and started from a DM setting that created a dark hole over the central three 2% filters (784nm, 800nm, 816nm). Thus, correction began from a position that already had good suppression, and rapidly pushed the coherent signal to approximately
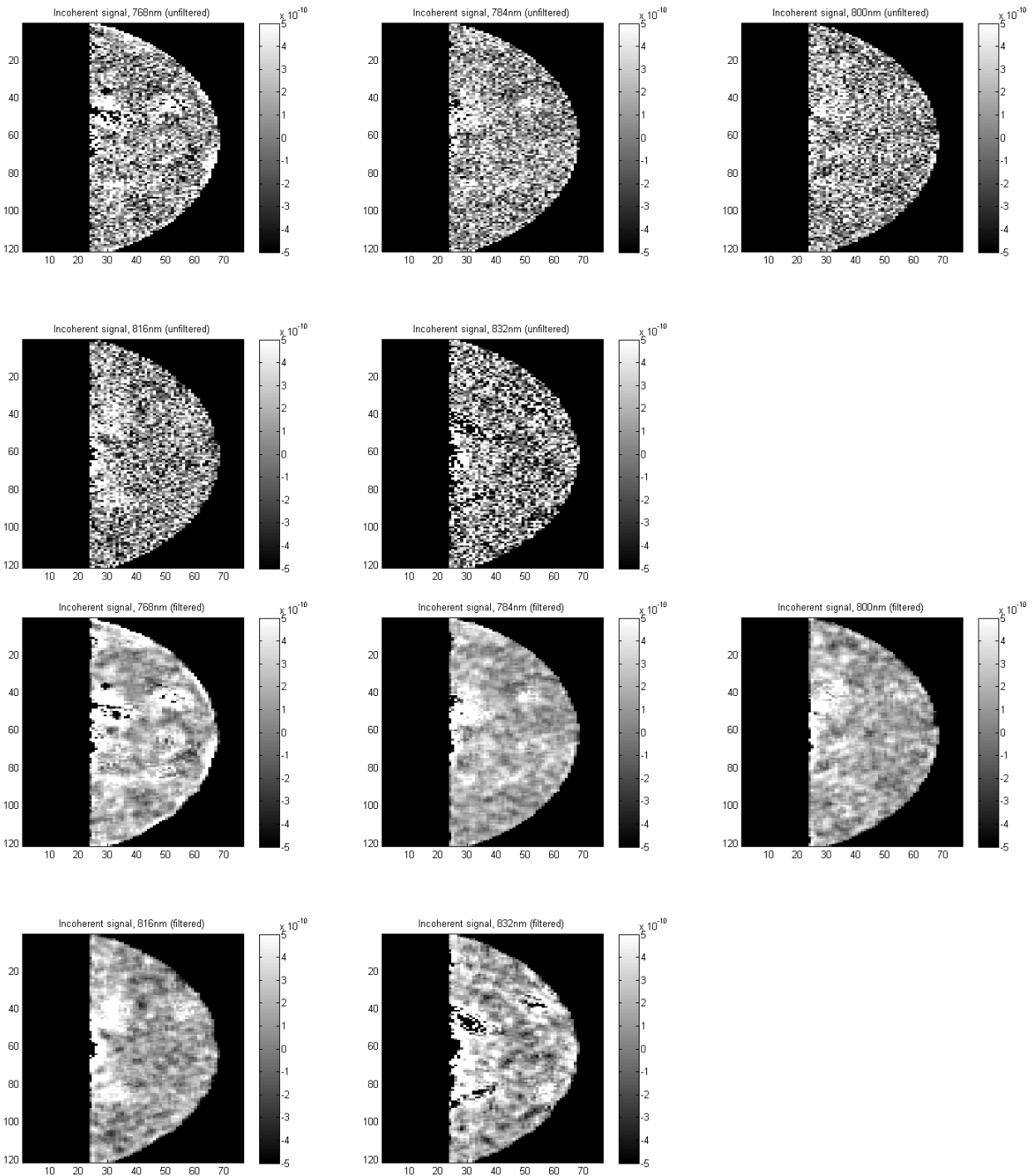
Figure 1. *Top.* Estimates of the incoherent light level in the dark hole over 2% bands, using raw data from the end of test #6. *Bottom.* Estimates of the incoherent light level in the dark hole, following the application of a Wiener filter to remove read and shot noise.
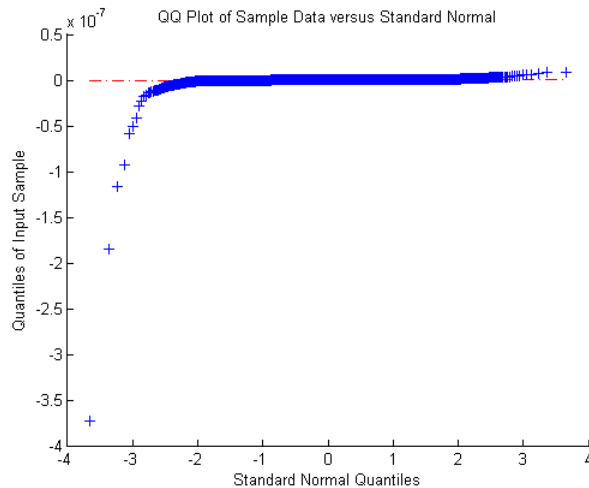
Figure 2. A quantile-quantile plot of quantiles of intensities in the dark hole for the 800nm channel of at the end of test #6, versus a quantiles of a standard normal distribution. The deviations from linearity near the ends indicate the distribution will have heavier tails than a normal distribution.

6×10^{-11}. The incoherent signal maintained its customary floor in the vicinity of 2×10^{-10}; Fig. 5 shows the overall performance across the 25 iterations of the test.

Fig. 8 and Fig. 9 show the estimated coherent and incoherent signal across the 25 iterations. Once the first few iterations are past, the incoherent signal changes very little, which a distinct and consistent morphology, while structures in the coherent signal appear and disappear from iteration to iteration. This stability is quantified in Fig. 10, which shows the MADN across the dark hole over the whole of test #12.

Moreover, when the same wavefront control (e.g. monochromatic suppression over a 2% filter centered at 768nm) is run on different days, the incoherent residual maintains the same speckle structure and intensity, though that structure is not the same from filter to filter. Fig. 11 shows the mean incoherent signal (from iteration to iteration) from 8 monochromatic suppression runs, taken on different days over the course of a week; from day to day the incoherent residual remains stable, while from filter to filter it changes significantly.

This suggests that, in the region in which the error from fitting out the coherent signal is small, something is creating real incoherent structures at the 2×10^{-10} level which are roughly stable over week timescales, but which have significant wavelength dependence. This mystery source is the current limiting monochromatic factor; the testbed could be getting at least 6×10^{-11} without it, based on coherent estimate in (for example) Fig. 5.

4. SUMMARY

Examination of incoherent portion of the signal in a high-contrast image suggests that the presence of a true contrast floor can be isolated from residual starlight. This can be done with standard estimation techniques using DM probes; some processing to compensate for noise also appears required for measurements at low flux. This incoherent floor contains structures which are largely stable over both short- and long-term time scales, but which have significant wavelength dependence.

However, our ability to extract this estimate is limited by the magnitude of the coherent field; roughly 25% of the coherent signal is incorrectly treated as incoherent, and this term dominates that signal until the contrast floor is neared. Nonetheless, this represents a factor of 4 suppression in post-processing without invoking any spectral diversity.
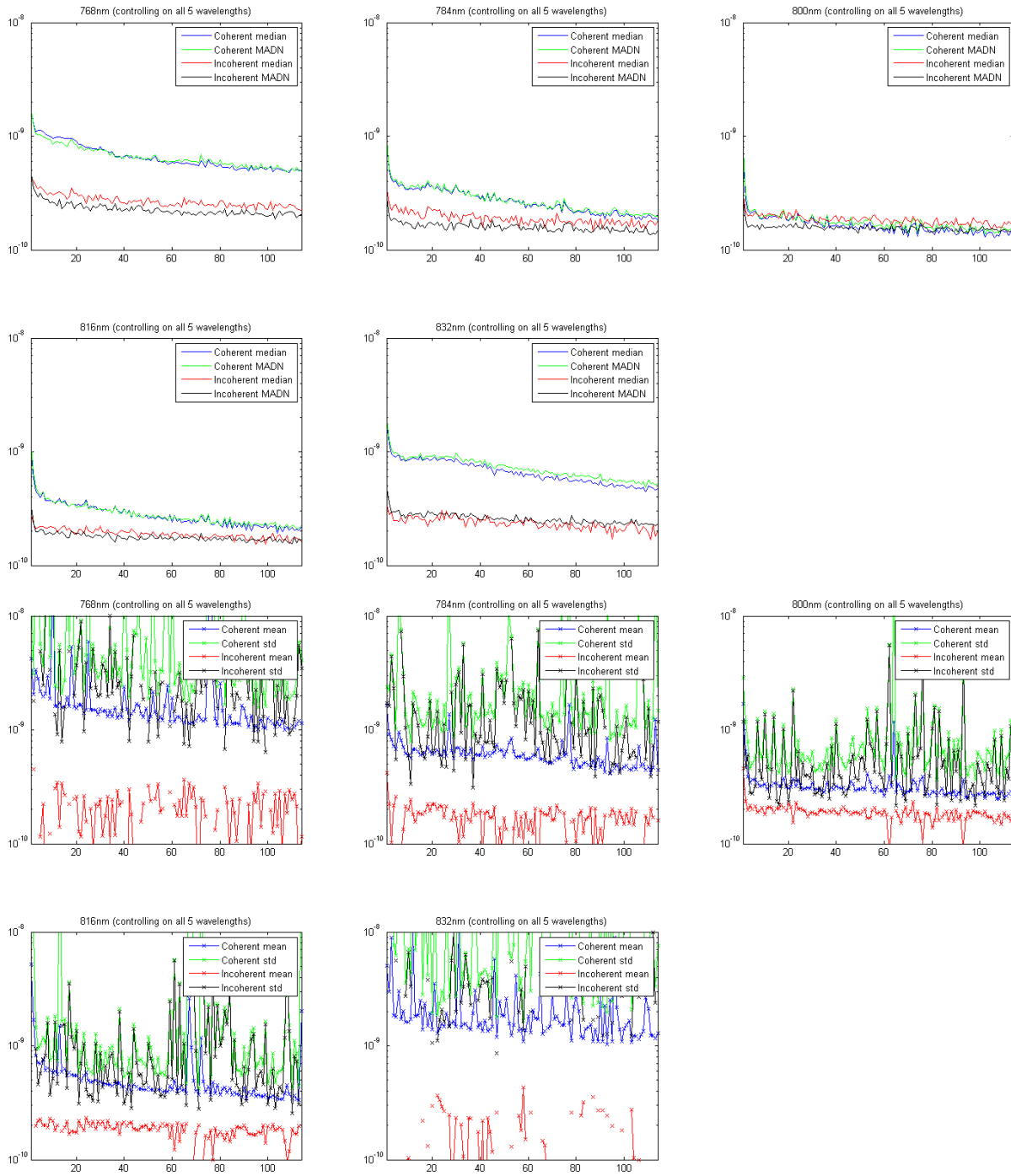
Acknowledgments

Figure 3. Central location and spread of distribution of coherent and incoherent light across 5 wavelengths, using data taken from test #6. *Top.* Location estimated with median, spread estimated with MADN. *Bottom.* Location estimated with mean, spread estimated with standard deviation. Missing points indicate estimates for the mean intensity in the dark hole less than zero.
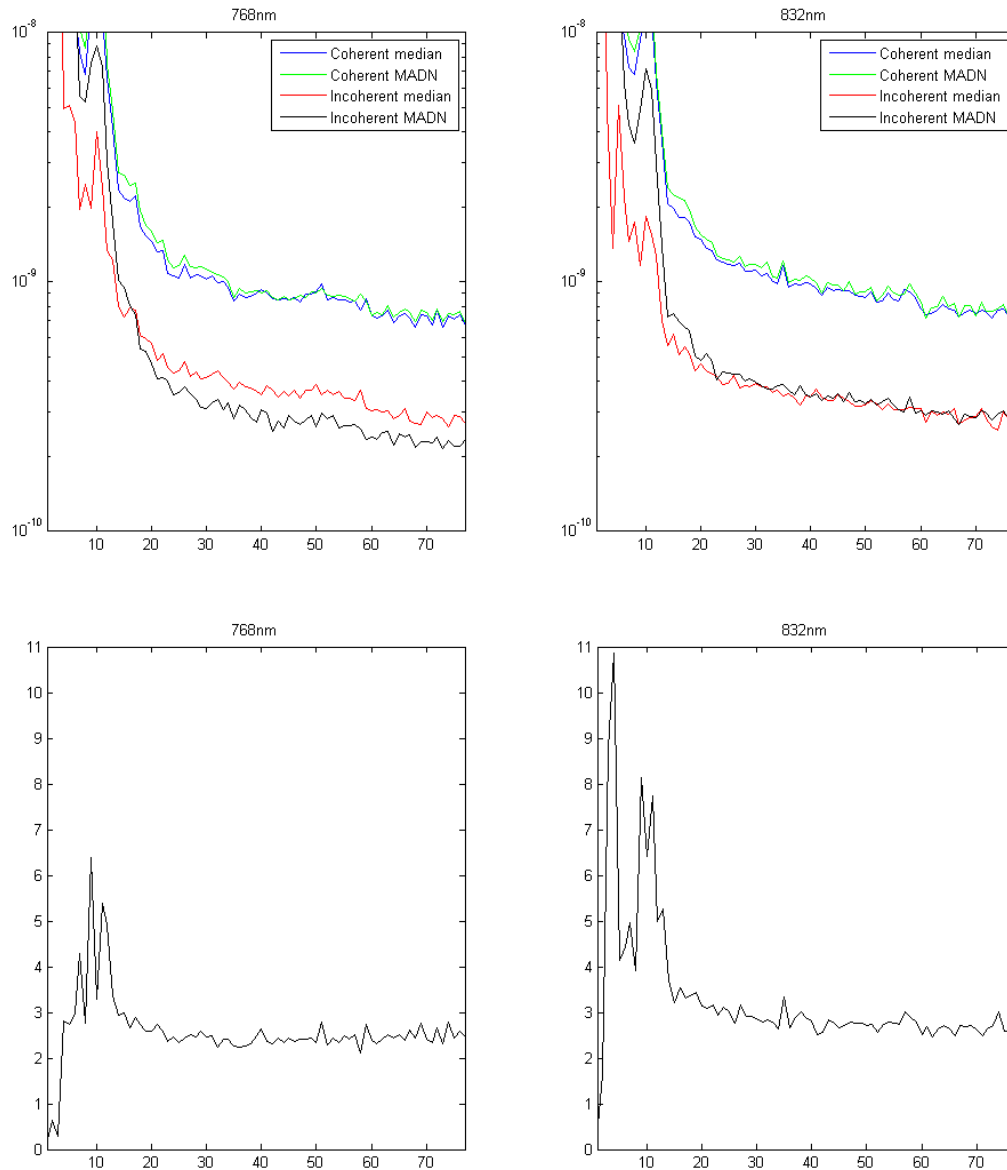
Figure 4. *Top.* Location and spread of coherent and incoherent light across 2 wavelengths, using data from test #5. Unlike most of the runs in this data set, this was initializes with a DM corresponding to a mediocre wavefront, rather than one that provides high contrast for a different bandpass, *Bottom.* Ratio of coherent and incoherent median.
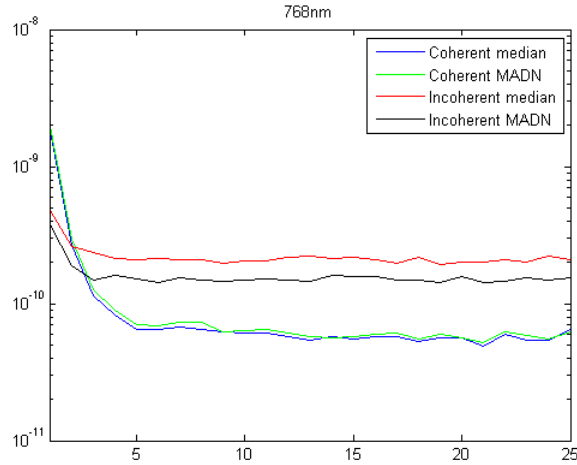
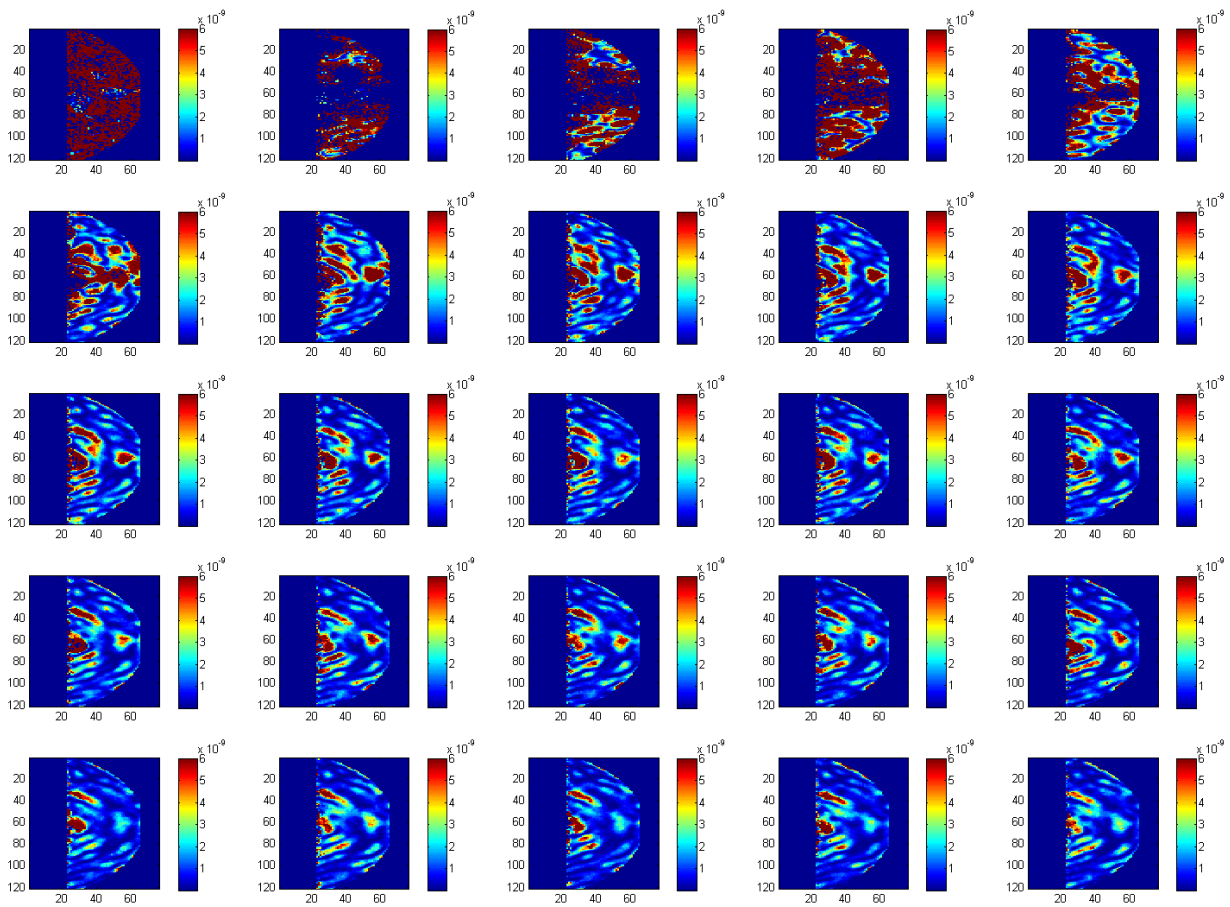Figure 5. *Top.* Location and spread of coherent and incoherent light in the 2% filter centered at 768nm, using data taken from test #12.

Figure 6. The estimated coherent part of the wavefront in test #5 over a 2% band centered at 768nm, using every third iteration and skipping regularization iterations in which probing was not done.
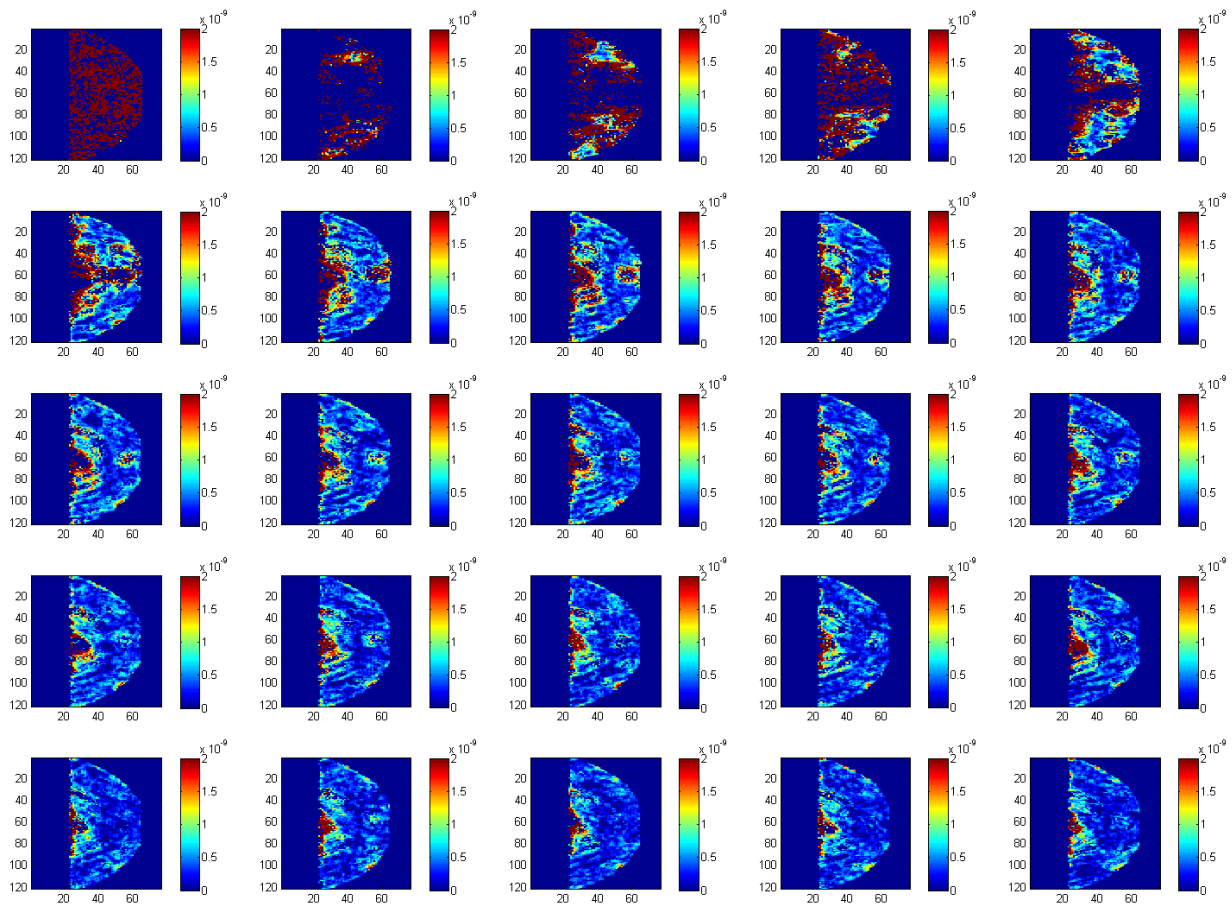
Figure 7. The estimated incoherent part of the wavefront in test #5 over a 2% band centered at 768nm, using every third iteration and skipping regularization iterations in which probing was not done. Note the color scale is 1/3 of that in Fig. 6.
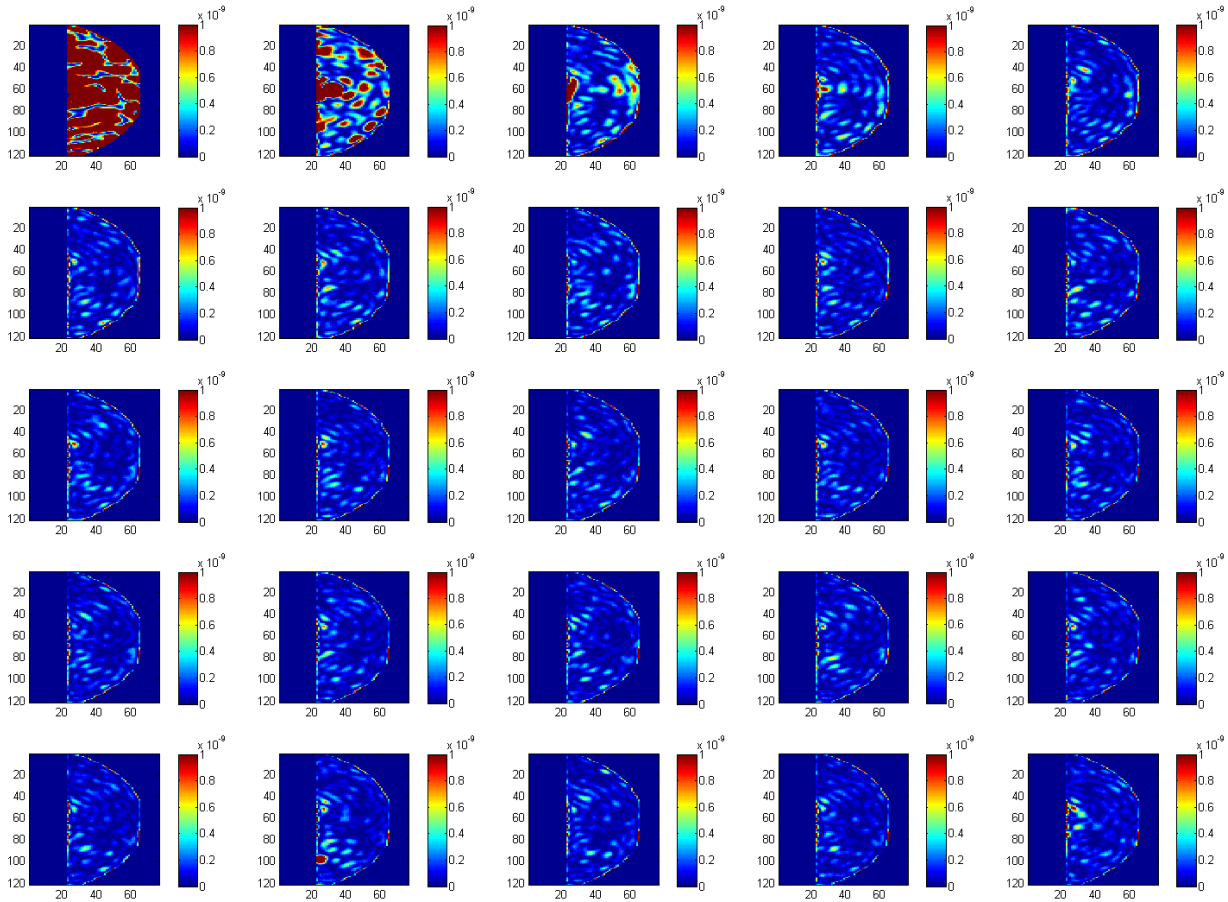
Figure 8. The estimated coherent part of the wavefront in test #12, over a 2% band centered at 768nm.

References

[1] Give'on, A., Kern, B. D., and Shaklan, S.. "Pair-wise, deformable mirror, image plane-based diversity electric field estimation for high contrast coronagraphy," Proc. SPIE 8151 (2011).

[2] Give'on, A., "A unified formalism for high contrast imaging correction algorithms," Proc. SPIE 7440 (2009).

[3] Bordé, P. J. and Traub, W. A., "High-Contrast Imaging from Space: Speckle Nulling in a Low-Aberration Regime", *The Astrophysical Journal*, 638:488–498, (2006).

[4] Dooley, J. and Lawson, P., Technology plan for the terrestrial planet finder coronagraph, http://exep.jpl.nasa.gov/files/exep/TPF-CTechPlan.pdf (2005).

[5] Trauger, J., Kern, B., and Kuhnert, A., TPF-C technology milestone #1 report, http://exep.jpl.nasa.gov/files/exep/TPFC_M1_Report_060710_final.pdf (2006).

[6] Kern, B., Kuhnert, A., and Trauger, J., Exoplanet exploration coronagraph technology: Technology milestone #2 report, http://exep.jpl.nasa.gov/files/exep/HCIT-Milestone2Signed-2008-08-08.pdf (2008).

[7] Shaklan, S., Technology milestone #3a white paper (revised): Coronagraph starlight suppression model validation, http://exep.jpl.nasa.gov/files/exep/ExEPCMilestone3whitepaperrevisedsigned.pdf (2013).

[8] Sidick, E., Shaklan, S., Krist, J., Cady, E. J., Kern, B., and Balasubramanian, K., "HCIT contrast performance sensitivity studies: simulation versus experiment," Proc. SPIE 8864 (2013).
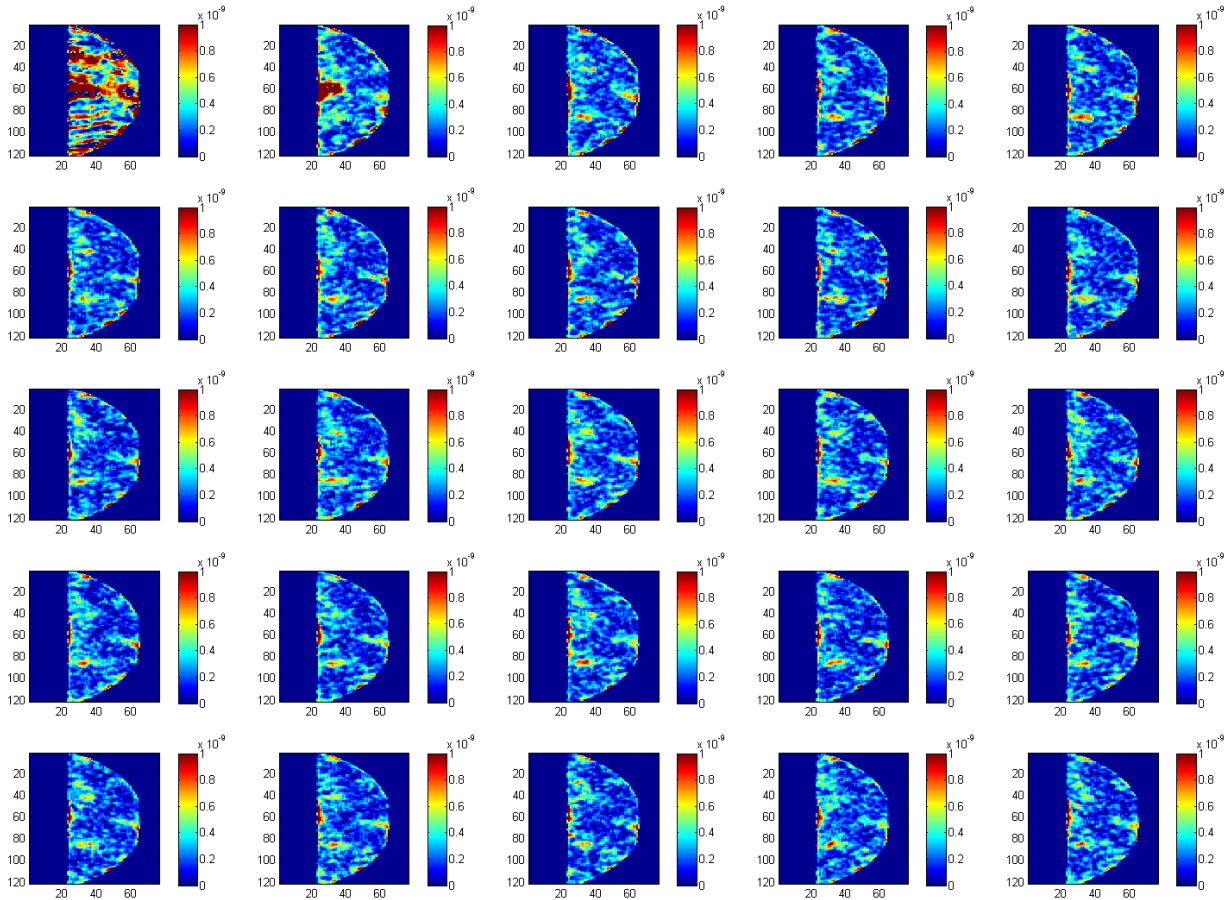
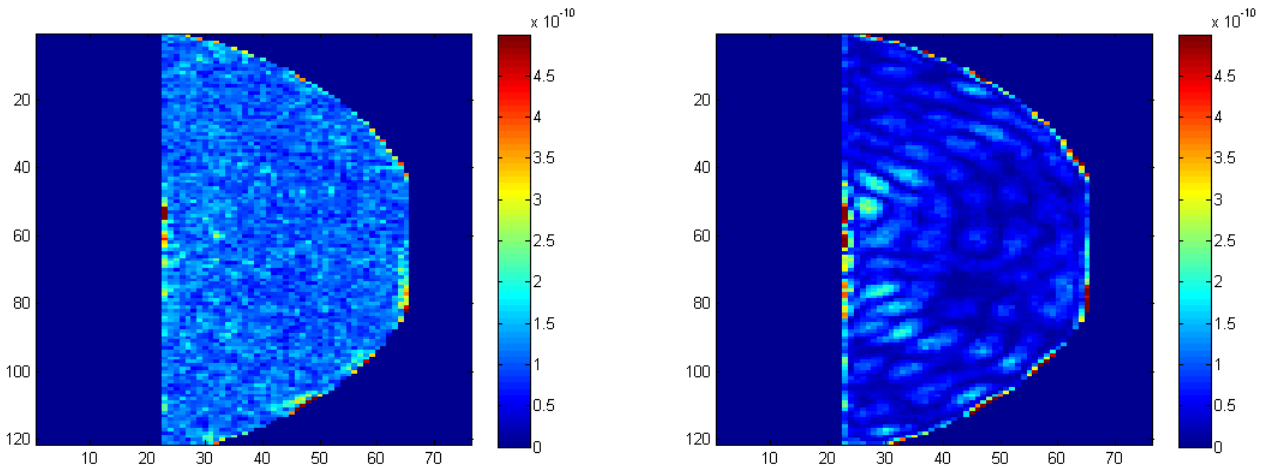Figure 9. The estimated incoherent part of the wavefront in test #12, over a 2% band centered at 768nm.

Figure 10. *Left.* MADN of contrast in dark hole across the 25 iterations of in test #12 (incoherent) *Right.* MADN of contrast in dark hole across the 25 iterations of in test #12 (coherent).
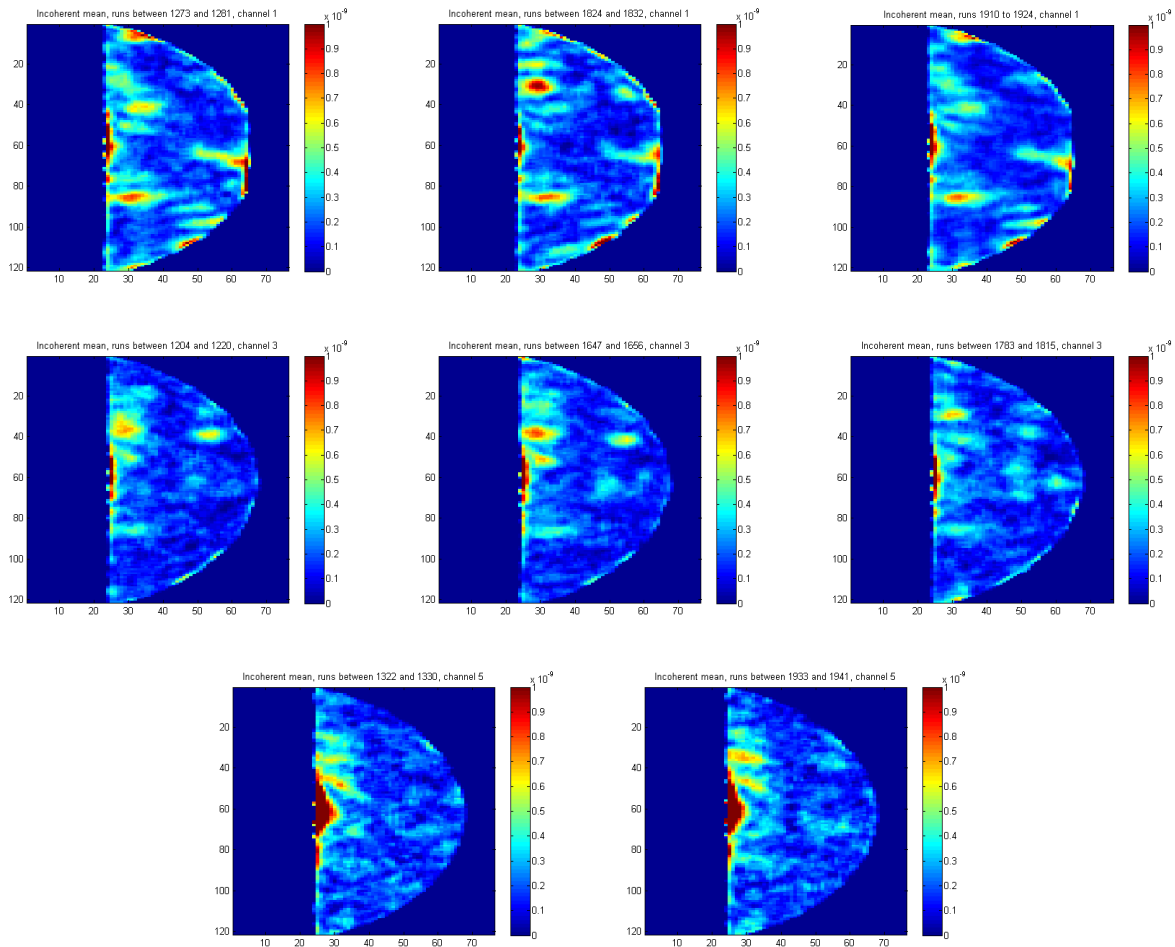
Figure 11. *Top row.* Incoherent means over the final iterations of runs suppressing over a 2% band centered at 768nm, taken on 1/22/13, 1/28/13, and 1/29/13. (Tests #3, 9, and 12.) *Middle row.* Incoherent means over the final iterations of runs suppressing over a 2% band centered at 800nm, taken on 1/22/13, 1/27/13, and 1/28/13. (Tests #1, 7, and 8.) *Bottom row.* Incoherent means over the final iterations of runs suppressing over a 2% band centered at 832nm, taken on 1/23/13 and 1/29/13. (Tests #4 and 13.)

[9] Sidick, E., Shaklan, S., Balasubramanian, K., Krist, J., and Cady, E. J., "High-contrast coronagraph performance in the presence of focal plane mask defects," Proc. SPIE 9143 (2014).

[10] Starck, J. L. and Murtagh, F., [Astronomical image and data analysis]. Springer (2007).

[11] Maronna, R. A., Martin, R. D., and Yohai, V. J., [Robust statistics]. (2006).

Appendix: Wavefront estimation algorithm

Estimation of the complex image-plane electric field in HCIT is done by applying probes: known offsets, generally in positive and negative pairs, to the deformable mirror which are expected to modulate the field in a region of interest. This currently requires:

- A data file containing 5 (or more) images. These include one image with no probes and two or more pairs of images. In each pair, the images are taken with identical offsets to the nominal DM position, but with opposite sign. We most commonly run with 5 images for speed, and the below algorithm reflects this.

- The current DM setting, as well as the settings used for the probes.

- A propagation model of the current coronagraph testbed configuration. This includes any knowledge of starting wavefront errors. This is required for estimation of the probe phases; the rest of the estimation is not model-based.

Given these elements, we run the following sequence (explained more fully in [1]):

1. Read in 5 images (I_0, I_{1+}, I_{1-}, I_{2+}, I_{2-})

2. Read in a list of 5 DM settings (unprobed, first pair, second pair)

3. Using the model, propagate the five DM settings, returning an electric field at the image plane.

4. Extract 4 complex delta electric fields (ΔE_{1+}, ΔE_{1-}, etc.) by subtracting the first unprobed field from each of the remaining 4.

5. Create 2 phase angles ϕ_1, ϕ_2 for these fields by computing:

$$\phi_1 = \arctan \frac{Im(\Delta E_{1+}) - Im(\Delta E_{1-})}{Re(\Delta E_{1+}) - Re(\Delta E_{1-})}, \tag{2}$$

$$\phi_2 = \arctan \frac{Im(\Delta E_{2+}) - Im(\Delta E_{2-})}{Re(\Delta E_{2+}) - Re(\Delta E_{,-})}. \tag{3}$$

(These represent the phase of the probe fields; we use the measured amplitude as the amplitude.)

6. Get probe amplitudes a_1, a_2 by computing

$$s_1 = (I_{1+} + I_{1-})/2 - I_0, \tag{4}$$

$$s_2 = (I_{2+} + I_{2-})/2 - I_0, \tag{5}$$

setting all $s < 0$ to $s = 0$, and computing $a_{1,2} = \sqrt{s_{s \geq 0|1,2}}$.

7. Compute probed intensity changes with

$$\delta_1 = (I_{1+} - I_{1-})/2, \tag{6}$$

$$\delta_2 = (I_{2+} - I_{2-})/2. \tag{7}$$

8. Estimate the complex coherent electric field (E_{coh}) at each image-plane pixel.

   (a) If either probe amplitude is zero at that pixel, set E_{coh} to zero.

   (b) Otherwise, compute the complex E_{coh} at each pixel from:

$$\begin{bmatrix} Re(E_{coh}) \\ Im(E_{coh}) \end{bmatrix} = \frac{1}{2} \begin{bmatrix} a_1 \cos \phi_1 & a_1 \sin \phi_1 \\ a_2 \cos \phi_2 & a_2 \sin \phi_2 \end{bmatrix}^{-1} \begin{bmatrix} \delta_1 \\ \delta_2 \end{bmatrix} \tag{8}$$

   If there are more than two probe pairs, the inverse will be replaced with a pseudoinverse.

9. Compute the incoherent intensity contribution I_{inc} at each pixel from $I_0 - |E_{coh}|^2$.